Nonlinear bio-imaging and detection with ultrafast lasers

Extermann, Jérôme

UNIVERSITÉ DE GENÈVE
Groupe de Physique Appliquée

FACULTÉ DES SCIENCES
Professeur J.-P. WOLF

Nonlinear Bio-Imaging and Detection with Ultrafast Lasers

THÈSE

présentée à la Faculté des Sciences de l'Université de Genève
pour obtenir le grade de Docteur ès Sciences, mention Physique

par

Jérôme EXTERMANN
de
Genève (GE)

Thèse No 4201

GENÈVE
Atelier de reproduction ReproMail
2010

UNIVERSITÉ
DE GENÈVE

FACULTÉ DES SCIENCES

Doctorat ès sciences
mention physique

Thèse de *Monsieur Jérôme EXTERMANN*

intitulée :

" Nonlinear Bio-Imaging and Detection with Ultrafast Lasers "

La Faculté des sciences, sur le préavis de Messieurs J.-P. WOLF, professeur ordinaire et directeur de thèse (Groupe de Physique Appliquée), L. BONACINA, docteur (Groupe de Physique Appliquée), D. PSALTIS, professeur ordinaire (Ecole Polytechnique Fédérale de Lausanne – Faculté des sciences et techniques de l'ingénieur – Institut de microtechnique – Laboratoire d'optique – Lausanne, Suisse), M. JOFFRE, professeur (Institut de la Santé et de la Recherche Médicale – Laboratoire d'Optique et Biosciences – Ecole polytechnique - Palaiseau, France), et Y. MUGNIER, docteur (Université de Savoie – Polytech'Annecy-Chambéry – Laboratoire Systèmes et Matériaux pour la Mécatronique – Annecy-le-Vieux, France), autorise l'impression de la présente thèse, sans exprimer d'opinion sur les propositions qui y sont énoncées.

Genève, le 12 avril 2010

Thèse - 4201 -

Le Doyen, Jean-Marc TRISCONE

N.B. - La thèse doit porter la déclaration précédente et remplir les conditions énumérées dans les "Informations relatives aux thèses de doctorat à l'Université de Genève".

Ad augusta per angusta

——— Victor Hugo

Remerciements

Une thèse est une aventure tant scientifique qu'humaine, car les résultats qui y sont présentés sont les fruits d'interactions avec de nombreuses personnes sans lesquelles cet exercice n'aurait été possible. J'ai eu la chance de pouvoir accomplir la mienne dans un environnement où régnait un savant équilibre entre travail assidu et discussions décontractées. Cela, je le dois à vous tous qui m'avez entouré, conseillé, formé mais aussi avec qui j'ai travaillé, discuté ou collaboré. A vous tous, je voudrais dire ma gratitude pour tous ces instants partagés ensemble. J'ai choisi un ordre chronologique quant à l'apparition de tous les acteurs de la pièce de théâtre que fut cette thèse.

J'aimerai remercier Jean-Pierre de m'avoir écouté comme il sait si bien le faire lorsque j'ai poussé, pour la première fois, à l'improviste la porte de son bureau et m'avoir proposé un ticket pour une aventure fantastique: celle d'intégrer un groupe qui venait de naître et où une grande partie de l'installation restait à réaliser. Merci de m'avoir fait confiance, d'avoir partagé continuellement sa créativité et sa curiosité scientifique sans cesse renouvelées. Je resterai toujours fasciné par le nombre d'idées à la seconde qui lui viennent mais surtout par l'enthousiasme qu'il met à les communiquer.

S'il y a une personne qui m'a suivi, encadré, soutenu mais aussi mis à contribution sur de nombreux projets, c'est bien Luigi. Merci pour toutes ces heures passées à échanger chaque jour davantage. Merci pour avoir mis à disposition chaque fois que cela était nécessaire ses capacités de programmateur pour contrôler tous les appareils du laboratoire. Ses relectures attentives de ce manuscrit ainsi que ses remarques m'ont permis d'en arriver au présent résultat.

Premier compagnon de l'entresol de l'ancienne école de médecine, Michel, le bastion suisse résiste à l'envahisseur avec comme armes humour, franchise et précision. Je retiens ses compétences en dessin mécanique et en informatique qui m'ont été d'un grand secours tout au long de ma thèse. Il m'a aussi fait passer mon permis de transpalette, moyen de transport fort utile mais dont la conduite est subtile. Et puis, je me dois de le souligner ici: L'Impossible encore au début de ma thèse se réalisa avant sa fin: son mariage. Je n'ai jamais su si j'avais mis longtemps à achever mon doctorat ou si en fait l'Impossible ne l'était en fait pas tant que ça.

Les premiers mois de cette aventure m'ont permis de travailler avec François. Voir un tel orfèvre à l'oeuvre m'a beaucoup apporté et l'application de nombre de ses préceptes m'ont été essentiel lors des nombreuses heures passées par la suite au laboratoire.

Ces heures passées, entrecoupées de pause clope, devant un tableau, un fragment de code matlab ou une feuille remplie d'équations à échanger sur nos travaux avec nos connaissances respectives ont été un des points forts de ces années. Outre ces moments de délire et franche rigolade, ses capacités tant d'interaction que celle à ronger tous les stylos et crayons à portée de main font de Pierre plus qu'un colocataire de bureau, un vrai compagnon de route. Merci donc pour tous ces moments et pour le legs du fauteuil de nabab roumain qui me fut si précieux lors de ma rédaction.

Je repenserai encore pendant longtemps à ces longues heures passées au laboratoire à la traque aux photons et leurs artéfacts avec Ariana. Bonne chance à elle, la prochaine sur la liste des diplômés du groupe!

Maître en développements tant mécaniques qu'électroniques, sa capacité et sa volonté à concevoir et réaliser des solutions pour tous types de problèmes sont toujours un exemple à suivre. Bol'shoe spasibo Denis.

J'aurai toujours en souvenir cette image de Pierre comme se donnant complètement pour ce qu'il entreprend, avec enthousiasme et énergie, ainsi que les nombreux fous rire partagés à Genève ou à Paris. Mais aussi le vrombissement de sa moto et les tremblements de ce majestueux bâtiment lors ses décollages et atterrissages.

Ma participation à une campagne de terrain, Alizé, et plus généralement cette approche différente de la recherche, Jérôme, m'ont permis de passer d'excellents moments. Merci pour sa créativité et ses apports originaux.

Toujours disponible pour mes nombreuses questions techniques sur les cristaux, Yannick, le voltigeur des tenseurs, sa pédagogie m'a rendu accessible des pans entiers de la physique et essentiels à ce travail. Un grand merci à toi, l'Auvergnat, et bon vent à Bordeaux!

Cela a été un vrai plaisir de pouvoir travailler et échanger des idées mêmes farfelues avec Stefan, pour aboutir finalement à un prototype de façonneur d'impulsions fait de micro-miroirs. Ces moments devant un tableau à imaginer comment réussir à déformer un solide de la manière désirée resteront gravée dans ma mémoire pendant de nombreuses années.

Grazie Stefano per non avermi lasciato dimenticare le mie basi d'italiano e questo rappresenta molto per me. Grazie per questi due anni in quest'ufficio a discutere di tutto.

J'ai aussi eu le plaisir de travailler avec Ludger, Rami et Christelle. Bon vent à Thibaut qui prend la suite de cette thèse. De nombreux stagiaires et étudiants ont intégré le groupe pour des périodes plus ou moins longues. J'ai fortement apprécié l'interaction avec vous tous, et particulièrement les désormais masterisés Enrique et Sarah.

Je suis reconnaissant envers tous les membres de mon jury de thèse pour avoir accepté cette tâche sans hésiter, et particulièrement à M. Joffre, Y. Mugnier et L. Bonacina pour leurs remarques et suggestions.

A notre formidable équipe administrative, pour leur patience et leur efficacité pour toutes les démarches administratives qui m'ont concerné. Isabel, Laurence, Cécile et Nathalie, un immense merci. De même, merci à Claudio et Jean-Daniel pour leurs explications et solutions à mes récurrentes questions d'électronique. Pour Marc et Philippe qui nous ont quittés trop vite et dont le travail remarquable et personnalisé nous fait indéniablement défaut. Comment ne pas remercier Roland et toute son équipe de virtuoses pour la qualité et la précision de leurs pièces mécaniques qui ont contribué au succès de nos expériences.

A nos collègues de réunions Lyon-Genève au début de l'aventure, Véronique, Jin, Estelle, Noëlle, Laurent, Benoît, Mathieu, Miriam et bien d'autres. Merci à Véronique pour le prêt de son laser quand, à Genève, le laboratoire en était dépourvu. Je me souviendrai toujours des soirées à Bordeaux où Estelle m'a expliqué le fonctionnement du laser alors que je n'étais qu'un novice dans ce domaine.

Pour notre collaboration intense et fructueuse avec l'équipe du SYMME à Annecy, j'aimerai remercier Yannick, Ronan, Djanta et le reste de l'équipe. Avec une pensée spéciale pour Yannick et ces six mois passés à Genève à traquer ensemble des dizaines de ces tout petits cristaux à coup de photons.

Collaborateurs de Goettingen, Bordeaux ou Paris, ce fut un plaisir de travailler avec vous. En particulier, ma participation aux présentations grand public au Palais de la Découverte à Paris en 2006 et 2008 restera comme une étape marquante, avec comme point d'orgue les visages illuminés de ces enfants de 6 ou 7 ans lorsqu'on leur explique notre quotidien au laboratoire.

Je suis grandement reconnaissant à Wilfried pour m'avoir ouvert les portes et initié à l'aventure magique des systèmes MEMS ainsi qu'à Nico pour son accueil chaleureux.

Amies et amis, vous qui m'avez interrogé sur mon travail puis écouté patiemment mes explications, merci à vous tous. Un remerciement appuyé entre autres à Maurizio, Philippe, Jean, Max, Séverino, JP, Angela, Charlotte, Vanessa, Marion, Jessica, Sophie, Juliane et Gijs, Lysiane et Kim.

Une mention spéciale pour toute ma famille qui me soutenez depuis longtemps. Un immense merci à mes parents, à Cyrille, à Paul, à Mandy et à mes grands-parents.

Finalement, à toi, Linda. Les mots ni les pages ne sauraient suffire pour décrire tout cela, c'est hors norme. Choukran Qlby.

Genève, *Jérôme Extermann*
Septembre 2010

Contents

Summary

This work takes place in a general effort of our research group to develop new optical tools with applications in biology, medicine and environmental science.

We first address the use of *nonlinear nanocrystals* as optical probes for multi-photon microscopy. We demonstrate the possibility of retrieval of their spatial orientation and propose their use as probes of the local electric field. We then start a comparative study of different type of crystals, and we demonstrate that exploiting the inherent wavelength-flexibility of the second harmonic process they can be used as probe for deep tissue imaging. Taking advantage of the coherence of the second harmonic generation, we demonstrate the possibility to obtain the phase function of the ultrafast laser pulses by a Frequency-Resolved Optical Gating experiment with unprecedented spatial resolution. Finally, we show the observation of second harmonic radiation induced by an evanescent excitation.

In the second part, we present the progresses realized towards an all-optical identification of complex biomolecules by *phase-coherent schemes*. In this context, we show the development and the fabrication of a new pulse-shaper device able to tailor the electric field at wavelength unaccessible by standard transmission-based approaches. In parallel, we implement a new generation of algorithm for optimal control experiments, improving the results obtained with usual algorithms. Finally, we report the first optical characterization of a pulse-shaper device in the deep ultraviolet, region where most of the biological molecules absorbs.

In the last part, we address the question of the survival of phase-encoding for femtosecond pulses traveling through an extended *turbulent region*. This study is primordial for developing new phase-coherent identification schemes for stand-off detection. We show the general conditions of this process, and evaluate by a numerical study the use of wavefront correction techniques in situation where the atmospheric turbulence has a non-neglectable effect.

Résumé

Ce travail s'inscrit dans un effort plus important de notre groupe de recherche qui vise à développer de nouvelles méthodes de détection pour des applications en biologie, en médecine et en environnement.

Tout d'abord, nous avons étudié l'utilisation de *nano-cristaux non-linéaires* comme sondes optiques pour la microscopie multi-photonique. Nous avons démontré la possiblité de retrouver l'orientation spatiale de chaque nanocristal. Puis nous avons proposé leur utilisation comme sonde du champ électrique environnant. Nous avons mené une étude comparative sur différents nanocristaux en vue de d'identifier celui qui avait les meilleures propriétés pour des applications biologiques. Nous avons aussi exploité la flexibilité en longueur d'onde, inhérente au processus de génération de second harmonique, pour leur utilisation en imagerie de tissus. Parallèlement, nous avons utilisé la cohérence du processus afin de retrouver la fonction de phase des impulsions laser ultra-brèves au moyen de la méthode FROG. Pour finir, nous avons rapporté l'observation d'une radiation de second harmonique résultant d'une excitation évanescente.

Dans la seconde partie, nous avons présenté les progès réalisés en vue d'une identification entièrement optique de biomolécules complexes au moyen d'approches basées sur le *contrôle cohérent*. Pour ce faire, nous avons conçu et fabriqué un nouveau façonneur d'impulsions capable de moduler le champ électrique à des longueurs d'ondes jusqu'à présent restées inaccessibles en raison de limitations technologiques. Nous avons parallèlement introduit l'utilisation d'une nouvelle génération d'algorithmes pour des expériences de contrôle optimal et démontré une amélioration et une plus grande diversité des résultats ainsi obtenus. Finalement, nous avons caractérisé optiquement, et pour la première fois, un façonneur d'impulsions dans l'ultraviolet profond, région spectrale où se trouve les bandes d'absorption de la plupart des molécules biologiques.

Dans la dernière partie, nous nous sommes intéressés au problème de la conservation de la modulation de la phase d'impulsions femtosecondes lors d'un long parcours dans une *atmosphère turbulente*. Cette étude est importante en vue de l'application de l'identification d'aérosols à distance en utilisant le contrôle cohérent. Pour des situa-

tions où la turbulence atmosphérique a des effets non négligeables sur la conservation de l'information de phase contenue dans l'impulsion laser, nous avons proposé et estimé d'après des simulations numériques l'utilisation de correcteurs de front d'ondes afin d'en diminuer les effets.

Introduction

In 1960, the work of T. Maiman led to one of the major technological breakthrough of the 20^{th} century: the LASER. [1] In the year of its 50^{th} anniversary, we can say that the laser has assumed a fundamental role in a wide series of technological applications, spanning from industrial production, material processing, to public safety, diagnostics and clinical treatments and also entertainment.

One relatively recent but rapidly growing application is the use of laser for rapid identification of cellular and bacterial species. In this case, observable quantities are generated by physical processes resulting from the interaction by light and photo-active molecules. These detected signals can be exo- or endo-genous, depending on the application. As example of exogenous process, we can mention cell labeling with fluorescent molecular dyes which are extensively used in cell biology and medicine. On the other hand, endogenous fluorescent molecules are at the basis of optical detection protocols recently extended to airborne species. It is worth pointing out that generally these approaches do not lead to clear-cut identification, because endogenous molecules are very numerous and present overlapping features difficult to disentangle.

Remote sensing and rapid identification of pathogenic biological airborne agents are also urgent safety issues. The use of LIght Detection And Ranging method (LIDAR) can provide a decisive tool in the domain of public safety, while a fast detector of pathogenic bacteria is highly needed for patient safety in hospitals.

The development of such fast and selective optical approaches will have a non-negligible and positive impact on our quality of life. This PhD work takes place in this interdisciplinary context, at the frontier of optics, physics, material science, biology and engineering. It is a contribution to this ambitious goal.

After a theoretical introduction (Chapter 1) of the concepts used in this thesis, we describe the experimental implementation (Chapter 2). We then present the results obtained in three different topics I worked on during these four years.

- Optical characterization of novel nonlinear nanoparticles and their application as exogenous probes for cell labeling (Chapter 3).
- Development of a new reflective pulse-shaper and progresses towards optical identification of biomolecules (Chapter 4).
- Evaluation of the possible application of phase-coherent schemes in remote sensing through a turbulent atmosphere (Chapter 5).

Optical characterization of novel nonlinear nanoparticles and their application as exogenous probes for cell targeting

Although some endogenous molecules exhibit fluorescent properties, the intensity of exogenous fluorescing labels is typically order of magnitudes higher, which makes them attractive for several biological applications.

In 1931, Maria Goppert-Mayer introduced theoretically the notion of multi-photon excitation of a quantum system [2]. The experimental observation of the first nonlinear process has been realized only in 1961 by Franken [3], because of the lacking of intense sources able to overcome the extremely small probability of the process to occur.

The first illustration of two-photon excited fluorescence microscopy has been reported in 1990 [4] and since this date, the interest on this imaging technique has grown exponentially. The origin of this success relays several advantages this approach presents with respect to its linear counterpart, including higher spatial resolution, deeper sample penetration, better spectral separation between signal and excitation, and virtually no out-of-focus bleaching. [5]

Fluorescent dyes (Cyanines, GFP, YFP, CFP,..) are commonly used as markers as recently highlighted by the 2008 Nobel Prize for chemistry awarded to Osamu Shimomura, Martin Chalfie and Roger Y. Tsien for the discovery and development of the green fluorescent protein, GFP. [6]. However these molecules suffer from a major drawback: fast photo-degradation. Bleaching occurs already after the emission of $10^6 - 10^8$ photons in organic dyes [7] and $< 10^5$ photons in autofluorescent proteins. [8] The origin of bleaching is inherent to the excitation process of a quantum system involving real states. Fluorescing semiconductor quantum dots provide much higher photostability, but are known to suffer from blinking (strong fluorescence intensity variations over unpredictable timescales). [9, 10]

In the quest for the next generation of imaging bio-markers, successful probes have to prove to be non toxic, bright, stable against long term excitation, and able to generate a sharp contrast against background fluorescence. In this context, nonlinear optics in nanoparticles recently emerged as a very active field of research. In particular, second harmonic generation (SHG) was investigated both theoretically [11–14] and

experimentally on metal- [15, 16], semiconductor- [17, 18], and organic nanoparticles. [19, 20] Although many studies were dedicated to nanostructures or to ensembles of particles, SHG imaging of single nanorods and single organic nanocrystals was only recently demonstrated using laser scanning microscopy [20] and SNOM. [18, 19]

Provided that SHG conversion efficiency is large enough, SHG appears as an attractive alternative to fluorescence, as no bleaching nor blinking effects are expected as no absorption occurs and only virtual states are involved. [21, 22] The absence of phase-matching requirements in nanoparticles allows a large tunability of the excitation, and provides the possibility to double the full frequency spectrum of broad sources. This capability could be used for identifying the multiple scattering paths of the various spectral components of the incoming light improving depth penetration in tissues. [23]

We choose iron iodate nanocrystals for cell labeling because one of their advantages with respect to other similar probes resides in its non-toxic chemical composition, which very likely will not prevent its future application for *in vivo* studies.

The study of SHG nanoparticles has opened a parallel but intimately connected research effort related to the studies of the modifications of femtosecond pulses interacting with turbid samples. In fact, as nonlinear excitation of the sample is typically achieved by ultrashort laser pulses, a large number of techniques developed in the fields of time-resolved and coherent spectroscopy have recently been bridged to microscopy. For instance, pulse-shaping has been applied to temporally recompress femtosecond pulses at the measuring site, to improve spatial resolution [24], and to increase fluorescence excitation and harmonic generation yield [25]. Intra-pulse micro-CARS [26, 27] and coherent control microscopy have demonstrated successful for obtaining higher selectivity in the imaging of structures in very diverse samples [28, 29]. More recently, interest has been focused on the effects of pulse polarization, and the related capability to achieve control of optical near field. [30] Simultaneously, and to fully exploit the potential of these techniques, equally developed pulse diagnostics capabilities are necessary. In particular, considering that femtosecond pulses are prone to undergo modifications during their propagation (temporal stretching by group velocity dispersion, higher order distortions in the spectral-phase induced by microscope objectives [31], spectral amplitudes modulation by sample scattering [32] and absorption) an *in situ* measurement of the excitation pulse is customary for any advanced application.

The present study demonstrate the potentialities of inorganic nanocrystals for a broad range of applications. We first retrieve the orientation of single nanocrystals under tight focusing conditions, and propose them as probes of the local surrounding electric field. We then present the first results of a comparative study on various nanocrystals to highlight their different potentialities according to the envisaged applications. Moreover, we demonstrate their application for deep imaging for biological tissues. In addition, we used the coherence properties of the nonlinear emission to retrieve with nanometric spatial resolution the phase properties of the electric field at a tight focus. The combination of the coherence properties and the absence of phase-matching constrains allow the generation of all nonlinear process within the transparency range of the crystal and therefore the characterization of few cycle laser pulses even in adverse

conditions. We finish the chapter with the observation of the excitation and interferences between two single dipolar nanocrystals by an evanescent field.

Development of a new reflective pulse-shaper and progresses towards optical identification of biomolecules

Ultrafast spectroscopy emerged as a very efficient tool to study the dynamics of physical, chemical and biological processes, by providing light pulses with duration comparable or smaller than the typical evolution of molecular processes. The success of this approach for simple systems, culminated with the awarding of the 1999 Nobel Prize for chemistry to A.H. Zewail for his studies of the transition states of chemical reactions using femtosecond spectroscopy. [6]

In parallel, during the 80's, emerged the idea of quantum coherent control and to tailor the laser electric field to control chemical reactions [33–35]. This idea has developed in later years thanks to technological developments [36, 37], and the proposition to use closed-loop approaches to avoid the necessity to fully calculate the quantum evolution of complex systems [38] and ease the experimental realization of quantum control experiments. [39]

In the last decades, several application of coherent control have been reported ranging from steering of molecular reactions in gas- [39–41] and condensed- [42] phase, to selective excitation of chromophores [43], control of biophysical processes [44–47], control of decoherence [48], new imaging techniques [24, 26, 28, 49], high harmonic generation [50, 51], and lot more. [52]

The application of coherent control scheme to identify biomolecules by means of endogenous and label-free fluorescence is one of the goal of our research group. Applying phase-coherent modulation will generate constructive and destructive laser field interferences which we will use to probe the photodynamics of excited states of the biomolecule.

However, most important applications of coherent control in organic chemistry and biology require excitation in the UV. For instance, absorption bands of amino acids, proteins and nucleic acids in DNA-RNA all lie in the 200-300 nm region. Recent approaches for direct femtosecond pulse shaping in the near UV made use of acousto-optic [53–55], while indirect schemes are essentially based on frequency mixing of shaped pulses in the visible and near-infrared [56, 57]. Although encouraging, these techniques still suffer either of low throughput (some percent) due to diffraction losses or of insufficient spectral bandwidth (typ. 10% of the central wavelength). Group velocity dispersion in the crystal usually further reduces the flexibility of the output waveforms.

Considering the broad absorption features of organic molecules in solution and the fast decoherence time of their vibronic excitations, it is highly desirable to have at disposal an UV pulse shaper with no strict bandwidth limitations, based for instance on reflective elements such as deformable mirrors [58] or micromirror arrays (MEMS).

While plain deformable mirrors usually lack in spectral resolution, MEMS appear as an appealing solution for these requirements. With their pioneering work, Hacker *et al.* demonstrated the aptness of a 2D MEMS device from Fraunhofer IPMS for phase-shaping applications at 400 nm [59]. Several groups successively exploited the 2D features of the same MEMS chip for shaping NIR pulses in diffraction mode [60], as well as for shaping two beams (NIR and UV-VIS) simultaneously [61].

In the present study we report the advances towards the experimental identification of biomolecules by coherent control schemes. We start the conception and fabrication of linear MEMS array device specially developed for tailoring laser electric field in phase and binary amplitude over a spectral range spanning from the deep ultraviolet to the near-infrared. In the meanwhile, we applied a new generation of genetic algorithms to close-loop experiments and show its advantages for quantum control experiments and specially for discrimination problems. Finally, we report the optical characterization in the deep ultraviolet of a 2D MEMS device from Fraunhofer IPMS, the unique available device at the beginning of this thesis capable of phase-modulation at those wavelength.

Evaluation of the possible application of phase-coherent schemes in remote sensing in a turbulent atmosphere

Optical approaches are characterized by the possibility of standoff detection and their rapidity. For example, LIDAR is a remote optical technique routinely used to measure the presence of simple molecular species in the atmosphere. However, selectivity of methods based on linear interaction is not sufficient to address more complex airborne species because of the above mentioned reasons (spectral congestion, overlap of fluorescence bands). The idea behind the application of coherent control is to improve selectivity to compete with chemical and biochemical methods (very specific but also very time consuming) without giving the advantages of optical methods. [62–65]

Therefore a natural extension is the application of phase-coherent scheme to remote sensing and to detect not only the chemical component but also to identify the bio-agent present in the atmosphere. However, transmitting an optimally shaped pulse at long distance through the atmosphere is not fully straightforward.

No demonstration of the applicability of quantum control of molecular species at a distance was reported at the beginning of this work. The molecular phase-encoded information needed for selective excitation could be affected by several processes during its propagation through the atmosphere. First, the dispersion is a quasi-static phenomenon and can thus be corrected by adding a negative chirp (even nonlinear if necessary) on the spectral phase, related to the given target distance. Then to avoid nonlinearities such as Kerr effect or filamentation, laser power has to be reduced to the linear propagation regime. Linear and nonlinear absorption as well as scattering on aerosols and water droplets can also affect the spectral and phase properties of the pulse and have to be considered very cautiously. Finally, pointing variation and wavefront distortion of laser beam resulting from atmospheric turbulence have been studied for nanosecond and continuous laser.

In the last chapter we describe our experimental investigations of the phase perturbations of femtosecond laser pulses induced by atmospheric turbulence. We support the analysis of the experimental datas with simulation. Finally, we conclude with a numerical study of a spatial pre-compensation of the wavefront distortions and its possible application in remote identification of biomolecules.

CHAPTER I

Linear and Nonlinear (Nano-) Optics

In this chapter, we introduce the mathematical framework underlaying our experimental work. After a short introduction, we describe the generation and the phase modulation of femtosecond laser pulses in vacuum (Sec. I.1). We proceed by the spatial propagation in vacuum (Sec. I.2), before considering the propagation in linear and nonlinear media (Sec. I.3). Then we focus specifically on the field expression in the tight focusing regime (Sec. I.4), which allow us summarizing the framework of nonlinear nano-optics (Sec. I.5). Finally, we conclude with an overview of the temporal characterization methods of femtosecond laser pulses (Sec. I.6).

We start with a mathematical description of laser pulses. Maxwell equations describes the propagation of electromagnetic waves [66]:

$$\begin{aligned} \nabla \times \vec{E}(\vec{r},t) &= -\frac{\partial \vec{B}(\vec{r},t)}{\partial t} \\ \nabla \times \vec{H}(\vec{r},t) &= \vec{j}(\vec{r},t) + \frac{\partial \vec{D}(\vec{r},t)}{\partial t} \\ \nabla \cdot \vec{D}(\vec{r},t) &= \rho(\vec{r},t) \\ \nabla \cdot \vec{B}(\vec{r},t) &= 0 \end{aligned} \tag{I.1}$$

where $\vec{E}$ and $\vec{H}$ denote the electric and the magnetic field, respectively, $\vec{D}$ and $\vec{B}$ the electric and magnetic flux density, ρ and $\vec{j}$ the charge and current density. The electromagnetic flux density are also described by the electric polarization $\vec{P}$ and the material magnetization $\vec{M}$. The interaction between electromagnetic waves and matter

is obtained trough the macroscopic polarization:

$$\begin{aligned}\vec{D}(\vec{r},t) &= \varepsilon_0\varepsilon\vec{E}(\vec{r},t) + \vec{P}(\vec{r},t)\\ \vec{B}(\vec{r},t) &= \mu_0\mu\vec{H}(\vec{r},t) + \vec{M}(\vec{r},t)\end{aligned} \tag{I.2}$$

where ε_0 and μ_0 are respectively the dielectric permitivity and the magnetic permeability, the light velocity in vacuum is $c = \sqrt{\varepsilon_0\mu_0}$. ε and μ are material-dependent parameters describing the electric and magnetic properties of the material.

So far no assumption has been made on the material properties and these expressions are general. In the rest of this work, we will neglect the contributions of material magnetization ($\vec{M}(\vec{r},t) = 0$), charge ($\rho(\vec{r},t) = 0$) and current density ($\vec{j}(\vec{r},t) = 0$). Only the electric dipolar contribution of the polarization will be considered and higher orders of the multipole expansion neglected. Finally, for the optical materials considered, the relative magnetic permeability can be approximated to 1. Under these assumptions, the combination of the two curl's equations (combined with the identity $\vec{\nabla}\times(\vec{\nabla}\times\vec{E}) = \vec{\nabla}(\vec{\nabla}\cdot\vec{E}) - \vec{\Delta}\vec{E}$, where $\vec{\Delta}\vec{E} = \vec{\nabla}^2\vec{E}$ is the Laplacian of E) gives the wave equation:

$$\vec{\Delta}\vec{E}(\vec{r},t) - \vec{\nabla}\cdot(\vec{\nabla}\cdot\vec{E}) - \frac{1}{c^2}\frac{\partial^2\vec{E}(\vec{r},t)}{\partial t^2} = \mu_0\frac{\partial^2\vec{P}(\vec{r},t)}{\partial t^2} \tag{I.3}$$

To this point, we will first consider the propagation of the electric field in vacuum ($\vec{P}(\vec{r},t) = 0$) and come back later on the linear and non-linear interactions between pulses and matter ($\vec{P}(\vec{r},t) \neq 0$, see Sec. I.3). As vacuum is isotropic and source-free, $\nabla\cdot\vec{D} = 0$ and the second term of the left hand side of Eq. I.3 can be neglected ($\vec{\nabla}(\vec{\nabla}\cdot\vec{E}) \simeq 0$), we obtain then:

$$\vec{\Delta}\vec{E}(\vec{r},t) - \frac{1}{c^2}\frac{\partial^2\vec{E}(\vec{r},t)}{\partial t^2} = \mu_0\frac{\partial^2\vec{P}(\vec{r},t)}{\partial t^2} \tag{I.4}$$

The solution of this wave equation in vacuum ($\vec{P}(\vec{r},t) = 0$) is:

$$\begin{aligned}\vec{E}(\vec{r},t) &= \mathcal{E}_0\cos(\omega t - \vec{k}\cdot\vec{r} + \phi_0)\cdot\vec{e}\\ &= \frac{1}{2}\left[\mathcal{E}_0^+ e^{i(\omega t-\vec{k}\cdot\vec{r})} + \mathcal{E}_0^- e^{i(\vec{k}\cdot\vec{r}-\omega t)}\right]\cdot\vec{e}\\ &= 2\Re\left[\mathcal{E}_0^+ e^{i(\omega t-\vec{k}\cdot\vec{r})}\right]\cdot\vec{e}\\ &= 2\Re\left[\vec{E}(\vec{r},t)\right]\end{aligned} \tag{I.5}$$

with $\Re\{A\}$ the real part of A, $\vec{e}$ the unitary vector defining the polarization of the light pulses, $\left|\vec{k}\right| = \frac{\omega}{c}$ the wave vector in vacuum, ϕ_0 the absolute phase, $\mathcal{E}_0$ the amplitude and $\mathcal{E}_0^{\pm}$ the complex amplitude including ϕ_0. Eq. I.5 is the definition of the electric field in (3+1, spatial + time) dimensions.

As the wave equation (Eq. I.4) is linear, any linear combination of Eq. I.5 is also a solution of Eq. I.4. Therefore, the electric field of laser pulses in time domain can

be seen as the coherent superposition of plane waves with different frequencies and directions of propagation, but with a fixed phase-relation:

$$\vec{E}(\vec{r},t) = \frac{1}{4\pi}\int_{-\infty}^{+\infty}\int_{-\infty}^{+\infty}\vec{E}(\vec{k},\omega)e^{i(\omega t-\vec{k}\cdot\vec{r})}d\omega d\vec{k} \tag{I.6}$$

where $\vec{E}(\vec{k},\omega) = \vec{\mathcal{E}_0}(\vec{k},\omega)e^{i\phi(\vec{k},\omega)}$ and $\mathcal{E}_0$ (resp. ϕ) is the spectral amplitude (resp. spectral phase). $\vec{E}(\vec{k},\omega)$ is a complex quantity. As we will see in the following sections, and particularly for pulse shaping applications, $\mathcal{E}_0$ and ϕ will be the two crucial parameters.

In the next sections for better clarity, we will consider separately the temporal and the spatial propagation of the electric field. We will consider laser pulses linearly polarized along the $\vec{e}$ propagating along the z-axis.

I.1 Femtosecond laser pulses

The relation between time- and frequency-domain is given by the Fourier Transform (FT):

$$\begin{aligned} E(t) &= \mathcal{E}(t)e^{i\psi(t)} = \mathcal{F}^{-1}(E(\omega)) = \int_{-\infty}^{+\infty}E(\omega)e^{i\omega t}d\omega \\ E(\omega) &= \mathcal{E}(\omega)e^{i\phi(\omega)} = \mathcal{F}(E(t)) = \frac{1}{2\pi}\int_{-\infty}^{+\infty}E(t)e^{-i\omega t}dt \end{aligned} \tag{I.7}$$

where $\psi(t)$ is the temporal phase, $\phi(\omega)$ the spectral phase and $\mathcal{F}$ (resp. $\mathcal{F}^{-1}$) the Fourier Transform (resp. inverse Fourier Transform).

As we will experimentally consider only laser pulses with a bandwidth much narrower than the wavelength ($\Delta\omega \ll \omega$), we can apply the "Slowly Varying Envelope Approximation" (SVEA). Concretely, this approximation allows us to express the electric field as a product of a complex envelope $\mathcal{E}(t)$ and a carrier frequency ω_0, as the slow variations of the envelope are not affected by the high variations of the carrier frequency (note that this approximation is not anymore valid for few-cycle laser pulses where $\Delta\omega \approx \omega$ [67]):

$$E(t) = \mathcal{E}(t)e^{i\omega_0 t} \tag{I.8}$$

We can also define two physical relevant quantities, the temporal and the spectral intensities:

$$\begin{aligned} I(t) &= |E(t)|^2 \\ I(\omega) &= |E(\omega)|^2 \end{aligned} \tag{I.9}$$

The intensities are real numbers and give information about the amplitudes of the field but as they do not take into account the respective phase information, they do not completely define the electric field. We will come back to this point in a further section (I.6).

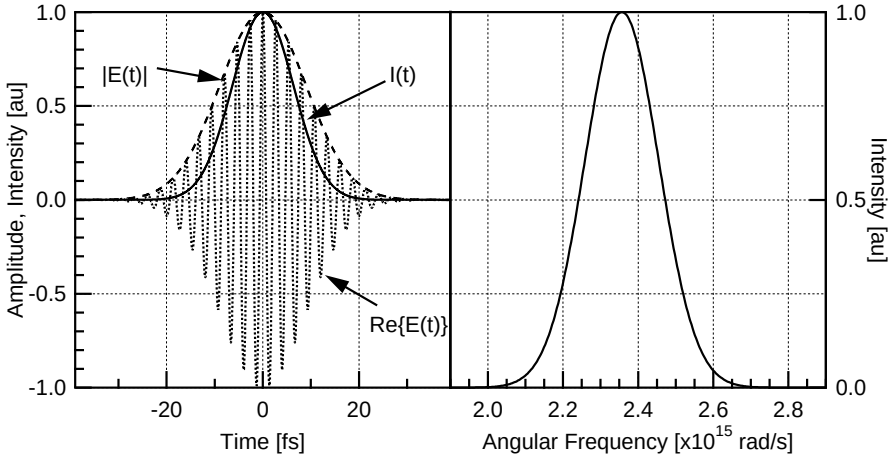

Figure I.1: Left panel: Temporal definition of a Gaussian pulse with $\Delta t_{\mathrm{FWHM}} = 15$ fs. The real part of the field $\Re\{E(t)\}$ is depicted (dotted line), together with the envelope $\mathcal{E}(t)$ (dashed line) and its intensity $I(t)$ (solid line). **Right panel:** In the reciprocal domain, the spectrum $I(\omega)$ is centered around the carrier angular frequency $\omega_0 = 2.35{\cdot}10^{12}$ rad/s, which corresponds to a central wavelength of $\lambda_0 = 800$ nm.

In the following, we will limit ourselves to the description of Gaussian-shape intensity profiles, as most of the experimental pulses can be reasonably approximated by this function. The envelope can be either defined in time or frequency (assuming, here and for the rest of this work, the amplitude E_0 of the field to be $E_0 = 1$):

$$\begin{aligned} \mathcal{E}(t) &= e^{-\frac{2\ln 2 t^2}{\Delta t^2_{\mathrm{FWHM}}}} = e^{-\frac{t^2}{\sigma_t^2}} \\ \mathcal{E}(\omega) &= \mathcal{F}(\mathcal{E}(t)) = \sigma_t\sqrt{\pi}e^{-\frac{\sigma_t^2\omega^2}{4}} \end{aligned} \tag{I.10}$$

As well as the intensities:

$$\begin{aligned} I(t) &= |\mathcal{E}(t)|^2 = e^{-\frac{2t^2}{\sigma_t^2}} \\ I(\omega) &= |\mathcal{E}(\omega)|^2 = \sigma_t^2\pi e^{-\frac{\sigma_t^2\omega^2}{2}} \end{aligned} \tag{I.11}$$

We will refer to these two expressions as temporal intensity and spectral intensity (or spectrum). We have defined Δt_{FWHM} as the full width at half maximum (FWHM) of the intensity of the pulse $I(t)$, the pulse duration σ_t at e^{-2} of $I(t)$. These two quantities are related by:

$$\Delta t_{\mathrm{FWHM}} = \sqrt{2\ln 2}\cdot\sigma_t \tag{I.12}$$

Clearly, it is also possible to choose to define the same quantities in the frequency domain. We choose the temporal domain definition for convenience and because this approach is more consistent with the experimental work we performed. Fig. I.1 shows $E(t)$, $\mathcal{E}(t)$ and $I(t)$ for pulses compatible with our sources.

From the FT relation between time and frequency domains, we can see that a shorter pulse in the time domain would result in a broader pulse in the frequency

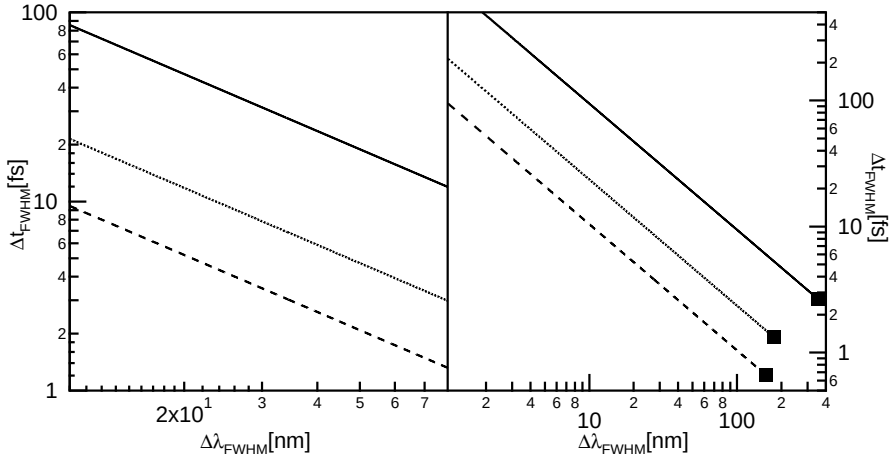

Figure I.2: The Time-Bandwidth product depicted in terms of Δt_{FWHM} and $\Delta\omega_{\mathrm{FWHM}}$ only for FT-limited pulses. The three experimentally used central wavelengths are represented $\lambda_\omega = 800$ nm (solid line), $\lambda_{2\omega} = 400$ nm (dotted line) and $\lambda_{3\omega} = 266$ nm (dashed line). ■ illustrate the value for single cycle Δt_{FWHM}. Left and right panels illustrate the same expression with different resolution.

domain. Defining the temporal pulse duration Δt as FWHM of the temporal intensity and the spectral width $\Delta\omega$ as the FWHM of the spectral intensity, we can define the Time-Bandwidth Product (TBP) (for Gaussian pulses, $\mathrm{TBP}_G = 0.44$) as:

$$\Delta t \Delta\omega \geq 2\pi \mathrm{TBP}_G \tag{I.13}$$

This relation is illustrated for the three central wavelengths ($\lambda_\omega = 800$ nm, $\lambda_{2\omega} = 400$ nm and $\lambda_{3\omega} = 266$ nm) of interest for this work in Fig. I.2. This figure represent the TBP for FT-limited pulses and allows for a fixed pulse duration immediate bandwidth conversion at different central wavelength.

So far, we did not consider the temporal phase function $\psi(t)$ (in Eq. I.7). By the definition of the pulse instantaneous frequency ω_{inst} (for a rigorous derivation, see [67]):

$$\omega_{inst}(t) = \omega_0 + \frac{\partial\psi(t)}{\partial t} \tag{I.14}$$

We can see that $\psi(t)$ gives the frequency as a function of time and can be expanded in a Taylor series around t_0:

$$\psi(t) = \psi_0 + \psi_1(t - t_0) + \frac{\psi_2}{2}(t - t_0)^2 + \cdots = \sum_{n=0}^{\infty} \psi_n \frac{(t - t_0)^n}{n!} \tag{I.15}$$

where $\psi_n = \frac{d^n\psi(t)}{dt^n}|_{t_0}$ is the temporal phase coefficient of the n-th order of the series.

By analogy, the spectral phase $\phi(\omega)$ (in Eq. I.7) permit us to express time as a function of frequency through a quantity called group delay (see also Sec. I.3.2):

$$\tau_{group}(\omega) = \frac{d\phi(\omega)}{d\omega} \tag{I.16}$$

The group delay corresponds at the arrival time of a given frequency ω. We can also expand $\phi(\omega)$ in a Taylor series around ω_0:

$$\phi(\omega) = \phi_0 + \phi_1(\omega - \omega_0) + \frac{\phi_2}{2}(\omega - \omega_0)^2 + \cdots = \sum_{m=0}^{\infty} \phi_m \frac{(\omega - \omega_0)^m}{m!} \tag{I.17}$$

where $\phi_m = \frac{d^m \phi(\omega)}{d\omega^m}|_{\omega_0}$ is the spectral phase coefficient of the m-th order of the series.

As for envelopes and intensities definitions, both spectral and temporal definitions are relevant. We have already discussed the choice of the temporal domain for the field definition. We see now the way phase contribution will be implemented in the simulation, keeping in mind our intention to match as close as possible the experiments.

We report two experimental observations. First, the addition of the two first terms of the Taylor series ($m, n = 0, 1$ in Eq. I.15 and Eq. I.17) has to leave the spectrum $I(\omega)$ unchanged. Secondly, experimentally adding a linear chirp implies a decrease of the temporal intensity. It is also well-known that an experimental linear chirp ($p = 2$) does not modify the spectrum of the laser (as example: prism or grating compressors, CPA amplifiers, chirp mirrors,...). For these reasons, the phase contribution to the electric field will be introduced in the frequency domain. Conceptually the definition of the temporal envelope with chirp ($\mathcal{E}_c(t)$) is:

$$\mathcal{E}_c(t) = \mathcal{F}^{-1}\left[\mathcal{F}\left(\mathcal{E}(t)\right) \cdot e^{i\phi(\omega)}\right] \tag{I.18}$$

In Fig. I.3, the effects of the first three terms of $\phi(\omega)$ are depicted. Please note that all temporal intensities have been normalized to allow direct pulse width comparison. First order spectral phase terms (ϕ_1) induce a pulse shift in time without any modification of the pulse. Linear chirp (ϕ_2 terms) will modify the pulse width by a linear increase or decrease of the instantaneous frequency (Eq. I.14). Finally, quadratic chirp (ϕ_3 terms) generate asymmetric pulses trains.

If one considers the case of pure linear chirp ($\phi_2 \neq 0$ and $\phi_{m\neq 2} = 0$), according to Eq. (I.18), the electric field can be expressed as:

$$\mathcal{E}_{\phi_2}(t) = \frac{\sigma_t}{\sqrt{\sigma_t^2 - 4i\phi_2}} e^{-\frac{t^2}{\sigma_t^2 - 4i\phi_2}} \tag{I.19}$$

One can notice the convergence of $\mathcal{E}_{\phi_2}$ to $\mathcal{E}(t) = e^{-\frac{t^2}{\sigma_t^2}}$ when ϕ_2 tends to 0. In this specific case, we can address the question of the modification of the FWHM pulse duration by the linear chirp ϕ_2. Having an initial pulse defined by $\Delta\tau_0$, the modified pulse duration $\Delta\tau_{\phi_2}$ can be expressed as:

$$\Delta\tau_{\phi_2} = \sqrt{\Delta\tau_0^2 + \left(\frac{4\ln 2 \cdot \phi_2}{\Delta\tau_0}\right)^2} \tag{I.20}$$

From Eq. I.19 and Eq. I.20, we can express the intensity of a pure linearly chirp pulse as (here also we set $I_0 = 1$):

$$I_{\phi_2}(t) = \frac{\Delta\tau_0}{\Delta\tau_{\phi_2}} e^{-\frac{2\sigma_t^2 t^2}{\sigma_t^4 + 16\phi_2^2}} \tag{I.21}$$

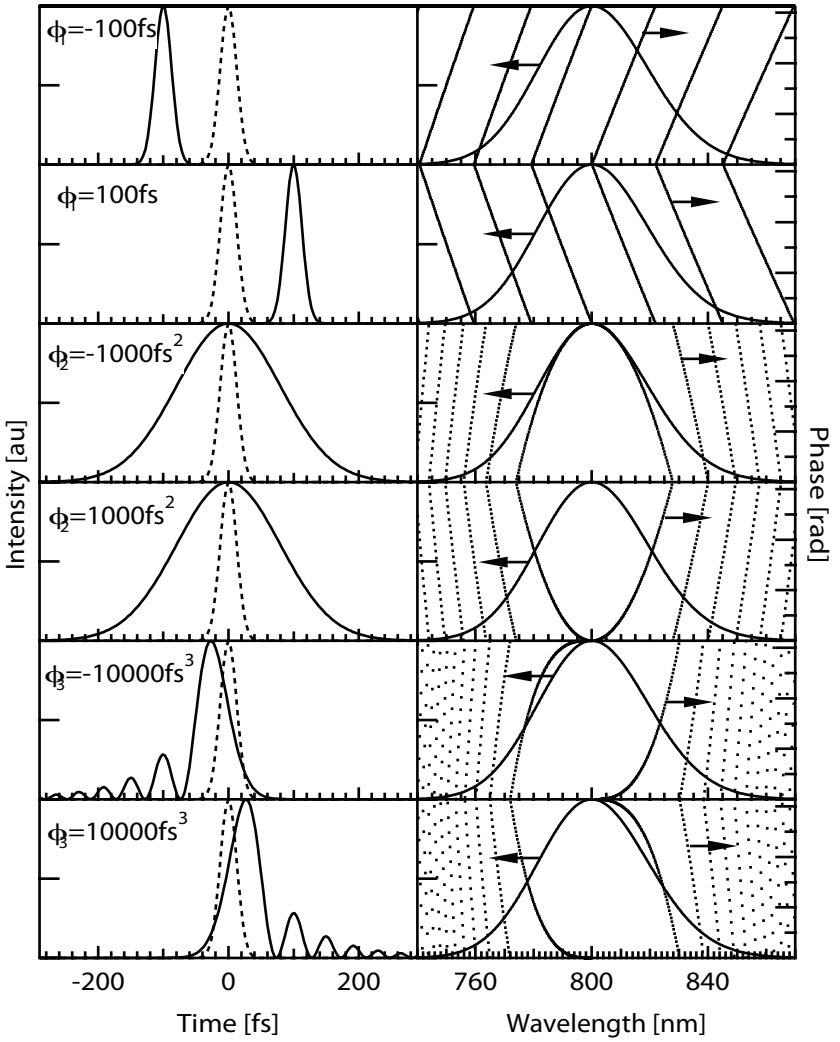

Figure I.3: Left column: Intensity of initial (dashed lines) and phase-modulated (solid lines) pulses are plotted as a function of time. **Right column:** Corresponding intensity (solid lines) and phase (dotted lines) are depicted as a function of the wavelength. Note that the phase functions have been wrapped on 2π and that the initial $\Delta t_{\mathrm{FWHM}} = 30$ fs. All intensity curves have been normalized.

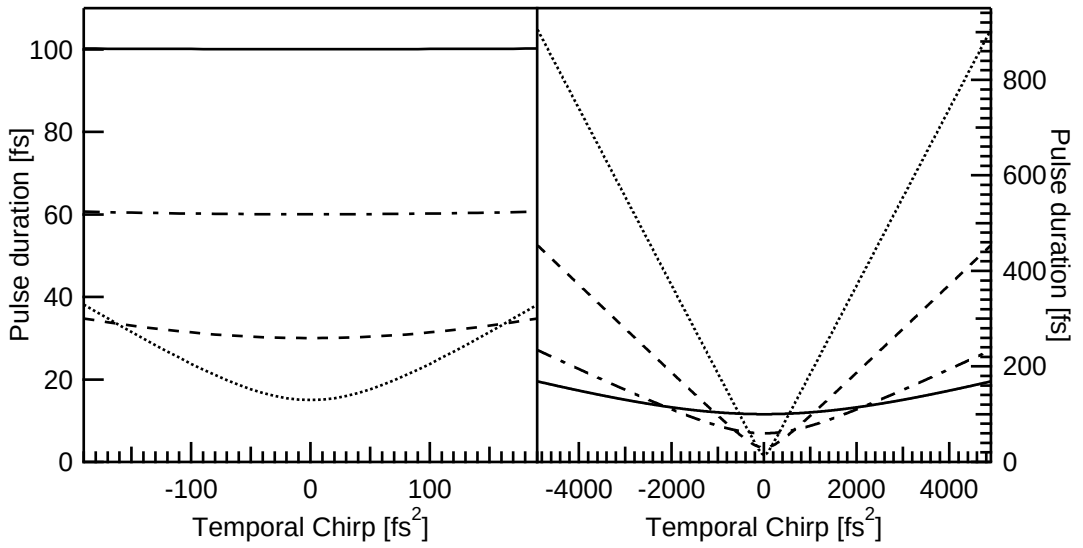

Figure I.4: Setting different pulses duration ($\Delta t_{\text{FWHM}} = 100$ fs (solid line), $\Delta t_{\text{FWHM}} = 60$ fs (dotted-dashed line), $\Delta t_{\text{FWHM}} = 30$ fs (dashed line), and $\Delta t_{\text{FWHM}} = 15$ fs (dotted line)). Δt is plotted as a function of linear chirp. For small chirps (left panel) $\Delta t_{\text{FWHM}} > 30$ fs are almost not affected, while for shorter pulses the effect is significant even for small chirp. The right panel depict the evolution of Δt_{FWHM} for larger linear chirps.

Fig. I.4 depicts Eq. I.20 and one can clearly see the larger effect of the linear chirp for smaller initial pulse durations. It is important to note that this expression is not a function of the carrier frequency nor of the central wavelength. Eq. I.20 is therefore valid for any pulse duration independently of the carrier frequency (provided the validity of the SVEA approximation).

So far we developed the mathematical framework to describe femtosecond laser pulses and consider also polynomial phase distortions together with their effect on the pulses. It is obvious that more complicated pulses can be generated by linear combination of the ϕ_m. Some examples, like sine modulations $\phi(\omega) = 1.23 \cdot \sin(x\omega)$ with x the frequencies of these modulations, are depicted in Fig.I.5 and illustrate the generation of pulse trains.

It is also possible to modulate other parameters of the pulse such as its amplitude ($\mathcal{E}(\omega)$) but also its polarization $\vec{e}$. We will not detail these modulations here, the related formalism together with some examples can be found in [68–70].

I.2 Propagation of femtosecond laser pulses

In this section, we will present the propagation of the electric field (Eq. I.10) in vacuum ($\vec{P} = 0$). For propagation in a linear medium, the wave vector including the medium response has to replace the vacuum wave vector (See Sec. I.3.2). In the following, we suppose the spatial dispersion of the frequencies to be homogeneous in the

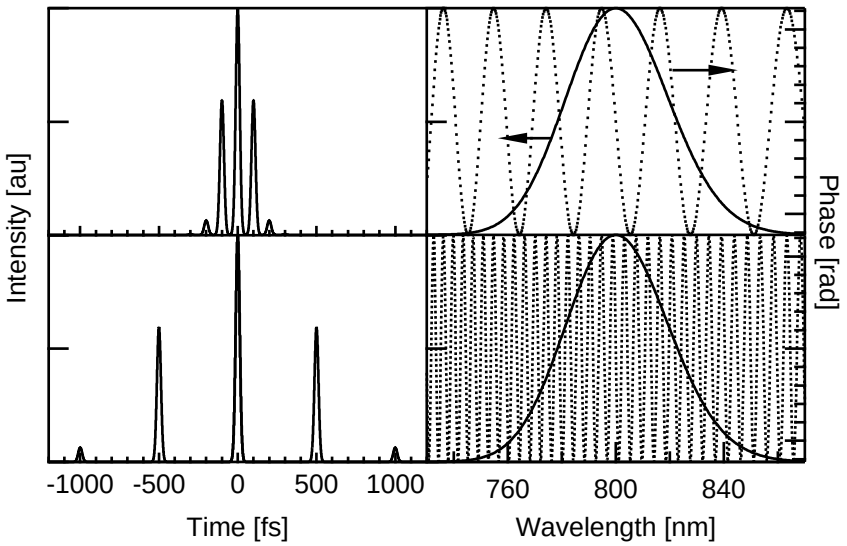

Figure I.5: Left column: Intensity of sine phase-modulated pulses are plotted as function of time for two values of the frequencies modulation $x = 100$ fs and $x = 500$ fs. **Right column:** Corresponding intensity (solid lines) and phase (dotted lines) are depicted as function of the wavelength. Note that the initial $\Delta t_{\text{FWHM}} = 30$ fs. All intensity curves have been normalized.

beam profile (i.e. absence of spatial chirp). Taking into account the initial wavefront curvature (R_{curv}) and radius (σ_{xy}) of the beam, the initial spatio-temporal envelope is defined as:

$$\mathcal{E}(x, y, t, z = 0) = \mathcal{F}(\mathcal{E}(x, y, \omega, z = 0)) \tag{I.22}$$

where $\mathcal{F}$ is the Fourier Transform with respect to the temporal coordinates (Eq. I.7). The previous equation can be decomposed in a temporal and a spatial part:

$$\mathcal{E}(x, y, \omega, z = 0) = \underbrace{\mathcal{E}(\omega) \cdot e^{i\phi(\omega)}}_{\text{Time-Frequency Definition}} \cdot \underbrace{e^{\left(-\frac{x^2+y^2}{\sigma_{xy}^2}\right)} \cdot e^{\left(-ik\left[\frac{x^2+y^2}{2R_{\text{curv}}^2}\right]\right)}}_{\text{Spatial Definition}} \tag{I.23}$$

In analogy with the treatment done for the temporal definition of femtosecond laser pulses (Sec. I.1), the beam propagation will be performed in the reciprocal space. We define a wave vector $\vec{k} = (k_x, k_y, k_z)$ and the spatial frequencies $\vec{\sigma} = (\sigma_x, \sigma_y, \sigma_z)$ (defined by $\sigma_i = k_i/2\pi$, $i = x, y, z$). The propagation of the beam in the spatial coordinates is the result of the convolution of the initial electric field (Eq. I.23) with the impulsive response $H(x, y)$ (propagator in direct space). As in the reciprocal space convolution is replaced by multiplication, we define the 2D spatial Fourier Transform ($\mathcal{F}_S$) supposing that the Fourier transform of each frequency component is defined in each point of the space. The initial electric field $\mathcal{E}(x, y, z = 0, \omega)$ can be associated

with its angular spectral density and *vice-versa:*

$$\begin{aligned}\mathcal{E}(x,y,z=0,\omega) &= \iint_{-\infty}^{+\infty} \mathcal{E}(k_x,k_y,z=0,\omega)e^{-i(k_x x+k_y y)}dk_x dk_y \\ \mathcal{E}(k_x,k_y,z=0,\omega) &= \frac{1}{4\pi^2}\iint_{-\infty}^{+\infty} \mathcal{E}(x,y,z=0,\omega)e^{i(k_x x+k_y y)}dxdy\end{aligned} \tag{I.24}$$

where $k_i = \frac{n\omega}{c}$ is the wave vector in each transverse direction ($i = x, y$).

According to the linear Maxwell theory, each monochromatic component is solution of the Helmholtz equation (Eq.I.4 with $\vec{P} = 0$). In the scalar approximation, one can show that the spectral density for any distance z can be deduced from the initial spectral density $\mathcal{E}(k_x, k_y, z = 0, \omega)$ as:

$$\mathcal{E}(k_x,k_y,z,\omega) = \mathcal{E}(k_x,k_y,z=0,\omega)\cdot\mathcal{H}_0(k_x,k_y,z,\omega) \tag{I.25}$$

where $\mathcal{H}_0$ is the free space propagator or optical transfer function. The free space is supposed to be homogeneous, isotropic and linear along the distance of propagation z. The propagation of the beam is performed independently for each frequency in the reciprocal space. The free space propagator is a filter function defined by (with $\vec{k} = \sqrt{k_x^2 + k_y^2 + k_z^2}$):

$$\begin{aligned}\mathcal{H}_0(k_x,k_y,z,\omega) &= e^{\pm ik_z z} \\ &= e^{\pm i|\vec{k}|\cdot z\cdot\sqrt{1-(k_x^2+k_y^2)c^2/\omega^2}}\end{aligned} \tag{I.26}$$

To calculate the propagation of a pulse from $z = 0$ to $z = d$, we apply the three successive operations. First the $2D$ spatial Fourier transform is applied in $z = 0$. Then it is multiplied by the adequate free space propagator $\mathcal{H}_0(k_x, k_y, d, \omega)$, and finally, the propagated electric field in Cartesian coordinates is directly calculated as the $2D$ inverse spatial Fourier transform (Eq. I.24).

As a consequence of Eq. I.26, it is important to note the two regimes of propagation. Assuming a propagation in vacuum ($n = 1$): when $k_x^2 + k_y^2 \leq (\omega/c)^2$ we have the planes wave propagation regime which turn into an evanescent waves propagation regime when $k_x^2 + k_y^2 > (\omega/c)^2$.

I.3 Linear and Non-linear Polarization and Propagation

When an electromagnetic wave is traveling through a medium, the response of the medium will be expressed in term of macroscopic polarization and will modify the temporal shape of the pulse through Maxwell's Equations (Eq. I.1). The present derivation is valid for isotropic homogeneous media far-from-resonance, i.e. for real refraction index. We can express the macroscopic polarization as a Taylor series of the

electric field [71]:

$$\vec{P} = \varepsilon_0(\underbrace{\chi^{(1)} \cdot \vec{E}}_{\vec{P}_{\mathrm{L}}} + \underbrace{\chi^{(2)} \cdot \vec{E}^2 + \cdots + \chi^{(n)} \cdot \vec{E}^n + \ldots}_{\vec{P}_{\mathrm{NL}}}) \tag{I.27}$$

where $\chi^{(n)}$ is the macroscopic n-th order dielectric susceptibility tensor of rank $(n+1)$. $\vec{E}^n = \bigotimes^n \vec{E}$ and is the n-th order tensor product of the electric field. As long as the field amplitudes remain small to moderate, the polarization is linear ($\vec{P}_{\mathrm{L}}$) but when the field amplitudes increase, the polarization become a nonlinear function of the electric field ($\vec{P}_{\mathrm{NL}}$). This nonlinear response will generate nonlinear optical effects. [72]

As femtosecond laser pulses are a discrete coherent superposition of monochromatic waves, the derivation of the polarization is less complicated in the spectral domain. Dealing with energy quanta and their combination instead waves superposition is also more intuitive. The Fourier relation between both polarization is:

$$\vec{P}^{(n)}(\omega) = \mathcal{F}\left[\vec{P}^{(n)}(t)\right] = \frac{\varepsilon_0}{2\pi}\int_{-\infty}^{+\infty} \vec{P}^{(n)}(t)e^{-i\omega t}dt \tag{I.28}$$

We can express the n-th order polarization in the spectral domain [72]:

$$\begin{aligned}\vec{P}^{(n)}(\omega) = \varepsilon_0 \int_{-\infty}^{-\infty}\int_{-\infty}^{-\infty}\cdots\int_{-\infty}^{-\infty} \chi^{(n)}(-\omega_\sigma;\omega_1,\omega_2,\ldots,\omega_n) \\ \times \vec{E}(\omega_1)\vec{E}(\omega_2)\ldots\vec{E}(\omega_n)\delta(\omega-\omega_\sigma)d\omega_n\ldots d\omega_2 d\omega_1\end{aligned} \tag{I.29}$$

where $\omega_\sigma = \sum_{i=1}^{n}\omega_i$ is the resulting frequency of the interaction process and the Dirac distribution holds for energy conservation, i.e. $\delta(\omega-\omega_\sigma) = 0$, if $\omega \neq \omega_\sigma$ and $\int \delta(\omega)d\omega = 1$.

If the process is linear ($n = 1$), $\omega_\sigma = \omega$ and the frequency will remain the same after the process, which is not always the case for nonlinear processes ($n > 1$). Eq. I.29 is general and can be adapted to all nonlinear processes. We will focus now on the susceptibility properties and then on the second order processes as it is the main nonlinear process used in this work.

I.3.1 Nonlinear susceptibility

The nonlinear susceptibilities of materials are expressed by tensors. Commonly, in order to reduce the number of independent coefficients, symmetry considerations can be applied [72]:

- Time-invariance and causality principle imply the invariance of the tensor under all the permutation of the (j_k, ω_k) pairs present in:[1]

$$\chi^{(n)}_{ij_1j_2\ldots j_n}(-\omega_\sigma;\omega_1,\omega_2,\ldots,\omega_n) \tag{I.30}$$

[1]This commonly accepted derivation is presently discussed in the community. For example, Prof. Joffre states that time-invariance is already necessary in Eq.I.29 and causality principle implies a relation between real and complex part of χ^n, type Kramers-Kronig. From this point of view, Eq.I.30 providing only a definition of the uniqueness of χ^n. [73]

- For a fixed crystalline structure, parity considerations on $P^{(n)}$ imply several component of the tensor to be zero. Each crystal class has a specific tensor associated. [74]

- When the optical frequencies are far from the lower resonance frequencies, $\chi^{(n)}$ is independent of frequency. Under this condition, permutation of the j_k index without permuting the corresponding frequency is allowed and known as *Kleinman Symmetries*. [75,76] If these assumptions hold, they will reduce the number of independent and non-vanishing coefficients of $\chi^{(n)}$.

- The ABDP symmetry states that for a medium transparent at the considered frequencies, the tensor is invariant under the $(n+1)!$ permutations between (i, ω_σ) and (j_k, ω_k). [77]

I.3.2 Linear and second order processes

Linear processes

In linear processes, the linear polarization can be expressed in term of the electric field and the susceptibility tensor $\chi^{(1)}$:

$$\vec{P}_{\mathrm{L}}(\omega) = \vec{P}^{(1)}(\omega) = \varepsilon_0 \chi^{(1)}(-\omega;\omega)\vec{E}(\omega) \tag{I.31}$$

We can substitute this equation into Eq. I.4 to obtain the wave equation in a linear medium in the frequency domain:

$$\vec{\Delta}\vec{E}(\omega) + \vec{k}^2(\omega)\vec{E}(\omega) = 0 \tag{I.32}$$

where the wave vector ($\vec{k}(\omega)$) is defined through the linear refractive index $n(\omega)$ which contains the linear response of the medium:

$$\vec{k}^2(\omega) = \frac{\omega^2}{c^2} n^2(\omega) = \frac{\omega^2}{c^2}(1 + \chi^{(1)}(-\omega;\omega)) \tag{I.33}$$

The combination of Eq. I.5 and Eq. I.33 give the solution of Eq. I.32. As no frequency mixing occur in linear propagation, each frequency component of the solution can be treated independently. The linear propagation of a femtosecond laser pulse over a distance L in a linear medium (Eq. I.25 and Eq. I.26 combined with Eq. I.33) will modulate the phase of the pulse (Eq. I.17) exactly as in Eq. I.18. We can express the relation between dispersion and linear medium response:

$$\phi(\omega) = |\vec{k}(\omega)|L = \frac{\omega}{c} n(\omega) L = \frac{\omega}{c} L \sqrt{1 + \chi^{(1)}(-\omega;\omega)} \tag{I.34}$$

As the dispersion induced is a Taylor series (Eq. I.17), we can develop Eq. I.33 in a Taylor series and identify term by term the medium contribution to the dispersion

(limiting to the first three terms):

$$\begin{aligned}\phi_0 &= k_0 L = \frac{\omega_0^2}{c^2} n^2(\omega_0) L \\ \phi_1 &= \left[\frac{dk(\omega)}{d\omega}\right]_{\omega=\omega_0} L = \left[\frac{n}{c} + \frac{\omega}{c}\frac{dn}{d\omega}\right]_{\omega=\omega_0} L \\ \phi_2 &= \left[\frac{d^2k(\omega)}{d\omega^2}\right]_{\omega=\omega_0} L = \left[\frac{2}{c}\frac{dn}{d\omega} + \frac{\omega}{c}\frac{d^2n}{d\omega^2}\right]_{\omega=\omega_0} L\end{aligned} \tag{I.35}$$

These expressions provide the origin of CEP, temporal translation, and group velocity dispersion in term of the material linear response and support the choice of defining the dispersion $\phi(\omega)$ in the spectral domain. The group delay definition (Eq. I.16) can also be linked to the medium properties.

Second order processes

For second order processes, according to Eq. I.29, the nonlinear polarization is written as ($n = 2$):

$$\begin{aligned}\vec{P}^{(2)}(\omega) &= \varepsilon_0 \int_{-\infty}^{-\infty}\int_{-\infty}^{-\infty} \chi^{(2)}(-\omega_\sigma;\omega_1,\omega_2)\vec{E}(\omega_1)\vec{E}(\omega_2)\delta(\omega-\omega_\sigma)d\omega_1 d\omega_2 \\ &= \varepsilon_0 \int_{-\infty}^{-\infty} \chi^{(2)}(-\omega_\sigma;\omega,\omega-\omega_\sigma)\vec{E}(\omega)\vec{E}(\omega-\omega_\sigma)d\omega\end{aligned} \tag{I.36}$$

where $\omega_\sigma = \omega_1 + \omega_2$ and $\chi^{(2)}_{ij_1j_2}$ is a component of a $(3 \times 3 \times 3)$ matrix.

Under the supposition $\omega_1 \geq \omega_2$, we can summarize the second nonlinear order processes in Tab.I.1 (if $\omega_1 = \omega_2$ we denote both frequencies as ω). [78]

Process name	Condition	$\omega_\sigma = \omega_1 + \omega_2$
Optical Rectification (OR)	$\omega_\sigma = \omega - \omega$ = 0	$0;\omega,-\omega$
Second Harmonic Generation (SHG)	$\omega_\sigma = -2\omega$	$-2\omega;\omega,\omega$
Sum Frequency Generation (SFG)	$\omega_\sigma = \omega_1 + \omega_2$	$-(\omega_1+\omega_2);\omega_1,\omega_2$
Difference Frequency Generation (DFG)	$\omega_\sigma = \omega_1 - \omega_2$	$-(\omega_1-\omega_2);\omega_1,-\omega_2$

Table I.1: Second order processes.

I.3.3 Second Harmonic Generation and Propagation

Second harmonic generation (SHG) is the principal nonlinear process investigated in this work. We will therefore focus on this specific case. In addition to the symmetries presented in the previous chapter resulting from macroscopic considerations, microscopic symmetry considerations have also to be taken into account. Having a spatial transformation $\vec{r} \rightarrow -\vec{r}$, the components of Eq. I.36 are modified as follows:

$\vec{P} \rightarrow -\vec{P}$ and $\vec{E} \rightarrow -\vec{E}$. Under this transformation and at the light of Eq. I.36, $\chi^{(2)} \rightarrow -\chi^{(2)}$. If the material possess an inversion symmetry, Eq. I.36 remains unchanged and $\chi^{(2)} = -\chi^{(2)} = 0$. For material where inversion symmetry holds, no SHG signal is generated and more generally no even nonlinear processes from bulk medium are allowed. But at every interface inversion symmetry is broken and even nonlinear process may occur. [78]

Generation

Because of the degeneracy of the excitation, the susceptibility tensor is invariant under j_k permutation for all k, ($\chi^{(2)}_{ij_1j_2}(-2\omega;\omega,\omega) = \chi^{(2)}_{ij_2j_1}(-2\omega;\omega,\omega)$). This degeneracy allow the reduction of the size of the tensor from 27 ($= 3^3$) to 18 ($= 3 \times 6$) elements. While the first index remains unchanged ($i \in [x,y,z] \equiv [1,2,3]$, with x,y,z the Cartesian coordinates), the simplification applies on the j_k index and occurs as follow [72]: $xx \rightarrow 1$, $yy \rightarrow 2$, $zz \rightarrow 3$, $yz = zy \rightarrow 4$, $xz = zx \rightarrow 5$ and $xy = yx \rightarrow 6$. The tensor coefficients in the reduced form are $\chi^{(2)}_{il}$ with $i \in [1,2,3]$ and $l \in [1,2,3,4,5,6]$. We can express the transformation in a matrix form:

$$\chi^{(2)}_{\mathrm{r}} = \begin{pmatrix} \chi_{11} & \chi_{12} & \chi_{13} & \chi_{14} & \chi_{15} & \chi_{16} \\ \chi_{21} & \chi_{22} & \chi_{23} & \chi_{24} & \chi_{25} & \chi_{26} \\ \chi_{31} & \chi_{32} & \chi_{33} & \chi_{34} & \chi_{35} & \chi_{36} \end{pmatrix} \tag{I.37}$$

We will used the reduced form of the tensor and voluntary omit the r symbol. As an example, the tensor for iron iodate crystals ($Fe(IO_3)_3$, symmetry class 6, widely used in this work) is expressed first in the general form and further simplified by applying the symmetries considerations as [74]:

$$\begin{aligned} \chi^{(2)}_{\mathrm{Fe(IO_3)_3}} &= \begin{pmatrix} 0 & 0 & 0 & \chi_{14} & \chi_{15} & 0 \\ 0 & 0 & 0 & \chi_{15} & \text{-}\chi_{14} & 0 \\ \chi_{31} & \chi_{31} & \chi_{33} & 0 & 0 & 0 \end{pmatrix} \\ &= \begin{pmatrix} 0 & 0 & 0 & 0 & \chi_{15} & 0 \\ 0 & 0 & 0 & \chi_{15} & 0 & 0 \\ \chi_{15} & \chi_{15} & \chi_{33} & 0 & 0 & 0 \end{pmatrix} \end{aligned} \tag{I.38}$$

Propagation

Having derived an expression for the polarization (Eq. I.36), we can substitute it into the wave equation (Eq. I.4) and obtain:

$$\vec{\Delta}\vec{E}_{\mathrm{SHG}}(\vec{r}) + k^2_{\mathrm{SHG}}\vec{E}_{\mathrm{SHG}}(\vec{r}) = -\frac{16\pi\omega^2}{c^2}\left[\mathbb{1} + \frac{\nabla\nabla}{k^2_{\mathrm{SHG}}}\right] \cdot \vec{P}^{(2)}(\vec{r}) \tag{I.39}$$

where $\mathbb{1}$ is the identity matrix of rank 3, k_{SHG} is the wave vector at $\omega_\sigma = 2\omega$, and $\mathcal{E}_{\mathrm{SHG}}$ the field envelope at frequency 2ω. For this section, we apply the slowly varying amplitude approximation (SVAA), meaning we can neglect the second term of the

right-hand side of Eq.I.39, which is equivalent to neglecting the $\nabla(\nabla \cdot E)$ term in Eq. I.3. If we apply the free space propagation (Eq. I.25) combined with Eq. I.5, Eq. I.39 can be expressed as [76, 78]:

$$\left(\Delta + k^2(\omega)\right) \mathcal{E}_{\text{SHG}} e^{ik_{\text{SHG}}z} = -\frac{16\pi\omega^2}{c^2}\chi^{(2)}\mathcal{E}_\omega \mathcal{E}_\omega e^{i(k_\omega + k_\omega)z} \tag{I.40}$$

where $\mathcal{E}_\omega$ is the field envelope at the frequency ω and for notation simplification, we have $\chi^{(2)} \equiv \chi^{(2)}(-\omega_\sigma; \omega, \omega - \omega_\sigma)$ here and for the rest of this work.

If we consider only the direction of propagation (z axis), we have:

$$\frac{\partial \vec{\mathcal{E}}_{\text{SHG}}}{\partial z} = \frac{i\omega^2_{\text{SHG}}\chi^{(2)}}{k_{\text{SHG}}c^2}\vec{\mathcal{E}}^2_\omega e^{i\Delta kz} \tag{I.41}$$

where $\Delta k = 2k_\omega - k_{\text{SHG}}$ is the *wave vector mismatch* or wave vector transfer. The solution of this equation is:

$$\vec{\mathcal{E}}_{\text{SHG}}(z) = \frac{i\omega^2\chi^{(2)}}{k_{\text{SHG}}c^2}\mathcal{E}^2_\omega \frac{e^{i\Delta kz - 1}}{i\Delta k} \tag{I.42}$$

The last term introduces intensity modulation in the generation of SHG field. At a distance z, the intensity of the SHG field is expressed as [78]:

$$I_{\text{SHG}}(z) \propto \left[\mathcal{E}_{\text{SHG}}(z)\right]^2 \propto \left[\frac{e^{i\Delta kz-1}}{i\Delta k}\right]^2 \equiv z^2 \left[\text{sinc}\left(\frac{\Delta kz}{2}\right)\right]^2 \tag{I.43}$$

The intensity of the SHG is a periodic function of the the distance z and is maximal when $\left[\text{sinc}(x)\right]^2 = 1$, therefore:

$$I \text{ is maximal when } \begin{cases} \Delta k = 0, \ \forall z \\ \text{size of } z \text{ is in the order of the wavelength} \end{cases}. \tag{I.44}$$

In this work, both situations are explored. The former usually referred as *phase-matching condition* is verified for harmonic frequency conversion of femtosecond laser pulses by bulk nonlinear crystals. When we will study the SHG from non-centrosymmetric nanocrystals with a size smaller than the wavelength, only the second condition in Eq.I.44 applies. Defining $L_c = \pi/\Delta k$ as the coherence length, we illustrate the SHG conversion efficiency in Fig. I.6. The effect of the phase matching condition on the conversion efficiency of the medium is evident for propagation in a medium over a distance $z > L_c/2$. However, when we do not consider anymore a propagation regime, but a scattering regime, as in the case of small nonlinear object with a size z_n smaller or in the order of the excitation wavelength, the SHG conversion grows monotonically with the size of the sample and the phase-matching condition is not a constrain anymore.

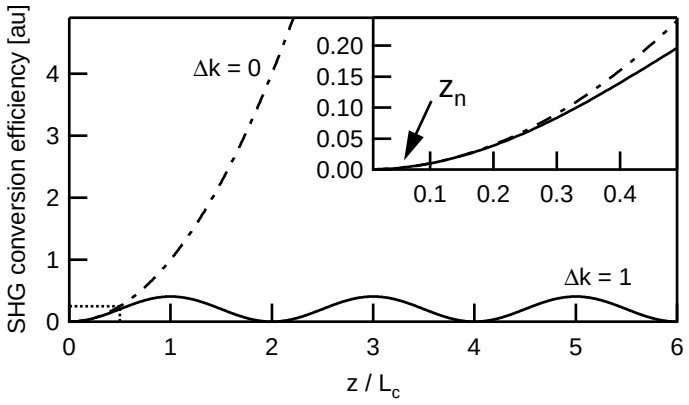

Figure I.6: Growth of the SHG conversion efficiency for perfect phase-matching ($\Delta k = 0$, dotted-dashed line) and non phase-matching ($\Delta k \neq 0$, solid line). Inset: enlargement for nanometric non-centrosymmetric structures Z_n where phase-matching condition is not anymore valid.

I.4 Focused Gaussian Beams

In the description of focusing field, notions of local and far field have to be carefully described. In this section we will consider only the spatial part of the beams. Based on the formalism presented in Sec. I.2 and following the derivation proposed by Richards and Wolf [79, 80] and extended by Novotny and Hecht for Gaussian beams profiles [81], we can find an analytical relationship between local and the far field distributions. We define the vector $\vec{s} = (s_x, s_y, s_z) = \left(\frac{x}{r}, \frac{y}{r}, \frac{z}{r}\right)$, with $r = \sqrt{x^2 + y^2 + z^2}$ the far field distance $r = r_\infty$ from the origin. We also neglect the contribution from the evanescent waves because of their rapid exponential decay, experimentally verified for microscopy experiments with far field detection. Under these assumptions, it can be shown [81] that the far field is the result of a single plane wave in the local field distribution while the contribution of other plane waves disappear due to destructive interferences. In other words, we can express the local field (in $z = 0$) as a function of the far field $\mathcal{E}_\infty$ in spatial coordinates and its reciprocal space respectively [81]

$$\begin{aligned} \mathcal{E}(x, y, z) &= \frac{ire^{-ikr}}{2\pi} \iint_{k^2 \geq k_x^2 + k_y^2} \mathcal{E}_\infty(k_x, k_y) \frac{e^{i(k_x x + k_y y \pm k_z z)}}{k_z} dk_x dk_y \\ \mathcal{E}(k_x, k_y, 0) &= \frac{ire^{-ikr}}{2\pi k_z} \mathcal{E}_\infty(k_x, k_y) \end{aligned} \tag{I.45}$$

We see that in the case of focusing field, the key parameters are the incident field $\mathcal{E}_{\text{in}}$ and the initial parameters of the focusing system.

This formalism provides us the tools for describing strongly focused Gaussian laser beams, which is necessary to generate nonlinear effect at low incident intensity. In Fig. I.7, we illustrate the *Sine Condition* from Geometrical Optics. The distance h to the optical axis to the focal length and the divergence angle θ between the refracted

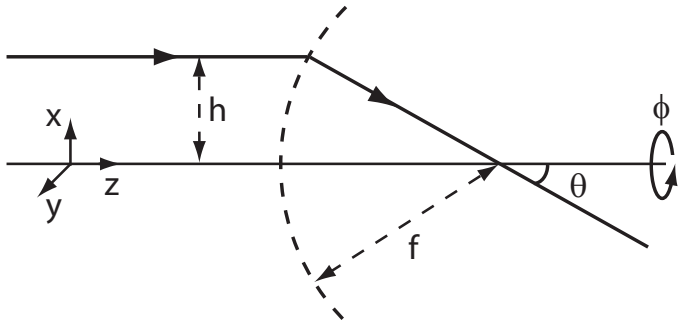

Figure I.7: Illustration in Geometrical Optics of an aplanatic focusing element by a spherical surface with radius f.

beam and the optical axis are related by:

$$h = f \sin\theta \tag{I.46}$$

As example, we can express the focal field in spherical coordinates ($x = \rho\cos\phi$ and $y = \rho\sin\phi$) and angular spectrum representation as a function of the far field: [81]

$$\mathcal{E}(\rho,\phi,z) = \frac{ikfe^{-ikf}}{2\pi}\int_0^{2\pi}\int_0^{\theta_{\max}} \mathcal{E}_\infty(\phi,\theta)e^{ik\cos\theta(z+\rho\tan\theta\cos(\phi-\varphi))}\sin\theta d\theta d\phi \tag{I.47}$$

where the integration over the θ angle is limited to a maximal angle corresponding to the objective properties.

I.4.1 Focused Gaussian Fields

Microscope objectives are classified according their *Numerical Aperture* (NA) defined by:

$$\mathrm{NA} = n\sin\theta_{\max} \tag{I.48}$$

where n is the surrounding medium refractive index and $\theta_{\max}$ the maximal angle of the refracted ray allowed by the objective (Fig. I.7).

Suppose an initial field $\mathcal{E}_{\text{ini}}$ linearly polarized along the x axis. The amplitude profile of the beam can be expressed either in Cartesian or Spherical coordinates:

$$\mathcal{E}_{\text{ini}}(\rho,\phi,z) = \mathcal{E}_0\cdot e^{-\left(x^2+y^2\right)/\sigma_{xy}^2} = \mathcal{E}_0\cdot \underbrace{e^{-f^2\cdot\sin^2\theta/\sigma_{xy}^2}}_{D(\theta)} \tag{I.49}$$

The factor $D(\theta)$ describes the spatial filling factor of the objective aperture (h, Fig. I.7) of the objective by the incoming beam radius (σ_{xy}). Experimentally, it is important to match the beam size with the dimensions of the optical aperture of the objective to have a diffraction-limited focus. We also assume that the waist of the beam coincides with the objective. It results a planar phase front when it impinges onto the objective. Here we assume the Fresnel losses to be negligible because of good anti-reflection coating.

Under these assumptions, we can express the far field $\mathcal{E}_\infty$ in spherical coordinates as a function of the initial field:

$$\mathcal{E}_\infty(\theta,\phi) = \frac{1}{2}\sqrt{\frac{n_1}{n_2}}\sqrt{\cos\theta}\mathcal{E}_{\text{ini}}(\theta,\phi)\begin{bmatrix} (1+\cos\theta)-(1-\cos\theta)\cos(2\phi) \\ -(1-\cos\theta)\sin(2\phi) \\ -2\cos\phi\sin\theta \end{bmatrix} \tag{I.50}$$

where n_1 and n_2 are respectively the refraction index of air and objective.

The use of the m-th order Bessel function J_m and its properties

$$\begin{aligned} \int_0^{2\pi} \sin(m\phi)e^{ix\sin(\phi-\varphi)}d\phi &= 2\pi(i^m)J_m(x)\sin(m\varphi) \\ \int_0^{2\pi} \cos(m\phi)e^{ix\cos(\phi-\varphi)}d\phi &= 2\pi(i^m)J_m(x)\cos(m\varphi) \end{aligned} \tag{I.51}$$

combined with Eq. I.47 and Eq. I.50 allow the expression of the focused field in spherical coordinates: [81]

$$\mathcal{E}_{\text{ini}}(\rho,\phi,z) = \frac{ikfe^{-ikf}}{2}\sqrt{\frac{n_1}{n_2}}E_0\begin{bmatrix} I_0+I_2\cos(2\phi) \\ I_2\sin 2\phi \\ -2iI_1\cos\phi \end{bmatrix} \tag{I.52}$$

with the I_m functions defined by ($m=0,1,2$):

$$I_m = \int_0^{2\pi} D(\theta)\sqrt{\cos\theta}\sin\theta\cdot g_m(\theta)\cdot J_m(k\rho\sin\theta)\cdot e^{ikz\cos\theta}d\theta \tag{I.53}$$

where $g_m(\theta) = \begin{cases} 1+\cos\theta, \text{if } m=0 \\ \sin\theta, \text{if } m=1 \\ 1-\cos\theta, \text{if } m=2 \end{cases}$ and $D(\theta)$ the filling factor.

In Fig. I.8, we present the simulation of the field intensities at the focus of a $NA = 1.3$ objective corresponding to a maximal angle of $\theta_{\text{max}} = 58.9°$. For this example, the initial field has been fixed as x polarized, the objective refractive index is $n_{oil} = 1.518$, the wavelength of the initial field is $\lambda = 800$ nm. From panels (A) and (B) of Fig. I.8, we can see that the focus is elongated along the z direction, which is the first effect of high confinement. Second, we notice the elongation of the lateral focal spot (in $z=0$) along the x direction compared to the y direction. Panels (C) to (E) show the field intensity in the focal plane ($z=0$) [82]. It is important to notice the field energy transfer between the initial x-polarized field into the longitudinal (z-axis) direction. These effects are not present in the paraxial approximation and illustrate the need of a vectorial description for tightly focused laser beams. In addition, when strong focusing is performed near a planar interface as for microscopy, additional effect have to be taken into account. Generation of symmetric reflected patterns occur, which incidentally may be very useful in the alignment of the laser beam into the microscope apparatus [81].

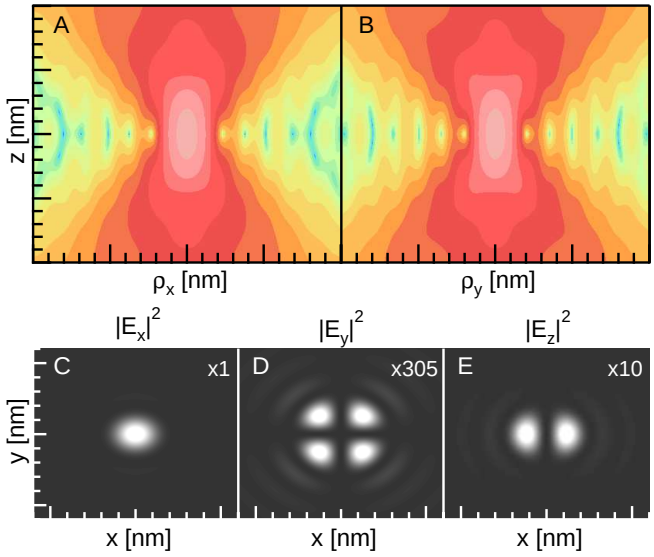

Figure I.8: Intensity distribution of a tightly focused Gaussian beam in a log scale represented in the XZ plane (A) and YZ plane (B). (C-E) plots depicts in the focal plane ($z = 0$) the intensity of the field components (linear scale). The incident beam is polarized along the x axis and the numerical aperture of the objective is NA=1.3. Distance between major ticks is $1\mu m$.

I.4.2 Spatial Resolution

As previously mentioned, in order to have a "diffraction-limited" focus, the diameter of the incoming beam and the size of the back aperture of the objective have to be matched. If it is not the case, the focus will have larger dimensions degrading the imaging resolution.

Having a point-like source object, the image obtained on a detector will be the convolution of the source object with the system's *point spread function* (PSF, also called system's impulse response). Its gives a measure of the quality of the imaging system by quantifying the spread of a point source [83]. Based on the angular representation formalism, a complete derivation of the point spread function can be performed. This derivation is beyond the scope of this chapter, but a detailed description can be found in [81, 83]. The point spread function in the paraxial approximation ($\theta_{\text{max}} \ll \pi/2$) in the image plane for a dipole oriented along the x axis is:

$$|E(x, y, z = 0)|^2 \propto \left[\frac{2J_1(2\pi\tilde{\rho})}{(2\pi\tilde{\rho})}\right]^2 \tag{I.54}$$

where $\tilde{\rho} = \text{NA}\rho/M\lambda$ and M the transverse magnification. From I.54, we can extract the width of the PSF $\Delta x = 0.6098M\lambda/\text{NA}$ which correspond to the distance between the maximum and the first minimum of the PSF (Eq. I.54).

We consider two emitters separated by a distance Δr in the focal plane and their associated PSF. Experimentally, the spatial resolution is defined by the numerical aper-

ture of the system and is defined by [81]:

$$\Delta r \geq \frac{\lambda}{\pi \mathrm{NA}} \tag{I.55}$$

Intuitively the distinction between two different emitters will be possible when the distance of the two PSF will be equal to the width of the PSF. The spatial resolution of our system is expressed by *Abbe*'s formula:

$$\Delta r = 0.6098 \frac{\lambda}{\mathrm{NA}} \tag{I.56}$$

This limit can be overcome in nonlinear microscopy, where the probability to excite a the sample through a nonlinear process is proportional to the n-th power of the process nonlinear order (i.e. square in the case of second processes). Therefore, the intensity needed to generate a two-photon process will be available in a very restricted volume compared to the one-photon process. This confinement will enhance the spatial resolution.

In confocal microscopy, the spatial resolution depends on the size of the pinhole inserted in the conjugated plane of the objective. The theoretical limit of spatial resolution is given by the diameter of the Airy disc and is never attained experimentally. [84] Contrarily, in nonlinear microscopy, the only limitation is the fulfilling of the back aperture of the objective and the theoretical limits can be reached. [84]

I.5 Second Harmonic Nano-Optics

Starting first with a general framework for the description of the SHG response in tight focusing microscopy, we proceed then to the description of a model to study the polarization response of nonlinear nanocrystals.

I.5.1 SHG in tight focusing microscopy

So far we have described the SHG process (in Sec. I.3.3) and the field in a tight focus (in Sec. I.4). In Chapter III, we present experimental results of SHG in microscopy with a high NA objective. The nonlinear media studied are non-centrosymmetric nanocrystals allowing SHG. We present an adaptation of the formalism developed by Cheng *et al.* for Coherent Anti-Stokes Raman scattering (CARS) [85] to the case of SHG microscopy.

The starting equation is the SHG wave equation (Eq. I.39). In the following we do not apply the slowly varying amplitude approximation, therefore, for a detection position $\vec{R}(R, \Theta, \Phi)$ and by introducing Green's function $G(x)$, we express the SHG field outside generated by a sample with a volume V:

$$\vec{E}_{\mathrm{SHG}}(\vec{R}) = -\frac{16\pi\omega^2}{c^2} \int_V \left[\mathbb{1} + \frac{\nabla\nabla}{k_{\mathrm{SHG}}^2}\right] \cdot G(\vec{R} - \vec{r}) \cdot \vec{P}^{(2)}(\vec{r}) dV \tag{I.57}$$

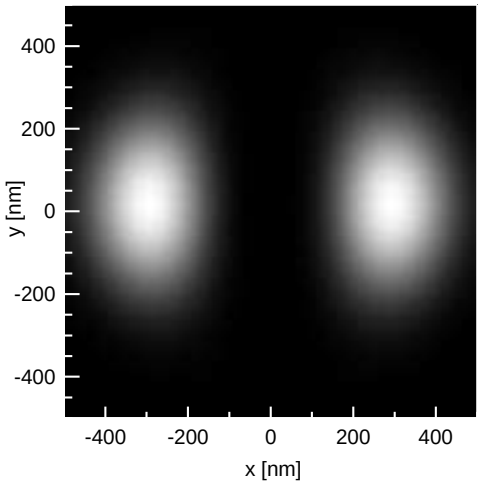

Figure I.9: Intensity distribution in the longitudinal direction $|E_z|^4$ of a tightly focused Gaussian beam in the focal plane ($z = 0$) the intensity of the SHG field components (linear scale). The incident beam is polarized along the x axis and the numerical aperture of the objective is NA=1.3.

The Green function can be defined ($\equiv$) and then approximated ($\simeq$) for far field ($|\vec{R}| \gg |\vec{r}|$) as follows:

$$G(\vec{R}-\vec{r}) \equiv \frac{e^{\pm ik_{\text{SHG}}|\vec{R}-\vec{r}|}}{4\pi|\vec{R}-\vec{r}|} \simeq \frac{e^{ik_{\text{SHG}}(|\vec{R}|-\frac{\vec{R}\cdot\vec{r}}{|\vec{R}|})}}{|\vec{R}|} \tag{I.58}$$

We can rewrite the Eq.I.39 which describes the SHG signal generated by a sample with an arbitrary shape and size.

$$\begin{aligned}\vec{E}_{\text{SHG}}(\vec{R}) = -\frac{4\omega^2}{c^2}\frac{e^{\pm ik_{\text{SHG}}|\vec{R}|}}{|\vec{R}|}\int_V e^{\pm ik_{\text{SHG}}|\vec{R}\cdot\vec{r}|} \\ \times\begin{bmatrix} 0 & 0 & 0 \\ \cos\Theta\cos\Phi & \cos\Theta\sin\Phi & -\sin\Theta \\ -\sin\Theta & \cos\Phi & 0 \end{bmatrix}\cdot\vec{P}^{(2)}(\vec{r})dV\end{aligned} \tag{I.59}$$

As we have so far limited ourselves to the far field approximation, no considerations on the shape of the sample or its size has been done, thus this equation is very general. [86]

We can integrate this field over a solid angle $d\Omega$ to take into account the presence of a collecting objective. If the objective collects the forward propagating signal, we take $\Theta \in [0\ \alpha_{\text{max}}]$ where α_{max} is the maximal collecting angle allowed by the objective. If the signal is epi-detected, the backward collection angle is $\Theta \in [-\pi\ \beta_{\text{max}} - \pi]$ (in the backward direction with the same objective having a maximal angle of β_{max}). The radiation power of the collected SHG signal is:

$$p_{\text{SHG}} = \frac{n_{2\omega}c}{8\pi}\int_0^{2\pi}\int_{\Theta_1}^{\Theta_2}|\vec{E}_{\text{SHG}}(\vec{R})|^2R^2\sin^2\Theta d\Theta d\Phi \tag{I.60}$$

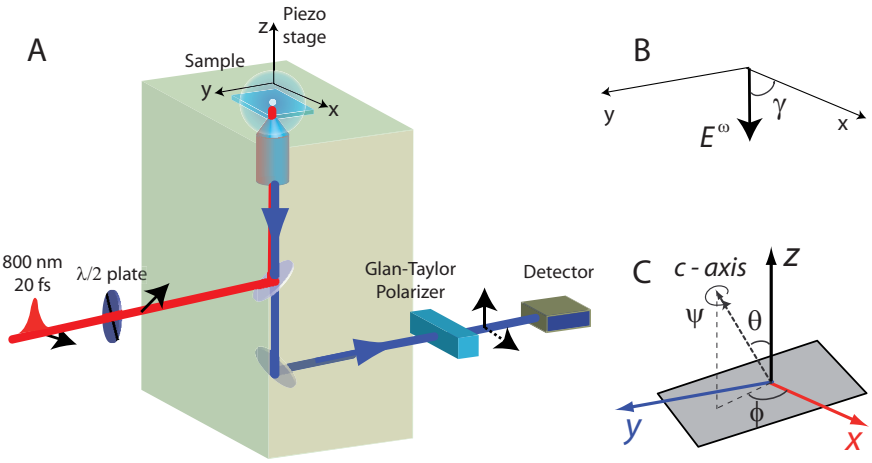

Figure I.10: Definition of the angles. The $c-$axis of the crystal is expressed in the laboratory frame $X,\ Y,\ Z$ by the Euler angles ϕ, θ and ψ, whereas the angle γ denotes the polarization of incident laser light on the sample plane.

In our specific case we are working with objects in the order of hundred nanometers and we can neglect the Gouy phase contribution: as illustrated in Fig. I.9, in the direction of polarization (x axis) the SHG field is zero on a distance of 150-200 nm. As the size distribution of the nanocrystals under study is around 80 - 200 nm (See Sec. II.7 and Sec. III.2), we can in first approximation neglect the contribution of the longitudinal component of the field ($|E_z|^4$, for representing the SHG field) [87]. In the rest of this work, we do not use the full model because of the need of analytical solution for fitting purposes, which is not possible using the framework presented in this section.

I.5.2 Polarization

We will present a framework developed in the group of J. Zyss (ENS, Paris) [20, 87]. Knowing the crystal tensor and having an excitation field with a well defined polarization, we can simulate the SHG response of the nanocrystals as a function of the linear polarization angle of the excitation. We will work out an analytical expression of the SHG intensity response recorded by the detector for two orthogonal polarization of the detection. This will allow us in Chapter III to fit the experimental data and retrieve the spatial orientation of individual nanocrystals in the laboratory frame. In Fig. I.10, we present a scheme of the experimental set-up (A) together with a graphical illustration of the parameters used in this model (B) and (C).

Before considering the interaction between light and crystal, we first have to define its orientation in the laboratory frame. According to Fig. I.10 (C), we use rotation matrices S (with Euler's angles ϕ, θ and ψ) to perform the change of the nonlinear susceptibility tensor orientation between the crystal ($\chi^{(2),C}$) and the laboratory frame

($\chi^{(2),L}$). Each tensor element $\chi^{(2),L}_{i,j,k}$ can be expressed:

$$\chi^{(2),L}_{ijk} = \sum_{\bar{i}\bar{j}\bar{k}} \chi^{(2),C}_{\bar{i}\bar{j}\bar{k}} S_{i\bar{i}} S_{j\bar{j}} S_{k\bar{k}} \tag{I.61}$$

corresponding to the tensorial notation:

$$\chi^{(2),L} = S \cdot \chi^{(2),C} \tag{I.62}$$

with the rotation matrix S given by:

$$S = \begin{pmatrix} \cos\psi\cos\theta\cos\phi - \sin\psi\sin\phi & -\sin\psi\cos\theta\cos\phi - \cos\psi\sin\phi & \sin\theta\cos\phi \\ \cos\psi\cos\theta\sin\phi + \sin\psi\cos\phi & -\sin\psi\cos\theta\sin\phi + \cos\psi\cos\phi & \sin\theta\sin\phi \\ -\cos\psi\sin\theta & \sin\psi\sin\theta & \cos\theta \end{pmatrix} \tag{I.63}$$

In the laboratory frame, we define the polarization as linearly varying over $\gamma = 360°$ in the transverse (XY) plane (Fig. I.10 (A) and (B)). The excitation field is supposed to be ellipticity-free, having no variation of its intensity over α, and to be at normal incidence, with at most two nonzero in-plane components [20]. Therefore it is defined at the fundamental frequency as [87]:

$$\vec{E}(\gamma,\omega) = E(\omega) \begin{bmatrix} \cos\gamma \\ \sin\gamma \\ 0 \end{bmatrix} \tag{I.64}$$

where $E(\omega)$ is the field in the frequency domain.

Simplifying the expression by removing the terms including $\vec{E}(z,\omega) = 0$, we express the SHG polarization in the laboratory frame as:

$$\vec{P}^{(2)}(\gamma,\omega) = \varepsilon_0 \chi^{(2),L} \begin{pmatrix} \cos^2\gamma \\ \sin^2\gamma \\ 0 \\ 0 \\ 0 \\ 2\sin\gamma\cos\gamma \end{pmatrix} \tag{I.65}$$

The radiation of the SHG field is obtained by introducing the nonlinear dipole moment $P^{(2)}$ in the expression for a radiating field perpendicular to $\vec{k}$ and the square of the field gives the expression of the radiated intensity:

$$\begin{aligned} \vec{E}_{radiated} &\propto \vec{k} \times (\vec{P}^{(2)} \times \vec{k}) \\ \vec{I}_{radiated} &= \left| \vec{E}_{radiated} \right|^2 \end{aligned} \tag{I.66}$$

We illustrate the radiated intensity in Fig. I.11 for a $Fe(IO_3)_3$ nanocrystal (Eq. I.38), for two orthogonal polarization of the detection and for an orientation (θ,ϕ) = (10,60). Varying the orientation (θ,ϕ) of the crystal will modify this figure. In Sec. III.1 and Sec.III.2, we will use this formalism to retrieve the orientation of each nanocrystal.

To finish the description of the signal detected (Fig. I.10 (A)), the integration over the solid angle $d\Omega$ of the objective (Eq. I.60) has to be performed.

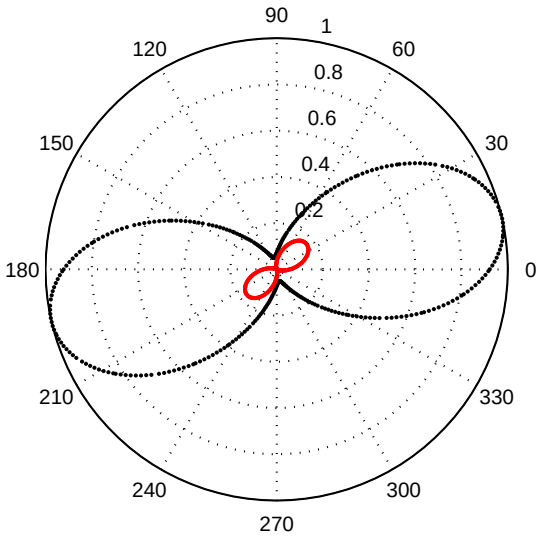

Figure I.11: Radiated intensity of a $Fe(IO_3)_3$ nanocrystal oriented in (θ,ϕ) = (10,60) for two orthogonal position of the analyzer (x axis in black and y axis in red).

I.6 Characterization of ultrafast laser pulses

This section is dedicated to the time-frequency characterization of femtosecond laser pulses. Soon after the generation of laser pulses, the problem of pulse characterization has appeared [88]. The reasons to characterize light pulses are numerous: determination of its pulse duration to know if the considered pulse is FT-limited or not (i.e. determination of the dispersion $\phi(\omega)$ of the pulse), better understanding of the light sources, retrieval of information about the traveled-across medium, characterization of the spectral/temporal phase for understanding the processes involved in quantum control and pulse-shaping experiments, etc. However, femtosecond pulse characterization remains challenging as it corresponds to a complex inverse problem. The extraction *in fine* of the intensity and the phase-characteristics as function of time and/or frequency is not easy and become harder for highly modulated pulses.

In the frequency domain, the spectral intensity $I(\omega)$ is measured by a spectrometer. As the light pulses are orders of magnitude faster than the best available electronic devices (detectors, circuits, oscilloscopes,...), no direct characterization is possible in the time domain. The temporal and spectral phase are also not directly measurable. Moreover using an integrating detector, Wong and Walmsley have shown that phase information can only be obtained by "time-non-stationary filtering" [89, 90].

This section will be separated into two parts: first the temporal retrieval of the temporal intensity $I(t)$ will discussed and secondly we will describe the full pulse characterization, by retrieving the phase functions, $\phi(\omega)$ and $\psi(t)$.

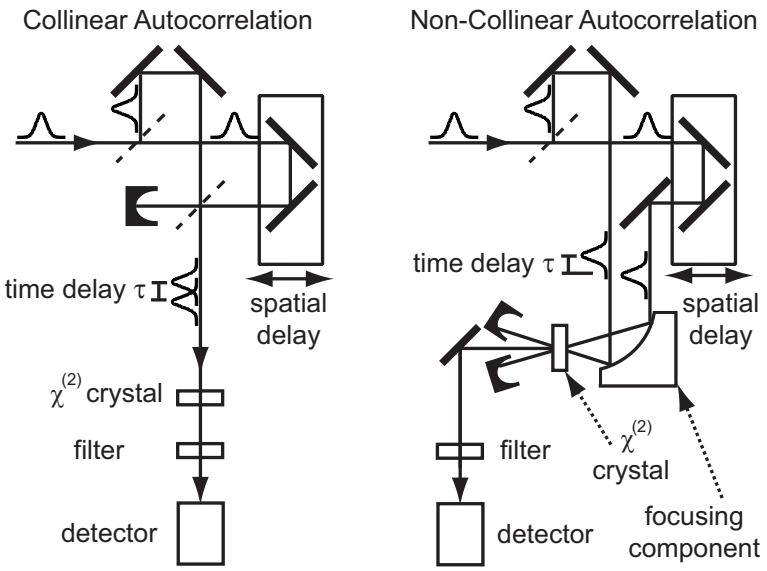

Figure I.12: Experimental implementation of (**Left Panel**) collinear autocorrelation and (**Right Panel**) non-collinear autocorrelations.

I.6.1 Temporal pulses characterization

The temporal characterization of a pulse f is done by performing a temporal convolution of this pulse with a reference pulse g, also called gate pulse. This method is called cross-correlation when $f \neq g$. The cross-correlation is defined by:

$$(f \star g)(\tau) = \int_{-\infty}^{\infty} f(t)\bar{g}(t-\tau)dt \tag{I.67}$$

where $\bar{g}$ is the complex conjugate of g and $\star$ denotes the convolution. When f and g originates from the same pulse, the cross-correlation is the convolution of the pulse with itself and is called autocorrelation. As in this work the majority of temporal pulse characterization are autocorrelations, we will focus our description on them.

As detectors do not allow us to resolve the temporal intensity ($I(t)$), the easiest solution is to translate the problem from the temporal to the spatial domain. In fact, one optical cycle at 800 nm is 2.67 fs and mechanical positioning systems have resolution of the order of ten nanometers. In an interferometric arrangement, one can change the optical path of one arm with nanometric precision and obtain the relative sub-single-cycle temporal resolution. At this point, to detect a signal proportional to the pulse overlap described in Eq. I.67, one needs a nonlinear medium. Depending on the experimental possibilities, can use two-photon fluorophores [91, 92] or two-photon photodiodes [93]. We used nonlinear crystals and the signal is then filtered and detected by an integrated detector.

From an experimental point of view as shown in Fig. I.12, two geometries can be adopted collinear (C) [94] or non-collinear (NC) [95]. Usually the NC-geometry is adopted because the interpretation of the data is easier, but in the case of experiments including objectives (as in microscopy or in micro-spectroscopy), the C-geometry has

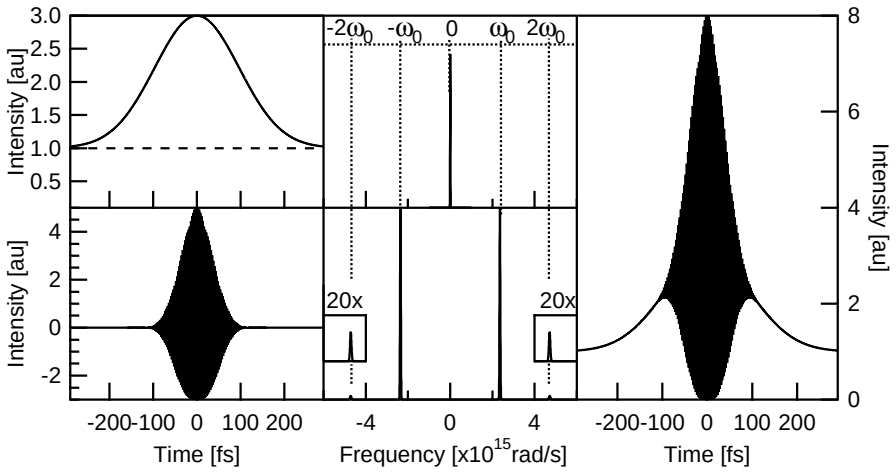

Figure I.13: Upper Left Panel: Graphical representation of constant and non-collinear terms of Eq. I.69. **Lower Left Panel**: Graphical representation of interferograms terms of Eq. I.69. **Central Panel**: Fourier transform representation of the corresponding traces in the left panel. $\omega_0 = 2.36 \cdot 10^{12}$ rad/s corresponds to a central wavelength of $\lambda_0 = 800$ nm. **Right Panel**: Graphical representation of collinear autocorrelation of a linearly chirped pulse. Pulse characteristics: $\Delta t = 30$ fs and chirp $\phi_2 = 1000$ fs^2.

to be adopted [96, 97].

We give here the full mathematical description of the outcome of the C geometry, which includes a term accounting for the result of NC geometry. After the recollimation of the two beams of the interferometer, the electric field is an explicit function of the delay τ induced by the moving-stage and can be written: $E_{col}(t) \propto [E(t) + E(t-\tau)]$. The integrated detector measures the interferometric second-order correlation of E_{col}:

$$G_2(\tau) = \int_{-\infty}^{+\infty} \left|[E(t) + E(t-\tau)]^2\right|^2 dt \tag{I.68}$$

It is important to notice that this expression is symmetric with respect to time, resulting from the equivalence of probe and gate pulse. This symmetry will result in

an uncertainty on the sign of the time axis. By expanding this expression, we have [98]:

$$\begin{aligned} G_2(\tau) &= \int_{-\infty}^{+\infty} \left| E^2(t) + 2E(t)E(t-\tau) + E^2(t-\tau) \right|^2 dt \\ &= \underbrace{\int_{-\infty}^{+\infty} \left[I^2(t) + I^2(t-\tau) \right] dt}_{\text{Constant term}} + \underbrace{2\int_{-\infty}^{+\infty} I(t)I(t-\tau)dt}_{\text{Intensity autocorrelation}} \\ &+ \underbrace{2\int_{-\infty}^{+\infty} \left[I(t) + I(t-\tau) \right] \Re\left\{ E(t)E^*(t-\tau) \right\} dt}_{\text{Modified interferogram of E(t)}} \\ &+ \underbrace{\int_{-\infty}^{+\infty} \Re\left\{ E^2(t)(E^*(t-\tau))^2 \right\} dt}_{\text{Interferogram of the SHG of E(t)}} \end{aligned} \tag{I.69}$$

Intensity autocorrelation corresponds to the usual result obtained by NC geometry.

One can note that the NC-autocorrelation term is contained into the collinear autocorrelation and NC-autocorrelation is also called intensity autocorrelation. A graphical representation can help out understanding the various contributions. In Fig. I.13, the left panels represent the terms of Eq. I.69 as follows: the constant and NC-autocorrelation terms are depicted in the upper panel, while the two interferograms in the lower one. We can observe that the fast oscillations coming from the mixing terms of Eq. I.69 are present only in the interferograms. They can be understood as interferences between the electric fields of the two pulses. Note that they are not graphically resolved because the pulse duration chosen here ($\Delta t_{\text{FWHM}} = 30$ fs) is much larger than one optical cycle at 800 nm (2.6 fs).

In the central panel, we depict on the left curves in the reciprocal space (by a Fourier transform) centered at ω_0. The origin of the contribution of each curve can be interpreted in terms of ω_0 shifts. Applying a filter in the frequency domain to remove interferometric terms results in converting a C-autocorrelation trace into a NC-autocorrelation. The sum of the left panels is depicted in the right panel and presents a typical collinear autocorrelation curve for linear chirped pulses. Constructive interferences are maximal when $\tau = 0$. Between $|\tau| = \pm 100$ fs and $|\tau| = \pm 200$ fs, wings typical for linearly chirped pulses are observed. When $|\tau| > 290$ fs, the two pulses are temporally separated and the autocorrelation signal is constant and results from the individual generation of the nonlinear signal by each pulse.

An example of autocorrelation for Fourier-limited pulses (left panel) and pure linear chirped pulses (right panel) are shown in Fig. I.14. In the case of the FT pulse, the wings are absent and interferences are present over the entire collinear autocorrelation signal. The NC-autocorrelation is super-imposed: one can appreciate an advantage of the C-autocorrelation, which is sensitive to the pulse phase (wings for example). The combination of C-autocorrelation and a spectrum can be sufficient to retrieve completely the electric field [99, 100] but the retrieval procedure needs highly resolved

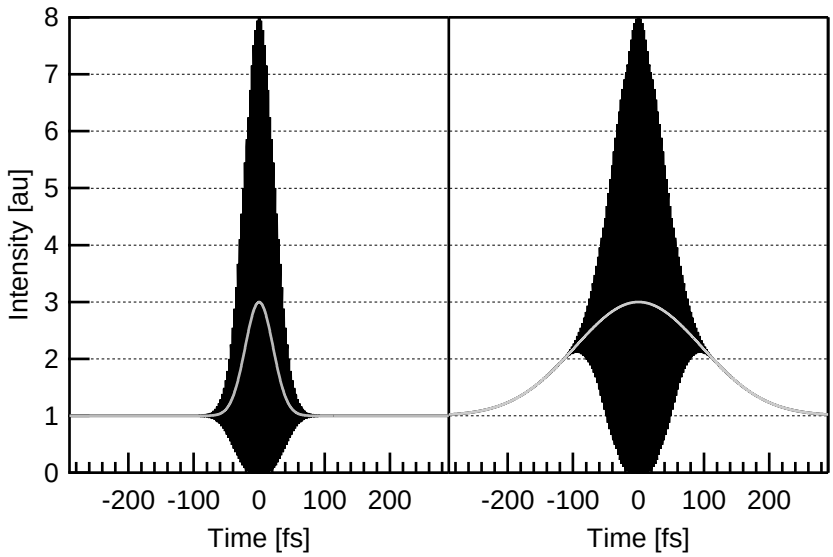

Figure I.14: Left Panel: Graphical representation of collinear autocorrelation of a Fourier-limited pulse. **Right Panel**: Graphical representation of collinear autocorrelation of a linearly chirped pulse. Pulse characteristics: $\Delta t = 30$ fs and chirp $\phi_2 = 1000$ fs^2. Superimposed in gray, the corresponding non collinear autocorrelation traces. All traces have been normalized, so the energy included in Fourier-limited and chirped pulses are not equal (no energy conservation).

traces with extremely low noise. Note also that correspondence between pulse duration in the C and NC traces can be easily done only when pulses are Fourier-limited.

In some situations, a single-shot approach is needed to measure the shot-to-shot variations of pulse characteristics (see for example Sec. V.2). In this NC case, the time delay among gate and probe pulses is projected over an angular coordinate and measured by an array detector. [67]

I.6.2 Phase characterization

An accurate and full characterization of femtosecond laser pulses can be obtained trough interferometric as well as non-interferometric measurements. Some examples of interferometric techniques are given in [27, 101–104].

In this work, we adopted the approach developed by Trebino and co-workers called FROG (Frequency-Resolved Optical Gating) [105–108]. The experimental implementation of FROG is an extension of an autocorrelation setup (Fig. I.12). It is sufficient to modify the detection by replacing the integrated detector by a spectrometer, a monochromator or an imaging spectrometer coupled with a charge coupled device (CCD) and to record spectrally dispersed the non-linear signal. However, the phase-matching condition on the nonlinear crystal has to be fulfilled, i.e. the bandwidth spectral acceptance of the nonlinear crystal has to be larger than the pulse bandwidth. As for cross-correlation, different type of FROG are possible depending on the exper-

imental conditions and non-linear process used: Second Harmonic FROG [109, 110], Polarization-Gating FROG [105,106], Third Harmonic FROG [111], Downconversion FROG or XFROG [112, 113] and lots more. Based on a comparison of these different techniques [114], SHG-FROG appear as the most sensitive and straightforward FROG which reinforces our choice of characterization technique. However and due to the transparency range of nonlinear crystals, this technique is clearly limited to the NIR and visible domain. Its description is given in a non-collinear (NC) geometry:

$$I_{\text{NC-FROG}}(\omega,\tau) = \left| \int_{-\infty}^{+\infty} E(t)E(t-\tau)e^{-i\omega t}dt \right|^2 \tag{I.70}$$

It is important to notice here that this expression is symmetric with respect to time ($I_{\text{SHG-FROG}}(\tau,\omega) = I_{\text{SHG-FROG}}(-\tau,\omega)$), like for autocorrelation. The result obtained from Eq. I.70 is a 2D trace usually depicted with time on the x-axis, wavelength on the y-axis and intensity recorded on the z-axis. Due to experimental constrains like microscope objectives, collinear (C) FROG description is [115]:

$$I_{\text{C-FROG}}(\omega,\tau) = \left| \int_{-\infty}^{+\infty} \left[E(t) + E(t-\tau)\right]^2 e^{-i\omega t}dt \right|^2 \tag{I.71}$$

By expanding this expression, we obtain an expression which can be related to the collinear autocorrelation (Eq. I.69) [116, 117]:

$$\begin{aligned} I_{\text{C-FROG}}(\omega,\tau) &= \left| \int_{-\infty}^{+\infty} \left|E^2(t) + 2E(t)E(t-\tau) + E^2(t-\tau)\right| e^{-i\omega t}dt \right|^2 \\ &= \underbrace{2\cdot\left|E_{2\omega}(\omega)\right|^2}_{\text{Constant term}} + 4\cdot \underbrace{\left| \int_{-\infty}^{+\infty} E(t)E(t-\tau)e^{-i\omega t}dt \right|^2}_{\text{NC-FROG}} \\ &+ \underbrace{2\cdot\left|E_{2\omega}(\omega)\right|^2\cdot\cos\left(\left(2\omega_0+\omega\right)\tau\right)}_{\text{Interferogramm of the SHG spectrum of E(t)}} \\ &+ \underbrace{8\cdot\cos\left(\left(\omega_0+\frac{\omega}{2}\right)\tau\right)\cdot\Re\left\{\int_{-\infty}^{+\infty} E(t)E(t-\tau)e^{-i\omega t}dt\cdot E^*_{2\omega}(\omega)\cdot e^{i\omega\tau/2}\right\}}_{\text{Spectrally resolved modified interferogram of E(t)}} \end{aligned} \tag{I.72}$$

where $E_{2\omega}(\omega) = \int_{-\infty}^{\infty} E^2(t)e^{-i\omega t}dt$ is the spectrum of the second harmonic generated by the non-linear medium. This expression will be useful in Chapter III, where a new technique of pulse characterization with nanometric nonlinear medium inside the focus of a high NA objective is presented. One can note that the NC-FROG term is contained into a CFROG. Fast oscillations are also present as in the case of C-autocorrelation and they can be removed by an appropriate filtering in the frequency space similarly to the case of the C-autocorrelation (See. Sec. III.4) and a NC-FROG trace can be extracted from a C-FROG by inversion algorithm. This procedure is not easy but by means of a specific software (see [118]), the electric field characteristics can be finally retrieved by an iterative process.

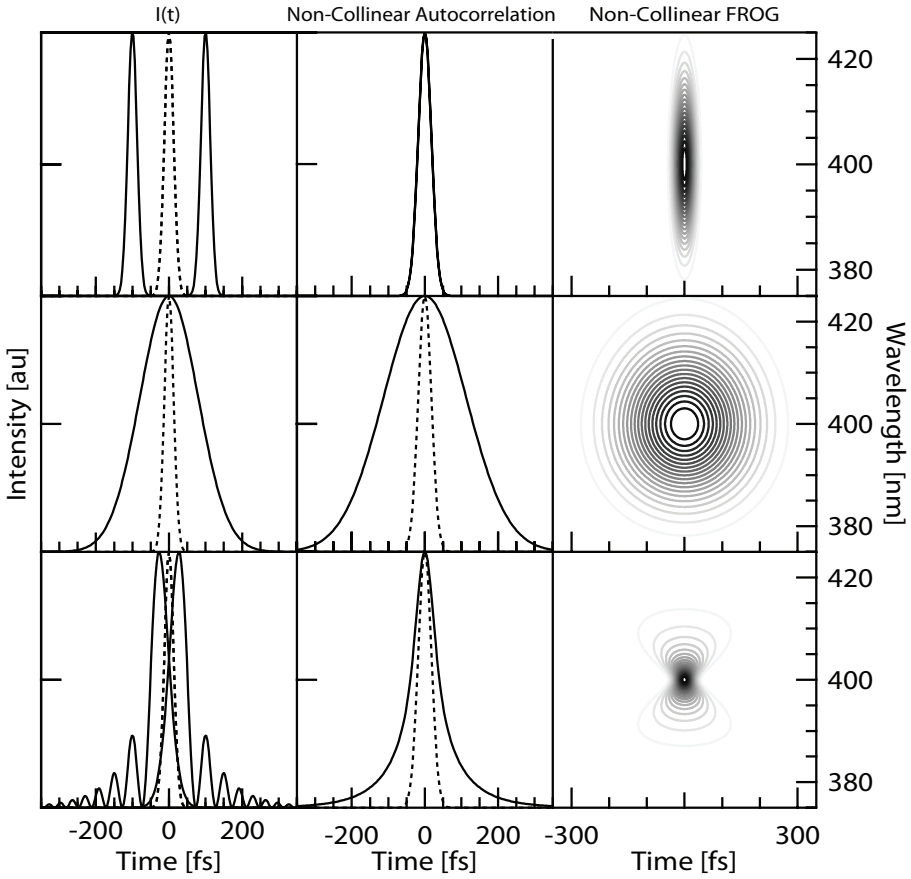

Figure I.15: Temporal characterization of phase modulated pulses. **Left column**: Pulses characteristics. **Central column**: Corresponding SHG NC-autocorrelation. **Right column**: Corresponding NC-SHG FROG. In all case, $\Delta t_{\text{FWHM}} = 30$ fs. First line, $\phi_1 = \pm 100$ fs. Second line, $\phi_2 = \pm 1000$ fs^2. Third line, $\phi_3 = \pm 10000$ fs^3. Dashed line, unmodulated pulse. All intensity curves have been normalized.

Before ending with this chapter, we will present typical NC-autocorrelation and NC-FROG traces obtained for phase-modulated pulses. We present in Fig. I.15 NC-autocorrelations and NC-FROG for the same parameters as in Fig. I.4. Note that due to the time inversion no difference due to the sign of the phase modulation can be seen and therefore the traces are superimposed. As a direct consequence, it is not possible to see the linear chirp as a tilt of the trace in the case of SHG-FROG as it is commonly observed in the case other FROG traces. We note also that the shape of SHG-FROG traces are not deformed for the first orders of the dispersion serie (precisely up to ϕ_2 included in Eq. I.17) and pulse trains are the consequence of the presence at least one $\phi_{n\geq 3}$ term.

Similarly, we present in Fig. I.16 the NC-autocorrelation and NC-FROG traces for the same spectral phase modulations as in Fig. I.5. It is interesting to notice the spectral amplitude modulation due to the sine modulations and the impossibility with a single phase modulation to obtain even number of pulses train. To this purpose, amplitude modulations have to be added to the phase modulations.

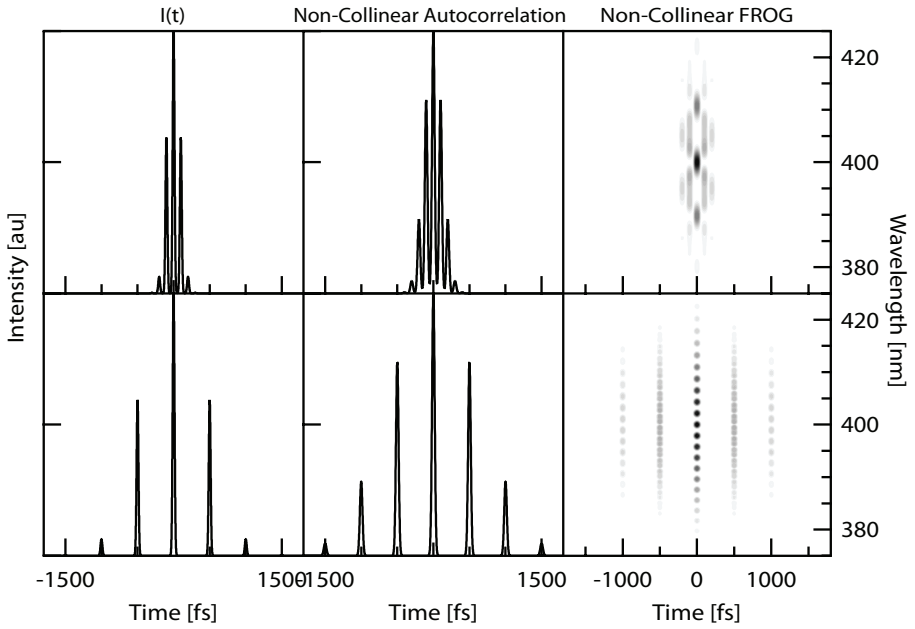

Figure I.16: Temporal characterization of modulated pulses by a sinusoidal spectral phase $\phi(\omega) = \sin(x\omega)$, with x the frequency of the modulation. **Left column**: Pulses characteristics. **Central column**: Corresponding SHG NC-autocorrelation. **Right column**: Corresponding NC-SHG FROG. In all case, $\Delta t_{\text{FWHM}} = 30$ fs. First line, $\phi_1 = \pm 100$ fs. Second line, $\phi_2 = \pm 1000$ fs^2. Third line, $\phi_3 = \pm 10000$ fs^3. All intensity curves have been normalized.

From the equations but also from these examples, it becomes evident that having the FROG trace, one can easily work out the spectrum (resp. the autocorrelation) by integrating the FROG trace along the time (resp. spectral) axis.

Complementary informations on complete pulse characterization by phase modulation techniques can be found in [27, 119, 120] and for characterization techniques of pulses non-linearly polarized the reader should refer to [121].

CHAPTER II

Experimental

II.1 Laser sources

In this experimental work, we used different laser systems to generate femtosecond laser pulses. We will describe separately these systems starting first with the sources for the non-linear microscopy experiments followed by the source for UV-spectroscopy and beam propagation experiments. In fact, nonlinear processes can be achieved by tight-focusing femtosecond oscillators using microscopes objectives or by using the output power of amplified systems.

II.1.1 Sources for nonlinear microscopy: oscillators

The standard excitation sources are Titanium:Sapphire (Ti:Sa, [122]) crystal based oscillators which are pumped by a frequency-doubled Nd:YAG-laser (Verdi, Coherent™), delivering an adjustable output power from 3-5 W. Passive mode-locking of the oscillator is reached via Optical Kerr effect. The compensation of the group-velocity dispersion is achieved by an intracavity prism compressor in one case (Chinook, Kapteyn-Murnane Labs™, [123, 124]) or by chirped mirrors in the second one [125] (Femtosource, Femtolasers™). These two sources deliver pulses with similar properties: $\Delta\lambda = 50 - 65$ nm centered around $\lambda_0 = 800$ nm, pulse energy $4 - 6$ nJ at 80 MHz repetition rate. The pulse characterization of the various systems are performed with a commercial SHG FROG device (Pulsecheck, APE™ Berlin).

In a single experiment (Sec. III.3), for comparing frequency-efficiency conversion between near-infrared (NIR) excitation (centered around 800 nm) and infrared (IR) excitation (centered around 1550 nm), we used an Erbium fiber laser (EFO-150, Avesta), providing pulses of 0.15 nJ at a 70 MHz repetition rate.

II.1.2 Source for UV-spectroscopy and propagation experiments

When higher energies were required we used a regenerative amplifier based on the Chirped-Pulse Amplification [126]. After being stretched in time by applying a giant spectral linear chirp to reduce their peak power and avoid damage in the Ti:Sa crystal when amplification occurs, the output of the oscillator is seeded into the cavity of a regenerative amplifier. In this cavity, a second Ti:Sa crystal is pumped by a frequency-doubled Nd:YAG-laser (Evolution, Coherent™) delivering 20 W at 1 kHz repetition rate with nanosecond pulse duration. The oscillator pulses provide a synchronization signal to two Pockels cells. They regulate the entrance of seed pulses and extraction of amplified pulses from the regenerative cavity. The amplified pulse is then compressed by a grating compressor [127], which compensates exactly the linear chirp of the pulse (stretcher and second order dispersion in the amplifier). The output characteristics after amplification are $\Delta\lambda_{\text{FWHM}} = 27$ nm centered around $\lambda_0 = 790$ nm, corresponding to an FT pulse duration of $\Delta\tau_{\text{FWHM}} = 34$ fs. The available pulse energy is 2.5 mJ.

II.2 Frequency conversion crystals

In some experiments, we used laser pulses at harmonics frequencies of the initial laser pulses $\omega_0 = 2.35 \cdot 10^{12}$ rad/s ($\lambda_0 = 800$ nm). All the crystals used are $\beta-$Barium Borate ($\beta - BaB_2O_4$, BBO). These crystals are cut along a precise axis to maximize the harmonic generation: pulses centered at $\lambda_{2\omega} = 396$ nm ($2\omega_0 = 4.70 \cdot 10^{12}$ rad/s) are obtained by SHG with $\theta = 29.2°, \phi = 0°$ crystals. UV pulses centered $\lambda_{3\omega} = 264$ nm ($3\omega_0 = 7.05 \cdot 10^{12}$ rad/s) are obtained via sum-frequency generation of a SHG pulse and the fundamental pulse trough a crystal cut at the angle $\theta = 44.3°, \phi = 0°$. Due to phase-matching considerations,, the thickness of the crystals has to be adapted to the spectral bandwidth of the pulses, while efficiency conversion prevents the use of very thin crystals.

Tab. II.1 gives a summary of the nonlinear crystals used in this work for excitation sources as well as for characterization nonlinear media.

Table II.1: List of Nonlinear Crystals

Material	$\theta[°]$	$\phi[°]$	Thickness [μ m]	Utilization
BBO	29.2	0	500	SHG for broadening in gas cells
BBO	29.2	0	150	SHG for pulse characterization, $\Delta\lambda \leq 30$ nm
BBO	29.2	0	10	SHG for pulse characterization, $\Delta\lambda \geq 30$ nm
BBO	29.2	0	200	SHG for sum-frequency generation
BBO	44.2	0	200	Sum-frequency generation at 264 nm

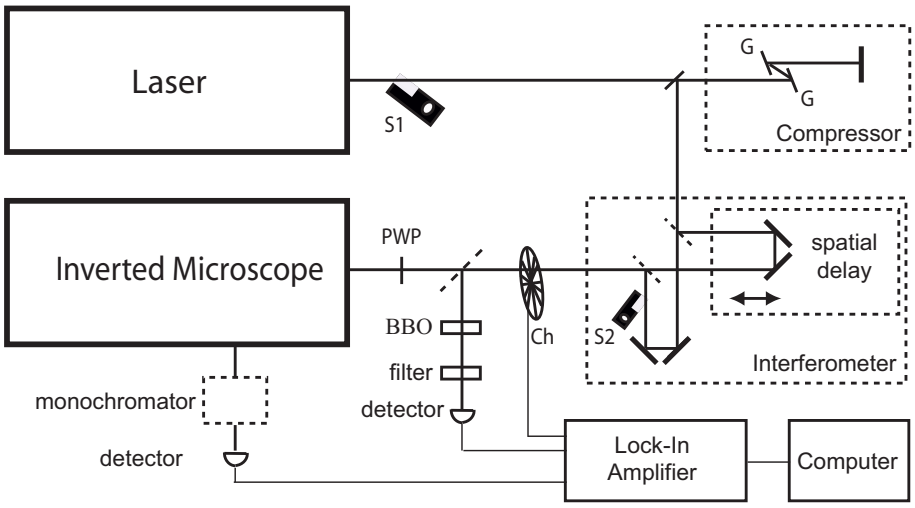

Figure II.1: Experimental scheme of the nonlinear microscopy set-up. C: folded grating (G) compressor for dispersion precompensation; I: interferometer; monochromator: scanning monochromator; The excitation polarization is controlled by a zeroth-order $\lambda/2$ plate (PWP). Shutter S1 is used to completely block the beam, while S2 for blocking one arm of the interferometer. Ch: Optical Chopper. Dashed mirrors: 50/50 beamsplitters.

II.3 Non-Linear Microscopy

We have presented an illustration of the microscope in Fig. I.10. In Fig. II.1, we show a schematic representation of the entire set-up. The following description is split in two parts: laser excitation and detection. Dashed-boxes are parts of the set-up who have been used exclusively for specific experiments as described in the text.

II.3.1 Laser Excitation

Depending on specific needs, experimentals blocks can be added to the set-up. For example a grating compressor (C) is added to stretch negatively the pulse to 364 fs to pre-compensate for dispersion of transmissive optics [97]. This value is consistent with the results of Eq. I.20 and the linear dispersion present by our experimental set-up. The beam can be splitted at the first beamsplitter (dashed line) into the two arms of an interferometer. A delay stage with 0.017 μm step resolution (Physik Instrumente™, M-505) is used to introduce a difference between the optical paths (See Chapter, SecI.6). The two pulses from the interferometer are then recombined at the second beamsplitter (dashed line).Polarization of the incident light can be linearly modified by a motorized rotating half wave plate (PWP) as well as its intensity by various neutral density filters.

The beam is collinearly injected into an inversed laser scanning microscope (Nikon™, model TE300), equipped with a 1.3 NA 100 $\times$ oil immersion objective or with a 0.6 NA 40 $\times$ objective. Their working distance are respectively 200 μm and 2 mm. The

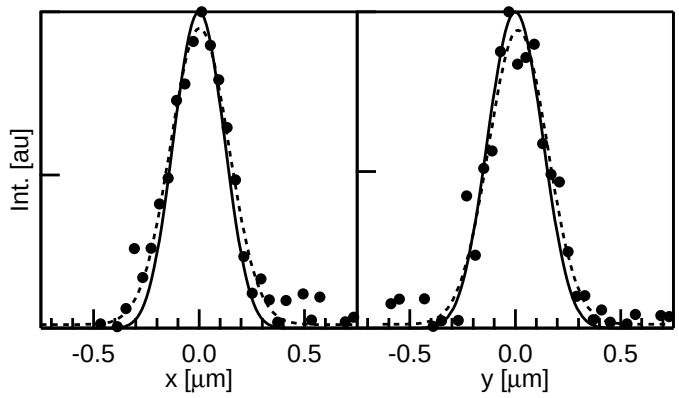

Figure II.2: Spatial resolution of the $NA = 1.3$ objective at the focal plane ($z = 0$) with an x-polarized field initially. The dots are the experimental datas, the dashed line is the Gaussian fit of the datas and the solid line results from the theoretical simulation. Panel (A) depicts the SHG field intensity in the x axis while panel (B) in the y axis.

transmission efficiency of the objectives vary with wavelength. From 77% transmission for the 800 nm excitation, it falls to 50% for the 1550 nm excitation. Notice that fully fill the whole aperture of the objective by the size of the beam width to maintain high spatial resolution is essential. The position of the sample was controlled by an XYZ piezo-scanner (Physik Instrumente™, P-517.3CL) with a scanning range of $100 \times 100 \times 20$ μm and resolution of $1 \times 1 \times 0.1$ nm. The Z axis of the scanner coincides with the propagation axis of the laser beam.

In Fig. II.2, we present the nonlinear spatial transverse resolution in the focal plane of the 100 $\times$ oil immersion objective. Nanometric nonlinear probes with a size of 10 nm are used. As the size of the probes is much smaller than the focal spot, the point spread function will be given only by the size of focal sport (See Sec. I.4.2). In Fig. II.2, we present for both direction (x and y axis) a Gaussian fit (dashed line) of the experimental datas (dots). We superimposed the theoretical spatial resolution obtained with the formalism of Sec. I.4.1. From this excellent agreement, we deduce the transverse spatial resolution of our system (See Sec. I.4.2) in both direction : $\Delta x_{\text{FWHM}} = 278$ nm and $\Delta y_{\text{FWHM}} = 276$ nm.

II.3.2 Detection

The signal is epi-collected by the same focusing objective used for excitation and separate from the fundamental by a dichroic mirror. We use for Ti:Sa (resp. Erbium) excitation the Chroma™ mirror: 670-dcspxru-3p (resp. 1025dcspxr-1500). A combination of two BG40 Schott filters and a bandpass filter assured an efficient rejection of the Ti:Sa excitation scattering. Alternatively, a scanning monochromator (H10, Jobin-Yvon™, 1 nm resolution) in front of the detector. The polarization of the output beam can also be analyzed by a Glan-Taylor polarization cube. The signal was measured by a photomultiplier tube (Hamamatsu™, H5701-51 for Ti:Sa and H6780-20 for Erbium).

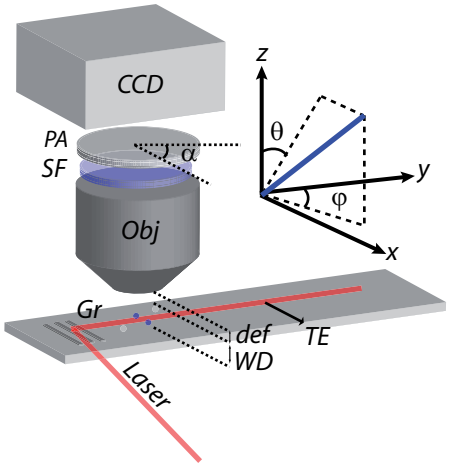

Figure II.3: Experimental setup. Laser radiation is coupled via grating couplers (Gr) into the tantalum pentoxide waveguide which is applied to the surface of a glass substrate. The SH as generated by the nanoparticles on the waveguide is observed by a CCD camera through a microscope objective (Obj). SF: Spectral Filter. PA: Polarization Analyzer. WD: Working Distance of the objective. def: defocusing parameter.

A lock-in amplifier was used to increase the detection sensitivity. The lock-in amplifier was determined by the frequency of a chopper wheel set in the beam right before the entrance of the microscope.

II.4 Evanescent Field Experiments

The experimental setup is described in Fig. II.3. The frequency doubled output of an ultrashort-pulse Erbium doped fiber laser (Menlo Systems TC1550, central wavelength 780 nm, bandwidth 9 nm, output power 45 mW, repetition rate 80 MHz, pulse duration 150 fs) is coupled with TE polarization under the resonance angle of -48° into a tantalum pentoxide waveguide of thickness 159 nm by a lithographic manufactured grating structure (Balzers Optics, Lichtenstein, grating period $\Lambda = 318$ nm). TE laser polarization denotes an electric field vector along the x axis of the laboratory frame. The coupling efficiency into the waveguide is approximately 20%. Due to the limited spectral acceptance of the grating, the spectral bandwidth of the coupled pulses is reduced to 4 nm, leading to temporal stretching.

Potassium-Titanyl-Phospate (KTiOPO4, KTP) powder (Cristal Laser S.A., Messein - France) of average grain size 220 nm were dissolved in demineralized water. A drop (1 μl) of the solution was dispensed onto the waveguide surface at some millimeters from the grating coupler where the solvent evaporated. The SH radiation emitted by individual SHRIMPs was collected by a $40\times$ magnification objective (Nikon, Plan Fluor ELWD 40x/0.60), spectrally filtered by a multiphoton fluorescence emission filter (Semrock, FF01-750SP, 380-720 nm passband), and detected by a CCD camera

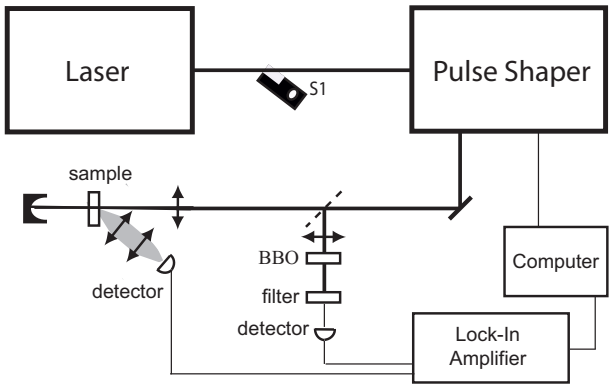

Figure II.4: Experimental scheme of the spectroscopy set-up. Femtosecond laser pulses are modulated in phase and amplitude by a pulse shaper before being focused into a flow cell and a BBO crystal. After adequate filtering signal is detected by photomultiplier in a synchronous scheme giving a feedback to the algorithm.

(pco.1600, 1200 x 1600 pixels, pixel size 7.4 μm). For polarization analysis, a polarizing plate (Schneider-Kreuznach, AUF-MRC) located in front of the camera sensor was rotated by an angle α, where $\alpha = 0$ corresponds to transmitted x-polarization. Defocused images were acquired by an accurately defined displacement, def, of the detection unit (objective, filter, CCD camera) and thus of the objective focal plane with respect to the waveguide surface.

II.5 Spectroscopy

A schematic set-up for control experiment is depicted in Fig. II.4, the description is organized according to the type of wavelength used.

II.5.1 Near-Infrared Spectroscopy

The prism compression of a Ti:Sa oscillator, capable of delivering $\Delta\omega_{\text{FWHM}} = 50$ nm pulses, was adjusted to limit the output bandwidth to 12 nm FWHM. This precaution was necessary to prevent the pulse spectrum dispersed by a 1200 grooves/mm gold grating to exceed the size of the liquid crystal pulse shaper (SLM-256, CRI; phase and amplitude modulation) placed at the Fourier plane of a zero-dispersion compressor in a 4-*f* arrangement. More details on the pulse shaper will be given in Chapter IV. The shaped pulses were separated by a pellicle beam splitter (R/T=8/92, 2 μm thickness) into two distinct optical paths (dashed line). The reflected beam, focused by a 5 cm lens onto a 150 μm thick BBO crystal, was used to generate the SHG signal detected by a photodiode equipped with a 40 nm bandpass filter at 400 nm. The transmitted part (50 mW average power) was focused by an identical lens, onto a 1 mm suprasil flow-cell where the Flavine Mono-Nucleotide (FMN) sample was constantly

refreshed. The fluorescence signal was collected by two lenses, spectrally filtered by means of a BG40 Schott glass and a 40 nm bandpass filter centered at 500 nm, and detected by a photomultiplier tube (Hamamatsu™, H7732-01). Both signals were fed into two independent lock-in amplifiers, before being acquired by computer, and processed to provide feedback to the Genetic Algorithm (see Sec. IV.3). For each sensitivity settings, the linearity in the response of both arms was carefully checked throughout the accessible dynamic range, by measuring the signals generated by an unmodulated pulse at different intensities. FROG traces were systematically acquired at the end of each optimization run.

II.5.2 Ultra-Violet Spectroscopy

The output of an amplified Ti:Sapphire laser system is first separated into two arms by a 50/50 pellicle beam splitter. The transmitted component is used to generate 266 nm (UV) light by an in-line frequency tripler. The position of the grating compressor of the amplifier is optimized to yield the most efficient conversion of the fundamental to the third harmonic. As shown in Fig.II.5, the UV is then focused by a lens of 35 mm focal length onto a 3 mm thick CaF_2 plate to broaden it spectrally up to 10 nm at $1/e^2$. The broadened pulses are then recollimated by a second 35 mm lens and sent into the all-reflective shaper apparatus (left of Fig.II.5). The shaper is based on a 1200 grooves/mm blazed grating and on a cylindrical mirror with a focal length of 250 mm, which collimates the spectrum dispersed by the grating along the y axis onto a Micro-ElectroMechanical Systems (MEMS) chip. The latter is protected by a window treated with a 250-440 nm UV anti-reflection coating. With these settings the device can theoretically access a maximal bandwidth of 40 nm at the Fourier plane, with a resolution of 0.13 nm/pixels and a corresponding temporal shaping window extending for ~ 3.5 ps [37]. Note that even though the full bandwidth potential was not exploited in the following measurements, there are no device restrictions to access, for example, the UV portion of the extremely broad spectra generated by filamentation, recently reported by [128, 129]. Spectral phase-shifts are introduced by creating a striped pattern along the x axis, by applying the same deflection to all the micromirrors belonging to the same line. More specification on pulse-shaping techniques can be founded in chapterIV. The 800 nm pulses (IR) reflected off by the beam splitter are first temporally compressed down to 120 fs by a grating compressor and then focused together with the shaped UV onto a 200 μm thick BBO crystal to generate a difference frequency mixing (DFM) signal at 400 nm detected by a Si photodiode. More details about the technical method used for recording the datas can be found in chapter IV.

II.6 Beam propagation Measurements

In this section, we will describe the experimental implementation of the wavefront deformation of a femtosecond pulses and then the characterization of ultrabroadened

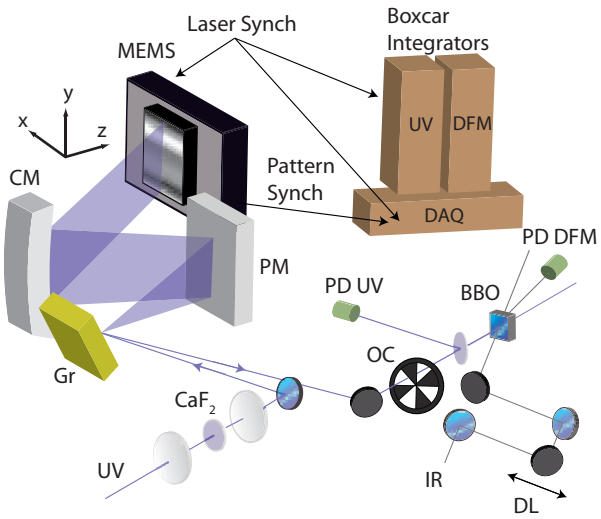

Figure II.5: Experimental scheme. Gr: grating; PM: plane mirror; CM: cylindrical mirror; DL: temporal delay line; OC: optical chopper. PD UV/DFM: detection photodiodes, DAQ: acquisition card. The OC is synchronized to half the repetition rate of the laser to reject every second UV pulse.

laser sources.

II.6.1 Pulse Propagation through Atmospheric Turbulence

The measurements were carried out under stable environmental conditions (relative humidity ≤ 40 %, temperature 20°C) with an amplified Ti:Sapphire laser system. The beam diameter is ~ 12 mm at $1/e^2$. After propagating over a distance of $d_1 = 3.8$ m, the beam goes across a highly turbulent region generated by the perpendicular flow of a hot air blower ($T \leq 500$°C with 500 l/min flux, output air velocity 20 m/s, angular divergence $20°$). The perturbation intensity is controlled by varying the distance between the blower and the beam axis. The strength of the perturbation, represented by the structure parameter of the refractive index C_n^2, was determined by measuring the variance in pointing angle of a He-Ne laser collinear with the fs beam. [130] The turbulence range achievable by the experiment ($C_n^2 = 7-15\times10^{-9}$ m$^{-2/3}$) represents a very strong perturbation, a few orders of magnitude higher than those typically encountered in the atmosphere. [131] After passing through the turbulent region, the pulses propagate for an additional distance $d_2 = 3.7$ m before being characterized by a single shot autocorrelator (by sampling a 28 mm^2 portion in the center of the beam profile) or imaged by a digital CCD camera equipped with a $f = 105$ mm objective (spatial resolution 150 μm/pixel, 10 ms exposure time). Alternatively, we characterized individual wavefront regions (0.25 mm^2) by frequency-resolved optical gating (FROG) inserting in the beam path a random phase plate. This time-invariant perturbation allowed multi-shots acquisition. We measured by interferometry that the plate introduces an average phase-difference of $\sim 4\pi/3$ among two points on the wavefront separated by 2 mm,

an analogous estimate for a perturbation strength of $C_n^2 = 9.6 \times 10^{-10}$ m$^{-2/3}$ gives $\sim 2\pi/3$.

II.6.2 Ultrabroadband Pulse Characterization

The direct output of a Ti:Sapphire amplified laser system (central wavelength $\lambda_0 = 792$ nm) is frequency-doubled in a 150 μm thick BBO crystal, providing a typical output energy of $150 - 300$ μJ. In a first experiment, the second harmonic pulses ($\lambda_{2\omega}$) are directly focused onto a nanoparticle pellet by an aluminium-coated spherical mirror ($f = 50$ cm). The scattered nonlinear UV signal is collected by a fused-silica lens-doublet and coupled into a monochromator with 0.4 nm spectral resolution. The spectrally resolved signal is finally detected by a solar blind photomultiplier (Hamamatsu™, R166UH). Alternatively, the $\lambda_{2\omega}$ pulses are temporally characterized using a collinear interferometric setup: the pulse train is separated by a 2 μm thick $50/50$ pellicle beamsplitter and the relative delay between the two arms adjusted with a motorized delay stage. In a third experiment, the $\lambda_{2\omega}$ pulses are slightly focused by a $f = 1$ m lens and injected collinearly with λ_0 pulses in an Ar-filled cell [132], via co-filamentation the spectral bandwidth broadens up from the initial 6.3 nm to 30 nm FWHM . The $\lambda_{2\omega}$ pulses are finally focused on the pellet for characterization using the generated UV-200 nm signal. In a last experiment, both λ_0 and $\lambda_{2\omega}$ are focused with adjustable delay and polarization onto the nonlinear sample to measure their sum-frequency signal at 264 nm. All the measurements around 200 nm are performed in an Argon saturated environment to prevent oxygen absorption below 190 nm. Linear polarization axes of the excitation beams are controlled by half wave plates.

II.7 Sample preparation and handling

In the last section of this chapter, we will consider first a succinct description of the synthesis of the non-centrosymmetric nanocrystals followed by their characterization, the handling and some specific preparations.

II.7.1 Synthesis of nonlinear nanocrystals

We started a collaboration with the Symme Institute at Polytech'Savoie (Annecy, France) because of their expertise in nanocrystals synthesis and more specifically on iron iodate nanocrystals. Due to their structure, these nanocrystals are stable in water, but present also high thermal resistance and low chemical reactivity. These properties make them very attractive for biological application such as cell labeling or targeting. The description of the synthesis of the nanocrystals presented here is valid for iron iodate ($Fe(IO_3)_3$) nanocrystals, for the other samples used several references can be consulted in [133–136].

Although dispersion of nanocrystals is crucial to obtain a homogeneous suspension

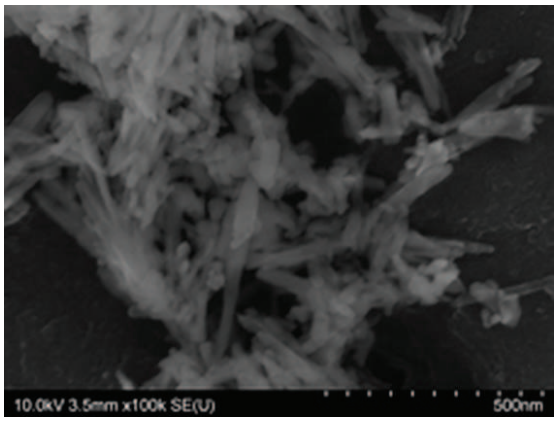

Figure II.6: High resolution SEM image of iron iodate nanosized powders.

suited for biomedical imaging, co-precipitation in aqueous solution is a cost-effective way to elaborate nanomaterials with specific properties. Recent studies have shown that the size of nanocrystals can be adjusted according to the experimental parameters of the synthesis. [137] Co-precipitation in aqueous solution of $Fe(IO_3)_3$ powder is obtained from iron nitrate ($Fe(NO_3)3{\cdot}9H_2O$, Sigma-Aldrich™, 98%) and iodic acid (HIO_3, Sigma-Aldrich™, 99.5%). The reactants are separately dissolved in distilled water, then the iron nitrate solution is progressively poured into the iodic acid solution while vigorous stirring is maintained. After being heated at 80°C for 2 days, the suspension is filtered ($30\ \mu$m) and dried in an air flow at room temperature. [138]

II.7.2 Characterization of nonlinear nanocrystals

The powder is successively diluted in water, and a drop of the filtered ($0.22\ \mu$m) solution is dried on a graphite substrate or a standard microscope glass slide. The grain size, estimated by the broadening of X-ray diffraction peaks [138], is around 30-40 nm which is consistent with High Resolution Scanning Electron Microscope (SEM) images (Fig. II.6).

Another confirmation of the grain size is given by intermittent-contact atomic force microscopy (IC-AFM) (Fig. II.7, left panel). These data were collected for nanocrystals dispersed on a graphite substrate. For the SHG experiments we had to work with standard microscopic glass slides (Fig. II.7, right panel), where we observed a stronger tendency of $Fe(IO_3)_3$ nanoparticles to aggregate, as illustrated by the size distribution in the right panel of Fig. II.7 centered around 76 nm. The nonlinearity of the generated signal has been carefully checked for every experiments presented in this thesis. In Fig. II.8, is presented the typical SHG response of $Fe(IO_3)_3$ nanocrystals.

Beside possibility of surface functionalization, $Fe(IO_3)_3$ nanocrystals possess a series of attracting properties, including low-chemical reactivity, stability in aqueous solution in a wide pH and temperature range (up to 400° C) [138], contrary to SHG active organic crystals [139]. The non-centrosymmetric crystal structure (space group

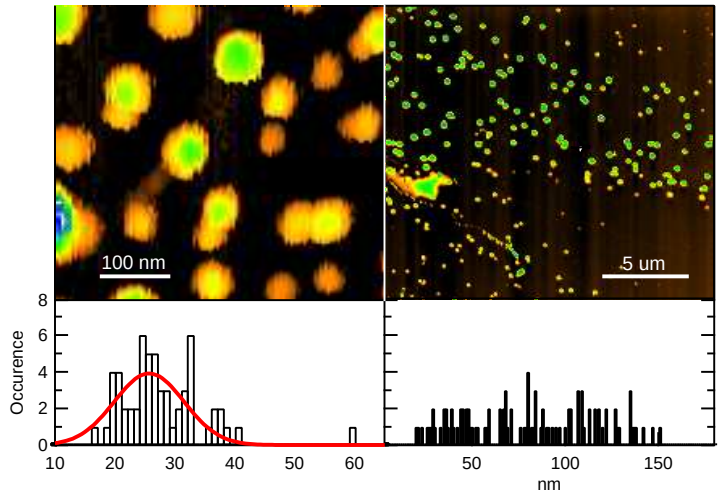

Figure II.7: Left Panel: IC-AFM image of fnanocrystals deposited on a graphite substrate. The histogram in the lower panel illustrates the size distribution of 60 nanocrystals, and it is fitted by a Gaussian centered at 27.7 nm of FWHM 13.7 nm. **Right Panel**: IC-AFM image of $Fe(IO_3)_3$ nanocrystals deposited on a glass slide. The histogram in the lower panel depicts the distribution of AFM heights of the sample.

$P6_3$) determines their polarization-sensitive nonlinear optical response. [140] $Fe(IO_3)_3$ nanocrystals are very efficient frequency doublers (nonlinear coefficients about 10 pm/V) and are transparent from visible up to 12 μm. [141] Moreover, given that their size is smaller than the excitation wavelength, no phase-matching constrains apply to the frequency-mixing process, allowing complete spectral doubling of broadband femtosecond pulses. [87] To provide a comparison with bulk crystals limit, the phase matching conditions have been calculated within the usual description of sum-frequency generation for a crystal of 1 μm length using the dispersion properties of $Li(IO_3)$ [142] since $Fe(IO_3)_3$ bulk properties are still partially unknown. In configuration ooe for SHG, the phase-matching acceptance angle results greater than π radians, and the acceptance bandwidth larger than 800 nm [143]. It could also be potentially used as a nanoprobe of the local electric field by taking advantage of its polar structure.

II.7.3 Other specific preparations

Murine Liver

According to the experiments presented in Sec. III.3, scattering tissue phantoms were prepared by placing spacers of calibrated thickness ($d = 90, 180, 300$ μm) between two microscope slides (170 μm or 1 mm thickness) and filling the gap with a water suspension of 0.1 μm polystyrene nanospheres at a concentration of 45.5 particles/μm^3 (Polysciences). Mouse liver was first fixed with a solution of Phosphate buffered saline (PBS)-4% paraformaldehyde at $4°$C overnight, then washed in PBS and incubated in

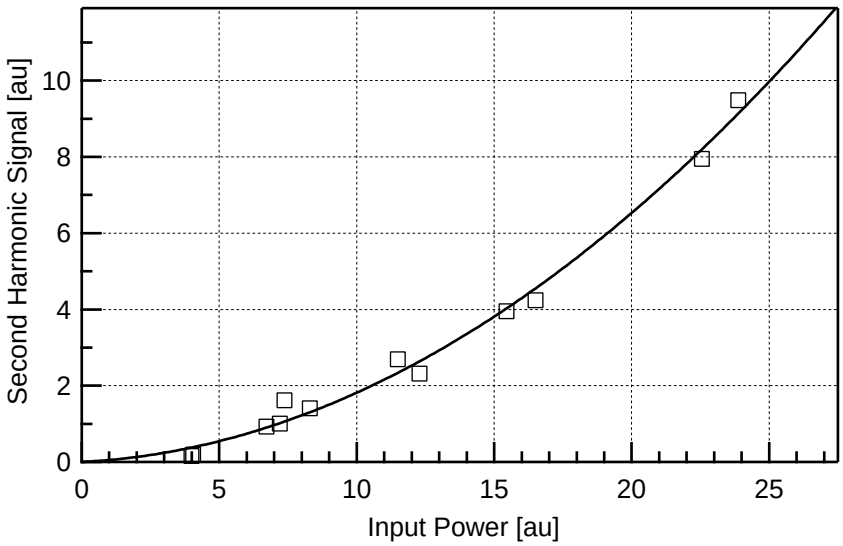

Figure II.8: Power dependence of the SHG signal as function of an arbitrary input pulse power (Experimental datas points (Squares) and its quadratic fit (Line)).

a solution of PBS - 30% sucrose. Tissue was then embedded in OCT medium for freezing and stored at minus $20°$C before cryosectionning at a nominal thickness of 20 μm.

Nanocrystal pellets

In Sec. III.5 we present an experiment involving pellets of compressed nanocrystals (3 mm thickness and 8 mm diameter) obtained by exerting a 250 MPa pression on dried powder for 15 minutes. The surface roughness is found to be in the micrometer range.

Flavin solutions

In Sec. IV.3, we used a FMN solution prepared using Flavin mononucleotide from Sigma-Aldrich™, dissolved in water at a concentration of 2 g/L. The spectra of one and two photon absorption is presented in Fig.II.9 [144].

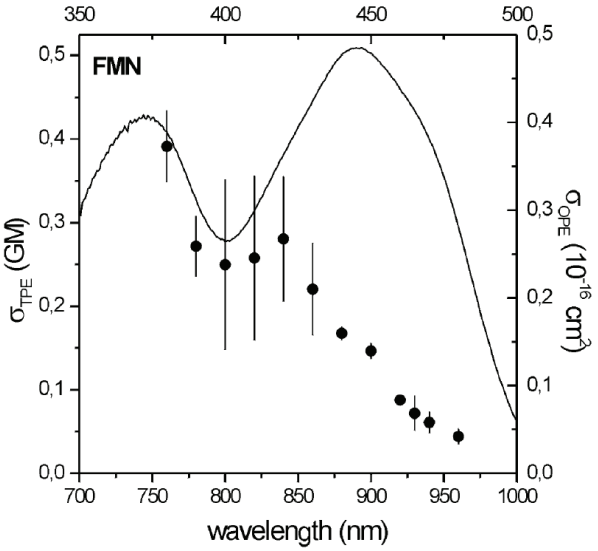

Figure II.9: Absolute Two-Photon Excitation (TPE) action cross-section (σ_{TPE}, left axis) of FMN in phosphate buffer (symbols). The one photon absorption cross-section (OPE) (σ_{OPE}, right axis) is shown for comparison (solid line, wavelength scale top). [144]

CHAPTER III

Results on Nonlinear Nanoprobes

The present chapter is dedicated to the experimental results obtained with inorganic non-linear nanocrystals. The presence of even harmonics in the optical response descends from their non-centrosymmetric crystal structure. In this experimental study we will focus our attention on the first non-linear process, Second Harmonic Generation (SHG), which is a coherent and non-resonant process for nano-objects smaller than the coherence length. and its response is very well spectrally separated from the excitation.

The goal of the experiments presented here is to use the nanocrystals, which we refer to as SHRIMPs ("Second Harmonic Radiation IMaging Probes" [136]), as probes for various applications. In Sec. III.1, we used the polarization of the incident electric field to optically characterize iron iodate ($Fe(IO_3)_3$) nanocrystals, i.e. determine the spatial orientation of the electric dipole associated to each probe and, as it does not exist in bulk form, retrieve the nonlinear properties of this material which were previously unknown. In Sec. III.2, we extend this analysis to others non-linear nanomaterials to point out the advantages/disadvantages of each materials regarding different applications. In Sec. III.3, we demonstrate the advantage of non-resonant excitation with respect to the resonant excitation (two-photon excited fluorescence), by exploiting the wavelength-flexibility of the nonlinear process. In Sec. III.4, taking into account the coherence properties of the SHG signal, we use a SHRIMP to probe and fully characterize the very tightly focused electric field. In Sec. III.5, we use the absence of phase-matching condition to characterize ultrabroadband UV femtosecond laser pulses, performing direct autocorrelation of a 400 nm pulse. In the last section (Sec. III.6), we present the excitation of SHRIMPs dispersed on a planar optical waveguide by the evanescent field of the guided mode.

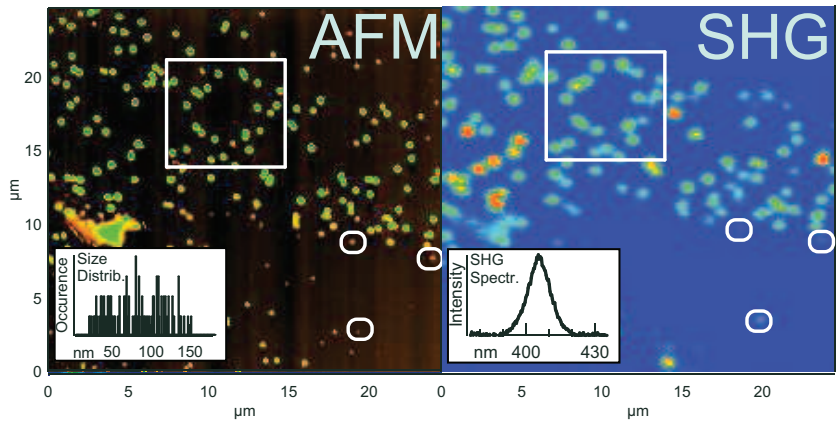

Figure III.1: Left panel: IC-AFM image of $Fe(IO_3)_3$ nanocrystals deposited on a glass slide. **Inset:** distribution of AFM heights of the sample. **Right Panel:** SHG image of the same sample region. The SHG image was obtained by averaging two scans associated with perpendicular polarizations of the excitation laser and no polarization selection at the detector. The three **open circles** highlight nanocrystals with measured height at 40 nm and AFM width below 350 nm. The **open square** is a guideline to the eye for an easier comparison of the two images. **Inset:** SHG spectrum emitted by a single nanocrystal.

III.1 Polar $Fe(IO_3)_3$ nanocrystals as local probes for nonlinear microscopy

We have investigated nanocrystals of $Fe(IO_3)_3$ by polarization-sensitive second harmonic generation (SHG) microscopy. As the nonlinear optical properties of this material were only poorly characterized, we have first determined the relative values of the elements of its second-order susceptibility tensor, by the global fitting of the polarization-resolved SHG response of an ensemble of nanocrystals. This information allows to optically retrieve the orientation of individual particles in the sample. The high SHG efficiency measured for nanocrystals of $Fe(IO_3)_3$ and their polar nature, could make them very attractive for nonlinear microscopy of biological samples.

The sample was first characterized (imaging and sizing) by AFM, and labeled to allow a straight comparison with the results obtained by SHG microscopy (Fig. III.1). Apart from its intrinsic lower spatial resolution ($\sim$ 280 nm), the latter technique was able to retrieve the positions of almost all the nanocrystals dispersed on the microscope slide. In scanning mode we were able to identify the SHG signal of individual crystals as small as 50 nm height and 150 nm lateral size. The white circles in the figure highlight three nanocrystals of 40 nm height and AFM width below 350 nm, to prove the spatial sensitivity of the technique. The inset in the lower panel shows the SHG spectrum emitted by a single nanocrystal. The spectral full width half maximum of the second harmonic emission is 12 nm, which corresponds to doubling the whole fundamental laser spectrum ($\sim$ 50 nm at 810 nm).

To detect the individual orientation in space of each nanocrystal the laser was first focused onto selected crystals, previously characterized in size by AFM. During this

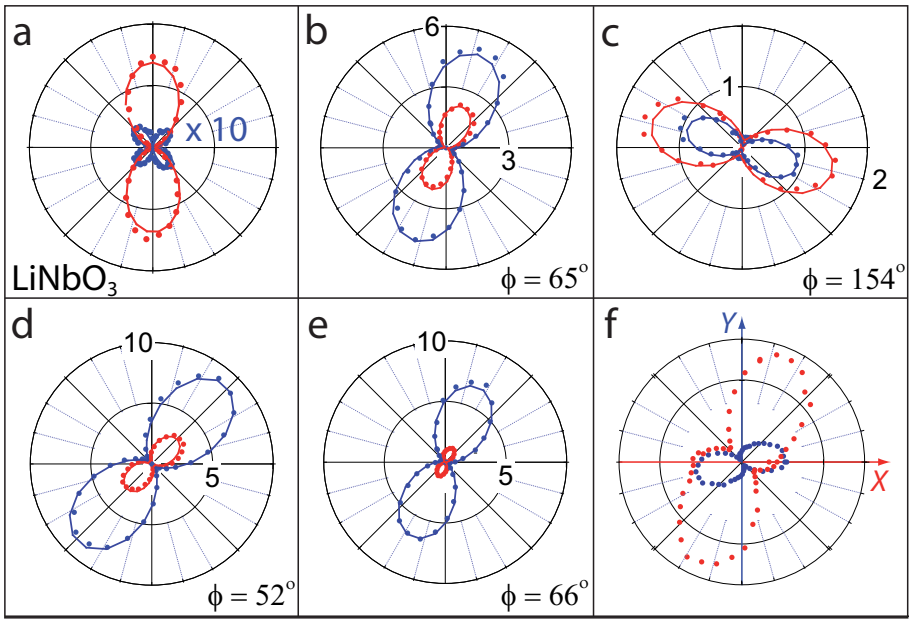

Figure III.2: Polarization response of SHG emission analyzed along the X (blue) and Y (red) direction. The **dots** are experimental points, the **solid lines** the best fit according to the model described in the text. (a) Bulk $LiNbO_3$ plate. I_X is multiplied by a factor 10 for easier inspection. (b-e) Examples taken from an ensemble of 12 nanocrystals simultaneously fitted. (f) Typical response from a non-monocrystalline aggregate.

operation, the SHG signal was carefully maximized by adjusting the microscope piezo-scanner displacements. The polarization response was successively acquired measuring the SHG signal as a function of the polarization angle of the incident light, γ, and of the detection polarization, setting the analyzer along the X or Y direction (see definitions in Fig. I.10). The data presented in Fig. III.2 were acquired integrating 100 ms on the lock-in with a post-averaging over 10 points.

Since the basic physical properties of $Fe(IO_3)_3$ are still unknown, as the bulk counterpart is not easily grown [145, 146], we first tested the procedure on a bulk crystal of well known nonlinear optical properties. As shown in Fig. III.2a, the SHG polarization response of bulk $LiNbO_3$ was found in excellent agreement with the theoretical curve obtained using the literature values for the χ_{ijk} tensor [147], and the experimentally measured Euler angles ($\phi = 88°$, $\theta = 90°$, $\psi = 90°$). Models more sophisticated than the present one have been proposed to describe the response of multiphoton microscopy [82, 85, 148, 149], accounting for the effect of a high NA objective in the collection of the backward propagating radiation and in the polarization dependent response. To verify the accuracy of our simplified approach which neglects these aspects, we have simulated the effect of wide angle collection of our 1.3 NA objective and included in the calculation the dichroism and ellipticity of our apparatus. Under certain crystals orientations, as shown in Fig. III.2a, we did not observe any difference between the measurements and both the complete and the simplified model. However, as discussed in reference [82], the axial components of the electric field can play a role in the polarization response. For example, we could remark some discrepancies

between the experimental response of bulk lithium niobate (Z-cut) and the predictions of the simplified model, which can be reduced applying the complete treatment. These effects were not retained in the fitting procedure described here exclusively for computational reason. In fact, we needed to dispose of an analytical compact expression for IX and IY that could not be derived in the framework of the complete model. On the other hand, small experimental defects as surface roughness or the sample planarity can explain these discrepancies.

Iron iodate belongs to the symmetry class 6, and thus only 4 components of the nonlinear tensor are expected to be non-zero: χ_{zzz}, $\chi_{zxx} = \chi_{zyy}$, $\chi_{xxz} = \chi_{xzx} = \chi_{yyz} = \chi_{yzy}$, $\chi_{xyz} = \chi_{xzy} = -\chi_{yzx} = -\chi_{yxz}$. Given that the absolute values of these nonlinear coefficients are not known, the symmetry of the nonlinear tensor represents the only fixed input parameter that can be employed in the model. As the SHG intensity in the X or Y direction of the n-labelled crystal can be computed as $I_X^n = K f_x(\phi^n, \theta^n, \chi_{ijk}) g(v^n)$ and $I_Y^n = K f_y(\phi^n, \theta^n, \chi_{ijk}) g(v^n)$, 7 free parameters remain to be adjusted for the fit: the 4 non-zero χ_{ijk} elements, the Euler angles ϕ^n and θ^n, and the function $g(v^n)$, which relates the crystal size v^n to the SHG intensity. The experimental factor K accounts for the incident laser intensity, the collection and the detection efficiency. Note that, according to the crystal symmetry ($P6_3$), the angle ψ has no influence on the nonlinear optical response. Siltanen *et al.* [150] have shown that it is possible to uniquely determine the values of 6 parameters by fitting the polarization responses I_X and I_Y of a sample. The system is thus under-determined when fitting exclusively the response of a single nanocrystal. On the other hand, when fitting simultaneously the polarized SHG emission of several nanocrystals, the system is over-determined, and the relative values of the nonlinear susceptibility tensor, as well as the orientation of each nanoparticle, become accessible. Consequently, we adopted a global fitting procedure, and we fitted simultaneously the SHG data collected from 12 nanocrystals considering χ_{ijk} as a global parameter.[1] The experimental curves in Fig. III.2 (panels b to e) are very well reproduced using the form of χ_{ijk} tensor associated to the $Fe(IO_3)_3$ symmetry. Although the intensities of the signals span more than one order of magnitude, the fitting procedure is very robust in indicating the in-plane orientation of each crystal, ϕ^n, which connotes unambiguously the shape and the relative intensities of I_X^n and I_Y^n. Note that even small differences of the ϕ^n angles lead to responses that can be distinguished by the experiment.

$\lvert\chi_{zxx}/\chi_{zzz}\rvert$	$\lvert\chi_{xyz}/\chi_{zzz}\rvert$	$\lvert\chi_{xxz}/\chi_{zzz}\rvert$
0.03 - 0.2	0.03 - 0.1	$< 10^{-2}$

Table III.1: Relative values of the non-zero elements of the χ-tensor of $Fe(IO_3)_3$ retrieved from the global fitting of 12 nanocrystals SHG polarization response.

The *absolute* intensities of I_X and I_Y are determined conjointly by the off-plane angle θ^n, the elements of the χ_{ijk} tensor, and the value assumed by the volume-function

[1] The same procedure applied to different ensembles/numbers of particles yielded similar results.

$g(v^n)$. A lack of modeling concerning the exact expression for $g(v^n)$, i.e. the correspondence between the nanocrystal size and the backward propagating SHG emission, is at the origin of the spread in the values of χ_{ijk}/χ_{zzz} obtained for different fits and summarized in table III.1. All fits coincide in indicating that the element χ_{zzz} is by far the dominant one, $\chi_{zxx} \geq \chi_{xyz}$, and that χ_{xxz} is almost negligible. The values obtained for the off-plane angles θ^n, directly reflect the indeterminacy shown for χ_{ijk}. As already pointed out, the results retrieved for the angles ϕ^n remain the same in all the fits performed.

The SHG signals emitted by larger structures, typically of $\geq 0.8\mu$m AFM lateral size, cannot be satisfactorily fitted using the assumptions described above. Very likely, these particles are polycrystalline aggregates made up by several crystal structures oriented in different directions, and their polarization response results in a superposition of signals generated by the different domains (Fig. III.2 (f)). Therefore, once the relative values of χ_{ijk} are known, the polarization response allows a rapid *in situ* inspection of the local crystalline order, and allows to tell apart monocrystalline structures from polycrystalline aggregates as recently observed for organic nanocrystals. [20]

The quantitative determination of χ_{ijk} of $Fe(IO_3)_3$ is under progress (first results are presented in Sec. III.2), by comparison with the responses of several different bulk materials, and by adopting an expression for $g(v^n)$ accounting for tight focused excitation, and coherent superposition effects as a function of sample size. [12, 82, 85] However, to give an estimate and allow a comparison with other recent works, we applied the procedure outlined by Delahaye *et al.* [151] to evaluate χ_{zzz} using as reference signal the response of a bulk $LiNbO_3$ crystal. Within this framework $g(v^n) = (v^n)^2$. Adopting for the calculation the response of a ~ 0.6 μm particle we estimated $\chi_{zzz} \simeq$18 pm/V, in agreement with the order of magnitude deduced from powder measurements. [141, 146] Nevertheless, this value should be taken with caution, because the approximations of this treatment lead to a strong dependency of its outcome on the size of the nanocrystal. The complementarity of AFM and SHG microscopy in our experiment has the advantage to expose immediately the limitations of stating such a simplified correspondence between the response of a massive crystal and that of a nano-object.

III.2 Comparative analysis of various nanodoublers

Depending on the application of the SHRIMPs different properties are needed spanning from their average size and size dispersion to their toxicity, but also generated signal intensity, polarization response, chemical stability, shape, etc. Our interest in the present section is to identify the best material available for biological applications such as cell targeting.

Therefore we started a comparative study on almost all the SHRIMPs available to this date. We collected seven different non-centrosymmetric inorganic nanomaterials: $Fe(IO_3)_3$ [138, 140], $KNbO_3$ [133], KTP [134], $LiNbO_3$ [152, 153], BBO, ZnO [135]

and $BaTiO_3$ [136]. In December 2009 to our knowledge, the only inorganic nanocrystal reported in literature not included in this systematic study is strontium barium niobate ($Sr_{0.6}Ba_{0.4}Nb_2O_6$ [154]).

We present here only some preliminary results of this ongoing study. According to the point group symmetries, we summarize the $\chi^{(2)}$ properties of the crystals in Tab. III.2. According to Kleinman conditions, which implies to limit frequencies far from resonance (Sec. I.3.1), the non vanishing terms of certain nonlinear susceptibilities are identical. For example: class 6, 6mm and 4mm present the same non-vanishing components, but coefficient values are different. We see also the resemblance of these classes with the mm2 class, only $\chi_{15} \neq \chi_{24}$.

Based on the properties of the nonlinear susceptibilities, we present a polarization analysis on several single nanocrystals of each material. The properties of these crystals are summarized in Tab. III.3. We chose a mean size of $100-200$ nm in consideration of an eventual application for bio-imaging, because for uptake in cells particles size have to be smaller than 250 nm. For this application, size matters and the smaller the better. On the other hand, the signal I decreases with the square of the volume, i.e. $I \propto R^6$, with R the radius. With our system we identify this size range to be a good compromise for the cell targeting. In addition we have experimentally verified that optical damage threshold of these nonlinear nanocrystals is much higher than the cell viability damage, which has been experimentally measured to be 150 GW/cm^2. [158, 159] Moreover, the power density needed for imaging the nonlinear nanocrystals, in the order of 1 GW/cm^2, is well below the cell damage threshold.

The experimental procedure is identical to the one presented in Sec. III.1. The size of the each nanocrystal is obtained by IC-AFM measurement, while the optical polarization response is obtained with the set-up described in Sec. II.3. In Fig. III.3, we present the typical SHG polarization response of different nanocrystals (Fig. III.3(B - F)). The experimental conditions have been carefully checked to be the same for each experiment, so we can safely compare the optical response. Due to the similarity of the nonlinear susceptibility tensor of these materials, they present pretty similar dipolar responses and such a good correspondence among theoretical and experimental traces also ensures that the nanocrystals are associated to a unique crystal orientation and not to crystal agglomerates. In (Fig. III.3 (a)), we present a simulated polarization response of a $Fe(IO_3)_3$ nanocrystal for an orientation ($\theta = 92°$, $\phi = 125°$, see Sec. I.5). Following the results of Sec. III.1 and given the similarity of the responses we can ensure the possibility to fit and retrieve the orientation of each nanocrystal. From theoretical considerations, we can report that dipolar signatures are present and maximal when the optical axis is almost parallel to the transverse plane (xy plane). If it is parallel to the propagation axis (z), the SHG signal vanishes.

For more complex nonlinear susceptibilities, as these obtained with crystals belonging to the 3m class, the presence of additional non-vanishing terms (see Tab. III.2) will modify the polarized radiation signature. In Fig. III.4, we show the presence of dipolar (first row) as well as quadrupolar (second row) signatures obtained theoretically (A&D) and experimentally measured ($LiNbO_3$ (B & E) and BBO (C & F)).

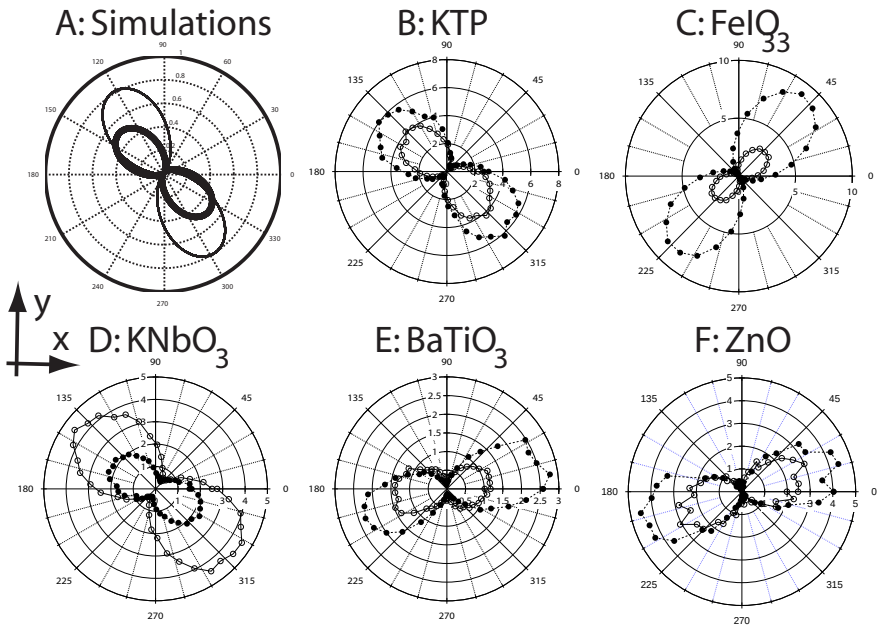

Figure III.3: (A) Simulated polarization emission of a $Fe(IO_3)_3$ nanocrystal ($\theta = 92°$, $\phi = 125°$). Polarization experimental response of SHG emission for different nanocrystals: (B)KTP, (C) $Fe(IO_3)_3$, (D) $KNbO_3$, (E) $BaTiO_3$, (F) ZnO. Each signal is analyzed along two orthogonal directions: X filled circles and Y open circles.

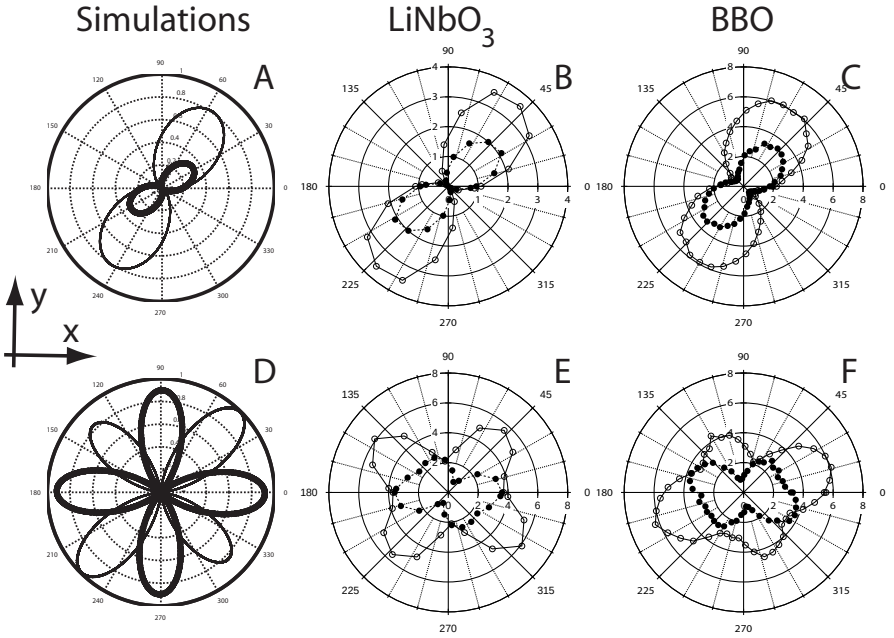

Figure III.4: Polarization emission for 3m crystals. .

Material	Symmetry class	General conditions	Kleinman Symmetry
$LiNbO_3$ & BBO	3m	$\begin{pmatrix} 0 & 0 & 0 & 0 & \chi_{15} & -\chi_{22} \\ -\chi_{22} & \chi_{22} & 0 & \chi_{15} & 0 & 0 \\ \chi_{31} & \chi_{31} & \chi_{33} & 0 & 0 & 0 \end{pmatrix}$	$\begin{pmatrix} 0 & 0 & 0 & 0 & \chi_{15} & -\chi_{22} \\ -\chi_{22} & \chi_{22} & 0 & \chi_{15} & 0 & 0 \\ \chi_{15} & \chi_{15} & \chi_{33} & 0 & 0 & 0 \end{pmatrix}$
$KNbO_3$ & KTP	mm2	$\begin{pmatrix} 0 & 0 & 0 & 0 & \chi_{15} & 0 \\ 0 & 0 & 0 & \chi_{24} & 0 & 0 \\ \chi_{31} & \chi_{32} & \chi_{33} & 0 & 0 & 0 \end{pmatrix}$	$\begin{pmatrix} 0 & 0 & 0 & 0 & \chi_{15} & 0 \\ 0 & 0 & 0 & \chi_{24} & 0 & 0 \\ \chi_{15} & \chi_{24} & \chi_{33} & 0 & 0 & 0 \end{pmatrix}$
$Fe(IO_3)_3$	6	$\begin{pmatrix} 0 & 0 & 0 & \chi_{14} & \chi_{15} & 0 \\ 0 & 0 & 0 & \chi_{15} & -\chi_{14} & 0 \\ \chi_{31} & \chi_{31} & \chi_{33} & 0 & 0 & 0 \end{pmatrix}$	$\begin{pmatrix} 0 & 0 & 0 & 0 & \chi_{15} & 0 \\ 0 & 0 & 0 & \chi_{15} & 0 & 0 \\ \chi_{15} & \chi_{15} & \chi_{33} & 0 & 0 & 0 \end{pmatrix}$
ZnO & $BaTiO_3$	6mm, 4mm	$\begin{pmatrix} 0 & 0 & 0 & 0 & \chi_{15} & 0 \\ 0 & 0 & 0 & \chi_{15} & 0 & 0 \\ \chi_{31} & \chi_{31} & \chi_{33} & 0 & 0 & 0 \end{pmatrix}$	$\begin{pmatrix} 0 & 0 & 0 & 0 & \chi_{15} & 0 \\ 0 & 0 & 0 & \chi_{15} & 0 & 0 \\ \chi_{15} & \chi_{15} & \chi_{33} & 0 & 0 & 0 \end{pmatrix}$

Table III.2: Summary of the second order nonlinear susceptibilities of $KNbO_3$, KTP, $LiNbO_3$, BBO, $Fe(IO_3)_3$, ZnO and $BaTiO_3$ crystals. Source: [74].

Name	Point Group	Mean Size [nm]	Transparency range [μm]	Reference
$LiNbO_3$	3m	[52 - 110]	[0.4 - 5.5]	[143]
BBO	3m	[260 - 280]	[0.189 - 3.5]	[143]
KTP	mm2	[200 - 250]	[0.35 - 4.5]	[155]
$KNbO_3$	mm2	[75 - 150]	[0.4 - >4]	[143]
$BaTiO_3$	4mm	[180 - 200]	[0.5 - 6]	[156]
ZnO	6mm	[100 - 230]	not known	[157]
$Fe(IO_3)_3$	6	[50 - 150]	not known	[140]

Table III.3: Specifications of the Nanocrystals of the study

The parameters of the theoretical response are for Fig. III.4 (A) (resp. (D)) $\theta = 60°$ (resp.$1°$), $\phi = 45°$ (resp.$80°$) and $\psi = 45°$ (resp.$70°$). The quadrupole responses appear for numerous orientations and result from the contribution of χ_{22} components. The retrieval of the orientation of 3m point group crystal is much more difficult and identical response for different crystal orientation are not excluded. Depending on the application envisaged, if we need to retrieve the orientation of the nanocrystal, we will exclude 3m crystals. On the other hand, for application where a signal is always needed, as cell targeting, we will prefer 3m crystal.

In addition to these preliminary results, the study will consider the toxicity and the bio-compatibility of each nanocrystal. The photostability and the frequency conversion efficiency are also important parameters to evidence the crystal more suited for biological applications.

III.3 Nanodoublers as deep imaging markers for multi-photon microscopy

To evidence the flexibility of the excitation wavelength of a non resonant process, we demonstrate the possibility to excite second-harmonic (SH) active $Fe(IO_3)_3$ nanocrystals with two distinct laser sources at 800 and 1550 nm. In addition we show, by a complementary experimental and numerical study, how the wavelength flexibility inherent to non-phase-matched SH nanoparticles can be efficiently exploited to increase imaging penetration depth of markers embedded in biological samples. We also demonstrate how in an epi-detected SHG measurement through a turbid sample, signal collection can be severely affected by the choice of excitation wavelength. To this end, we first use artificial tissue phantoms made of submicrometric polystyrene spheres, and subsequently a section of murine liver. This is to our knowledge the first demonstration of the potentialities of wavelength excitation flexibility in a biological application and is a starting point for numerous bio-applications of the SHRIMPs.

Table III.4: Monte Carlo Input Parameters

# Photons	dz**[cm]**	dr**[cm]**	R_{IN}**[cm]**	R_{OUT}**[cm]**	θ°_{IN}	θ°_{OUT}
5e6	10^{-5}	10^{-5}	10^{-4}	10^{-2}	10	36.9

λ **[nm]**	μ_a[cm^{-1}]		μ_s**[cm^{-1}]**		g	
	Poly Spheres	Liver	Poly Spheres	Liver	Poly Spheres	Liver
400	0.79	53.90	137.23	242.74	0.19849	0.90
800	2.16	5.67	10.01	100.85	0.04674	0.95
1550	10.74	10.78	0.77	35.89	0.01221	0.91

III.3.1 Monte Carlo simulation

For simulating the epi-detection of the signal from a SHRIMP embedded in a turbid tissue, we employed a Monte Carlo code of light transport in multilayered samples, which already proved very successful for a variety of studies. [160] The simulation assume an infinitely narrow photon beam, perpendicularly incident on a tissue layer supposed much wider than the spatial extent of photon distribution. The model is restricted to a cylindrical symmetry by assuming an optically isotropic medium. At every computation step, a photon, which is treated as a classical particle, neglecting polarization effects, has a certain probability of being absorbed or scattered. These probabilities are determined directly from the macroscopic values of scattering efficiency (μ_s), absorption efficiency (μ_a), and anisotropy (g) calculated applying Mie theory for a suspension of nanospheres in water [161], using the real and imaginary reflective indices for polystyrene provided by ref. [162]. Alternatively, for the liver sample, we used the values of μ_s, μ_a, and g experimentally determined by Parsa *et al.*. [163] The input parameters used for the simulation are summarized in Tab. III.4.

As indicated on the right of Fig. III.5, the effective excitation for a SHRIMP placed after a scattering layer of thickness d for an excitation wavelength ω_i (i=800, 1550 nm), was obtained by integrating the fraction of photons $\alpha(\omega_i, d, R_{IN}, \theta_{IN})$ exiting from the substrates+layer system through a limited circular area of R_{IN} =1 μm diameter (comparable with the experimental focal spot) with propagation axis deviating $\theta_{IN} < 10^{\circ}$ from the incident direction. This way we ensured to limit the excitation process to ballistic photons, which conserve the temporal structure (i.e. photon density) of the incoming pulse. [164] This quantity was then squared to account for the nonlinear power dependence of SHG. An independent simulation was successively run to calculate the fraction of SH photons $\beta(2 \cdot \omega_i, d, R_{OUT}, \theta_{OUT})$ that can reach the microscope objective after traveling backwards through the substrate/scattering system. Contrary to excitation, in this case, the transmitted photons were integrated over a large exit area R_{OUT} and over an angular range θ_{OUT} calculated by taking into account the objective N.A. and the refractions of the SH photons at the substrate/sample and substrate/air interfaces. The epi-detected signal I_{SHRIMP} as a function of the incident laser intensity

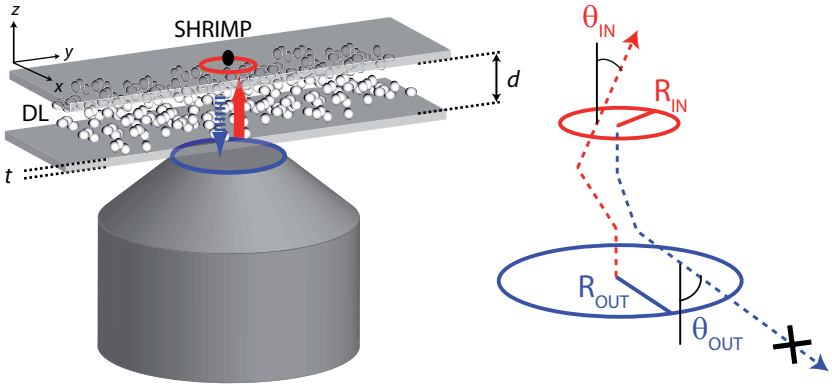

Figure III.5: Left: NIR and IR light (red arrow) are focused by the objective onto the SHRIMP particle, placed on the upper side of a system of two microscope substrates of thickness t delimiting a diffusive layer (DL) (polystyrene beads suspension or liver section) of variable thickness d. The backwards traveling fraction of SH emission (blow arrow) is epi-collected by the same objective. Images are reconstructed by scanning sample position along x and y axes. **Right:** Example of the approach used in the Monte Carlo simulation. The incoming photon (red dashed line) is considered effective for SH excitation because, after two scattering events, it enters the SHRIMP region (red circle) with a small angle θ_{IN} with respect to normal incidence. On the other hand, the outgoing SH photon (blue dashed line) is not accounted for the signal calculation, as it exits the sample with a large angle exceeding θ_{OUT}, i.e. the collection capability of the objective.

I was finally determined as $I_{SHRIMP} = (I \cdot \alpha)^2 \cdot \beta$.

III.3.2 Experimental Results

SHRIMP particles have so far been investigated only by means of Ti:Sapphire lasers, so we first characterized their response to IR excitation by reporting in Fig. III.6 the up-converted spectrum generated by a single nanocrystal. The fundamental Erbium laser spectrum is shown in the inset for reference. The second harmonic peak between 730 and 850 nm is the predominant structure. Note that the tiny spectral dip at 780 nm correlates well with the minimum appearing in the calculated frequency-doubled spectrum (dotted line) and that the original bandwidth is completely up-converted. The peak at 520 nm corresponds to the third harmonic (TH) emission, which, although much weaker, is clearly visible in the semi-logarithmic plot. TH was always co-localized with SH, evidencing that it is an effect genuinely related to the presence of a nanocrystal.

In Fig. III.7, panels (a) and (b) present a comparison of the same region of a sample of randomly dispersed nanocrystals obtained by drying a drop of $Fe(IO_3)_3$ filtered solution on the upper microscope substrate as illustrated in Fig. III.5. From independent atomic force microscope measurements of samples prepared in the same way, we know that filtered $Fe(IO_3)_3$ particles ($\sim$30 nm) have a tendency to aggregation on mi-

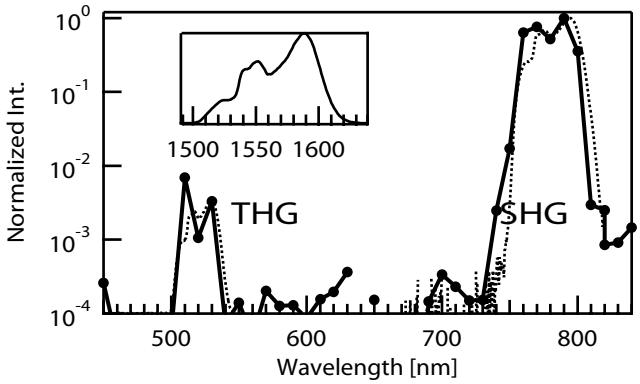

Figure III.6: Semi-logarithmic spectrum of the second and third harmonic emission (continuous line) from a single $Fe(IO_3)_3$ nanocrystal excited by the IR laser. The dotted lines correspond to the calculated frequency doubled and tripled fundamental IR laser spectrum (shown in the inset).

croscope substrate and their actual size on the sample is 80 ± 40 nm. [140] The images were realized by detecting the SH signal from the particles excited first by the IR and successively by the NIR laser. A quick inspection indicates that all the particles are retrieved using both excitations and they show comparable relative intensities. The darker halo surrounding the particles in the IR-excited scan (Fig. III.7(b)) can be originated from diminished imaging performances of the objective, which is optimized for the visible region, but it can also be ascribed to interference effects among the SHG radiation generated at different location within the focus, as previously observed for other coherent microscopy signals. [165]

The different light transport properties of NIR and IR excitation and their corresponding SH (400 and 775 nm) through a strongly scattering medium were then investigated using calibrated tissue phantoms. In the series of SH scans reported in Fig. III.7 (c)-(f) and (h), the different rows correspond to different layer thickness, each containing two images of the same sample region excited by the two laser sources: NIR (left) and IR (right). Note that the images on different rows do not correspond to the same sample region. For a sample thickness of 90 μm [(c), (d)], two particles are present on the scan. The left one is characterized by a much weaker signal and its size is comparable with the lateral resolution of the microscope.

The poorer resolution of this particle in the IR scan is partially attributed to the larger diffraction limit at 1.55 μm, as well as the aforementioned reduced performances of the objective at this wavelength. The right SHRIMP is probably a larger particles aggregate, with a size exceeding the set-up resolution. At 180 μm [(e), (f)], the comparison between the IR scan evidence the presence of a SHRIMP which does not appear in the corresponding NIR scan, although several NIR-excited scans were performed systematically varying focusing and detection parameters. A similar observation resulted from the measurement performed with the diffusive layer of 300 μm thickness (Fig. III.7(h)), even in this case we were not able to detect any particle in the

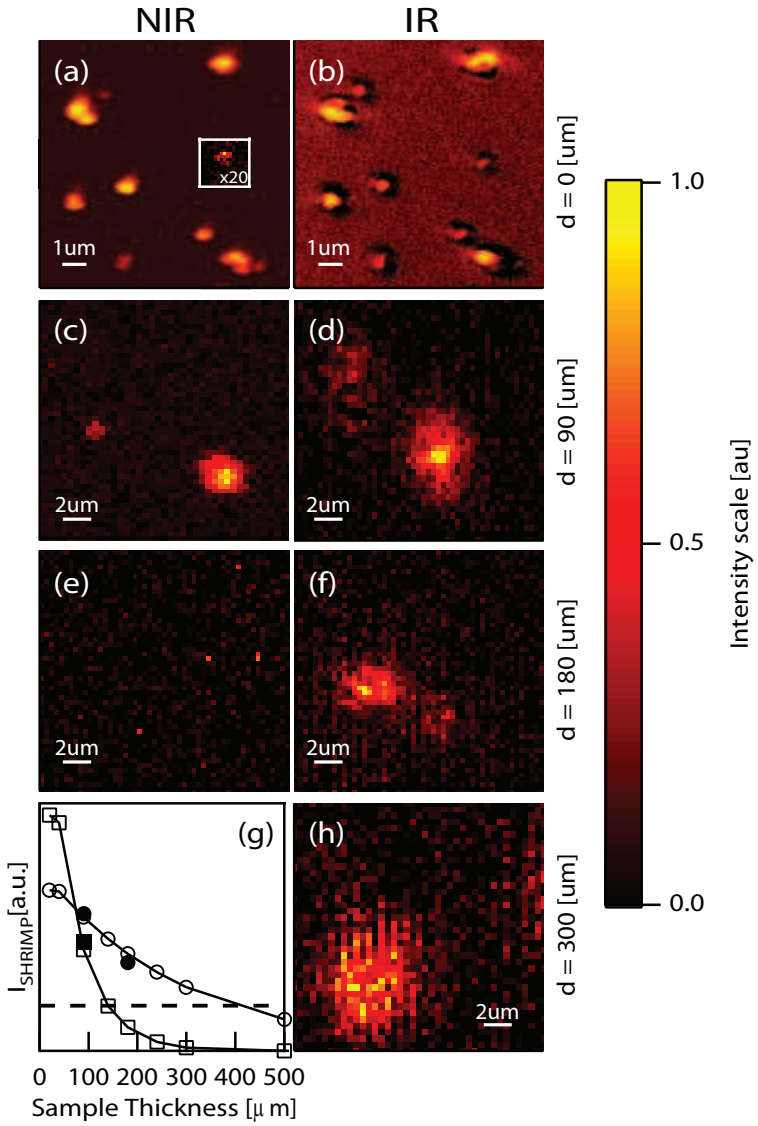

Figure III.7: Comparison of nanocrystals samples illuminated by NIR (left column) and IR (right column) laser with no diffusive layer [**(a)**, **(b)**], and with diffusive layer of polystyrene nanospheres suspension in water of 90 μm thickness [(c), (d)], 180 μm thickness [**(e)**, **(f)**], and 300 μm [**(h)**]. **Panel (g):** Result of a Monte Carlo simulation showing the intensity of the epi-detected signal (I_{SHRIMP}) as a function of the penetration depth for NIR (□) and IR excitation (○). Experimental values measured on microscopic $Fe(IO_3)_3$ structures by NIR (■) and IR (●) are also reported on the plot as additional reference.

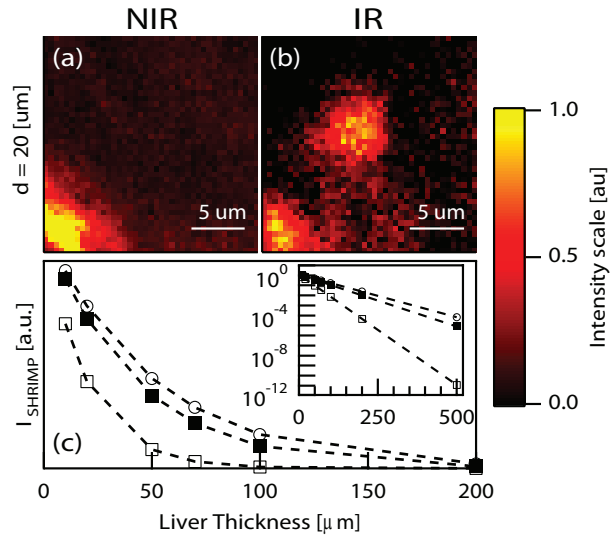

Figure III.8: Comparison of excitation of $Fe(IO_3)_3$ nanocrystals through a 20 μm murine liver sample: **(a)** NIR excitation and **(b)** IR excitation. **(c)** Monte Carlo simulation of the epi-detected signal fom a SHRIMP excited and epi-detected through a layer of murine liver as a function of thickness calculated for various excitation wavelengths: NIR (□), IR (○), and 1320 nm (■). **Inset:** Semi-logarithmic representation of the same dataset.

NIR-excited image.

The corresponding simulation are presented in Fig.III.7 (g). One can observe that for $d < 80$ μm, the NIR-generated signal is expected to be larger than the IR one. This finding can be correlated to the slightly higher contrast shown by the NIR scan in the comparison between panels (c) and (d). For thicker samples, the SH signal collected under IR excitation becomes dominant, and indeed already for $d = 180$ μm, no NIR-excited signal could be detected. The dashed horizontal line corresponds to an upper estimate for the detection limit, determined by the absence of signal for $I_{SHRIMP}(\omega_{800}, 180\ \mu\text{m})$. We observe that its position is consistent with the detection of the SHRIMP at $d = 300$ μm (Fig.III.7 (h)), whose simulated intensity lies above this threshold. To further assess the agreement between calculations and experiment, we measured the epi-detected SH signal from a micrometric $Fe(IO_3)_3$ structure excited by NIR and IR. The relative intensities of the corresponding datapoints are well superimposed to the curves in Fig. III.7(g) and corroborate the correctness of the numerical approach within the thickness range investigated.

Given that the performance of SHRIMP detection cannot be simply ascribed to the deeper penetration of longer wavelengths, but are set by the interplay between excitation and backward detection of the SH signal, we extended the investigation by substituting the sample with a 20 μm thick murine liver tissue. In this case, in fact, rather strong scattering is accompanied by the specific spectral response of the tissue, dominated by heme proteins absorption around 400 nm and water absorption around 1.4 μm. [163] Panels (a) and (b) of Fig. III.8, report the results of NIR- and the IR-excited images, respectively. The intense spot on the lower left corner of both images

is a reference SH signal generated by a micrometric $Fe(IO_3)_3$ structure, placed on the substrate close to the SHRIMP nanocrystal to verify the correct experimental settings for both measurements. As in the preceding comparison, the SHRIMP signal could be easily epi-detected exclusively in the IR case. In Fig. III.8(c), the simulated signal intensity again indicates that IR-excitation (○) remains the most favorable choice for this representative biological sample, not only with respect to NIR (□), but, contrary to our expectations, also with respect to 1320 nm excitation (■), which was also simulated as it presents no spectral overlap with the tissue absorption for both excitation and SH. From calculations it appears that, even though scattering properties in the excitation process assume a major role in affecting the signal intensity by setting the fraction of ballistic photons reaching the SHRIMP with enough power density to nonlinearly excite it, the stronger diffusion of bluemost wavelengths results the dominant factor at the origin of the intensity differences as penetration depth increases. Clearly, to identify the most efficient excitation option, signal intensity is not the unique criterion, as sample heating by water absorption should also be taken into consideration for long-term measurements.

III.4 Nano-FROG: Frequency Resolved Optical Gating by a nanometric object

Exploiting the fact that SHG is a coherent process, we present a technique to characterize ultrashort pulses at the focal plane of a high numerical aperture objective with unprecedented spatial resolution, by performing a FROG measurement with a single nanocrystal as nonlinear medium. This approach, which can be implemented on a conventional or an inverted laser scanning microscope, can be further developed to provide phase-sensitive information by monitoring the distortions induced by the microscopic local environment around the NP on femtosecond pulses. Benefiting from the coherent properties of the SHG, application of this methods can be implemented to characterize *in situ* different pulse shapes resulting from coherent control schemes in bio-samples [43]. Inversely and taking additionally advantage of confinement effects, we can use the SHRIMPs as photo-inducers of chemical reaction by coherent control schemes.

Considering the long irradiation of the sample, shutter 1 (S1 in Fig. II.1) can be used to reduce photodegradation by regularly blocking the laser for a few seconds to allow heat evacuation at the sample site. In interferometric experiments, shutter 2 (S2 in Fig. II.1) is closed to measure the reference signal generated by a single arm of the interferometer for post-processing data correction.

Due to the constrains of the experimental setup, all characterizations traces, autocorrelation and FROG, were taken in a collinear geometry [94]. The autocorrelation trace reported in Fig. III.9(a) was recorded after maximizing the SHG response as a function of the incident laser polarization as described in [140]. The time increment corresponds to 1.8 fs, the interference fringes of the two electric fields at 800 nm

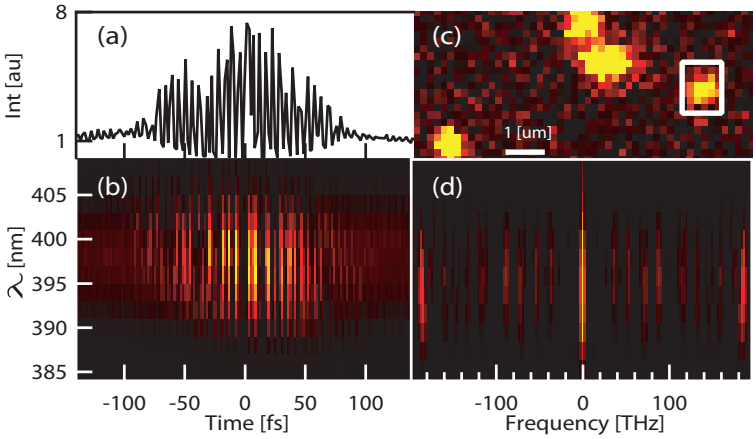

Figure III.9: **A.** Interferometric autocorrelation trace. **B.** cFROG trace. **C.** Image of the nanoparticles dispersed on a microscopic glass slide. The particle highlighted by the 1 μm square was used as nonlinear medium for acquiring the autocorrelation and the cFROG trace. **D.** Result of the Fourier transform along the time axis of the cFROG trace in B.

(T=2.66 fs) are therefore not fully resolved. On the other hand, the expected 8:1 ratio between the trace maximum and the wings is almost perfectly recovered.

The retrieval of a symmetric autocorrelation trace, showing the theoretical fringes-to-offset ratio confirms the good alignment of the two interferometer arms, the balance among their intensities, and the absence of saturation in the frequency-mixing process. After this preliminary characterization, which indicates a FWHM pulse duration of 69 fs, we could proceed to acquire the full collinear-FROG (cFROG) trace of Fig. III.9(b). Due to the long acquisition time necessary for measuring the full cFROG curve, it was necessary to correct for slow sample photodegradation. To this end, we systematically monitored a reference value corresponding to the SHG generated by a single arm of the interferometer. The correction procedure incorporates the experimental time-dependence extracted from the autocorrelation trace to associate the right weight at different time delays to the photodegradation baseline correction. For the measurement in Fig. III.9(b) photodegradation amounts to $\sim$50% decrease of the SHG signal intensity over the complete scan.

The result of a numerical Fourier transform along the time axis of the cFROG trace is displayed in Fig. III.9(d). Note that the frequency of the modulation at ω_0, expected at 375 THz is downshifted to $\sim$180 THz due to undersampling, while the $2\omega_0$ component is not resolved. It has been shown that undersampled acquisition of a cFROG trace can be safely performed under certain conditions without loss of information on the final FROG. [116, 117]

The FROG in Fig. III.10(a) was extracted by first filtering out the modulation components in the Fourier space, and then by applying the inverse transformation back to the time/wavelength space. After this operation, we subtracted to the trace the DC offset, i.e. the second term in Eq. I.72. The treated data were successively fed into a commercial FROG-inversion program [118] to determine the pulse characteristics.

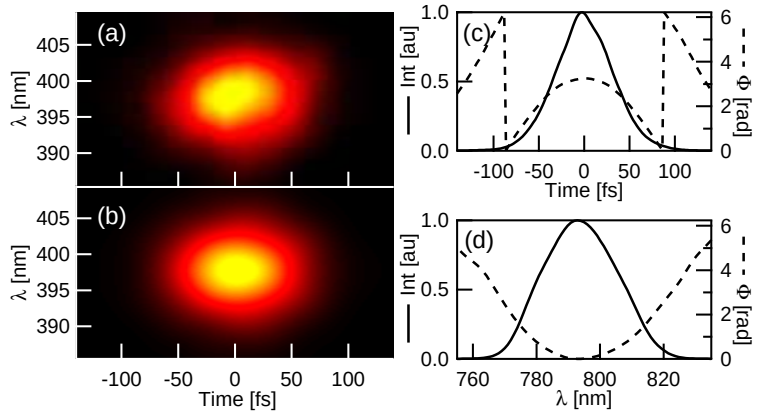

Figure III.10: A. Experimental FROG trace. **B.** Retrieved FROG trace. Electric field intensity (solid line) and phase (dashed line) as a function of time (**C**) and of wavelength (**D**).

The retrieval error corresponds to $2.5^{0}/_{00}$. The retrieved FROG trace is shown in Fig. III.10(b), along with pulse electric field intensity temporal profile (corresponding to a pulse duration of 75 fs) and spectrum reported in (c) and (d). The corresponding phase-functions are also shown. The latter indicate the presence of a residual quadratic chirp on the pulse due to group velocity dispersion accumulated during propagation through the microscope optics, which is not fully corrected by the grating compressor. By comparing the pulse duration at the input of the microscope and at the focal plane, we can quantify the second-order dispersion parameter to 4416 fs^2, in line with the values determined by Wolleschensky *et al.* for similar but not identical optical systems. [97]

In the present section the particle investigated has dimensions comparable to the size of the nonlinear focal spot (~ 300 nm), the spatial resolution is therefore already one order of magnitude higher than the spatially-resolved FROG and TADPOLE techniques recently proposed. [104, 166] Our approach can be easily extended to smaller NPs down to a dimension of a few tens of nanometers. The major experimental difficulty is represented by the extremely long acquisition time (five hours) compared to the photostability of the nanoscopic samples: the use of an imaging spectrometer equipped with an array detector capable of simultaneous acquisition of the whole spectrum would reduce the acquisition time by orders of magnitudes, allowing stable measurements on smaller samples. Note that size-dependent signal intensity does not represent a limitation: thanks to the very good frequency conversion efficiency of $Fe(IO_3)_3$, we recently succeeded in imaging and measuring the polarization response of NPs with sizes as small 40 nm on the same experimental set-up. [140] For NPs smaller than the focal spot of a high NA objective, the resolution of sub-focal features theoretically predicted in the framework of phase and polarization shaping microscopy will be reachable. Recent calculations indicate, for example, that clearly different spatio-temporal evolution of the electric field are expected at locations 400 nm apart in the focal plane for tightly focused shaped pulses. [167] In addition, the polarization-

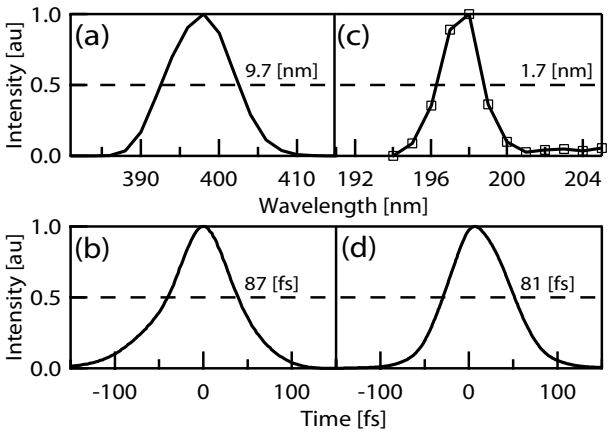

Figure III.11: (a) SHG spectrum of a λ_{396}-centered pulse performed on single nanocrystal and (b) its autocorrelation [170]. (c) SHG spectrum of the λ_{198}-centered pulse generated on the pellet and (d) its autocorrelation.

dependent response of $Fe(IO_3)_3$ NPs can be exploited to characterize the polarization evolution by combining two orthogonal cFROG measurements of the same shaped pulse. [168] The absence of phase-matching constrains for subwavelength NPs can be useful for broadband pulse characterization allowing the frequency mixing of virtually any wavelength in the transparency window of $Fe(IO_3)_3$. This possibility can result particularly advantageous for broadband single pulse CARS and coherent microscopy, which are increasingly based on the use of supercontinuum broadened pulses in photonic crystal fibers. [169]

III.5 Ultrabroadband Pulse Characterization using Nanocrystals Pellets

In this section we report the ability of pellets made up of compressed Iron Iodate nanocrystals to frequency double the whole visible spectrum. We suggest their use for complete characterization of intense ultrabroadband laser pulses.

Thanks to their small size ($l = 20 - 150$ nm) and large second order susceptibility, we succeeded in frequency doubling 800 nm radiation on individual nanocrystals (see Fig. III.11(a)). As reported in Fig. III.11(b), the nonlinear response of the nanoparticle was used to acquire a pulse autocorrelation trace at the focal plane of a high numerical aperture objective [170]. Due to the geometry imposed by the microscopic setup, the interference fringes typical of collinear measurements were removed by an *ad hoc* cut-off filter in the Fourier space [117].

Since $Fe(IO_3)_3$ nanocrystals are smaller than coherence length, the material can simply be considered as an ensemble of nonlinear radiating dipoles, providing complete doubling of an incident spectrum centered at any wavelength independently from

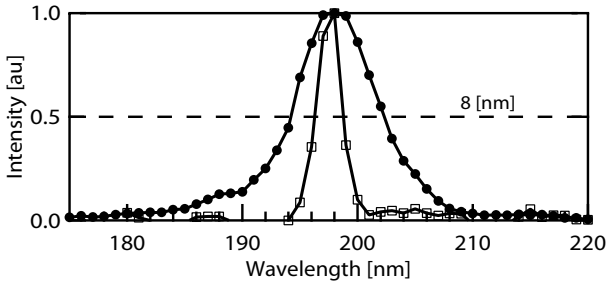

Figure III.12: (Dots) UV spectrum (at 200 nm) of a λ_{396}-centered-broad source obtained by co-filamentation. (Squares) Original spectrum corresponding traces for a 400 nm-pulse without broadening (data reported from (Fig. III.11(c))).

any phase-matching consideration. This property is exemplified by the plot in Fig. III.11(b), showing the result of the spectral doubling of an input UV pulse (centered at $\lambda_{396} = 396$ nm, bandwidth $\Delta\lambda = 6.3$ nm, obtained by frequency-doubling a λ_{792}-centered pulses). As reported in Fig. III.11(d), the corresponding autocorrelation trace indicates a λ_{396}-centered pulse duration of 81 fs.

The above results demonstrate the ability of $Fe(IO_3)_3$ to generate an easy detectable scattered SHG signal from a UV-Vis pulse focused onto the pellet. As seen in Fig. II.8, even though the detection efficiencies was limited by the low numerical aperture of the collection lens, a clear background-free quadratic dependence is observed on the scattered 200 nm signal. Within the scope of few-cycle pulses characterization, we show now that bandwidth increase does not limit this capability, by repeating the measurement using as input filamentation-broadened λ_{396}-centered pulses with spectral bandwidth spanning from 350 nm to 440 nm. As illustrated in Fig. III.12, their doubled spectrum extends from 175 nm to 220 nm fully matching the spectral range of the input pulse. The measured width is 8 nm FWHM, which could theoretically be recompressed down to 7 fs pulse duration.

In order to accurately perform a few-cycle pulses autocorrelation, the nonlinear material has to efficiently support a nonlinear polarization $\mathcal{P} \propto E^2(t)$, where $E(t)$ is the *real* electric field. In the Fourier reciprocal space, this nonlinear source term corresponds to all the frequency mixing pairs within the spectrum. We show that $Fe(IO_3)_3$ pellet support sum-frequency generation (SFG). In particular, when launching simultaneously λ_{792}-centered and λ_{396}-centered pulses onto the nanoparticles agglomerate, a delay-dependent signal centered at 264 nm was recorded both for orthogonal and parallel polarization of the two input pulses (Fig. III.13(b)). In Figure III.13 we summarize the results of these measurements: in (a) one can observe that, also in absence of the λ_{396}-centered pulse on the sample, a weak 264 nm signal is present, which is a signature of λ_{792}-centered pulse frequency tripling. By subtracting to the zero-delayed curve (Fig. III.13(b)) this third harmonic component, we obtain the signature of SFG spectrum at 264 nm (about 7.3 nm FWHM) (Fig. III.13(c)).

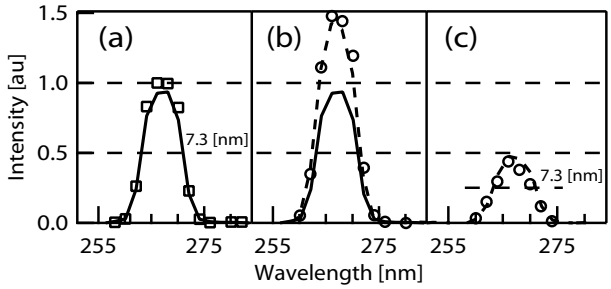

Figure III.13: Solid line: Signal generated only by the IR beam. (a) Signal (Squares) for UV and IR laser pulses temporally separated by 750 fs, (b) simultaneous and parallel (dotted line)(resp. perp. (Circles)) λ_{396}-centered- and λ_{792}-centered- laser pulses. (c) Signature of the SFG signal.

III.6 Evanescent-Field-Induced SHG by Nonlinear Nanoparticles

Planar optical waveguides have already been used as a suitable excitation platform in a number of fluorescence analysis applications. [171–173] They enable highly efficient and selective excitation of fluorescent molecules in close proximity to the waveguide surface by the evanescent field of the guided mode. Typically the waveguide is composed of a single layer of a metal-oxide with high index of refraction. High intensity of the evanescent field is assured by using an appropriate film thickness for single mode operation, usually in the range 100 - 200 nm. The strong evanescent field of such waveguide modes allows the design of highly sensitive devices and provides the possibility for two-photon fluorescence excitation on comparatively large areas. [174, 175]

Inorganic non-centrosymmetric nanocrystals, often referred to as SHRIMPs (Second Harmonic IMaging Probes), have attracted increasing attention and stimulated a wide series of proposals for their applications in bioimaging [135, 136, 176], micromanipulation [153], and exploitation of their coherent optical response [170, 177, 178] since the appearance of the first studies on their nonlinear optical properties. Due to their sub-wavelength dimensions and related absence of phase-matching constraints [179], there is no spectral limitation for the nonlinear excitation of such nanoparticles. Moreover, in contrast to resonantly excited nanoprobes (such as fluorescent molecules and quantum dots), SHRIMPs are not affected by bleaching nor blinking, the former being one of the principle drawbacks reported in previous waveguide experiments. [175]

In this section we demonstrate non-scanning excitation of the second harmonic (SH) response of several individual SHRIMPs scattered over a large area on a planar waveguide. Although evanescent-field-induced two-photon fluorescence was already demonstrated for homogeneous organic layers, this work provides for the first time the evidence of evanescent excitation of the SH response of nanometric objects. The results are discussed in terms of efficiency and polarization properties. Further infor-

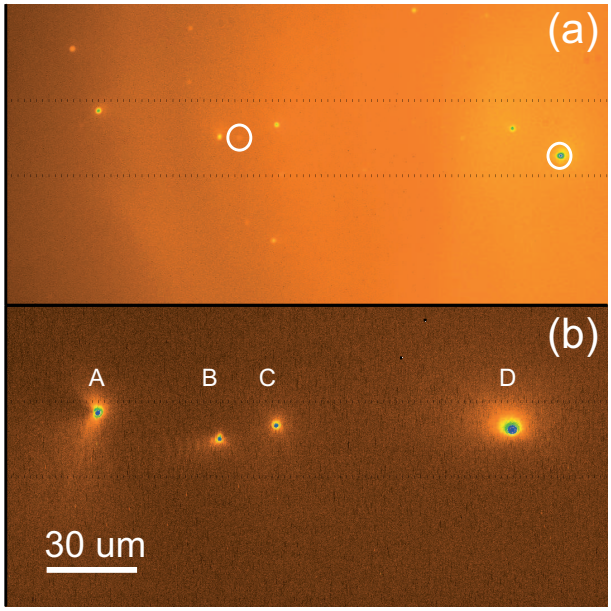

Figure III.14: **(a)** White light image of the scatterers on the waveguide. The dashed lines indicate the extension of the waveguide mode. **(b)** SH image of the same sample region. Note that the particles highlighted in the upper plot are not present in the SH image.

mation about individual nanoparticles orientation and coherent emission are derived within the defined image defocusing framework first developed by Sepiol [180] and later expanded by Enderlein and co-workers. [83, 181]

Figure III.14(a) presents an image of the nanoparticles spread on the waveguide under white light illumination. The differences in intensity revealed by the particles scattering, originate from the size dispersion of the sample. The lateral extension of the guided mode inside the waveguide is indicated by the two parallel dashed lines. Figure III.14(b) represents the same sample region imaged at the SH frequency. The four nanoparticles appearing in this image, labeled $A - D$, are evanescently excited by the laser radiation propagating inside the waveguide. Their positions spatially correlate with those of the nanoparticles observed in Fig. III.14(a). Figure III.15(a) shows the power dependence of the normalized SH signal generated by these nanoparticles. The response exhibits a square dependence shown by the superimposed fit (thick line) bearing a value for the exponential term of 2.00 ± 0.07. This result supports the good spectral selection of the experiment, appreciable also from the extremely high contrast in the SH response of Fig. III.14(b). However, one can notice the absence in the SH image of the two nanoparticles encircled in Fig. III.14(a) although they are both within the excitation region. The lack of the SH counterparts for these particles cannot be trivially ascribed to a difference in size, at least for the right one, which presents a higher scattering intensity than the average under white light illumination, rather to an unfavorable orientation of their crystal axis with respect to the excitation light polarization.

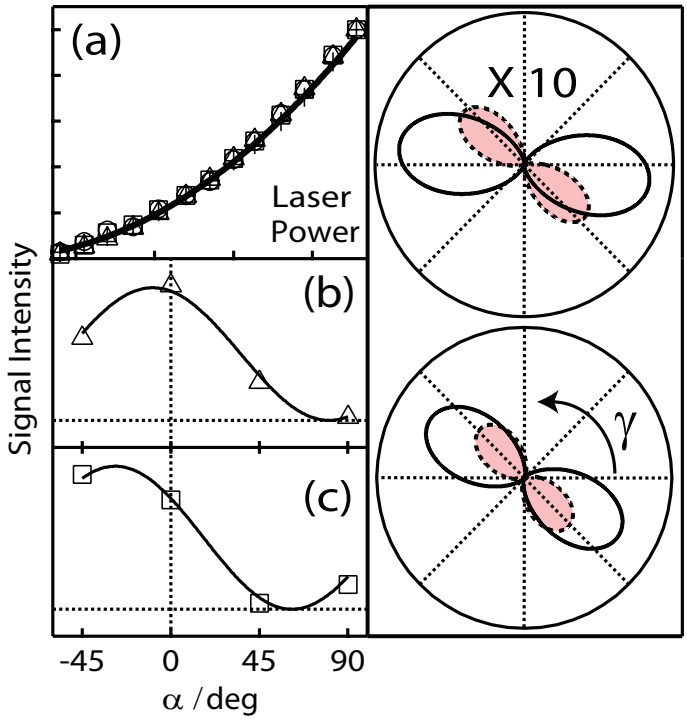

Figure III.15: **(a)** Normalized power dependence of the SH of nanoparticles $A - D$ of Fig. V.2(b). **(b)** and **(c)** Polarization dependence of SH emission from particles D ($\triangle$) and C ($\square$) as a function of the analyzer angle α. **Right panel.** Calculated intensity dependence of SH emission from two differently oriented KTP nanoparticles as a function of excitation light polarization (γ) and analyzer angle (continuous line $\alpha = 0$, dashed line $\alpha = 90°$). Waveguide evanescent excitation corresponds to $\gamma = 0$. Note that the $\alpha = 90°$ response in the upper plot is multiplied by ten for easier inspection.

KTP presents an orthorombic crystal structure, where the $\chi^{(2)}_{\overline{zzz}}$ element is at least four times larger than any other tensorial contribution. [182] The particles highlighted in Fig. III.14(a) very likely present an orientation of the crystal frame leading to a vanishing result for Eq. I.36, assuming an electric field vector aligned along x. For particles $A - D$, on the other hand, the SH response is generated quite efficiently. The polarization of the corresponding $P_i^{2\omega}$ vector is reported in Fig. III.15(b) and (c) for particles D ($\triangle$) and C ($\square$), respectively. The datapoints represent the SH intensity as a function of the analyzer angle α. Particle D (resp. C) presents a polarization response peaking at -10° (-28°) and complete signal extinction for 80° (60°), fulfilling the predictions of Malus' law as confirmed by the good agreement with the $\cos^2$ fit (thick line). Starting from Sec. I.5, we could simulate the curves in the right panel of Fig. III.15, which illustrate the theoretical SH intensity dependence for the two KTP nanocrystals as a function of excitation polarization (γ) and analyzer angle (continuous line $\alpha = 0$, dashed line $\alpha = 90°$). Unlike previous analysis carried out with tight focusing excitation [140, 182], the evanescent wave polarization along x ($\gamma = 0$) cannot be simply changed in the present scheme. Therefore the Euler angles $\theta,\ \phi,\ \psi$ determining the relative orientation of the crystal to the laboratory frame were inferred by matching the intensity of the experimental values obtained for $\alpha = 0$ and $\alpha = 90°$ (Fig. III.15(b), (c)) to the corresponding values assumed for $\gamma = 0$ by the simulated traces. Clearly, for a fixed value of γ, the 3-d orientation retrieval remains an underdetermined problem. We therefore applied an additional empirical criterion to identify the in-plane crystal orientation ϕ among the ensemble of possible solutions by setting $\theta, \psi = 90°$ accounting for the experimental bias represented by the most likely detection of intense SH radiation, that for KTP is associated to this orientation. The best correspondence for particles D and C was finally found for $\phi_D = -10°$ and $\phi_C = -37°$.

As just mentioned the fixed laser polarization of the present approach prevents a complete and rigorous orientation retrieval, nevertheless information about the out-of-plane angle θ of the nonlinear dipole can be derived by applying the theoretical model developed by J. Enderlein [83, 181] and already used by Sandeau *et al.* for analyzing the defocused images of SHRIMPs. [182] The left column of Fig.III.16(a) contains a series of images of two nanoparticles at around 7 μm distance recorded by displacing the focal plane of the collection objective from 0 to 70 μm from the substrate. By examining panel (b), which corresponds to a defocusing distance def = 20 μm, one can see that the upper particle presents a radial symmetric emission structure with concentric rings of different intensity, while the lower particle is characterized by the presence of a weaker intensity region in the emission pattern. Nevertheless, the latter still presents a clear axial symmetry, testifying to the fact that the nonlinearly excited nanocrystal presents a unique monocrystalline domain. [182] To understand the origin of the differences between the two responses, we performed a simulation modeling two neighboring dipoles, radiating at twice the frequency of the laser ($\lambda = 390$ nm). The defocused images were elaborated taking into full account the imaging set-up, the CCD pixel dimension (7.4 μm), and the waveguide characteristics ($n = 2.092$, 159 nm thickness sustained by a $n = 1.52$ glass substrate). The in-plane and out-of-plane

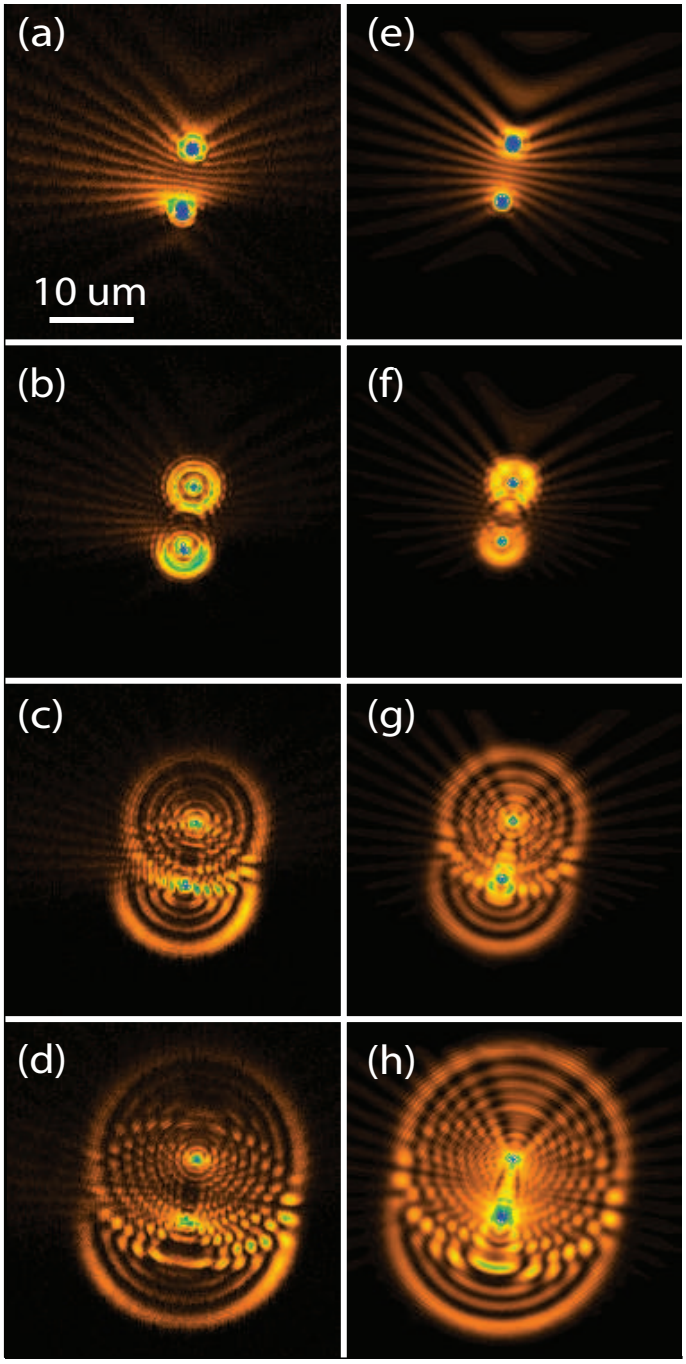

Figure III.16: Experimental (**a,b,c,d**) and numerical (**e, f, g, h**) images of two adjacent nanoparticles excited by the evanescent field and interfering at the SH frequency for different defocusing parameters: def =0 (**a, e**), 20 (**b, f**), 50 (**c, g**) and 70 (**d, h**) μm. The length scale is the same for all plots; the intensity scale is adjusted to facilitate the inspection of interference details. The out-of-plane orientation of the emitting dipole associated to the upper particle and to the lower particle are $\theta_1 = 90°$ (in-plane) and $\theta_2 = 33°$, respectively.

angles of the two dipoles were finally adjusted to obtain the best qualitative agreement with the experimental image. After this procedure, we could ascribe the difference in the symmetry of the two emission patterns principally to a difference in the out-of-plane angles θ. In the case of the upper one, the dipole orientation is parallel to the substrate and to the exciting polarization ($\theta_1 \simeq 90°$), while for the lower one, θ presents a much larger out-of-plane component ($\theta_2 \simeq 33°$).

One very intriguing - although not unexpected - characteristic emerging from all the images in Fig.III.16 is the presence of interference fringes, occurring because of the coherent superposition of the SH emission of the two nanoparticles. Interferences appear for small defocusing as stripes in the region between the two particles and then develop as a dashed motif on the concentric rings of the emission pattern. The simulations capture even the finest details observed in the experimental images. The best agreement was obtained by convoluting the numerical results with a disk of two pixels radius, to account for the smoothing effect of the not perfectly planar waveguide surface. It is worth noting that - unlike the case of harmonic holography, where interferences are created with an external reference beam - we show here interferences originated directly among the nonlinear emissions of two distinct nano-objects for the first time.

III.7 Conclusions and Perspectives

In conclusion, we have performed a detailed analysis of the polarization response of nanocrystals of iron iodate ($Fe(IO_3)_3$), which can be easily synthesized by an inexpensive chemical method. Due to the difficulty of growing bulk crystals of this material, its nonlinear properties were previously only partially known. We demonstrated that $Fe(IO_3)_3$ is an efficient frequency doubler, and this property, together with its remarkable stability in aqueous solution even under extreme pH and temperature conditions, makes of it a very attractive probe for SHG microscopy. Moreover, the possibility to interrogate optically the orientation of each nanocrystal opens the way to a large number of applications. Contrary to similar studies where SHG active particles were embedded in host media (sol-gel matrices, polymers, inclusion compounds), the present measurements were taken directly on nanocrystal isolated on a substrate to prove their aptness as markers for microscopy. We have also analyzed differents SHG-active of nanomaterials and performed a comparative study. This will allow us to identify the advantages/disadvantages of each material and to select the best suited for future applications. In addition, we have demonstrated the possibility to excite SHRIMPs with two distinct laser sources and we have experimentally evidenced and rationalized by numerical simulation how the wavelength flexibility inherent to non-phase-matched SHG can be a crucial factor to increase sample penetration for non-linear microscopic measurements based on these markers. Based on the non resonant properties of SHG and the absence of phase-matching constrains, we demonstrate the wavelength-flexibility of SHRIMPs compared to the existing probes (GFP, Quantum dots), which permit to avoid auto-fluorescence. Moreover, we have exploited the co-

herence properties of the harmonic radiation by proposing a technique (nanoFROG) to characterize tightly focused femtosecond laser pulses with unprecedented spatial resolution. We also have successfully demonstrated that SHRIMPs pellets can support both ultrabroadband SHG and broadband SFG. Because the nonlinear material is used in a reflective configuration, no dispersion occurs allowing its use for few-cycle pulses measurement. Since phase-matching condition does not apply because of the nanometric dimensions of the doubling particles, SHRIMPs pellets open the way to its utilization with ultrabroadband spectra in whole transparency region of the material. Unlike nonlinear crystals which need a careful polishing and are quite expensive, SHRIMPs pellets are inexpensive enough to be used in adverse condition such as within pulse core where the intensity can exceed damage threshold. Finally, we demonstrate the possibility to employ SHRIMP nanoparticles as molecular probes in experiments based on evanescent excitation, taking full advantage of their photostability and of their non-resonant optical response. High selective evanescent excitation at the substrate surface can be associated to nonlinear transverse resolution for imaging. We demonstrated that polarization analysis can be carried out under reasonable assumptions and for the first time, we observed interferences from the nonlinear signals generated by distinct nanometric objects.

Fundamental optical properties of SHRIMPs have been demonstrated so far and applications of these novel probes are numerous. From a fundamental point of view based on recent results [17, 183], further studies should be performed to determine the influence of the shape and the size of the SHRIMPs on the SHG signal. As applications, the possibility of functionalizing the NPs' surface to embed them into biological samples is currently in progress. This would allow the labeling and targeting of cells using SHRIMPs. Combined to a *in vivo* nano-FROG measurement, this might provide a new method for elucidating the interactions between the different spectral components of femtosecond pulses and the NP local environment (cell membranes, biological solutions, local pH). The nano-FROG technique can also be extended to develop novel phase-sensitive techniques in laser scanning microscopy, probing the microscopic environment by monitoring phase, amplitude and polarization distortions of femtosecond laser pulses. There is in fact a growing evidence of the applicability of pulse shaping techniques for improving functional imaging [184, 185], for reducing photo-bleaching of fluorescent labels [186], and for acquiring excitation selectivity [42, 187] also with respect to the local fluorophore environment [184]. Our *in situ* pulse diagnostic technique could in principle be used to decipher the control mechanism underlaying these observations. Prospectively the dipole moment associated to SHRIMPs crystal structure can be used as optical probe of the local field [153] in large areas of a waveguide for monitoring, for instance, cells membrane potential. More exotics applications can also include chemicals process optically photo-induced by SHRIMPs, nonlinear nanoemitters and nanoantennas.

CHAPTER IV

Progresses towards label-free coherent identification

In this chapter, we will first introduce the available techniques to implement coherent control experiments and discuss their limitations(Sec. IV.1). We then present three different studies realized during this thesis. First, the conception and the development of a new MEMS-based linear pulse shaper device (Sec. IV.2). Then, the application of a new class of genetic algorithm to the coherent control is discussed (Sec. IV.3), finally the implementation and the characterization of a direct MEMS-based pulse shaper in the deep ultraviolet region as a first step towards coherent control of bio-molecules (Sec. IV.4).

IV.1 Approaches to pulse-shaping

In this section, we introduce the different technologies that allow us to generate arbitrary pulse-shapes. Considering the central wavelength needed for the applications, the choice of the device will be different. First, the general optical set-up will be described, followed by the different available devices: Liquid Crystal based devices (LCD) and Micro-ElectroMechanical Systems (MEMS).

IV.1.1 Pulse-Shaping

As no electronic devices is able to modulate femtosecond laser pulses in the time domain, the modulation has to be applied in the frequency domain by acting in the Fourier-plane in order to modulate the frequencies separately. This is achieved using a dispersion-free 4-f compressor [127, 188, 189] which allows the spatial separation of

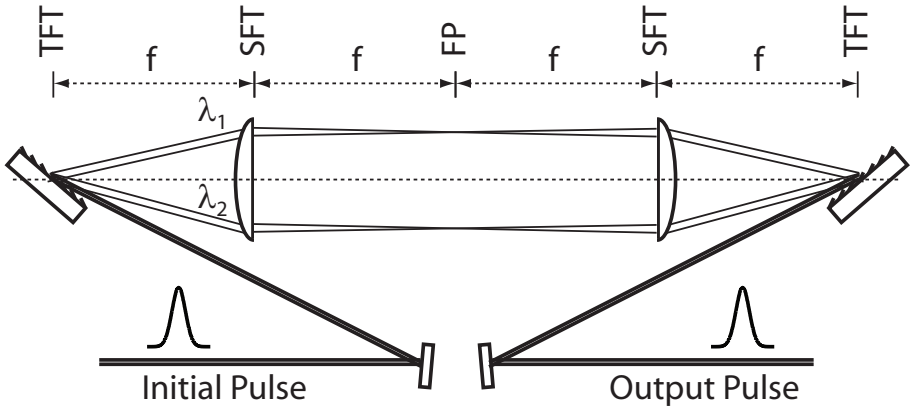

Figure IV.1: Schematic set-up of a 4-f dispersion-free compressor. the grating spreads the spectrum acting as a Temporal Fourier transformer (TFT) and the cylindrical lenses focus the identical frequencies into a vertical line in the Fourier Plane (FP), The lenses act as Spatial Fourier Transformers (SFT).

the frequencies in the Fourier-plane before being recollimated in the temporal domain. Figure IV.1 shows the dispersion-free compressor. The gratings provide the *temporal* Fourier-transform (TFT) between the temporal and frequency domain or *vice versa*. As laser beams have a non zero radius, the same frequency at different place of the beam (as λ_1 and λ_2 in Fig. IV.1) has to be focused into a vertical line. This is obtained by the cylindrical lenses which provide the *spatial* Fourier-transform (SFT). The combination of TFT and SFT applied to the femtosecond laser beam generate a plane (referred as Fourier Plane, (FP)) where the frequencies are spatially separated. The distance f between each optical element of the dispersion-free compressor has to be the same. If this was not the case, the output beam will be spatially chirped, i.e. we would observe spatial variation of the frequencies distribution within the beam. If no distortion is induced by the 4f compressor, the temporal and spatial properties of the beam at the output have to be identical to those of the input beam. These issues are reviewed in detail by Weiner in a seminal paper [37].

When the spectral bandwidth of the laser is broad ($\Delta\lambda \geq 30$ nm), for minimizing the chromatic aberrations, we used an all reflective dispersion-free compressor whose geometry is based on the work of Monmayrant [190, 191].

The modulated pulses are generated by placing a device in the Fourier plane and addressing individually the frequencies by applying a linear filter function $M(\omega)$ to the spectrum (Fig. IV.2). The control parameters of the pulse can be phase, amplitude and/or polarization. In this work we will focus on both phase only and phase-amplitude modulation. Contrary to other parameters, the polarization control requires devices modifying actively the polarization in the Fourier plane (actually only Liquid Crystals devices can perform this task). This is beyond the scope of this work and references for polarization shaping set-ups can be found in [168, 192–199].

In the case of phase or phase-amplitude modulation and the application of a linear frequency function by the device, the output pulse envelope, $\mathcal{E}_{\text{shaped}}(t)$, is mathemati-

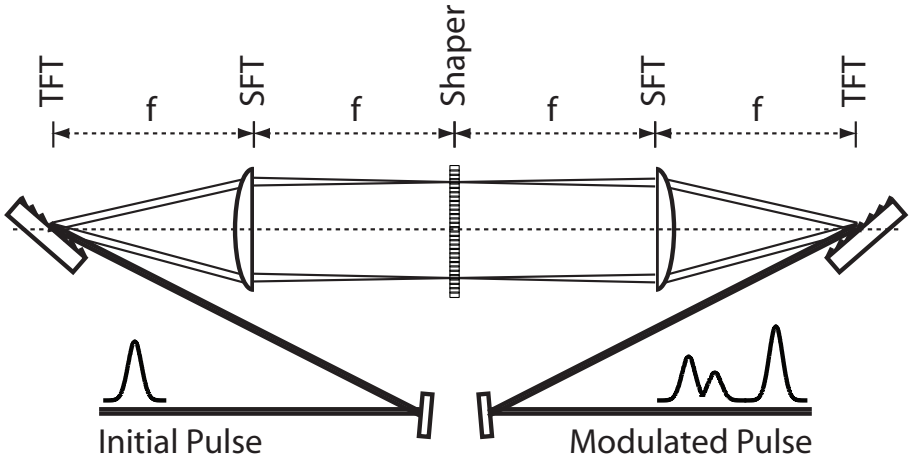

Figure IV.2: The shaper is placed into the Fourier Plane of a 4-f dispersion-free compressor. This device can modify the pulse profile by applying spectral modulation masks.

cally described by [200, 201]:

$$\mathcal{E}_{\text{shaped}}(t) = \mathcal{F}^{-1}(E_{\text{shaped}}(\omega)) = \frac{1}{2\pi}\int_{-\infty}^{+\infty} M(\omega)E(\omega)e^{i\omega t}d\omega \tag{IV.1}$$

The mapping of the spatial position of the linear frequency modulation $M(\omega)$ on the device is given by the convolution of the device modulation $M(x)$ with the spatial position $x_m(\omega)$ of each frequency ω in the Fourier Plane $f(x)$ [200, 201]:

$$M(\omega) = \int_{-\infty}^{+\infty} M(x)f(x_m(\omega) - x)dx \tag{IV.2}$$

The modulation in phase or phase-amplitude are described by:

$$M(x) = A_{\text{shaped}}(x)e^{-i\Delta\Phi_{\text{shaped}}(x)} \tag{IV.3}$$

where A_{shaped} is the amplitude modulation and $\Delta\Phi_{\text{shaped}}$ the phase modulation.

IV.1.2 Shaping devices

We focus now on the device which generate the modulation function $M(x)$. To this date, several kinds of devices based on different techniques have been proposed. As we are interested in temporal pulse shaping we will consider only mono-dimensional (1-D) devices (or use 2-D device as 1-D device). Information about pulses shapers with 2-D devices can be found in references [202–205]. In this work, experiments were performed using liquid crystal- and micro-electromechanical systems - based shapers. Others modulators exist as Acousto-Optics Modulators (AOM) and Deformable Mirror (DM). References for these devices can be found in: AOM [206–210] and DM [211–213].

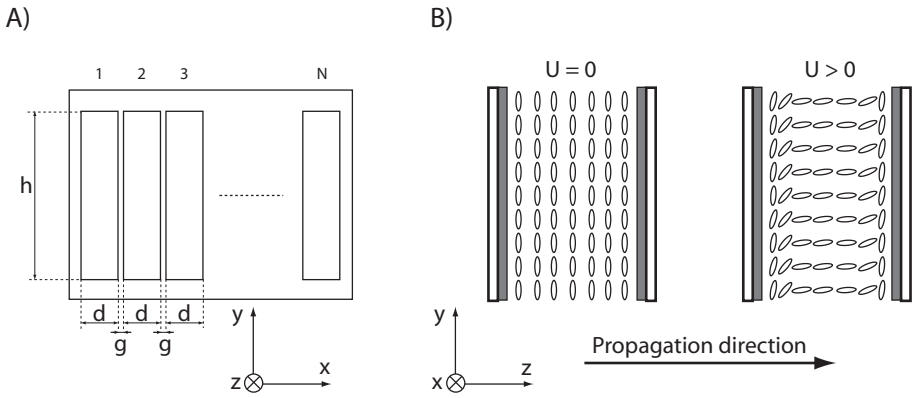

Figure IV.3: Left panel: Front scheme of a mono-dimensional LCD pulse shaper (height of the pixel h, the pixel width d and the gap g between the pixels). **Right panel**: The light cross first a glass plate (white), then the transparent electrode (gray), the liquid crystals, the second electrode and finally the output glass plate. The orientation of the optical axis of the liquid crystal varies with the applied tension U.

Liquid Crystal Device (LCD) Modulators

Liquid Crystal systems have common properties with solid crystals and liquids [214]. At the interface of solid and liquid states of the matter, some substances present thermodynamically stable intermediate states at the phase-transition point. The state is liquid but exhibits physical properties of an anisotropic solid crystal in terms of molecular orientation and arrangement. By applying an electric field on a liquid crystal, the molecular orientation can be controlled and therefore the optical properties, i.e. the effective refractive index. Under these conditions, liquid crystals exhibit similar optical properties as birefringent crystals. Fig. IV.3 depicts the 1-D LCD-based modulation masks used in this work and their characteristics are referenced in Tab. IV.1. The N electrodes are conducting and transparent thin layers of Indium-Tin Oxide deposited on the glass plate. A nematic liquid crystal layer, with typical thickness of 10 μm, fills the space between the electrodes. Induced by the voltage modulations on each pixel and combined with the birefringent properties of the nematic phase of the liquid crystal, the variations of the index of refraction modify the optical path and therefore the spectral phase.

	Pixel Number	Double Mask	d [μm]	g [μm]	h [mm]
CRI™	128	Yes	97	3	2
JenOptik™	640	No	97	3	10

Table IV.1: Specifications of the Liquid Crystals Devices used in this thesis.

If α is the angle formed by the the optical axis of the liquid crystal in the XY plane (Fig. IV.3) and the X axis, phase-only modulation is generated by a single LCD layer ($\alpha = 0°$) while phase-amplitude modulations by a double LCD layers with an orthogonal orientation ($\alpha = \pm 45°$) between each other and combined with polarizers to allow

continuous amplitude variation [215].

Micro-ElectroMechanical Systems (MEMS) Modulators

The dispersion-free compressor (Fig. IV.1) can be folded by placing a plane mirror in the Fourier Plane [127, 189]. A small vertical deflection is experimentally introduced to extract the output beam after the second passage on the grating. In terms of alignment, this geometry is very convenient because the optical components performing the spatial and temporal Fourier transforms are not distinct, and therefore automatically self-aligned. With this geometry, modulations can be induced by an LCD device place in front of the mirror, but also by a Linear Deformable Mirror (DM, polymers membranes with metallic coating) or Micro-ElectroMechanical Systems (MEMS).

Modifying the optical path by moving the DM or the MEMS of a quantity Δz will result in a spectral phase modulation in the Fourier Plane of a 4-f compressor. For each frequency, the relation between the phase modulation and the displacement is given by [216]:

$$\Delta\phi(\omega) = \frac{2\omega}{c}\Delta z(\omega) = \frac{4\pi}{\lambda}\Delta z(\omega) \tag{IV.4}$$

In this work and to our knowledge, we used the only available MEMS device which fulfill the requirements for pulse shaping: a 2-D MEMS phase-former kit [217] from Fraunhofer IPMS and as we will see further in this chapter, we started the development of a new 1-D pulse shaper (See Sec. IV.2). In the present section, we will consider only the Fraunhofer device whose characteristics are reported in Tab. IV.2. As shown in Fig.

	Pixel Number	Mirror size [μm]	Gap size [μm]	Δz_{max} [nm]
Fraunhofer	200×240	35.8	4.2	450

Table IV.2: Specifications of the MEMS Device used in this thesis.

IV.4, the mirrors are structured in a device layer and linked to the substrate by thin support posts. The motion is generated by applying a voltage to an electrode placed under each micro-mirror and separated by a small air gap. Increasing the voltage on the electrode produce a deflection of the mirror into the air gap by the electrical acting forces [59]. To this date and for pulse shaping, only one other proof of principle MEMS-based device has been reported [218].

General Considerations

- In terms of wavelength flexibility and phase-shift range, the MEMS devices present the non-negligible advantage to be limited only by the reflectivity of the chosen metallic coating and of the piston stroke.
- As a consequence of the time-bandwidth product (Eq. I.13), the shaped pulses cannot present temporal features with rise and fall times faster than the FT-limited pulse.

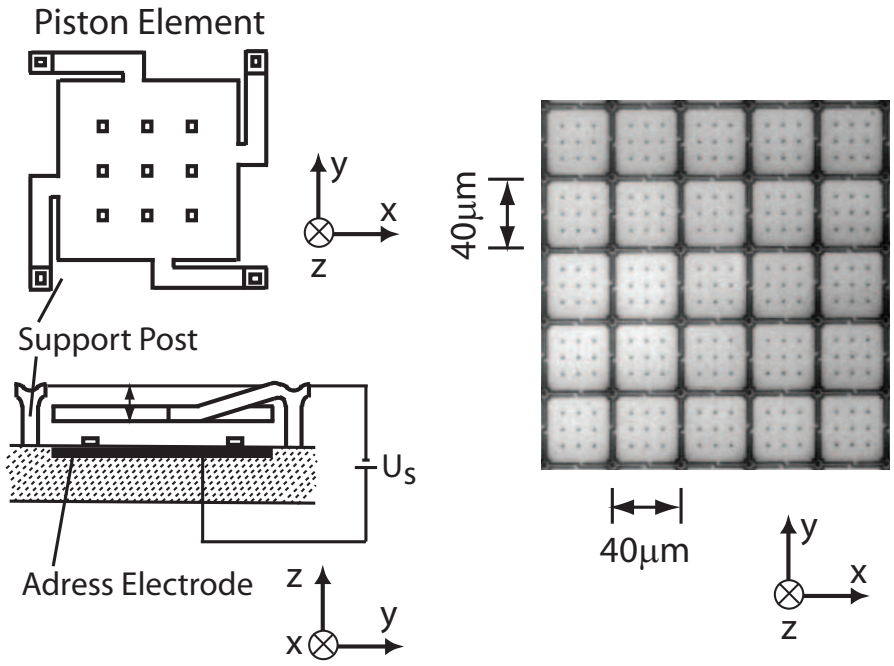

Figure IV.4: Left panel: A schematic top- and side-view of a single piston element of the MEMS-SLM. [59] **Right Panel:** a scanning electron microscopy (SEM) photograph of the arrayed elements. Each of the 240×200 piston (including gap) elements has a size of 40×40 μm^2 and can perform vertical deflections of 450 nm.

- With the apparition of computer controlled devices capable of pulses modulations [36] and the high number of independent parameters, complex pulse shape can be generated. Therefore, a mapping between the input parameters of the device and the optical properties generated is needed through a 2-D calibration: first, we need to know which frequency is on which pixel (mapping: $\omega \Leftrightarrow x$). Secondly, the phase modulation as a function of the tension applied on each pixel has to be worked out (mapping: $\Delta\Phi \Leftrightarrow U$). For the LCD devices, both calibrations are necessary, while for the MEMS, only the mapping ($\omega \Leftrightarrow x$) is needed as the mapping ($\Delta\Phi \Leftrightarrow U$) can be retrieved by Eq. IV.4 and an interferometric mapping of the stroke given by the supplier. For the LCD mappings, we choose the calibration procedure described by Postma [219], but other methods are reported, for example in [220, 221].

IV.1.3 Discussion

The devices used in this thesis present some well known limitations and drawbacks. Before looking to them in details and evaluate the possible improvements, let us summarize the status of the available devices before the beginning of this work (Tab. IV.3). The DM technology presents a important lack in the **number of actuators** and there-

[1]The full spectral range is covered by different devices: 250-400nm, 480-700nm, 530-900nm, 1150-1600nm and 1550-2700nm.

	Phase	Amplitude	Wavelength [nm]	Independent Parameters
LCD	X	X	450-1600	128, 640, 4096 or 12288
MEMS	X		200-900	200 or 240
AOM	X	X	250-2700[1]	Several hundreds
DM	X		200-2000	19 or 38

Table IV.3: Properties of existing devices

fore in the control parameters. This is the main limitation of this technology and its pulse shaping applications are very limited. This limitation is not present for the other devices. The DM devices are used for 1-D and 2-D wavefront correction as well as second order dispersion compensation (linear chirp). The resolution of the correction is low because of the limited number of independent parameters.

Another constrain for the transmitting devices (LCD and AOM) is their **spectral acceptance** limited to the VIS-NIR region (Tab. IV.3), while for reflective devices (MEMS and DM) metallic coating prevents this limitation. To overcome this limitation, several groups used frequency up-conversion processes of LCD-based shaped pulses [56, 57], but the retrieval of the physical process involved are extremely difficult or biased because of the convolution of the sample process with the up-conversion process and interplay between conversion efficiency and spectral throughput. Very recently, an extension of the LCD working range down to 260 nm have been reported with good transmission coefficient (85%) [222, 223], but no measurement with this device has been reported, and this device is not commercially available yet.

For pixelated devices (LCD and MEMS), the **fill factor** η defined by the transmission/reflectivity of the device in terms of losses due to the presences of gaps between the pixels is relevant. Having η as high as possible is important because it limits losses (mostly diffraction) induced by the devices. The variation of η is significant depending on the devices: for the LCD, from $\eta = 0.97$ for CRI [224] and JenOptik [225] devices it decrease to $\eta = 0.625$ [226] and even 0.56 [227] for the devices with a high number of pixels. For MEMS device, $\eta = 0.895$ in each dimension (the coverage by the pixel in the 2-D are therefore $\eta = 80.1\%$ of the total area).

A second limitation of pixelated device results from the finite resolution of the device in the Fourier plane (**pixelisation**). Having a fixed frequency separation $\Delta\Omega$ between pixels, the maximal temporal duration of the modulated pulse is defined by [228, 229]:

$$\Delta t_{\text{max}} = \frac{2\pi}{\Delta\Omega} \tag{IV.5}$$

With the devices used in this work, Δt_{max} is of the order of few picoseconds, and it is called temporal shaping window. Correlated to this limitation, the regular pattern printed in the frequency domain by the mask formed by the gaps and the pixels induced also replicas in the temporal domain (the Fourier Transform of a rectangular mask is the Sinc function). The temporal separation between the replica and the pulse is also Δt_{max}. Smaller the $\Delta\Omega$, i.e. more pixels available for the same spectrum, more temporally separated are the replicas to the shaped pulse. This is the main interest in having

devices with the number of pixels N as high as possible. The presence of replicas can affect the control experiments, and have to be checked in every experiment involving shaped pulse generated by pixelated devices. Obviously for the MEMS device as it is pixelated in the two dimensions additional artifacts are presents and described in Sec. IV.4.

A limitation of all devices is generated by the maximal value of the phase modulation. Typically, the maximal phase coverage for existing devices are for the LCD devices at 800 nm the phase interval $[0 - 4\pi]$, while at the same wavelength the MEMS device we have $[0 - 2.25\pi]$. If the phase modulation needed exceeds the device capabilities, the phase function is wrapped modulus 2π or 4π depending the device capabilities. The wrapping is synonymous of discontinuities of the phase function which generates undesired replicas pulses. For this reason, devices with large phase modulation capabilities are recommended [229]. For AOM similar limitations of the pulse modulation occur as the modulating wave (RF or Electrical) is limited by spatial imprecisions for complex pulse modulations.

AOM devices working in the UV domain have been recently reported [53–55, 230] but present as well some drawbacks. They present a **low transmission coefficient** ($\simeq 20\%$) compared to the LCD pulse shaper systems ($\simeq 48\%$), a limited input peak power acceptance, but also the device has first to compensate the dispersion induces by its own crystal, which is not negligible in the UV. Another limitation of the AOM is the repetition rate of the laser which can not exceed $\simeq 25$ kHz, and prevents direct utilization with oscillators which have MHz repetition rate.

The last limitation of pulse shaping is the **spatio-temporal coupling** when the shaped pulse is focused. This effect is more important for the AOM as the shaped pulse is the first order diffracted beam, but it is also present in the LCD- and MEMS-based pulse shaper and artifacts resulting from it have to be carefully checked especially for experiments involving tightly focused pulses [228, 231–233].

IV.2 Development of a phase and amplitude MEMS-based pulse shaper

At the beginning of the project, there was only one existing pulse shaper devices capable to work in the UV-range, i.e. the region where the great majority of biomolecules absorb light: the Fraunhofer MEMS. Even if this device produced promising results (See Sec. IV.4), it was not developed for femtosecond pulse shaping but for wavefront correction, therefore it presents some severe limitations and drawbacks. In parallel to the utilization of the Fraunhofer device, we started the development of a new MEMS-based device specially developed for femtosecond pulse shaping, in collaboration with the Samlab-IMT institute at the University of Neuchâtel (EPFL since 2009).

IV.2.1 Requirements from femtosecond pulse shaping considerations

We describe here the development of a linear array of micromirrors designed for optical, femtosecond laser pulse shaping. It is a bulk micro-machined device, capable of retarding or varying the amplitude of defined laser frequencies in order to perform phase and binary amplitude modulation within a frequency band spanning the deep UV to the infrared. In the following, the presentation of the requirements of the device and the establishment of a list of parameters are presented.

Spatial dimensions

Pixel specifications. From the optical point of view, the height (h, in Fig. IV.3) of the device should as large as possible, in a range spanning from 500 μm to 1 cm, to ease the alignment of the device in the Fourier plane but mostly the necessity to match the spatial size of the laser beam and decreasing the damage threshold. On the other hand, the usual size of MEMS devices spans from ten to few hundred of microns, because bigger the size lower the resonances frequencies. The planarity of each mirror and of the whole device are also to be carefully considered. As a compromise, we therefore decided to begin with a $h = 1$ mm device. The width of the mirror has to be chosen as small as possible as the spectral resolution is proportional to the achievable temporal shaping window [37]. As we will see further, in the first run of production it was set at $d = 80$ μm and augment to $d = 120$ μm and $d = 160$ μm for packaging considerations. As seen in the Sec. IV.1.3, the fill factor has to be as high as possible. This implies the presence of small gaps between the mirrors. Taking advantage of the precision of the MEMS fabrication, gaps interval of $g = 2 - 3$ μm are chosen. The **fill factor** is therefore $\eta = 97 - 98.5\%$, which is even better than LCD shapers.

From Sec. IV.1.3, we know the importance of the **number of pixels** N. This determines the variety of the pulse shapes that can be generated. The bigger N the more complex the pulses shapes that can be generated. The final number of pixels desired is $N = 512$, but the first devices will be produces with $N = 100$, which is a minimum value for performing optimal control experiments.

The total length L_{Device} of the shaping device is defined as:

$$L_{\text{Device}} = N \cdot (d + g) \tag{IV.6}$$

For the $N = 100$ element device, $L_{\text{Device}} \simeq 1$ cm and for the $N = 512$ elements $L_{\text{Device}} \simeq 5 - 6$ cm according the mirror width. In this calculation we are not taking into account the mirror actuation and the connection to the electronics. The final size of the device will be several centimeters squared.

Optical requirements

The mirror have to be "optically" flat. This **flatness** has to be of the order of $\lambda/20$. As the initial application of the device is to shape UV pulses (mainly pulses centered

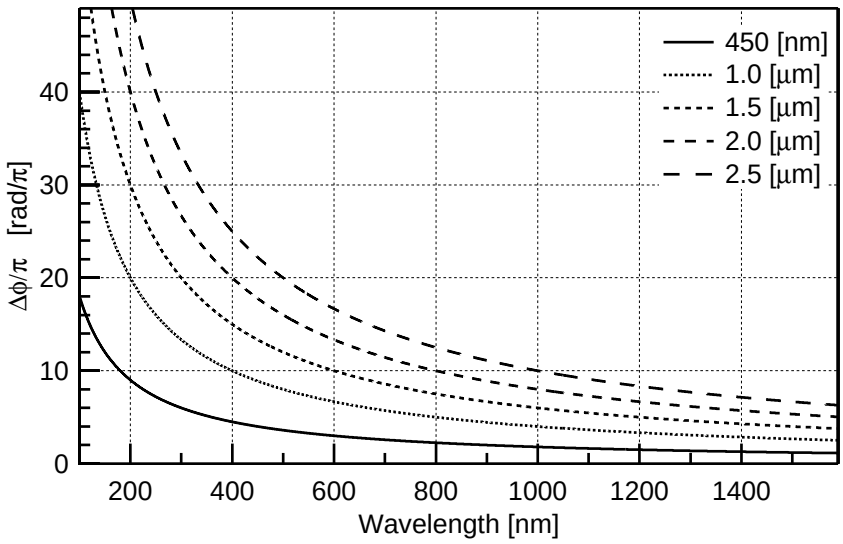

Figure IV.5: Illustration of the wavelength dependence of maximal unwrapped phase generated by different MEMS mechanical stroke. The Fraunhofer maximal potentialities are depicted by the solid line.

around 400 nm and 266 nm), this means a flatness (Peak-To-Valley (PTV)) of the order of 20 to 40 nm over one millimeter length. As we will see, this requirement will imply strong design constrains. The reflectivity of each mirror can be adjusted by an adequate metal coating according to the envisaged application.

Phase-shaping requirements

From Eq. IV.4, the phase interval generated by a MEMS device depends on the wavelength used and on the **mechanical stroke** Δz. From Sec. IV.1.3, we know also the artifacts generated by phase wrapping on pixellated devices. Based on Eq. IV.4, Fig. IV.5 presents for different mechanical strokes the maximal phase interval that can be generated as function of wavelength. From the MEMS point of view, mechanical strokes as high as $\Delta z_{\text{max}} = 10$ μm have been already generated [234]. We decide to develop a system capable of $\Delta z_{\text{max}} = 2$ μm, knowing that this parameter can be doubled if needed. According to Fig. IV.5, this maximal piston stroke will allow direct phase modulation of $\Delta\Phi = 10\pi$ at 800 nm, $\Delta\Phi = 20\pi$ at 400 nm and $\Delta\Phi = 30\pi$ at 266 nm.

Binary amplitude-shaping requirements

The goal is to produce a device capable of tilting a mirror in order to reject defined spectral components. The naive approach will be to **tilt** all the desired mirrors of the same angle in the same direction in order to avoid the rejected wavelength to come back into the lens as shown in Fig. IV.6. With this method and a simple derivation

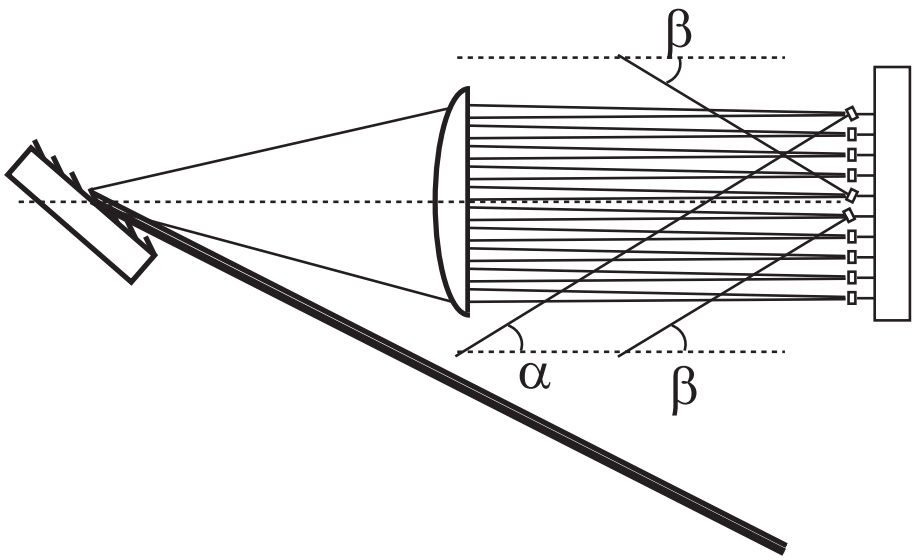

Figure IV.6: Scheme of the naive approach for rejecting the frequencies by tilting the mirrors.

based on a lens ($f = 22.5$ cm focal length) and L_{Device}, we deduce the values of the minimal angles needed to reflect the rejected frequency out of the lens (as in Fig. IV.6): $\alpha = \arctan(L_{\text{Device}}/f) = 15°$ and $\beta = \arctan(L_{\text{Device}}/2f) = 7.5°$. Generating such angle is possible in MEMS, but for devices performing only tilt motion. A solution involving smaller tilt angle has to be found. As $\alpha_t < 7.5°$, the rejected frequency goes back the lens-grating system and goes out from the grating with a different angle compared to the non-tilted frequencies. A pinhole at a distance D of the grating allow to spatially reject the tilted components. According to a trigonometry calculation and considering a reasonable distance ($D = 30$cm), a tilt angle of $\alpha_t = 1°$ is sufficient to reject the frequency and to produce binary amplitude shaping. More details are given in Appendix.

Summary

The requirements from an optical point of view are summarized in Tab. IV.4. To these requirements, we have to add some considerations. First, the device and the mirror has to be stable in time against voltage. Second, its duty cycle has to be high (as we will see in Sec. IV.4, it is not the case for all designs). Finally, we would like this device to be able to operate at a repetition rate of some tens of Hertz.

IV.2.2 State of the art

In order to realize two independent mechanical degrees of freedom (piston and tilt), several options were considered. The challenge from the requirements list is to produce a device with an high aspect ratio, without pixel crosstalk, very good optical flatness and having two independent degrees of freedom. As we will see, the stabilization of

Number of Mirrors	100, 512
Mirror size, $d \times h$ $[\mu m]$	80-160×1000
Gap size, g $[\mu$m]	2-3×1000
Fill factor, η	$\geq 97\%$
Mirror flatness [nm]	< 30
Mechanical stroke, Δz_{max} $[\mu$m]	1-2
Tilt angle, α_t $[^\circ]$	1-2
Repetition Rate, [Hz]	≥ 10

Table IV.4: Summary of the requirements for the new phase and amplitude MEMS-Device.

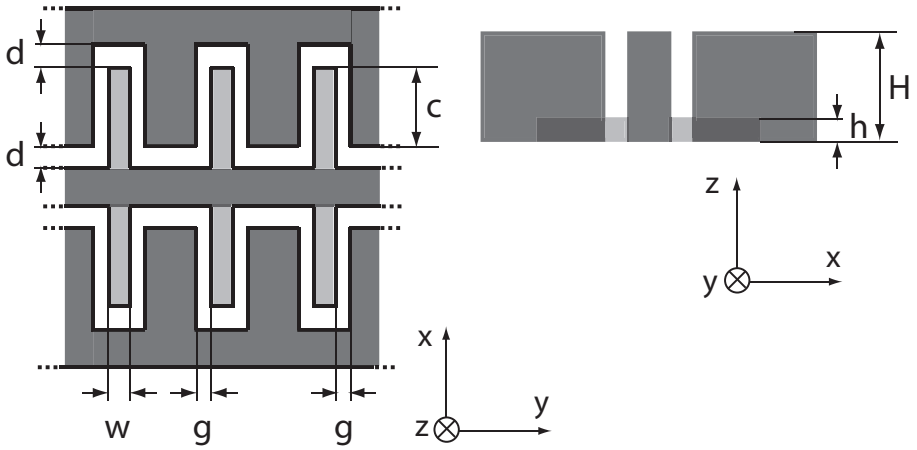

Figure IV.7: Left panel: Top view of vertical comb drive. **Right panel:** Top: Side view. c, d, h, H, g and w are the parameters which have to be determined.

the device in four degrees of freedom will be an important issue. The actuation of the mirror will implies electrostatic actuators called vertical comb drives, as shown in Fig. IV.7. Formed by two sets of static combs (inner parts in Fig. IV.7) and a set of movable combs (outer part in Fig. IV.7), the system has two different heights and is usually referred to as vertical comb drive. By applying different voltages to the movable and to the fixed part and due to the capacity formed by the geometry, only the vertical component of the forces resulting from the capacity will act on the movable part up to reach value $H/2$. This way of actuation provides a very precise displacement.

IV.2.3 Design Considerations

The combination of piston motion with tilt is not so frequent in the MEMS technology. The first idea for the design was to structure two different wafers, one with the mirrors and their suspension, the second with the electrode as in Fig. IV.8. This design has the advantage to be very simple but the disadvantage to be fabricated in two different wafers. The mirrors are produced in one wafer and the two electrodes (U_1 and U_2) on another one. The assembly has to be done afterwards and the mirror actuation is very

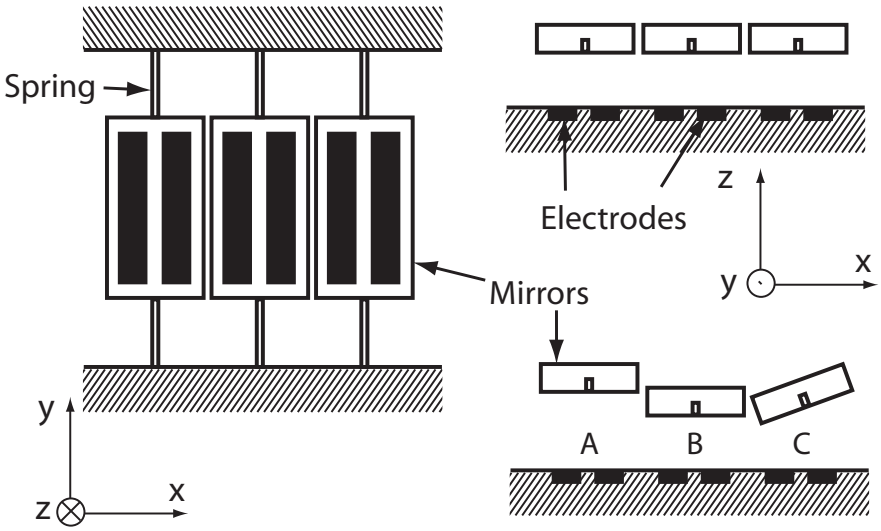

Figure IV.8: Left panel: Top view of the naive design. **Right panel:** Top: Side view. Bottom: Example of actuation for piston (A), tilt (C) and a un-actuated reference (B). The black rectangles are the mirrors.

basic. According to case B of Fig. IV.8, if $U_1 = U_2 = U_0$, the mirrors do not move. When the voltage is set on, we can have either the piston motion if $U_1 = U_2 \neq U_0$ (case A) or tilt motion if $U_1 \neq U_2 = U_0$ (case B). This design was not realized because of the limited precision of the alignment of the two wafers. With this design, crosstalk can already be present without any misalignment because of the vicinity of the i-th mirror to the electrodes of the $i-1$-th and $i+1$-th mirrors. Moreover, due to the sizes of the mirrors and the electrodes, a small misalignment would result in crosstalk between the mirrors, non planar or parallel motions. These two drawbacks are incompatible with the planarity requirements.

The philosophy of the actual design is to be self-aligned to avoid the assembly step and to use the asymmetrical vertical comb drive actuation either for the out-of-plane motion (phase shaping) or for a rotational switch (amplitude binary shaping). A dedicated section of symmetric combs is devoted to the piston motion, symmetric with respect to the spring (See Fig. IV.11). The majority of the combs are asymmetric to produce the torque motion for realizing the tilt angle. Both actuators are arranged as shown in Fig. IV.9.

Having chosen the actuation concept, we now explain in a general way the determination of the dimension of the actuation of the device. From simulation based on solid deformation theory [235, 236] and experimental production constrains, we determine a reduced set of parameters for the spring (length, height, width), the combs (the parameters c, d, h, H, g and w in Fig. IV.7), the gaps, the suspension of the mirror,... On one hand, the outline of this work is to calculate the vertical force generated by the different size of the combs and on the other hand to know the force needed for vertical actuation (phase modulation) and the torque needed for rotational motion (shear moduli, binary amplitude modulation). For each dimension of the spring, a new set

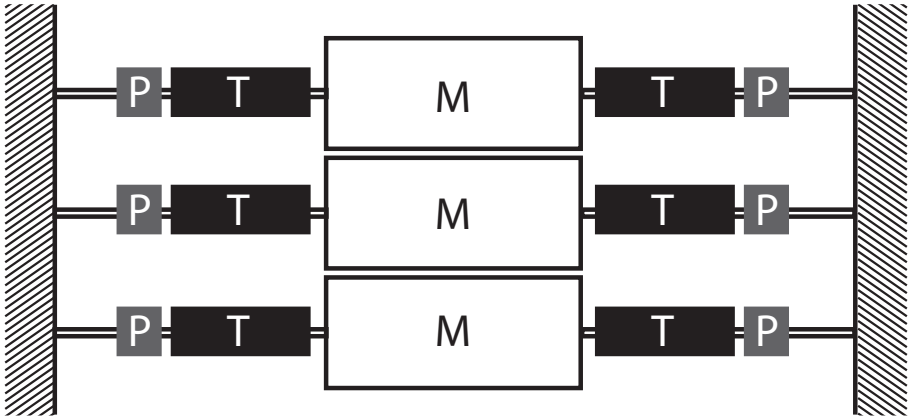

Figure IV.9: MEMS actuation concept: the individual, rectangular mirrors (M) are held in place by thin springs at both sides. The two degrees of freedom are obtained by two sets of comb drives, one for tilt motion (T) and one for out-of-plane piston motion (P). The black rectangles are the mirrors.

of parameters is defined. We summarize here the conclusions of this study. It has to be noticed that sorting these design parameters was extremely critical because of their large numbers.

One last parameter is the suspension of the mirror, which is important to avoid the appearing of internal stress during the release process. The suspension has to be flexible in one direction, but very stiff in the others. If the suspension is not flexible enough, the stress generated will bend the mirror and the optical flatness will be degraded. On the contrary, if the suspension is too flexible, the stability of the mirrors will decrease. Thin suspension structures were used to compensate for chip-intrinsic stress and stress induced by packaging. All these parameters allow us to realize a first design and a first production run.

IV.2.4 First production run and characterization (2007 - 2008)

The micromirror device is fabricated using silicon-on-insulator (SOI) substrates of 350 μm handle layer, a 2 μm buried silicon dioxide, and a 30 μm device layer (see Fig. IV.10, A). The two height steps of the vertical comb drives are realized utilizing a self-aligned, delay-mask deep reactive ion etching (DRIE) process.

After 300 nm Thermal Oxidation wafers (B), the resin (C) is deposed for a rough definition of the first mask in oxide by photo-lithography (structuring the resin) and buffered hydrofluoric acid (BHF, structuring the silicon dioxide) (D). The wafer is then cleaned in plasma O_2 and the second mask process start with another resin deposition (E). The second height (photo-lithography, not shown) and a fine structuring of the oxide (BHF, not shown) are generated. The first DRIE is performed and $7-8$ microns are etched to define the height of the lower comb (F). The resin is removed (G, plasma

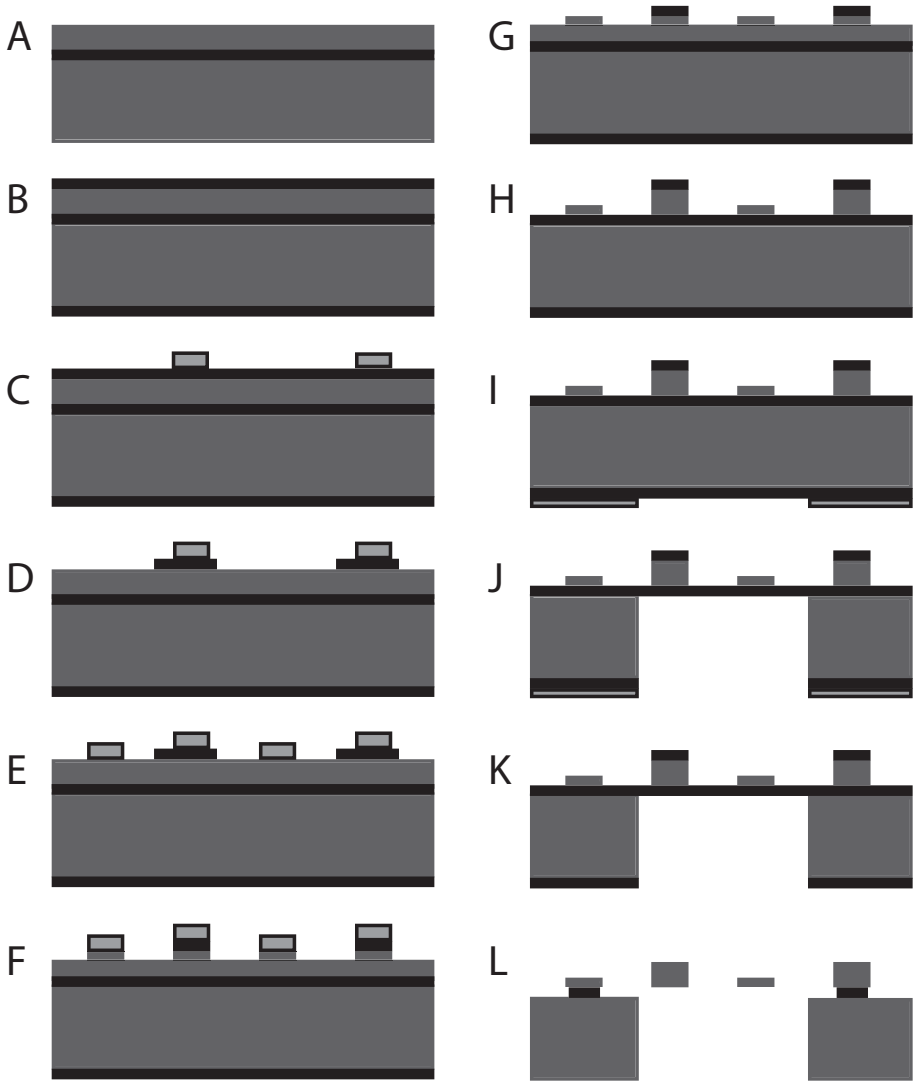

Figure IV.10: Process sequence for the fabrication of the MEMS Device. In gray silicon (Si) is depicted, in black the silicon dioxide (SiO_2) and in gray with black contour, the resin. Explication given in text.

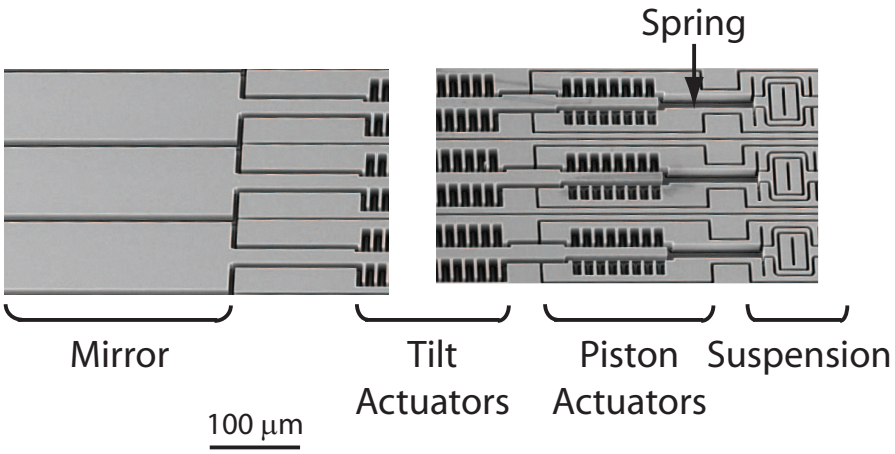

Figure IV.11: Two SEM pictures illustrate the first run of production and the general parts of the device.

O_2) before the second DRIE process (H) to etch the remaining height of the wafer (here 23 microns).

The micro-structuring of the backside start with resin deposition on the backside (I) but also on the front side for protecting it during the rest of the fabrication (not shown). After photo-lithography on the backside oxide (not shown), DRIE process is used to etch the backside (J). The resin then is removed (K, plasma O_2). A hydrofluoric (HF) process in gas-phase performs the release of the mirrors, the combs and the chips, but maintaining the desired structures fixed to the backside (L).

With SOI technology, we obtained the mirror thickness of 28 μm which minimizes the mirror bend in the actuated state compared devices using thin film technology. So far, we have manufactured and characterized $N = 1, 7,$ and100 mirrors variants. Fig. IV.11 displays a partial scanning electron microscopy (SEM) view of a 100 mirror device, the spring, the piston and tilt actuators. The release of the movable parts without releasing the fixed structures was critical, as a too long exposure releases the outer parts of the comb drive as well. As an under-etch of the tilt-actuator voltage feedthroughs can not be avoided, so various platforms, which are still attached to the underlying oxide after the HF etch, were incorporated.

As results, the first devices have a very good mirror surface flatness over the whole mirror length allowing the full surface to be used as reflective area. It changes slightly after the aluminum coating, from a peak-to-valley deformation of $8 - 15$ nm to $20 - 25$ nm after packaging. This is already at or even below the original requirements. The packaging furthermore did not influence the surrounding area to a large extent due to the decoupling of mirror and surrounding device.

The tests of the device achievable performance resulted in a maximum piston stroke of 80 nm (Fig. IV.12) and a maximal tilt of 0.2 degree. which is not yet within the design specifications. The reason for the limited range of the first generation devices was an insufficient spring stability in the lateral direction even with the precaution we took in the conception, leading to pull-in of the vertical comb-drives at voltages

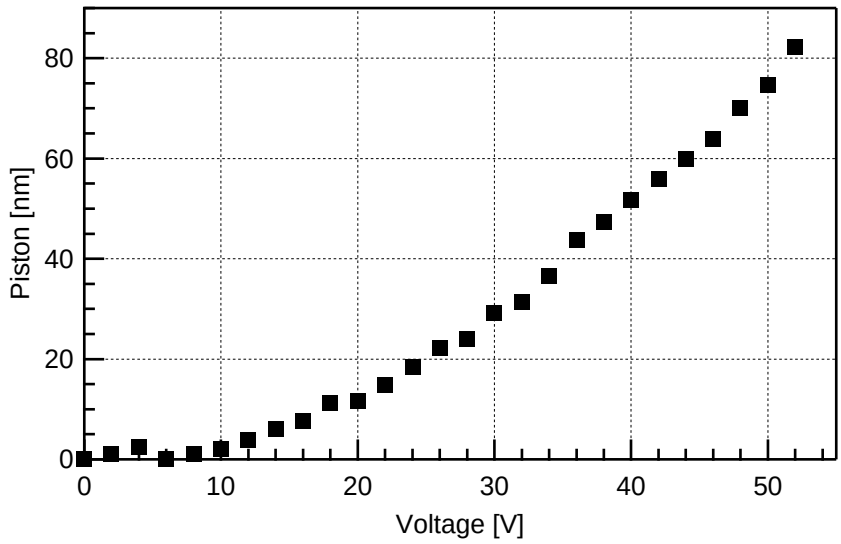

Figure IV.12: Demonstration of the piston actuation with a first run device. The height variation is depicted as function of the applied voltage.

above 50 V. Another issue identified was a early release of the stabilizing platforms, causing contacts of neighboring mirrors when actuated. In Fig. IV.13 a white-light interferometer image of the piston actuator is presented, revealing the two different height steps in the device layer.

Before ending with the results of the first production run of a comb-based MEMS device for femtosecond pulse shaping, we present a 1:1 comparison (Fig. IV.14) of the fill factor of the existing device (Fraunhofer) and our device. It is then evident the wavefront distortion of the output beam will be minimized with the new device.

IV.2.5 Second production run (2009 - 2010)

With the first run, a proof-of-principle of the piston and tilt actuation has been realized, validating the philosophy of the actuation chosen. In the meantime, the electronic device capable of generating the 1024 high voltage channels needed for the actuation of a $N = 512$ linear array has been developed in our research group [237].

Based on the observations of the first run, a redesign has been done to improve the range of motion in both direction capable of achieving the design specifications. An important effort has been devoted to increase the stability in the lateral direction together improving the flexibility properties of the spring and preserving the excellent mirror flatness obtained in the first run. The production of the second run has been realized and very promising results have been obtained. The piston motion reaches now the 2 μm required and the tilt motion has also been improved ($\alpha_t = 0.6°$ has been obtained with a limited voltage). A strong effort has been also done for finding a packaging solution, i.e. to rely the MEMS chip to the existing electronics, allowing an independent actuation of each mirror.

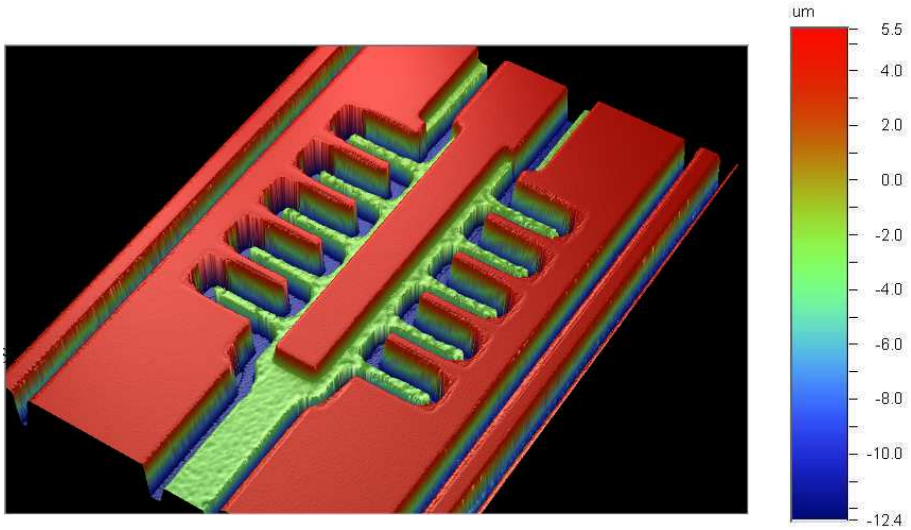

Figure IV.13: White light interferometer image of the piston actuator displaying the height steps in the device layer.

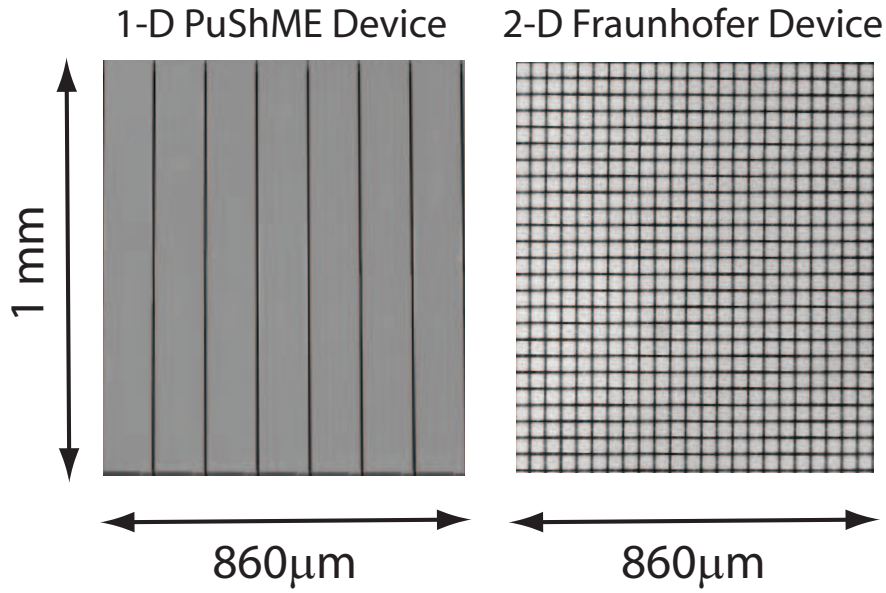

Figure IV.14: Illustration of the difference of the fill factor of the newly processed and the Fraunhofer devices. Both are SEM images.

Actually all steps of the realization of a completely new device for pulse shaping have been done. Several devices with $N = 100$ mirrors are in the packaging phase. In April 2010, the device will be inserted at the Fourier plane of a 4-f dispersion-free compressor and the first optical experiments will be performed. Its mirrors will either retarded the specific laser frequencies by moving out-of-plane, or sorted out from the optical path by tilting and the pulse will be therefore shaped by an independent phase- and by a binary amplitude modulation.

IV.3 Pulse Shaping Experimental Implementation

In this section, the experimental implementation of a pulse shaper is presented without any considerations on the kind of device. As we will see, there are two different experimental approaches to coherent control: **Open -** and **Close - Loop**, which are briefly discussed below.

IV.3.1 Open-loop approaches

In *open-loop* approaches, experiments or simulation are performed by sending a set of N pre-determined pulse shapes, i.e. the application of N phase masks on the device. The effects of these pulse shapes are then interpreted in terms of physical process by sorting the experimental signal for each phase function applied. Open-loop experiments are generally closely related to theoretical calculations to understand the mechanism involved in the physical processes. Based on multiphoton field interferences, this methods can be applied to various nonlinear processes such as second order process [28,29,40,49,238–241] or third order processes [242,243]. Usually this approach is used for simple systems as atomic atoms or clusters, where the computation and the theoretical simulation can be applied.

IV.3.2 Close-loop approaches

In a seminal paper of 1992, Judson and Rabitz proposed to solve the Schrödinger equation of a given physical problem in a close-loop experiment [38]. A feedback iteratively optimizes (Fig. IV.15) the laser pulse characteristics (phase, amplitude and/or polarization) to maximize specifically the desired target. To this purpose, the computer-controlled pulse shaper device uses a feedback from the experiment (signal(s) from the detector(s)) and applies a learning algorithm to solve the unknown Hamiltonian of the sample. With this method, highly complex Hamiltonian of molecules and especially of bio-molecules can be addressed. [44,46,220,244,245] The optimal solutions are found after M iterations in the hyper-space formed by the system parameters. Coherent-control performed with this iterative procedure will be referred as *Optimal Control*. This method is very general and can be applied to all kind of experiments involving sample in liquid, solid or gaseous phase.

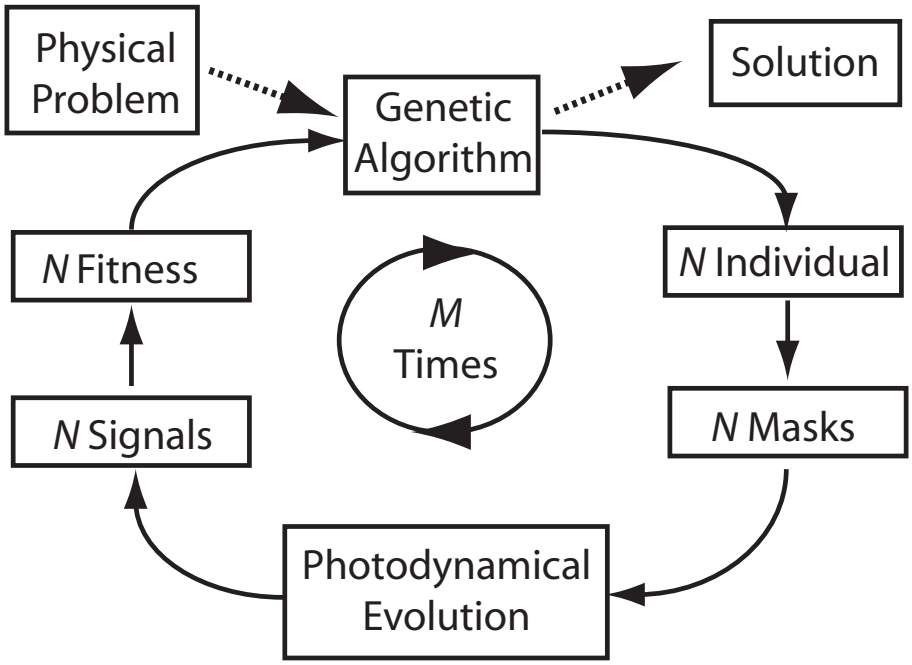

Figure IV.15: Scheme of an optimal control experiment.

Genetic algorithms

Even if procedures based on deterministic algorithms [246, 247], gradient pressure [248] and evolution strategy [249] have been proposed and successfully exploited, Genetic Algorithms (GAs) [250] remain the most common approach in the field, as demonstrated by the increasing number of GA-based applications, ranging from steering of molecular reactions in gas- [39, 41] and condensed- [42] phase, to selective excitation of chromophores [43], control of biophysical processes [44–47], new imaging techniques [24, 49], high harmonic generation [51, 251], and lot more. [52]

Mutating their name from the similarity with biological evolution, Genetic Algorithms (GAs) based on the procedure scheme shown in Fig. IV.16. At the beginning of an optimization, an initial population P_0 of N individuals is randomly chosen with no restriction of the size of the population. In our case, we chose $N = 20$. Each individual correspond to a pulse shape, i.e. a mask printed by the pulse shaper device, and therefore to a possible interaction between the electromagnetic field and the system Hamiltonian. For an objective (for example, maximizing a signal), the feedback signal obtained by the experiment will be different for each mask. The N signals resulting from the N masks (individuals) can be classified according to the fulfilling of the control objective. This way a fitness function is defined and can contain many control parameters. An ensemble of the fittest results is selected for reproduction, i.e. the formation of the next generation (P_{i+1}). A *crossover operator* is introduced for emulating the mating process by exchanging chromosome pattern between the individuals. A *mutation operator* is also introduced to avoid convergence to a local and not to a global solution by inserting a modification of chromosome spontaneously and without

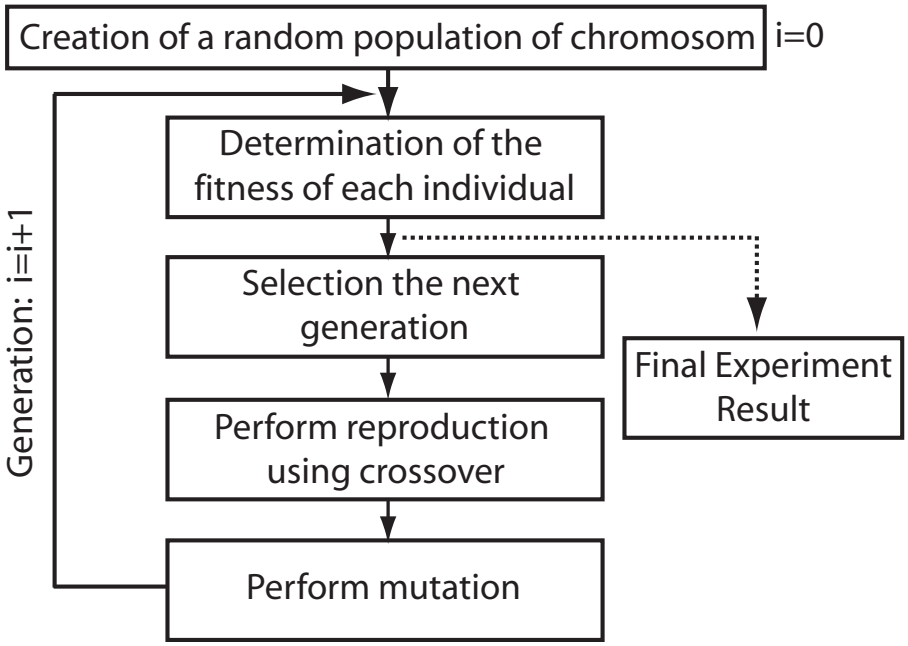

Figure IV.16: Illustration of the Genetic Algorithm procedure.

any reference to the other individuals of the population. If the mutation is beneficial for the convergence process, the individual will survive and influence the next reproduction process, if not, it will be removed at the next generation. From the fittest results of the population of the i-th generation P_i and using the crossover and mutation operators, a new generation population P_{i+1} is created. The *child* population P_{i+1} shears many characteristics with the *parent* population P_i, but in average the average fitness will have to increase as only the fittest parents, i.e. the solutions fulfilling the better the objective, were selected. The P_{i+1} population is then ready to be tested again. As the mutation and crossover parameters are set at the beginning of the optimization, no external intervention is needed during the optimization. One limitation is related to the absence of a convergence criterion ending the optimization. If the problem is simple (like pulse compression), good solutions may appear after 20 to 30 generations only. For more complicated problems (and this is usually the case for optimal control of biological systems), the number of generation will be higher (frequently 100 to 200 generations). The optimization is then stopped at the end of the -M-th loop. Due to experimental considerations (integration time, instrumentation response time, ...) a generation takes typically one minute. Therefore, the time needed for a complete optimization is of the order of hours.

Multi-objective genetic algorithm for optimal control

To adapt the GA approach to discrimination problems we extended its scope to include the optimization of multiple target simultaneously. Our study shows the advantages that this approach can offer to experiments based on adaptive shaping of femtosecond

pulses. The algorithm outperforms single-objective standard optimizations, being totally independent from the bias of user defined parameters, and giving simultaneous access to a large set of feasible solutions. The global inspection of their ensemble represents a powerful support to unravel the connections between pulse spectral field features and excitation dynamics of the sample.

This well recognized versatility of the GA approach for the control of photo-induced processes [252, 253], is accompanied by a few drawbacks. The principal ones concern the robustness of the solution and the difficulty to identify the global maximum. The goal of the optimization is often hindered or in conflict with other experimental aspects. The maximization of multi-photon vibronic transitions falls in this category of problems, as the dominant solution, likely corresponding to transform limited excitation, prevents the retrieval of the subtle pulse features matching the target molecule dynamics. [254] To cope with this limitation, the original optimization goal is usually modified inserting *ad hoc* cost functions, meant to avoid the convergence towards unsuitable or meaningless solutions. On the other hand, this procedure may entail undesirable consequences, as the relative weights adopted for the cost functions inevitably bias the algorithm evolution, and may divert the system to converge to valuable solutions.

Optimal discrimination experiments [42, 43, 63] share similar difficulties. The optimization goal is the selective enhancement of the signal from a specific chromophore in competition with a second one, characterized by similar or overlapping absorption bands. The target objective is typically defined as the ratio between the signals simultaneously generated by the two systems. Obviously to avoid numerical artifacts (division by zero), or convergence to solutions yielding very small signal intensities, it is compelling to add an offset (ε) to the denominator and include a term (α) proportional to the quantity to maximize.

Procedures based on the parametrization of the GA target have been developed also to strengthen [255] the identification of the essential features of optimal pulses, and unravel their connections to the sample photodynamics. [256, 257] More recently, the issue of continuity of solution hypersurfaces has been experimentally addressed with a technique based on the introduction of a scalar variable in the GA objective. [258]

Here we apply an optimal control algorithm capable of handling simultaneously multiple target objectives. [259] The results demonstrate that it increases the versatility and the robustness of the GA approach, avoiding the artificial limitations dictated by user defined scalar cost-function parameters.

To evaluate the performance of this new approach, we set up a benchmark experiment based on the two-photon excitation of a molecule of biological interest: Flavin Mononucleotide (FMN), one of the main source of autofluorescence in living organisms. [260] A typical application of optimal dynamic discrimination [63] could for instance be the efficient detection of bacteria among background aerosols that exhibit similar fluorescence emission. [62, 261] Given the nonlinearity of the excitation process, the maximization of the fluorescence intensity (I_{fluo}) is expected to have a trivial solution corresponding to Fourier transformed pulses. Following Brixner *et al.*, this

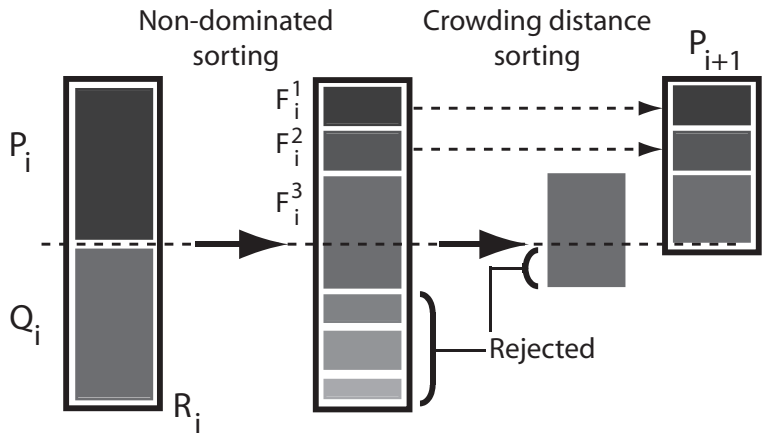

Figure IV.17: The NGSAII procedure [259].

dominant intensity dependence can be lifted by normalizing FMN fluorescence by the second harmonic (SHG) signal (I_{SHG}) generated by the same shaped pulse in a nonlinear crystal. [254] In the following, we discuss the results of a systematic series of optimizations that we performed using both single (two scalar parameters α and ε), and multiple targets, expressed respectively in the form:

$$\begin{array}{rc} \text{Single objective:} & \left[\frac{I_{fluo}}{(\varepsilon+I_{SHG})} + \alpha \cdot I_{fluo}\right] \\ \text{Multi-objective:} & \left[\frac{I_{fluo}}{I_{SHG}} \; ; \; I_{fluo}\right] \end{array}$$

NSGA-II algorithm

We adapted to our experimental needs the Elitist Nondominated Sorted GA (NSGA-II) developed by the group of K. Deb. [259]. Let us summarize its main differences with respect to GAs typically employed for coherent control of photodynamics. [253, 262] NSGA-II varies from single-objective GAs substantially in the way the selection operator acts. The key concept is associated to the notion of *domination*: a solution is said to dominate another solution, if it is not worse in any of the objectives, and it is strictly better in at least one. Conversely, a solution is *nondominated* if no solution can be found that dominates it. After random initialization, at the i^{th} iteration, the population P_i of size N generates an offspring population Q_i of N new individuals by standard tournament selection, recombination, and mutation operators. The combined population $R_i = P_i \bigcup Q_i$ is successively sorted according to nondomination: the solutions fulfilling the definition of nondomination are ranked in the first nondominated front, F_i^1. If the size of F_i^1 is smaller than N, all its members are retained in the next parent population P_{i+1}. The remaining individuals of P_{i+1} are selected in the next nondominated front F_i^2, computed after eliminating F_i^1 from R_i. The same procedure is continued until a set, say F_i^n, cannot be entirely accommodated in P_{i+1}. The elements of F_i^n are then sorted according to the crowding distance operator, which is introduced for preserving the population diversity. The difference among the individuals is calculated in the multi-dimensional target space, from the signals generated

on each objective. [259] The NSGA-II procedure is also graphically depicted in Fig. IV.17.

This naive description of the algorithm is sufficient to clarify the concept of *Pareto* optimal set, extensively used in the forthcoming discussion, which simply corresponds to the final set of nondominated solutions. The latter are assumed to balance the objectives in a unique and optimal way.

Population size	20
Real variables	128
Crossover probability	$8{\cdot}10^{-1}$
Mutation probability	$1{\cdot}10^{-2}$
Distr. index crossover	10
Distr. index mutation	20

Table IV.5: Algorithm parameters used for all optimizations described in this section.

For this study a real-codification of the NSGA-II algorithm is used. The optimizations were restricted to a maximum of two objectives, even if there is no computational limitation regarding this point. The parameters used for the measurements are summarized in Tab. IV.5. No systematic study on these values for improving convergence speed and/or quality of the outcome were performed. The interest being limited to a straight comparison between single- and multi-objective approaches.

Figure IV.18 displays the comparison between the evolution of a single objective optimization of $[I_{fluo}/(I_{SHG}+\varepsilon)+\alpha\cdot I_{fluo}]$ (a), and that of a run of the NSGA-II algorithm simultaneously maximizing $[I_{fluo}/I_{SHG}\,;\,I_{fluo}]$ (panels (b) and (c)).

In (a), we observe the monotonous growth of the discrimination ratio I_{fluo}/I_{SHG} generated by the best individual of each generation. Notice that the plotted quantity differs from the actual feedback signal. At the beginning of the optimization, we identify a transient phase of 10-20 generations characterized by $I_{fluo}/I_{SHG}<1$. This regime is associated to larger efficiency of the SHG process with pulses with random amplitudes and spectral phases. Since we carefully verified the linearity and the balance between the two optical arms, this finding does not constitute a major limitation for the optimization. After this short phase, the discrimination ratio steadily increases with values constantly above one. After $\sim$120 generations, it converges to a final value of 1.25.

The evolution driven by the multi-objective algorithm depicted in Fig. IV.18(b) and (c) is somehow less straightforward. During the first generations, the algorithm output is associated to a single solution per iteration, evidencing the existence of an individual exhibiting simultaneously the greatest discrimination ratio and fluorescence intensity. Once the system has exited this region (dashed vertical line), the number of feasible solutions suddenly inflates, eventually saturating the number of individuals in the population ($\dim(F^1_{i>40})>N$). This behavior is representative of conflicting targets. In fact, consistently with the nondomination ranking performed by the algorithm, each individual yielding high values on one target is bound to be weak on the other one. If this was not the case, there would be an individual dominating all the others, and

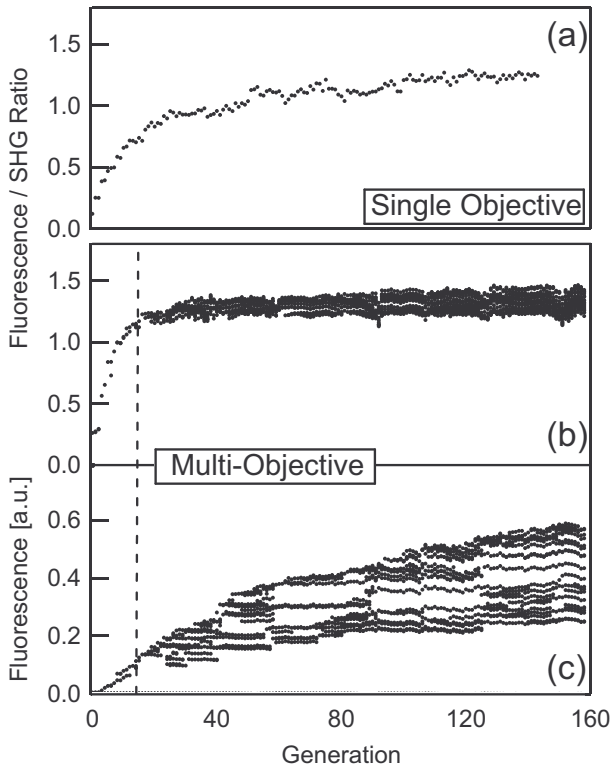

Figure IV.18: Comparison between the evolution of a single objective optimization of $[I_{fluo}/(\varepsilon + I_{SHG}) + \alpha \cdot I_{fluo}]$ with $\alpha = 0;\ \varepsilon = 0.3$, and that of a run of the NSGA-II algorithm maximizing simultaneously $[I_{fluo}/I_{SHG}\ ;\ I_{fluo}]$. Evolution of the discrimination ratio I_{fluo}/I_{SHG} in the single-objective **(a)**, and in the multi-objective **(b)** case. **(c)** Evolution of I_{fluo} in the multi-objective run.

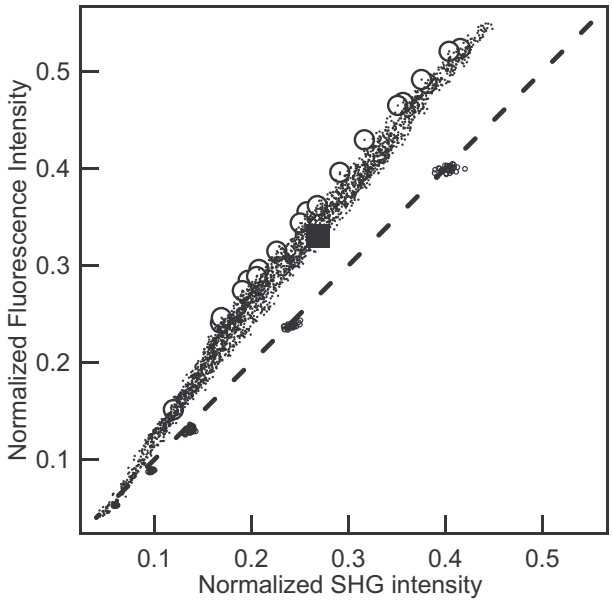

Figure IV.19: Global output of the multi-objective optimization of Fig. 1. Dots: individuals tested during the evolution. Circles: final feasible population (*Pareto* front). Dashed line: undiscriminating solution $I_{fluo} = I_{SHG}$, retrieved by an unmodulated pulse at different intensities, as demonstrated by the experimental data points lying along the diagonal.

$\dim(F_i^1) = 1$. We observe that the NSGA-II algorithm keeps on increasing both targets during the whole optimization. At each step, the feasible solutions represent the best compromise found between the two conflicting goals. The large distribution of the solutions is preserved by the crowding distance operator, which retains for the next optimization step the pulses characterized by maximal distance in the two-dimensional signal space. After 120 generations, as in the case of the single objective optimization, the signals converge to steady values. [259]

The result of the evolution can be more easily appreciated when I_{fluo} is plotted against the control variable (I_{SHG}) [254], as in Fig. IV.19. As both I_{fluo} and I_{SHG} are normalized with respect to the signal generated with a reference unmodulated pulse, the dashed diagonal line corresponds to the undiscriminating situation $I_{fluo} = I_{SHG}$. This condition was systematically verified at different intensities, as indicated by the experimental data points along the diagonal. The global output of the optimization is represented by the dots above this line, where $I_{fluo} > I_{SHG}$. They correspond to all the individuals tested during the optimization, while the circles highlight the final feasible population constituting the Pareto front of optimal solutions. For comparison, the filled square indicates the final solution obtained with the single-objective optimization reported in Fig. IV.18(a).

The convergence of two opposite multi-objective optimizations are illustrated in Fig. IV.20. Above the dashed line ($I_{fluo} = I_{SHG}$) are depicted Pareto fronts of the $[I_{fluo}/I_{SHG}\,;\,I_{fluo}]$ optimization from the beginning (2^{nd} generation, ▼) to the final results (•) with the intermediates Pareto fronts at the 40^{th} (□), 80^{th} (Δ) and 120^{th} (◊) generation. Below the $I_{fluo} = I_{SHG}$ line, we show the convergence of the optimization with the opposite

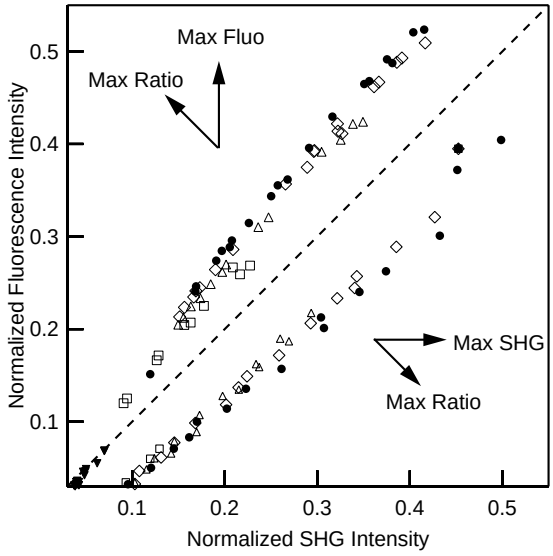

Figure IV.20: Illustration of the convergence of two opposite multi-objective optimizations $[I_{fluo}/I_{SHG}\ ;\ I_{fluo}]$ and $[I_{SHG}/I_{fluo}\ ;\ I_{SHG}]$. Filled shapes denotes the beginning and the end of the optimization while open shapes are intermediate Pareto fronts. Dashed line: undiscriminating solution $I_{fluo} = I_{SHG}$, as in Fig. IV.19. More details in text.

objective $[I_{SHG}/I_{fluo}\ ;\ I_{SHG}]$ (2nd, ▼; 20th, □; 60th, Δ; 80th, ◊; last generation, •). For both optimizations, the trend of the successive Pareto fronts follows clearly the directions pointed by the arrows: maximization of the ratio and increase of the target signal.

The discrimination ratios of all solutions belonging to the Pareto front and their corresponding fluorescence intensities, are illustrated Fig. IV.21. The plot contains the results of various multi-objective (opened shapes) and single-objective (filled shapes) optimizations associated to different $[\alpha;\varepsilon]$ parameters pairs, together with the outcome of the optimizations presented above (filled square and open circles, respectively). The dotted line is an upper estimate of the experimental error in I_{fluo}/I_{SHG}, calculated from the dispersion of the fluorescence and SHG measurements generated by unshaped pulses at different intensities.

From this general comparison it is evident that the Pareto front is a common solution for all the optimizations, and that single-target outcomes fit well in the general trend. Greater α and ε values give more weight to signal intensity leading to solution characterized by stronger signals and weaker fluorescence/SHG discrimination. Smaller or vanishing α and ε values privilege the ratio at the expense of fluorescence intensity. Notice that, for all the I_{fluo} values associated to solutions of the single-objective optimizations, the discrimination ratio retrieved by the multi-objective algorithm is slightly but systematically higher. It is remarkable that the same computational effort (the number of individuals tested in the various optimizations is roughly the same), gives access in the case of multi-objective optimization to a much richer ensemble of solutions without affecting, even improving, their quality. The pulse best adapted for

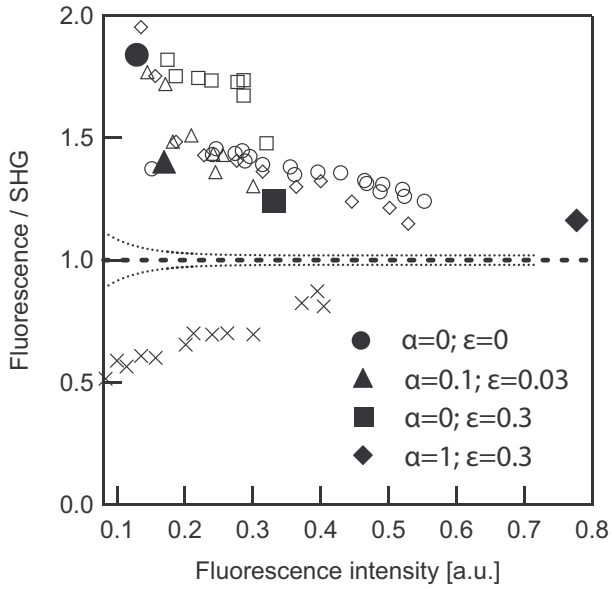

Figure IV.21: Comparison between the results of several independent multi- (open shapes) and single- (filled shapes) objective optimizations. The single objective GAs results are obtained using different $[\alpha\ ;\ \varepsilon]$ parameter pairs. The crosses correspond to maximizing the opposite goal with NSGA-II, namely $[I_{SHG}/I_{fluo}\ ;\ I_{SHG}]$. The dotted curve indicates the experimental error at different signal intensities.

a specific application can be readily selected within this collection.

The discriminating capacity and the signal magnitude associated to the different final pulses were tested several days after the optimization, yielding results well inside the error estimate given in the plot. As additional check, we also performed the opposite optimization, i.e. the simultaneous maximization of $[I_{SHG}/I_{fluo}\ ;\ I_{SHG}]$. The crosses in Fig. IV.21 with ratio below unity represent the feasible solutions obtained this way. We observe a remarkable symmetry of this ensemble with respect to that obtained by maximizing the fluorescence.

This finding is consistent with the physical explanation that can be formulated after inspection of Fig. IV.22(a), showing a comparison between the SHG non-collinear FROG traces of two pulses respectively maximizing (left) and minimizing (right) the I_{fluo}/I_{SHG} ratio, and that of a reference unmodulated pulse (center). The optimizations principally act suppressing one or the other edge component of the pulse spectrum, in order to enhance or reduce the nonlinear excitation of FMN (two-photon absorption maximum at 760 nm, Fig. II.9, [144]). This strategy modulates the I_{fluo}/I_{SHG} ratio, taking into consideration that the SHG process for a 150 μm crystal is insensitive to wavelength within the excitation pulse bandwidth ($<$15 nm).

As a consequence, the FROG spectral slices taken at zero time-delay in Fig. IV.22(b), indicate an overall bandwidth reduction of $\sim 25\%$ for both the SHG ($I_{fluo}/I_{SHG} = 0.7$) and fluorescence ($I_{fluo}/I_{SHG} = 1.77$) enhancing pulses with respect to reference pulse. Similar trends have already reported for Coumarin [263] and results that the two-photon absorption is governed by the SHG spectrum. [264] Beside this major

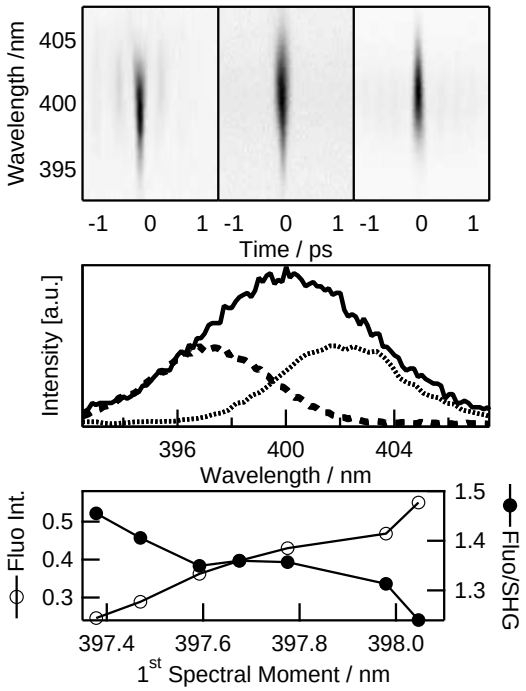

Figure IV.22: **(a)** FROG traces corresponding to pulses maximizing FMN fluorescence (left), undiscriminating (center), and maximizing SHG (right). **(b)** Spectral cuts at zero time-delay extracted from the FROG traces in the top panel. **(c)** Behavior of the multi-objective optimization targets I_{fluo} and I_{fluo}/I_{SHG} as a function of the first spectral moment of the optimal pulses retrieved by the algorithm.

effect on the amplitude of the spectral components, we also observe a reduction of the pulse duration for both optimal pulses with respect to the reference one.

In Fig. IV.22(c), we analyze the relationship between the two targets of the multi-objective optimization presented in Fig. V.3, and the position of the first spectral moment (See Sec.V.4) of the pulses belonging to the final Pareto front. One clearly recognizes the competition between the two targets: discrimination decreases as the pulse spectral edge shifts to the red, towards the laser output maximum (800 nm). At the same time, I_{fluo} increases, as the incident pulse intensity augments, enhancing nonlinear excitation. Similar trends were found for all the optimizations shown in Fig. IV.21, and a complementary behavior at the blue side of the spectrum was observed for the SHG maximization.

The NSGA-II algorithm is applicable to a vast ensemble of control problems. It allows acquiring the complete Pareto front of feasible solutions with a computational effort comparable to traditional GAs. Picking a single solution from this set is an *a posteriori* judgment, which can be done in terms of concrete experimental needs. Moreover, we observed a slight improvement in the quality of the individual solutions retrieved by the multi-objective algorithm in comparison to the ones indicated by single-target approach. Eliminating all scalar parameters in the objective expression (and in the crowding distance procedure [259]), assures an unbiased convergence.

The distribution of solutions in the target space, gives access to primary information for unraveling the relationship between pulse spectral field features and sample photodynamics. In particular, any global trend in the final ensemble of solutions, may help associating specific pulse characters to different outcomes of the photo-process. In this respect, the unambiguous understanding of the strategy underlaying the optimizations presented in this work, facilitates the comparison between the single and the multi-objective approaches.

IV.4 Characterization of a MEMS-Based Pulse Shaping Device in the Deep Ultraviolet

An introduction on the MEMS devices and properties is given in Sec. IV.1.2 and Sec. IV.2. In this section, the implementation and characterization of a MEMS-based set-up for femtosecond pulse shaping in the deep UV is presented. At the beginning of this work, this was the unique available device capable to modify directly the pulse shape of UV femtosecond laser pulses. The capability of this device to spectrally re-compress broadened UV pulses with a closed-loop approach based on a genetic algorithm is demonstrated. A single-shot synchronization scheme, taking advantage of the limited duty cycle of the device and allowing on-line correction of the signal, is described. The second dimension of the MEMS chip can be used to partially reduce the spatial chirp of the beam.

The development of a MEMS-based custom design for broadband femtosecond pulse shaping in the deeper UV around 266 nm is reported. The device is characterized

in this wavelength region, a series of technical details related to its operation are addressed, and its capability of re-compressing self-phase modulation (SPM) broadened UV pulses with a closed-loop approach based on a genetic algorithm is demonstrated.

According to Eq. IV.4 and Fig. IV.5, at this wavelength, the device allows $\simeq 6\pi$ unwrapped phase modulations. The actuation of the micro-mirrors is done by a 21×30 cm electronic driving board on which is attached the chip, as shown in Fig. IV.23. Given the increasing interest shown by various research groups for this device - which was originally intended for wavefront correction and not for temporal pulse shaping [217] - we will describe in some details the issues related to its efficient addressing in combination with an amplified femtosecond laser system. A dedicated synchronization was developed to adapt the detection to the limited duty cycle of the MEMS shaper. According to its specifications, the MEMS chip can set a deflection pattern in 50 μs and successively maintain it for a period τ_{ON} ranging from 100 μs to 1 s, followed by an idle period τ_{OFF} lasting at least $17 \times \tau_{ON}$. Normally, to minimize the idle time τ_{OFF}, the best approach would be to trigger externally the device and use the shortest possible τ_{ON}, so that an operation cycle is completed in 1.8 ms and every second pulse at kHz rate can be shaped. Unfortunately, we found out that even for τ_{ON} of the order of 100 μs the shortest idle time is $\tau_{OFF} > 3$ ms. Therefore, the settings used for the measurements presented here correspond to $\tau_{ON} = 320$ μs, chosen to maximize the active shaping time window without reducing the most efficient exploitation of the device as compared to the kHz laser output. The signal detected during the τ_{OFF} period was used to record a running reference associated to the 'flat' mask, corresponding to no deflection applied to the micromirrors. Note that, even if we were warned by the supplier that the τ_{OFF} period could be associated to a quasi-random pattern, we only noticed a minor and constant difference, of the order of 5%, between the signal intensities detected during τ_{OFF} and those measured with a flat pattern imposed. We decided therefore to take advantage of the idle period for recording a reference signal of the laser intensity.

Detection is based on a single-shot approach according to the following scheme: the pattern-ready synchronization signal from the MEMS device is used as principal trigger to start an acquisition cycle of *N* consecutive samples of four independent analog channels (UV and DFM intensity, chopper status (UV blocked or not), and MEMS device status (pattern applied or not)). The acquisition of each sample series is synchronized with the repetition rate of the laser system. At the end of the acquisition the driving software sorts the DFM and the UV signal shots according to their respective MEMS device status (pattern ON or OFF) and chopper status (UV pulse present on the BBO crystal or not), calculating the UV fluctuation-corrected DFM signal as:

$$\frac{I_{DFM}(\text{IR,UV})^{\text{ON(OFF)}} - I_{DFM}(\text{IR})^{\text{ON(OFF)}}}{I_{\text{UV}}^{\text{OFF}}}.$$

This approach enables performing a series of statistical checks on the signal noise, allowing the rejection of isolated bad laser shots or correct for long term laser drifts [265].

As technical remarks, we consider useful reporting here three main drawbacks

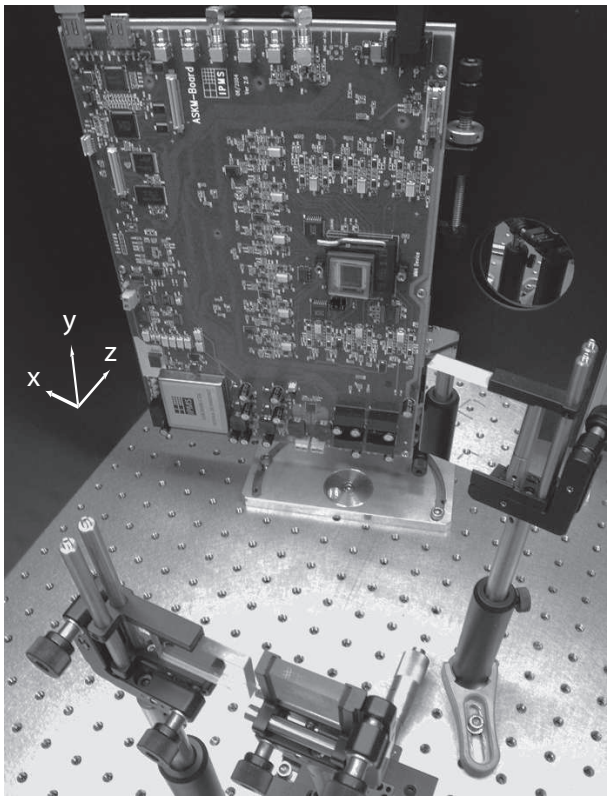

Figure IV.23: Picture of the shaper set-up. We recognize the MEMS chip, placed in the middle right of the driving board. The axes are equivalent to those in Fig.II.5.

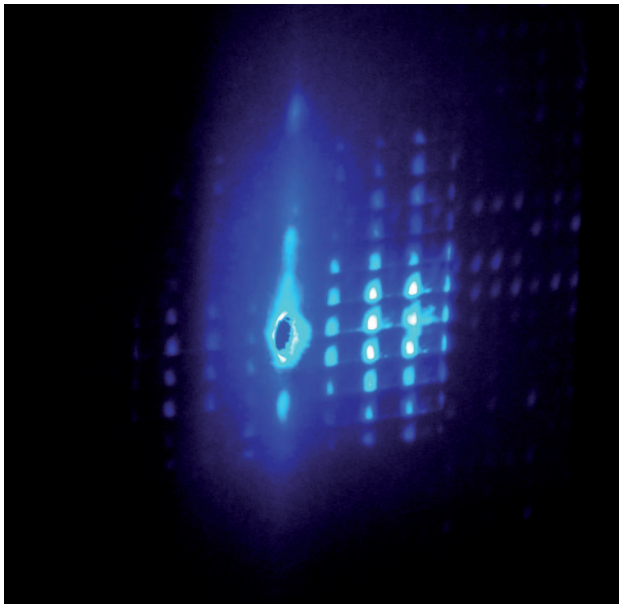

Figure IV.24: Picture of the diffraction pattern created after reflection on the MEMS chip (left: hole for the incident beam; right: diffraction pattern). The reflected beam intensity in the zeroth order amounts to 10% of the incident beam intensity.

associated to the use of this device in the context of femtosecond pulse shaping. 1) A strong diffraction of the beam (Fig.IV.24), even though this effect is inherent to any pixellated device, which limits the actual I_{out}/I_{in} throughput to 0.1. We also observed a dependence of the diffraction efficiency on the mask pattern applied, leading to a complex phase/amplitude coupling. In some cases, the relative amplitude of the shaped pulses (nominally phase-only) could be as low as 70% of the unshaped ones. 2) A long thermalization time (of the order of a few tens of minutes) after powering on of the device, which influences the relative time delay between the UV and the IR pulse. 3) When $\tau_{ON} > 1$ ms, we systematically remarked a variation of the optical signal over successive shots in the pulse train, suggesting a change in the deflection pattern during long mask application (longer than a few ms).

In the present study our attention was exclusively focused on a closed-loop approach, to verify the aptness of the device to perform long term feedback-driven optimizations. In Fig.IV.25 the results obtained by closed-loop optimizing the DFM signal with UV pulses of different characteristics impinging on the BBO crystal are summarized. The time-resolution of the measurement is given by the independently measured IR autocorrelation (thick line in Fig.IV.25.(b) and (e)) yielding 120 fs. The duration of the unshaped and not spectrally broadened UV, strongly chirped by the presence of 4 mm of fused silica, clearly dominates the UV/IR cross-correlation in Fig.IV.25.(b) (dots). When the shaping mask found for maximizing the DFM signal is applied on the UV, on the other hand, the UV/IR crosscorrelation (open circles) results practically coincident with the IR autocorrelation, evidencing the shorting of the UV pulse, which should now present a duration of the order of 100 fs. For emphasizing the control possibilities on the ultrafast molecular dynamics of biological systems, we are interested in shaping UV pulses of larger bandwidth [63, 266]. Consequently the shaping capability of the set-up on a nonlinearly broadened spectrum were tested. The insets (a) and (d) in Fig.IV.25 compare original and SPM broadened spectra, indicating an increase from 5 nm to 10 nm at $1/e^2$. The crosscorrelation trace of the unshaped pulse in Fig.IV.25.(e) indicates a significant increase of the UV pulse duration, and a change in the overall shape of its time envelope. It is noteworthy to point out that masks based on chirp compression calculations cannot work effectively on such a peculiar pulse-shape, and the closed-loop approach pursued here emerges as the most natural approach. Not surprisingly, the signal intensity fluctuations in the broadened case are stronger, due to the highly nonlinear interactions at the basis of the spectral broadening, and the correction of the DFM signal by $I_{\mathrm{UV}}^{\mathrm{OFF}}$ becomes essential for the optimization procedure. The latter is performed using the nonelitist genetic approach first developed by Deb [259], more recently modified and adopted for pulse-shaping applications [267] and presented in the previous section. For the measurements presented, typically convergence was obtained after ~ 60 generations, with a population of 16 individuals. The final outcome shows a sensible decrease in pulse duration and a clear symmetrization of the temporal profile. However, the resulting trace remains longer than the IR autocorrelation. A possible reason justifying the diminished outcome of the optimization can be ascribed to the worsening of the spatial chirp as a consequence of the broadening mechanism [268], as evidenced by the plots in Fig.IV.25.(c) and (f),

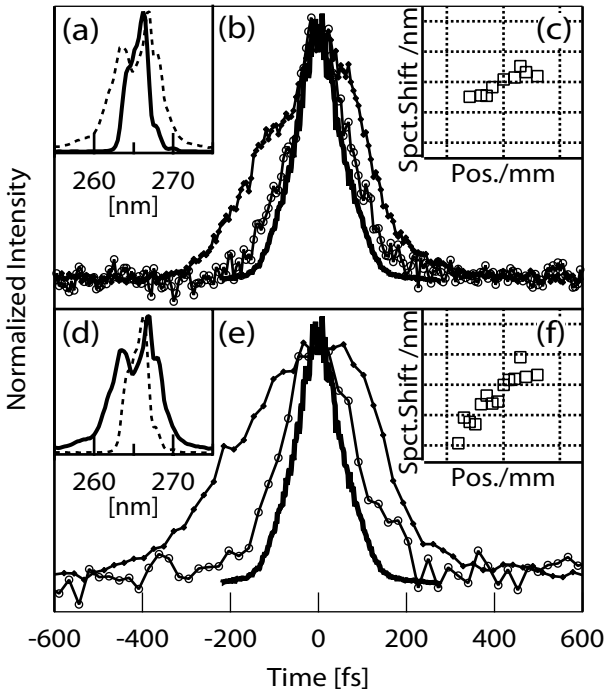

Figure IV.25: Original (a) and SPM broadened (d) pulse spectra. IR autocorrelation (thick line), UV/IR crosscorrelation for UV unshaped (dots) and shaped (open circles) pulses in the case of original (b) or broadened (e) spectra. First spectral moment shift at different positions within the beam profile for the original (c) and broadened (f) pulses. In panels (c) and (f), the horizontal grid lines are spaced by 1 mm and vertical grid lines by 1 nm.

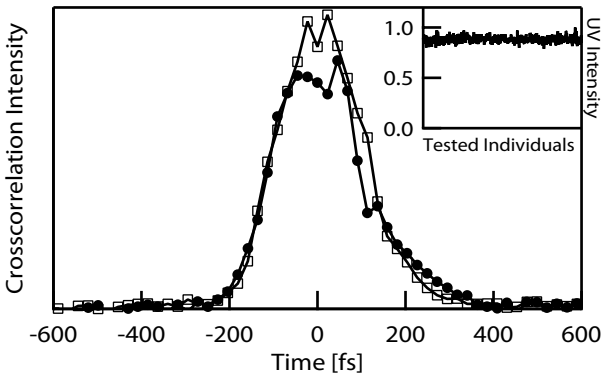

Figure IV.26: UV/IR crosscorrelation for 1D- (dots) and 2D-shaped (open squares) pulses in the case of a broadened spectrum. Assuming Gaussian pulse-shapes, the 266 nm duration at FWHM is 115 fs for the 1D optimization and 104 fs for the 2D optimization. Inset: evolution of the shaped UV pulse intensity during the 2D optimization.

which report the shift of the first moment of a series of spectra sampled with a 50 μm fiber at different positions of the UV beam profile.

One can expect that, by taking advantage of the second dimension of the MEMS chip, this effect can be partially corrected. Thus, we proceeded in further optimizing the result of striped-pattern optimizations by lifting the constrain of equal deflection for all the micromirrors of a given line along x. In doing so, we generally obtained a systematic increase of the shaped signal amplitude I_{DFM} of the order of 10-15%, which was accompanied by a very slight decrease of pulse duration, and only a limited improvement on the wings of the crosscorrelation traces (Fig.IV.26). Interestingly, the increase of I_{DFM} was not associated to any augmentation of I_{UV} (inset of Fig.IV.26), ruling out the trivial explanation of this intensity increment as a diffraction-driven effect. We therefore ascribe these observations to the partial re-phasing of the spatial frequencies along x which, not being sustained by a similar correction along the y axis, determines only a small improvement of the temporal traces.

In conclusion, we have described the implementation of a reflective 2D-MEMS chip for direct broadband UV pulse shaping. We demonstrated here that with a proper synchronization scheme the drawbacks of a limited duty-cycle can be greatly reduced, allowing an efficient addressing of the device with a kHz system. This way, we realized the temporal pulse compression of both a narrow and a spectrally broadened pulse. In the former case only one dimension of the MEMS mask is independently addressed, in the second case, for partially reducing the effect of the spatial chirp, both dimensions can be kept independently active. Among the different pulse-shaping techniques, MEMS-based devices present clear advantages in terms of wavelength and bandwidth flexibility. On the other hand, the strong diffraction inherent to the pixellated nature of the device should be taken into account because it results the principal factor at the origin of the low optical throughput of the set-up.

IV.5 Conclusions and Perspectives

In this chapter, various technical advances with application to optimal control, especially for applications with biomolecules, have been reported.

The development of a new 1-D MEMS-based pulse shaper is reported. This project has pushed the limits of micro-mirrors technology by setting a highly challenging technological problems. By an innovative design the actuation in both out-of-plane and tilting direction of high aspect ratio micromirrors has been demonstrated. The pulse shaping capabilities of the device will be tested in April 2010 as the second production run has just been finished. The next step of development of this project is to increase the number of pixels up to $N = 512$ and even more, allowing the production of more complex pulse shapes and augmentation of phase-coherent control independent parameters. As illustrated in Fig. IV.27, at the beginning of this work, the unique device able to directly work in the UV and the deep-UV for femtosecond pulse shaping was the Fraunhofer MEMS. With the actual specification of the new MEMS device, the spectral shaping possibilities have been more than doubled. The drawback due to the 2D pixelisation has been removed while preserving the number of pixels and adding the binary amplitude modulation (Fig. IV.27). As potentialities of this new device and in addition to experiments on coherent control on bio-molecules, topics as direct modulation of high harmonics or attosecond pulses are on the top of the list of envisaged applications. The limitation in the UV will be given by the optical flatness of the mirrors (the peak-to-valley) and the resolution of the electronics to be able to generate very precise phase-shifts. In the infrared region, the limitation will come from the maximum stroke allowed, but with the present status of the development, $\Delta z_{\text{max}} = 1$ μm, corresponding to a modulation potentiality up to $2\mu m$, are performed. Increasing the stroke up to $\Delta z_{\text{max}} = 5$ μm should not be too complicated if applications at larger wavelength are considered but will demand some additional efforts. Obviously, under the validation of the promises of this device, as its wavelength flexibility and with a strong interest in its applications, its commercialization should be considered.

The application of a new generation of genetic algorithm (GAs) to the field of optimal control has been presented in Sec. IV.3. We observed that multi-objective optimization may improve the performances of the so-called *control pulse cleaning* procedure described by Lindinger *et al.* [256]. In that case, the optimization target is modified including a one-parameter cost function elaborated to suppress all unessential field components to facilitate the deciphering of the optimal pulse. A sensible combination of the two approaches, by introducing genetic pressure against appearance of unnecessary pulse features as a parameter-free objective, may bring fruitful results. Since our experimental demonstration, the multi-objective optimization has been reported experimentally [269] and theoretically [270, 271] in the field of optimal control by other research groups. For future improvement in the field of the learning algorithms, attention may be payed to various interesting developments, such as the application of evolution strategies (see for example Covariance Matrix Adaptation [272, 273]). This approach improves the convergence time by a factor four [249] with respect to the standard genetic algorithms [252, 253]. Experimentally this is very

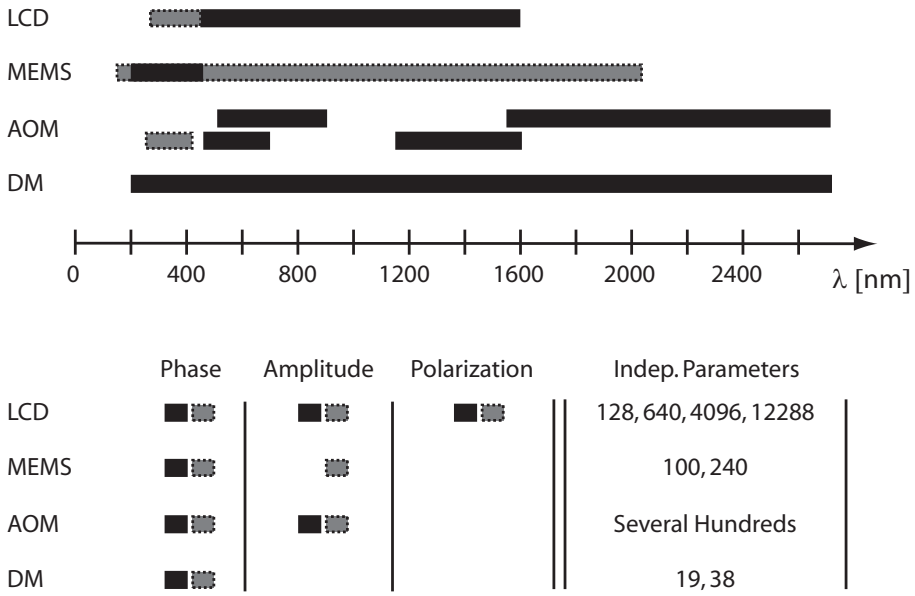

Figure IV.27: Graphical representation of the spectral properties of the various pulse shaping devices existing at the beginning of this work (black rectangles) and in February 2010 (gray rectangles).

interesting because the total duration of the experiment will be reduced by the same factor and will be of around $20 - 30$ minutes only, contrary to the actual $80 - 120$ minutes needed. From an experimental point of view, this improvement is crucial as longer the experiment harder maintaining stable experimental conditions. The same study study [249] reports also the improvement of the robustness of the convergence to external noise. An algorithm which combines the advantages of the evolution strategy and the multi-observable tool already exists [274], and waits only to be implemented on an optimal control experiment to demonstrate its advantages.

Interest on the physical processes occurring during an optimization has been reported theoretically and experimentally in several works. [258, 275–277] Based on the diversity of the Pareto front solutions of multi-objective optimizations, a natural perspective is to study carefully the underlaying physics of each solution and to extract the differences between each quantum path. Such approach can be correlated with *ab initio* calculation to have a better physical understanding of the considered sample.

Several technological breakthrough have been realized in parallel and independently in the LCD, AOM and MEMS technology during the last four years. The existence of devices working in the UV (AOM [53–55, 230], MEMS [59] and LCD [223]) will allow their application to perform direct quantum control on biomolecules. The first results have just been reported [278, 279]. In addition to our work and even with its limitations the Fraunhofer device is used by different groups and one result has also been reported [280]. Optimal control experiments on biomolecules with this device are under progress. Finally the implementation of the newly developed 1-D MEMS device should open new ways to the dream of the quantum control of biomolecules, bacteria and living organisms.

CHAPTER V

Linear propagation of femtosecond laser pulses through atmospheric turbulence

A series of applications of ultrashort laser for remote sensing have been recently proposed. [281–284] In this context, we have been interested to the propagation of femtosecond laser pulses through atmospheric turbulence and the modifications induced by the laser-turbulence interaction on the pulse characteristics. In this chapter we investigate both experimentally and numerically the linear propagation through turbulence and extract how it affects the properties of femtosecond laser pulses. The underlaying question is the possibility of performing remote control under turbulent conditions.

With the rise of femtosecond lasers, coherent white light source for Lidar (Light Detection and Ranging) detection of atmospheric species has proven as a very attractive method [281]. Recently, time-resolved and coherent control schemes have been used to efficiently discriminate between aerosol particles that exhibit identical spectral signatures. [62, 261] There is now a particular interest to apply control schemes, such as fluorescence depletion and multi-pulse impulsive Raman spectroscopy [64, 65], directly in the atmosphere, especially since first field applications were demonstrated within the Teramobile project. [281, 285]

However, transmitting an optimally shaped pulse over long distance through the atmosphere is not fully straightforward. Although it has been demonstrated that optimal control can be used to control filamentation remotely [286], no demonstration of the applicability of quantum control of molecular species at distance has been reported yet. Among the processes that may affect the propagation of an ultrashort laser pulse, thermal turbulence is likely the most effective in preventing remote application of phase-coherent techniques. In fact, contrary to dispersion and Kerr-related effects,

distortions induced by turbulence cannot be avoided by a sensible choice of the pulse characteristics, or pre-compensated [287, 288], due to their random nature. Pointing variation but also static and dynamic wavefront distortions (speckles) of nanosecond or CW laser beams induced by atmospheric turbulence have been extensively studied. [289] This chapter is the first steps towards the extension of this study to femtosecond laser pulses.

V.1 Theoretical concepts

We first describe some basic concepts in atmospheric turbulence followed then by its numerical implementation.

V.1.1 Atmospheric turbulence

In fluid dynamics and contrary to laminar flow, a turbulent flow is characterized by irregularities in velocity flow, variations of temperature, humidity and pressure in the spatial and the temporal coordinates. Turbulence is also highly dissipative process and require a continuous kinetic energy input. The formation of eddies at various length scales are consequence of turbulence. At a large eddy scale (called *Outer scale*, L_0), the kinetic energy injected by friction or convection generates and maintains the turbulence. An energy cascading process occurs up to the smallest scale (called *Inner scale*, l_0) where the viscous dissipation of the kinetic energy occurs. The spatial and temporal distribution of these structures are irregular and interfere between each other. In nature, lots of outflow phenomena are turbulent such as the cigarette smoke, the air flow over an airplane wing or the atmospheric mixing of warm and cold air by the wind.

The dynamic of an incompressible fluid is governed by the Navier-Stokes equations (expressing momentum conservation and continuity) [290]:

$$\begin{aligned} \frac{\partial \vec{v}}{\partial t} + [\vec{v}\nabla]\,\vec{v} &= -\frac{\nabla \mathcal{P}}{\rho} + \nu \nabla^2 \vec{v} \\ \nabla \vec{v} &= 0 \end{aligned} \tag{V.1}$$

where $\vec{v}$ is the velocity, $\mathcal{P}$ the pressure, ν the viscosity and ρ the density. Due to the high degree of nonlinearity and the sensitivity to the initial conditions of these equations, no solution for turbulent dynamics can generally be found. The description of such stochastic process has therefore to be based on a statistical approach.

In 1941, Kolmogorov proposed the first statistical theory of turbulence [291, 292], using the concept of energy cascade from the outer to the inner scale. Based on energy conservation, this theory allows to define a structure parameter C_n^2 of the velocity fluctuations (for a derivation see: [132] and references therein). For optical turbulence, the turbulence cells modify locally the refraction index via a local gradient of temperature, humidity and/or pressure. Experimentally it results that for the same experimental

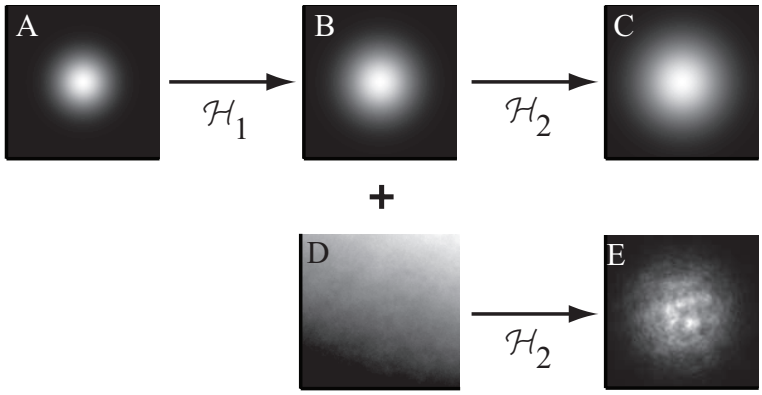

Figure V.1: Principle of the simulation scheme. Transverse beam profiles at (A) the beginning , (B) an intermediate distance (d_1) and (C) & (E) the end of the propagation ($d_1 + d_2$). For non turbulent regime, profiles are not distorted at the propagation distance (C). When the medium of propagation is turbulent (spatial phase mask (D)), distortions of the beam profile appear at the end of the propagation (E).

conditions (in our case the propagation of laser pulses), each measurement in the spatial domain (i.e. the transverse spatial intensity) gives a different result, because the completely randomized modulation of the refraction index by C_n^2 affects each transverse portion of the beam. When the beam is larger than l_0, several parts of the beam will propagate through an atmosphere with slightly different refraction index and can interfere after a propagation distance d. The wavefront of laser pulse is perturbed or distorted and speckle features are generated.

In the atmosphere and according to climatic conditions (pressure, humidity, temperature,...), the variations of the structure parameter span from $C_n^2 < 10^{-16}$ m$^{-2/3}$ (weak turbulence) to $C_n^2 \simeq 10^{-13}$ m$^{-2/3}$ (strong turbulence).

V.1.2 Propagation through atmospheric turbulence

We studied the propagation of a linearly polarized Gaussian pulse (Fig. V.1 (A)) centered at $\lambda_0 = 800$ nm with wavefront curvature and radii matching the experimental values. Every spectral component is first propagated in free space ($\mathcal{H}_1$, according to the expressions reported in Sec. I.2), supposed to be linear and homogeneous, along a distance d_1 (Fig. V.1 (B)). When the propagation occurs in a non-turbulent medium, the pulse propagate over an additional distance d_2 in free-space ($\mathcal{H}_2$). The resulting transverse beam profile is shown in Fig. V.1 (C). To simulate the propagation through turbulence, we apply a spatial phase screen (Fig. V.1 (D)) generated according to the Kolmogorov theory [293] for the different C_n^2 values. Finally, the pulse spectral components are propagated again in free space for an additional distance d_2 (Fig. V.1 (E)).

Assuming d_1 and d_2 small enough to neglect turbulence variations on temporal scale $\frac{(d_1+d_2)}{c}$, the pulses propagates through a static turbulence, modeled as a spatial phase mask $\phi_M(x, y)$ in Cartesian coordinates and following the Kolmogorov statis-

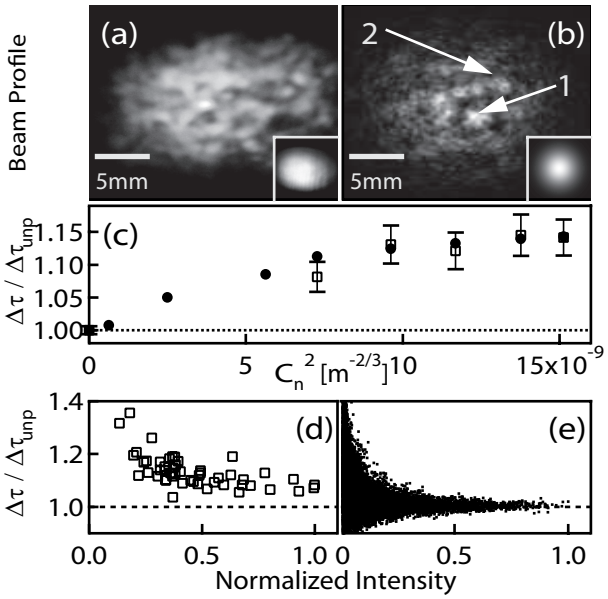

Figure V.2: Experimental (A) and simulated (B) beam profile. Arrows indicate the strong (1) and a weak (2) intensity spots discussed in the text. C) Pulse duration normalized to that of a pulse propagating the same distance in absence of turbulence as a function of turbulence strength, from experiment (□) and simulation (•). Relative pulse duration as a function of pulse intensity at fixed $C_n^2 = 9.6 \times 10^{-10}$ m$^{-2/3}$ from experiment (D) and simulation (E).

tics. Formally, the final electric field $\mathcal{E}_f$ at a distance $z = d_1 + d_2$ can be expressed as:

$$\mathcal{E}_f(x,y,z,t) = \mathcal{F}_S^{-1}\left\{\mathcal{F}_S\left[\mathcal{F}_S^{-1}\left(\mathcal{F}_S\{\mathcal{E}(x,y,z=0,t)\}\times\mathcal{H}_1\right)\times\Phi_M\right]\times\mathcal{H}_2\right\} \quad \text{(V.2)}$$

where $\mathcal{F}_S$ (resp. $\mathcal{F}_S^{-1}$) is the Fourier transform (resp. the inverse Fourier transform) with respect to the spatial coordinates, $\Phi_M \equiv e^{i\cdot\phi_M} = e^{i\cdot\phi_M(x,y)}$ and $\mathcal{H}_j$ the free space propagator for a distance $z = d_j$ ($j = 1, 2$) (See Sec. I.2).

V.2 Experimental and Simulation

As shown in Figures V.2.A (experiment) and V.2.B (simulation), the beam profile is spatially distorted in a typical speckle pattern as a result of the propagation through turbulence. The experimental and simulated wavefront bear a strong resemblance, especially considering that the former is the superposition of 10 successive laser shots. The strongly inhomogeneous distribution of intensity, ranging from 10^{-3} to 2 times that of the unperturbed wavefront, results from the superposition of the multiple interferences among beam portions experiencing different phase-shifts through turbulence repeated at each wavelength in the bandwidth. [294] Beside spatial distortions, we investigated also global temporal modifications, as reported in Fig. V.2.C. Pulse autocorrelation widths averaged over 50 independent laser shots show a clear increase with turbulence strength. The experimental datapoints (squares) are normalized by

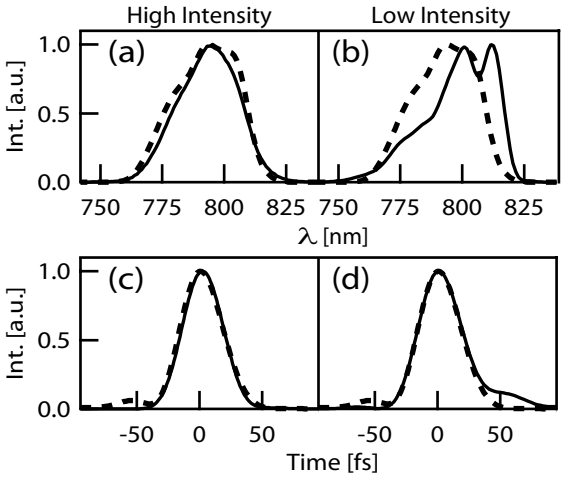

Figure V.3: Solid lines: experimental $I(\lambda)$ and $I(t)$ retrieved inverting the multi-shots FROG measurement of an high (A,C) and a weak (B,D) intensity spot on the wavefront. Dotted lines: corresponding traces for a pulse propagating without turbulence over the same distance.

the duration of a pulse propagating the same distance in the unperturbed laboratory atmosphere, $\Delta\tau_{unp}$. Note that this duration does not correspond to that of a Fourier limited pulse. We derived from the simulation a comparable quantity by calculating the average of the temporal second moment of different beam portions normalized by the unperturbed value (circles). Note that, even in presence of strong perturbations, the average relative variation $\Delta\tau/\Delta\tau_{unp}$ does not exceed 15%. The quantitative agreement between experiment and calculations over the whole range of turbulence strengths investigated, authorizes to extend the simulation to the $C_n^2 = 2 - 7 \times 10^{-9}$ m$^{-2/3}$ range, which was not accessible in the experiment.

Figure V.2.D and E compare the results of experiment and simulation by plotting the relative distortion of pulse duration as a function of the local wavefront intensity. The observed temporal distortions are strongly correlated with intensity, evidencing that the major deviations from the unperturbed case are concentrated in weak intensity regions. Pulse duration converges to the unperturbed one ($\Delta\tau/\Delta\tau_{\rm unp} = 1$) as intensity increases.

We can gather more insight by investigating locally the spectral and temporal characteristics of regions of different intensity on the beam profile. As mentioned above, these measurements required the use of a random phase plate, which entails a much higher distortion than that generated by the hot air blow. In Fig. V.3 we report two illustrative experimental temporal ($I(t)$) and spectral ($I(\lambda)$) profiles retrieved by inverting multi-shots FROG measurements from regions of different intensities: high (A and C) and low (B and D). Similarly, Fig. V.4 displays characteristic examples of simulated $I(t)$, $I(\lambda)$, and Wigner plot of a strong (A, C, and E) and of a weak (B, D, and F) intensity region. The inspection of these traces further confirms the strong correlation between local intensity and pulse distortions. In low-intensity regions, the existence of substructures in the temporal profiles and major spectral alterations is

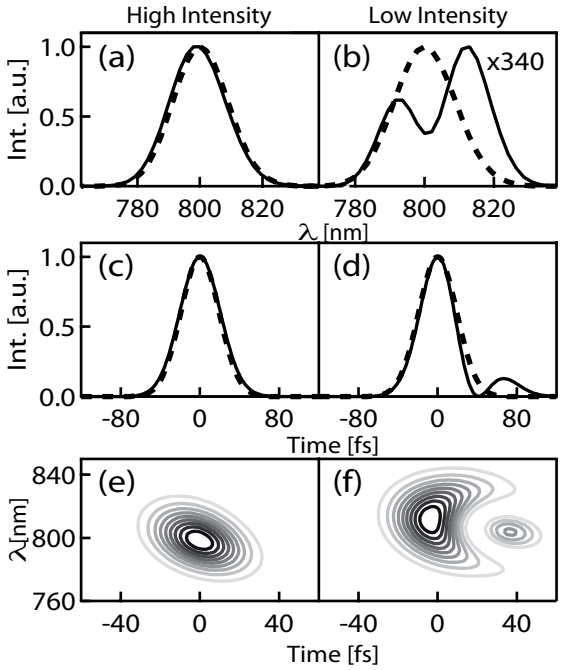

Figure V.4: Simulated $I(\lambda)$ (A, B), $I(t)$ (C, D), and Wigner representation (E, F) of the pulse characteristics in the high (left column) and low (right column) intensity spots on the beam profiles indicated by arrows 1 and 2 in Fig. V.2.B.

clearly apparent from the plots. Conversely, for high intensities, little or no distortions are present and the traces almost perfectly overlap with those calculated for a pulse propagating in absence of turbulence (dotted lines). Simulation allowed us to determine that in the intense spots, the effect of multiple interferences account for minor amplitude deviations in both $I(t)$ and $I(\lambda)$, not exceeding a few percent fraction of the relative intensity. These observations altogether are consistent with a scenario where interferences act similarly at all wavelengths: in a defined portion of the beam profile, the spectral components experience a similar phase-shift when passing through turbulence. Such a condition holds exclusively because of the narrow bandwidth of the femtosecond laser pulse ($\Delta\lambda = 35$ nm around $\lambda = 790$ nm) as compared with the wavelength dependence of the index of refraction of air, n_{air}.

By integrating $I(t)$ across the beam profile, we conclude that the *overall* pulse duration is only slightly affected by turbulence: 6% on the temporal second moment with respect to the unperturbed situation for $C_n^2 = 9.6 \times 10^{-10}$ m$^{-2/3}$. This C_n^2 value is four orders of magnitude higher than typical atmospheric conditions (a strong atmospheric turbulence structure parameter is $C_n^2 = 2.5 \times 10^{-13}$ m$^{-2/3}$ [131]).

V.3 Compensation of atmospheric speckle by spatial beam shaping

We present now the first results of a study to assess the capability of compensating the effect of atmospheric turbulence on a femtosecond pulse by spatial phase modulation. Existing 2-D LCD phase modulators [202–205] can be used to compensate the phase distortions resulting from atmospheric turbulence. Clearly the dynamic character of turbulence implies a real-time correction with a correction speed faster than the velocity of atmospheric variations. Such approach is already used in astronomy [295] and needs a feedback. In astronomy, artificial star generated by laser are used. For remote control detection, a laser induced feedback has to be used.

In this preliminary study, we will limit ourselves to the compensation of static turbulence. It can be seen as an analogy to the work of Vellekoop and Mosk [296, 297] in opaque strongly scattering media and the work of Finck on time-reversed acoustics [298, 299]. This works propose an extension to broadband laser spectrum and atmospheric-turbulence-induced distortions.

V.3.1 Monochromatic compensation

By an adequate spatial precompensation, temporal and spatial distortions induced by atmospheric turbulence can be compensated. Hence, applying this spatial compensating mask $\Phi_c \equiv e^{-i\cdot\phi_C} = e^{-i\cdot\phi_C(x,y)}$ to $\mathcal{E}$ would allow remote coherent control experiments, even in adverse conditions.

The compensation scheme is added into the numerical procedure described by Fig. V.1 in the following way. We back-propagate along a distance d_1 the modulated pulse spatial profile (in Fig. V.1, after the addition of the spatial phase mask (panel (D)) and before the second propagation).

Translating this in a formal way, we have the modulated electric field $\mathcal{E}_M$ after a propagation along a distance $z = d_1$ (represented by $\mathcal{H}_1$) and the application of the phase mask Φ_M that can be written as:

$$\mathcal{E}_M(x, y, \omega, d_1) = \mathcal{F}_S^{-1}\left(\mathcal{F}_S\left[\mathcal{E}(x, y, \omega, 0)\right] \times \mathcal{H}_1\right) \times \Phi_M \tag{V.3}$$

Therefore, the initial ($z = 0$) pre-compensated electric field $\mathcal{E}_{\text{pre-compensated}}$ reads:

$$\mathcal{E}_{\text{pre-compensated}}(x, y, \omega, 0) = \mathcal{F}_S^{-1}\left[\frac{\mathcal{F}_S\left[\mathcal{E}_M(x, y, \omega, d_1) \times (\Phi_M)^{-1}\right]}{\mathcal{H}_1}\right] \tag{V.4}$$

Experimentally, the compensation mask applied on the device may be done for one and unique wavelength. Even though compensation might be different for different wavelengths within the pulse bandwidth. Therefore and under the assumption of the symmetry of the spectrum with respect to the central wavelength, we compute a compensation mask for one precise wavelength, corresponding at the central wavelength and evaluate the global effect on the pulse.

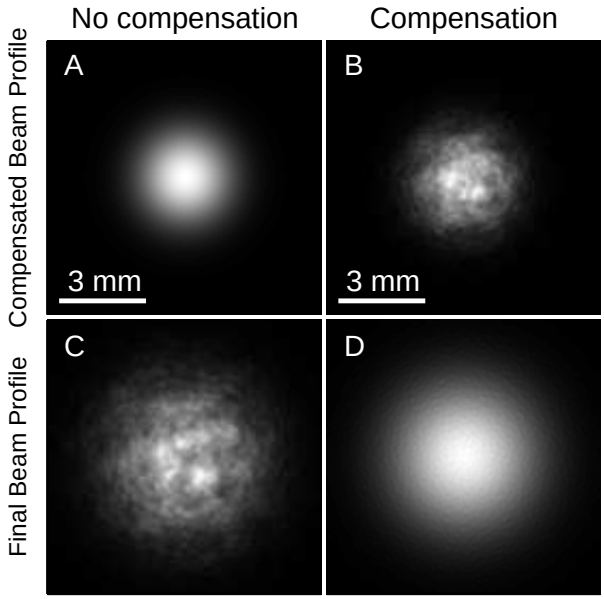

Figure V.5: Illustration of the method. The final spatial transverse profile (C) of the pulse is distorted when no compensation is applied to the initial profile (A). *A contrario* and for an adequate precompensation (B), the final profile is less distorted (D).

As experiment such as two color pump-probe scheme are envisaged for remote sensing [62, 64, 300], wavefront distortions including the wavelength dependence of the refraction index of air have to be studied. The wavelength dependence of the real part of the index of refraction of air is implemented as follows [301]:

$$n(\lambda) = 1 + 10^{-8}\left[8340.78 + \left(\frac{2405640}{130 - \lambda^{-2}}\right) + \left(\frac{15994}{38.9 - \lambda^{-2}}\right)\right] \qquad \text{(V.5)}$$

V.3.2 Results

Fig. V.5 depicts the success of the application of a pre-compensating mask to an initial pulse transverse profile. The simulation are performed with standard pulses parameters: central wavelength $\lambda_0 = 800$ nm, pulse duration $\Delta t_{\text{FWHM}} = 30$ fs and a fixed structure parameter of $C_n^2 = 10^{-9}$ m$^{-2/3}$. The other parameters of the pulse (radii, divergence,...) are the same used in the previous section. In Fig. V.5, an initial non compensated pulse profile (A) is strongly modified by the atmospheric turbulence (C), while from the application of a pre-compensation mask to the initial beam profile (C), a quasi-unaffected profile is obtained (D). The remaining modulations result from the monochromatic compensation.

Again for a fixed structure parameter of $C_n^2 = 10^{-9}$ m$^{-2/3}$ and a fixed pulse width $\Delta t_{\text{FWHM}} = 30$ fs, the illustration of the wavelength-dependency of the influence of the atmospheric turbulence on the transverse beam profile of the pulse is reported in

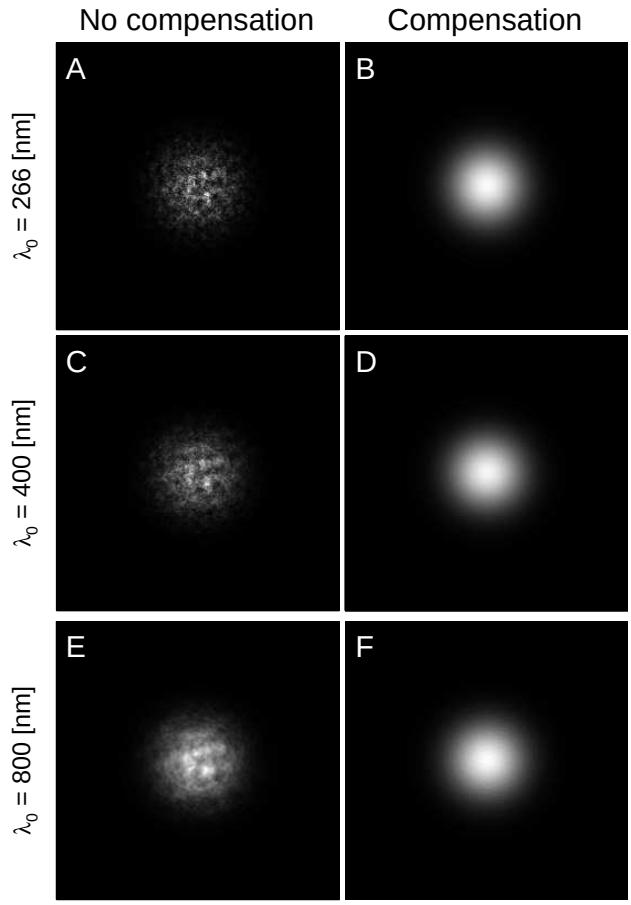

Figure V.6: Illustration of the wavelength dependency for similar pulses durations and turbulent distortions.

Fig. V.6. Not surprisingly, more the central wavelength in the UV more important the wavefront distortions.

V.3.3 Binning effect

Experimental devices able to perform wavefront distortions of laser pulses, i.e. spatial beam shaping, have a number limited of parameters/pixels. Therefore the experimental mask printed on the device can be an approximated compensation. To this purpose, Fig. V.7 illustrate this effect. The pulse parameters are $\Delta t_{\mathrm{FWHM}} = 30$ fs and the perturbation structure parameter is $C_n^2 = 10^{-9}$ m$^{-2/3}$. For two different central wavelength $\lambda_0 = 266$ nm and $\lambda_0 = 800$ nm and a numerical grid of $N_x \times N_y = 256 \times 256$ points in the transverse direction, the effect of the number of independent parameters is important and gets worse more the central wavelength of the pulse is short.

We did not consider the effect of gap between the pixels which would result in additional periodic 2-D diffraction patterns. This is out of the scope of this study, but it

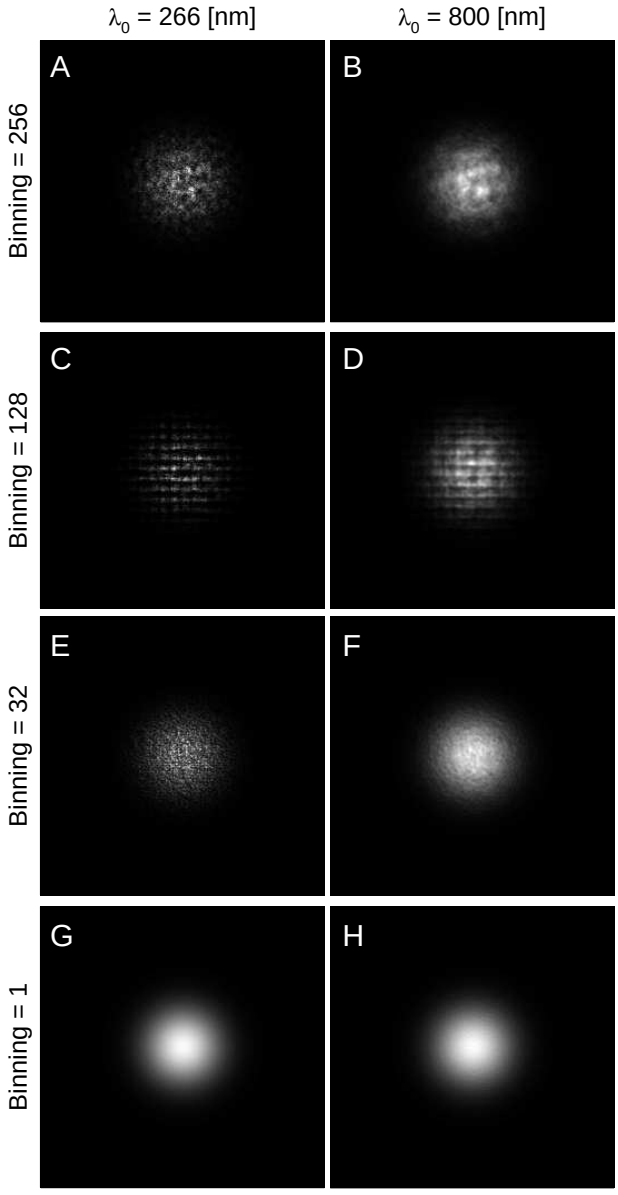

Figure V.7: For two different central wavelengths, the effect of the number of independent parameters is depicted.

cannot be overlooked for experimental implementations.

V.4 Conclusions and Perspectives

The effect of atmospheric turbulence on linearly propagating femtosecond laser pulses can be simply treated as the superposition of interferences independently acting on the components of the pulse spectrum. Bright spots on the wavefront correspond to weakly perturbed regions, which essentially maintain the spectral and temporal properties of the original pulse. The degree of alteration anticipated for actual atmospheric propagation 6% does not constitute an overwhelming limitation but it is a factor to take into account to design robust remote control applications. A partial compensation to the effects of turbulence can be achieved by adopting control strategies based on multiple photon interactions, as nonlinear power dependence limits higher order interactions within intense beam regions, where the original spectral and temporal pulse features are conserved.

In analogy with what is currently done in astronomy [295], we have proposed and numerically demonstrate the effect of an adaptive wavefront correction on the spatial beam profile, but also on the temporal shape of the femtosecond laser pulse. We also numerically investigated the spectral dependence over the pulse bandwidth over the index of refraction of air and the binning effect one the compensation. Experiments have to be performed to support our theoretical predictions with pulses at different central wavelengths, but also the monochromatic spatial precompensation by 2-D devices.

As perspective, we first have to estimate the effect of the residual variations remaining after the compensation and resulting from a monochromatic correction. Attention has also to be payed to the effect of these variations on the temporal profile of the laser pulses at different central wavelength. Moreover, the possibility to perform a real-time correction with available devices has to be studied to evaluate the application of adaptive wavefront correction to remote control detection.

In addition, theory and experiment of femtosecond laser pulses propagation have to be performed in parallel to maintain a direct understanding of the involved physical processes. Different orientations can be explored theoretically, numerically and experimentally, such as introducing a complex refractive index to account for absorption during pulse propagation. Further numerical developments can include the propagation of femtosecond laser pulses in biological tissues and to join the effort presented in Sec. III.3.

Conclusion

The development of rapid and selective tools for detection, imaging, localization and/or identification of bio-agents by optical methods is a challenging but fascinating field of research to respond to a need of our society. This thesis proposed and developed a contribution to three different specific applications: cell labeling, optical identification of bio-molecule and application of phase-coherent schemes to remote sensing.

In the quest of the new generation of exogenous cell markers, we present the first results obtained with nonlinear nanoparticles. As second harmonic generation (SHG) does not involve real states, no bleaching nor blinking is observed, contrary to fluorescent molecules or quantum dots. This property combined with their high contrast with respect to endogenous biological response, makes nonlinear nanocrystals very attractive candidates to be used as markers for biology. In this work, we show the retrieval of the orientation for different nanocrystals, in a standard microscope configuration as well as on a waveguide by evanescent excitation. These demonstrations open the door to use them as local probes of the surrounding electric field and for example to monitor cell membranes or neurons potentials. Among the various nonlinear nanocrystals, we point out the advantages of $Fe(IO_3)_3$ in regards to its low toxicity for future *in vivo* application. Due to the small size of the nanocrystals and the non resonant properties of the SHG, we exploited the absence of phase-matching constrains to point out the wavelength-flexibility of the nonlinear nanocrystals compared to the existing fluorescent probes, which permit to avoid autofluorescence background signals and to increase the depth penetration. Exploiting the coherence properties of the harmonic radiation, we demonstrate the *in situ* pulse characterization inside the focus of a high NA objective with nanometric spatial resolution. Finally, and taking advantage of the broad spatial excitation generated at the surface of a waveguide, we observed interferences of the second harmonic radiation of distinct dipolar nanocrystals.

On the way to an all-optical identification of biomolecules by means of phase-coherent schemes, we report first the conception and the realization of a new MEMS-based linear array specially developed for femtosecond pulse shaping applications in the ultraviolet region, in order to deal with the absorption bands of biomolecules. After its successful design concept validation, the device is actually characterized and will be used in an proof-of-principle optical experiment in April 2010. In the meanwhile, for close-

loop control experiments, we demonstrated that a novel multi-objective discrimination approach that we developed overcomes the results of standard genetic algorithms minimizing the bias related to the choice of optimization parameters. In addition, we show that based on an *a posteriori* judgment resulting from experimental needs, the user can pick a single solution from the Pareto front. We also characterized the first pulse shaper device operating in the deep ultraviolet and demonstrate its capacity to tailor the electric field by producing desired phase modulation.

Finally, we evidenced that the effect of atmospheric turbulence on linearly propagating femtosecond laser pulses can be simply treated as the superposition of interferences independently acting on the components of the pulse spectrum. Bright spots on the wavefront correspond to weakly perturbed regions, which essentially maintain the spectral and temporal properties of the original pulse. We also proposed and supported by a numerical study the use of adaptive techniques to correct the wavefront distortions.

To sum up, I worked on three different topics, and for each I tried to answer a series of precise questions by an intense experimental works punctually supported by numerical studies. The results presented in this work open several possibilities of future developments within each topics, but also by mixing different parts of the work.

In the field of exogenous markers, the possibility of functionalizing the surface of nonlinear nanocrystals to embed them into biological samples is currently in progress. Once achieved, it can be envisaged to use them either as local probes of the electric field potentials of the surrounding medium, either as local probe of the laser electric field to evaluate the modifications resulting from the light-matter interaction. This duality is a direct consequence of the intrinsic properties of the second harmonic, and will encourage the applications of phase-coherent schemes to microscopy allowing the *in situ* characterization of the field properties.

For identification of biomolecules by means of endogenous signal, the development of an appropriate all-reflective pulse shaper will provide a decisive tool to the application of coherent schemes to biomolecules. In case of encouraging results, its commercialization should be envisaged thanks to the growing interest for a device capable of modifying the pulse spectrum from less than 200 nm up to 2 μ m.

In addition to the case of atmospheric turbulence, the application of spatial wavefront correction has recently (March 2010) been bridged with success to exploit disordered materials for achieving perfect focusing of optical fields [302]. Exploiting these results, we can imagine several attractive experiments. While these experiments are performed with monochromatic optical fields, we use femtosecond laser pulses who have much smaller coherence length. In order to apply these results to our field, the first experiment to realize is to apply wavefront correction of femtosecond laser pulses to compensate the temporal delay of the first snake photons [164] with respect to the ballistic photons, and to increase the efficiency of the excitation. This can be shown as a spatial counterparts of the temporal coherent control of the decoherence [48]. Afterwards, in nonlinear microscopy, in combination with nonlinear nanocrystals, one can imagine to reveal spatial, spectral and phase-related properties of disordered materials.

In parallel a very recent reported result (March 2010) on the measure and the control of transmission matrix in disordered media [303], opens the door to the very exciting field of coherent control experiments in disordered media mixing spatial and temporal pulse shaping.

Appendix: Statistical Moments

Ultrashort laser pulses are very sensitive in both temporal or spatial domain. As distortions are present in every beam path (due to absorption, dispersion, scattering, diffraction or reflection), analyzing tools are needed to characterize the laser pulses. Statistical moments can provide these tools. In this appendix, we present the application of statistical moments to the spectral characteristics of ultrashort laser pulses.

In general, the spectral distribution are assumed to be homogeneous, while the inhomogeneities are ignored. In this case, the characterization of the pulses is usually restricted to full-width at half-maximum considerations (See Section I.1). The restriction is strong as the FWHM can be applied only to spectral distributions which are continuous, symmetric, Gaussian like and with an unique maxima (do not present any minima). This analysis is not anymore sufficient when several peaks, dips, asymmetries or edges are present within the spectrum. The first four moments give in a simple computing way the characteristics of highly complex spectra, but can also provide useful 2D spatio-spectral cartography of laser beams. In this work, we use statistical moments in Sec. IV.3 but further promising applications can also be envisages in the field of laser beam propagation through turbulent atmosphere or turbid media.

The **first spectral moment**, M_1, also called the weighted arithmetic average function, extract the weighting of the wavelength λ by its related spectral intensity $I(\lambda)$. This represent the wavelength barycenter (λ_B), or center of gravity of the wavelength. It match exactly with the maximal wavelength only in the case of symmetric spectra that exhibit only one maximum. The first spectral moment is defined by:

$$M_1 = \frac{\int_{-\infty}^{+\infty} \lambda I(\lambda) d\lambda}{\int_{-\infty}^{+\infty} I(\lambda) d\lambda} \equiv \lambda_B$$

To extract more information from complex shape of spectral distributions, it is necessary to work out higher statistical moments. The **second spectral moment**, M_2, is obtained replacing the wavelength by squaring the deviation of the wavelength to the barycentre λ_B:

$$M_2 = \frac{\int_{-\infty}^{+\infty}(\lambda - \lambda_B)^2 I(\lambda)d\lambda}{\int_{-\infty}^{+\infty} I(\lambda)d\lambda} = \sigma^2 = \lambda_{RMS}^2$$

Extracting the root of the second spectral moment, we obtain the standard deviation, which describes the statistical spread of the spectral distribution as a function of the wavelength. The second moment includes also the shape of the spectrum. One has to note its reduction to Eq. I.12 occurs for pure Gaussian spectra, modulo the multiplication by an adequate factor.

The **third spectral moment**, M_3 also called skewness, allows to break the symmetry of the spectral distribution and is defined by:

$$M_3 = \frac{\int_{-\infty}^{+\infty}(\lambda - \lambda_B)^3 I(\lambda)d\lambda}{\left(\sqrt{M_2}\right)^3 \int_{-\infty}^{+\infty} I(\lambda)d\lambda} \equiv S$$

Finally, the **fourth spectral moment**, M_4, describe the flatness or *a contrario* the peakness of the spectral distribution and is defined by:

$$M_4 = \frac{\int_{-\infty}^{+\infty}(\lambda - \lambda_B)^4 I(\lambda)d\lambda}{\left(\sqrt{M_2}\right)^4 \int_{-\infty}^{+\infty} I(\lambda)d\lambda}$$

As for a Gaussian spectral profile $M_4 = 3$, permit the definition of the Kurtosis coefficient:

$$K = M_4 - 3$$

Both skewness and kurtosis are relative quantities and dimensionless.

By the mean of only four coefficient, it is possible to describe complex spectra and it makes such analysis very promising for ultrashort pulse laser characterization. Statistical moments analysis provide powerful tools also for spatio-spectral analysis. Indeed, intensity beam profile (see for example Chapter V) are represented as $(x, y, I(x, y))$, where x and y are the two transverse dimensions of the beam and $I(x, y)$ its transverse intensity distribution. The use of statistical moments can provide additional information by depicting the the spatial distribution of the moments as $(x, y, M_i(\lambda, I))$, where M_i depicts the four moments with $i = 1, 2, 3, 4$. It could also be interesting to look to the correlation between intensity and moment through plots like $(I, M_i(\lambda, I))$. These analysis can give useful information for example for beam propagation through turbulent atmosphere or turbid media.

List of Publications

Publications are separated between Papers and Conference Proceedings. Symbols are used for different subject/chapter to which they relate, i.e. nonlinear nanoprobes (Chapter III) are hightlighted by ($\triangle$), progess for label-free identification (Chapter IV) by ($\lozenge$) and propagation through turbulent atmosphere (Chapter V) by ($\star$). ($\cdot$) indicates publications in fields not directly related to this work (gravitational wave sensing and atmospheric propagation of high power lasers).

Publications covered by this thesis

Papers:

$\triangle$ L. Bonacina, Y. Mugnier, F. Courvoisier, R. Le Dantec, J. Extermann, Y. Lambert, V. Boutou, C. Galez and J.-P. Wolf, Polar $Fe(IO_3)_3$ nanocrystals as local probes for nonlinear microscopy, *Applied Physics B-Lasers and Optics*, 87 (3), 399-403, 2007.

$\lozenge$ L. Bonacina, J. Extermann, A. Rondi, V. Boutou and J.-P. Wolf, Multiobjective genetic approach for optimal control of photoinduced processes, *Physical Review A*, 76 (2), 023408, 2007.

$\star$ J. Extermann, P. Bejot, L. Bonacina, P. Billaud, J. Kasparian and J.-P. Wolf, Effects of atmospheric turbulence on remote optimal control experiments, *Applied Physics Letters*, 92 (4), 041103, 2008.

$\triangle$ J. Extermann, L. Bonacina, F. Courvoisier, D. Kiselev, Y. Mugnier, R. Le Dantec, C. Galez and J.-P. Wolf, Nano-FROG: Frequency resolved optical gating by a nanometric object, *Optics Express*, 16 (14), 10405-10411, 2008.

$\triangle$ J. Extermann, L. Bonacina, E. Cuna, C. Kasparian, Y. Mugnier, T. Feurer and J.-P. Wolf, Nanodoublers as deep imaging markers for multi-photon microscopy, *Optics Express*, 17 (17), 15342-15349, 2009.

△ J. Extermann, P. Bejot, L. Bonacina, Y. Mugnier, R. Le Dantec, T. Mazingue, C. Galez and J.-P. Wolf, An inexpensive nonlinear medium for intense ultrabroadband pulse characterization, *Applied Physics B-Lasers and Optics*, 97 (3), 537-540, 2009.

◊ A. Rondi, J. Extermann, L. Bonacina, S.M. Weber and J.-P. Wolf, Characterization of a MEMS-based pulse-shaping device in the deep ultraviolet, *Applied Physics B-Lasers and Optics*, 96(4), 757-761, 2009.

△ R. Bäumner, L. Bonacina, J. Enderlein, J. Extermann, T. Fricke-Begemann, G. Marowsky and J.-P. Wolf, Evanescent-Field-Induced Second Harmonic Generation by Non-centrosymmetric Nanoparticles, *submitted*.

△ R. Le Dantec, Y. Mugnier, G. Djanta, L. Bonacina, J. Extermann, L. Badie, C. Joulaud, J.-P. Wolf and C. Galez, Characterization of ZnO and BaTiO3 nanoprobes efficiency for Second Harmonic Generation microscopy, *in preparation*.

Conferences Proceeding:

◊ A. Rondi, J. Extermann, S.M. Weber, L. Bonacina, J. Roslund, M. Roth, H. Rabitz and J.-P. Wolf, MEMS for femtosecond pulse shaping applications, *Proc. SPIE*, 7208, 72090A, 2009.

◊ S.M. Weber, J. Extermann, W. Noell, F. Jutzi, S. Lani, D. Kiselev, L. Bonacina, N.F. de Rooij and J.-P. Wolf, Linear MEMS Micromirror Array For UV-NIR Femtosecond Pulse Shaping, *Proc. SPIE*, 7594, 75940J, 2010.

Others publications

Papers:

· F. Dubath, J. Extermann and L. Gottardi, On the sensitivity of a hollow sphere as a multi-modal resonant gravitational wave detector, *Classical and Quantum Gravity*, 24 (9), 2231-2251, 2007.

· P. Bejot, L. Bonacina, J. Extermann, M. Moret, J.-P. Wolf, R. Ackermann, N. Lascoux, R. Salame, E. Salmon, J. Kasparian, L. Berge, S. Champeaux, C. Guet, N. Blanchot, O. Bonville, A. Boscheron, P. Canal, M. Castaldi, O. Hartmann, C. Lepage, L. Marmande, E. Mazataud, G. Mennerat, L. Patissou, V. Prevot, D. Raffestin and J. Ribolzi, 32 TW atmospheric white-light laser, *Applied Physics Letters*, 90 (15), 151106, 2007.

◊ F. Courvoisier, L. Bonacina, V. Boutou, L. Guyon, C. Bonnet, B. Thuillier, J. Extermann, M. Roth, H. Rabitz and J.-P. Wolf, Identification of biological microparticles using ultrafast depletion spectroscopy, *Faraday Discussions*, 137, 37-49, 2008.

◊ S. M. Weber, W. Noell, S. Lani, F. Jutzi, N. F. de Rooij, P. Brühlmeier, D. Kiselev, J. Extermann, L. Bonacina and J.-P. Wolf, Development of a high aspect ratio micromirror array with two degrees of freedom for femtosecond pulse shaping, *submitted*.

◊ S.M. Weber, J. Extermann, L. Bonacina, W. Noell, D. Kiselev, S. Waldis, N.F. de Rooij and J.-P. Wolf, UV and NIR Femtosecond Temporal Pulse Shaping with a New High Aspect-Ratio 1D Micromirror Array, *Optics Letters*, 35 (18), 3102-3104, 2010.

Conferences Proceeding:

· L. Bonacina, P. Bejot, J. Extermann, M. Moret, J.-P. Wolf, R. Ackermann, N. Lascoux, R. Salame, E. Salmon, J. Kasparian, L. Berge, S. Champeaux, C. Guet, N. Blanchot, O. Bonville, A. Boscheron, P. Canal, M. Castaldi, O. Hartmann, C. Lepage, L. Marmande, E. Mazataud, G. Mennerat, L. Patissou, V. Prevot, D. Raffestin and J. Ribolzi, TW lasers in air: ultra-high powers and optimal control strategies, *Proc. SPIE*, 6733, 67332K, 2007.

◊ S. Waldis, S. M. Weber, W. Noell, J. Extermann, D. Kiselev, L. Bonacina, J.-P. Wolf and N. F. de Rooij, Large linear micromirror array for UV femtosecond laser pulse shaping, *2008 IEEE/LEOS International Conference on Optical Mems and Nanophotonics*, 39-40, 2008.

◊ S. M. Weber, S. Waldis, W. Noell, D. Kiselev, J. Extermann, L. Bonacina, J.-P. Wolf and N.F. de Rooij, Linear micromirror array for broadband femtosecond pulse shaping in phase and amplitude, *Proc. SPIE* 7208, 720805, 2009.

Bibliography

[1] T. H. Maiman. Stimulated optical radiation in ruby. *Nature*, 187(4736):493–494, 1960.

[2] M. Goppert-Mayer. Elementary file with two quantum fissures. *Annalen Der Physik*, 9(3):273–294, 1931.

[3] P. A. Franken, G. Weinreich, C. W. Peters, and A. E. Hill. Generation of optical harmonics. *Physical Review Letters*, 7(4):118–119, 1961.

[4] W. Denk, J. H. Strickler, and W. W. Webb. 2-photon laser scanning fluorescence microscopy. *Science*, 248(4951):73–76, 1990.

[5] W. R. Zipfel, R. M. Williams, and W. W. Webb. Nonlinear magic: multiphoton microscopy in the biosciences. *Nature Biotechnology*, 21(11):1368–1376, 2003.

[6] Nobel Prize. http://nobelprize.org/.

[7] L. Cognet. *Lasers et Technologies Femtosecondes*. Publications de l'Universite, Saint-Etienne, 1st edition, 2005.

[8] G. S. Harms, L. Cognet, P. H. M. Lommerse, G. A. Blab, and T. Schmidt. Autofluorescent proteins in single-molecule research: Applications to live cell imaging microscopy. *Biophysical Journal*, 80(5):2396–2408, 2001.

[9] M. Nirmal, B. O. Dabbousi, M. G. Bawendi, J. J. Macklin, J. K. Trautman, T. D. Harris, and L. E. Brus. Fluorescence intermittency in single cadmium selenide nanocrystals. *Nature*, 383(6603):802–804, 1996.

[10] X. Brokmann, J. P. Hermier, G. Messin, P. Desbiolles, J. P. Bouchaud, and M. Dahan. Statistical aging and nonergodicity in the fluorescence of single nanocrystals. *Physical Review Letters*, 90(12):120601, 2003.

[11] J. I. Dadap, J. Shan, K. B. Eisenthal, and T. F. Heinz. Second-harmonic rayleigh scattering from a sphere of centrosymmetric material. *Physical Review Letters*, 83(20):4045–4048, 1999.

[12] J. Mertz and L. Moreaux. Second-harmonic generation by focused excitation of inhomogeneously distributed scatterers. *Optics Communications*, 196(1-6):325–330, 2001.

[13] Y. Pavlyukh and W. Hubner. Nonlinear mie scattering from spherical particles. *Physical Review B*, 70(24):245434, 2004.

[14] K. Nappa, I. Russier-Antoine, E. Benichou, C. Jonin, and P. F. Brevet. Wavelength dependence of the retardation effects in silver nanoparticles followed by polarization resolved hyper rayleigh scattering. *Chemical Physics Letters*, 416(4-6):246–250, 2005.

[15] J. Nappa, G. Revillod, I. Russier-Antoine, E. Benichou, C. Jonin, and P. F. Brevet. Electric dipole origin of the second harmonic generation of small metallic particles. *Physical Review B*, 71(16):165407, 2005.

[16] M. L. Sandrock, C. D. Pibel, F. M. Geiger, and C. A. Foss. Synthesis and second-harmonic generation studies of noncentrosymmetric gold nanostructures. *Journal of Physical Chemistry B*, 103(14):2668–2673, 1999.

[17] S. W. Chan, R. Barille, J. M. Nunzi, K. H. Tam, Y. H. Leung, W. K. Chan, and A. B. Djurisic. Second harmonic generation in zinc oxide nanorods. *Applied Physics B-Lasers and Optics*, 84(1-2):351–355, 2006.

[18] J. C. Johnson, H. Q. Yan, R. D. Schaller, P. B. Petersen, P. D. Yang, and R. J. Saykally. Near-field imaging of nonlinear optical mixing in single zinc oxide nanowires. *Nano Letters*, 2(4):279–283, 2002.

[19] Y. Z. Shen, P. Markowicz, J. Winiarz, J. Swiatkiewicz, and P. N. Prasad. Nanoscopic study of second-harmonic generation in organic crystals with collection-mode near-field scanning optical microscopy. *Optics Letters*, 26(10):725–727, 2001.

[20] S. Brasselet, V. Le Floc'h, F. Treussart, J. F. Roch, J. Zyss, E. Botzung-Appert, and A. Ibanez. In situ diagnostics of the crystalline nature of single organic nanocrystals by nonlinear microscopy. *Physical Review Letters*, 92(20):207401, 2004.

[21] R. M. Williams, W. R. Zipfel, and W. W. Webb. Multiphoton microscopy in biological research. *Current Opinion in Chemical Biology*, 5(5):603–608, 2001.

[22] J. Mertz. Nonlinear microscopy: new techniques and applications. *Current Opinion in Neurobiology*, 14(5):610–616, 2004.

[23] J. M. Dela Cruz, I. Pastirk, M. Comstock, V. V. Lozovoy, and M. Dantus. Use of coherent control methods through scattering biological tissue to achieve functional imaging. *Proceedings of the National Academy of Sciences of the United States of America*, 101(49):16996–17001, 2004.

[24] J. M. Dela Cruz, V. V. Lozovoy, and M. Dantus. Coherent control improves biomedical imaging with ultrashort shaped pulses. *Journal of Photochemistry and Photobiology a-Chemistry*, 180(3):307–313, 2006.

[25] J. A. Squier, M. Muller, G. J. Brakenhoff, and K. R. Wilson. Third harmonic generation microscopy. *Optics Express*, 3(9):315–324, 1998.

[26] N. Dudovich, D. Oron, and Y. Silberberg. Single-pulse coherently controlled nonlinear raman spectroscopy and microscopy. *Nature*, 418(6897):512–514, 2002.

[27] B. von Vacano, T. Buckup, and M. Motzkus. In situ broadband pulse compression for multiphoton microscopy using a shaper-assisted collinear spider. *Optics Letters*, 31(8):1154–1156, 2006.

[28] J. P. Ogilvie, D. Debarre, X. Solinas, J. L. Martin, E. Beaurepaire, and M. Joffre. Use of coherent control for selective two-photon fluorescence microscopy in live organisms. *Optics Express*, 14(2):759–766, 2006.

[29] R. S. Pillai, C. Boudoux, G. Labroille, N. Olivier, I. Veilleux, E. Farge, M. Joffre, and E. Beaurepaire. Multiplexed two-photon microscopy of dynamic biological samples with shaped broadband pulses. *Optics Express*, 17(15):12741–12752, 2009.

[30] M. Aeschlimann, M. Bauer, D. Bayer, T. Brixner, F. J. de Abajo, W. Pfeiffer, M. Rohmer, C. Spindler, and F. Steeb. Adaptive subwavelength control of nano-optical fields. *Nature*, 446(7133):301–304, 2007.

[31] U. Fuchs, U. D. Zeitner, and A. Tunnermann. Ultra-short pulse propagation in complex optical systems. *Optics Express*, 13(10):3852–3861, 2005.

[32] E. Tal and Y. Silberberg. Transformation from an ultrashort pulse to a spatiotemporal speckle by a thin scattering surface. *Optics Letters*, 31(23):3529–3531, 2006.

[33] D. J. Tannor and S. A. Rice. Control of selectivity of chemical-reaction via control of wave packet evolution. *Journal of Chemical Physics*, 83(10):5013–5018, 1985.

[34] M. Shapiro and P. Brumer. Laser control of product quantum state populations in unimolecular reactions. *Journal of Chemical Physics*, 84(7):4103–4104, 1986.

[35] D. J. Tannor, R. Kosloff, and S. A. Rice. Coherent pulse sequence induced control of selectivity of reactions - exact quantum-mechanical calculations. *Journal of Chemical Physics*, 85(10):5805–5820, 1986.

[36] A. M. Weiner, J. P. Heritage, and E. M. Kirschner. High-resolution femtosecond pulse shaping. *Journal of the Optical Society of America B-Optical Physics*, 5(8):1563–1572, 1988.

[37] A. M. Weiner. Femtosecond pulse shaping using spatial light modulators. *Review of Scientific Instruments*, 71(5):1929–1960, 2000.

[38] R. S. Judson and H. Rabitz. Teaching lasers to control molecules. *Physical Review Letters*, 68(10):1500–1503, 1992.

[39] A. Assion, T. Baumert, M. Bergt, T. Brixner, B. Kiefer, V. Seyfried, M. Strehle, and G. Gerber. Control of chemical reactions by feedback-optimized phase-shaped femtosecond laser pulses. *Science*, 282(5390):919–922, 1998.

[40] D. Meshulach and Y. Silberberg. Coherent quantum control of two-photon transitions by a femtosecond laser pulse. *Nature*, 396(6708):239–242, 1998.

[41] T. Hornung, R. Meier, D. Zeidler, K. L. Kompa, D. Proch, and M. Motzkus. Optimal control of one- and two-photon transitions with shaped femtosecond pulses and feedback. *Applied Physics B-Lasers and Optics*, 71(3):277–284, 2000.

[42] T. Brixner, N. H. Damrauer, P. Niklaus, and G. Gerber. Photoselective adaptive femtosecond quantum control in the liquid phase. *Nature*, 414(6859):57–60, 2001.

[43] J. M. Dela Cruz, I. Pastirk, V. V. Lozovoy, K. A. Walowicz, and M. Dantus. Multiphoton intrapulse interference 3: Probing microscopic chemical environments. *Journal of Physical Chemistry A*, 108(1):53–58, 2004.

[44] J. L. Herek, W. Wohlleben, R. J. Cogdell, D. Zeidler, and M. Motzkus. Quantum control of energy flow in light harvesting. *Nature*, 417(6888):533–535, 2002.

[45] V. I. Prokhorenko, A. M. Nagy, and R. J. D. Miller. Coherent control of the population transfer in complex solvated molecules at weak excitation. an experimental study. *Journal of Chemical Physics*, 122(18):184502, 2005.

[46] W. Wohlleben, T. Buckup, J. L. Herek, and M. Motzkus. Coherent control for spectroscopy and manipulation of biological dynamics. *Chemphyschem*, 6(5):850–857, 2005.

[47] V. I. Prokhorenko, A. M. Nagy, S. A. Waschuk, L. S. Brown, R. R. Birge, and R. J. D. Miller. Coherent control of retinal isomerization in bacteriorhodopsin. *Science*, 313(5791):1257–1261, 2006.

[48] M. P. A. Branderhorst, P. Londero, P. Wasylczyk, C. Brif, R. L. Kosut, H. Rabitz, and I. A. Walmsley. Coherent control of decoherence. *Science*, 320(5876):638–643, 2008.

[49] I. Pastirk, J. M. Dela Cruz, K. A. Walowicz, V. V. Lozovoy, and M. Dantus. Selective two-photon microscopy with shaped femtosecond pulses. *Optics Express*, 11(14):1695–1701, 2003.

[50] R. Bartels, S. Backus, E. Zeek, L. Misoguti, G. Vdovin, I. P. Christov, M. M. Murnane, and H. C. Kapteyn. Shaped-pulse optimization of coherent emission of high-harmonic soft x-rays. *Nature*, 406(6792):164–166, 2000.

[51] T. Pfeifer, R. Spitzenpfeil, D. Walter, C. Winterfeldt, F. Dimler, G. Gerber, and C. Spielmann. Towards optimal control with shaped soft-x-ray light. *Optics Express*, 15(6):3409–3416, 2007.

[52] V. V. Lozovoy and M. Dantus. Coherent control in femtochemistry. *Chemphyschem*, 6(10):1970–2000, 2005.

[53] M. Roth, M. Mehendale, A. Bartelt, and H. Rabitz. Acousto-optical shaping of ultraviolet femtosecond pulses. *Applied Physics B-Lasers and Optics*, 80(4-5):441–444, 2005.

[54] S. Coudreau, D. Kaplan, and P. Tournois. Ultraviolet acousto-optic programmable dispersive filter laser pulse shaping in kdp. *Optics Letters*, 31(12):1899–1901, 2006.

[55] B. J. Pearson and T. C. Weinacht. Shaped ultrafast laser pulses in the deep ultraviolet. *Optics Express*, 15(7):4385–4388, 2007.

[56] C. Schriever, S. Lochbrunner, M. Optiz, and E. Riedle. 19 fs shaped ultraviolet pulses. *Optics Letters*, 31(4):543–545, 2006.

[57] P. Nuernberger, G. Vogt, R. Selle, S. Fechner, T. Brixner, and G. Gerber. Generation of shaped ultraviolet pulses at the third harmonic of titanium-sapphire femtosecond laser radiation. *Applied Physics B-Lasers and Optics*, 88(4):519–526, 2007.

[58] E. Zeek, K. Maginnis, S. Backus, U. Russek, M. Murnane, G. Mourou, H. Kapteyn, and G. Vdovin. Pulse compression by use of deformable mirrors. *Optics Letters*, 24(7):493–495, 1999.

[59] M. Hacker, G. Stobrawa, R. Sauerbrey, T. Buckup, M. Motzkus, M. Wildenhain, and A. Gehner. Micromirror slm for femtosecond pulse shaping in the ultraviolet. *Applied Physics B-Lasers and Optics*, 76(6):711–714, 2003.

[60] K. W. Stone, M. T. W. Milder, J. C. Vaughan, and K. A. Nelson. Spatiotemporal femtosecond pulse shaping using a mems-based micromirror slm. *Ultrafast Phenomena XV*, 88:184–186, 2007.

[61] T. Abe, G. Wang, and F. Kannari. Femtosecond pulse shaping on two-color laser superposition pulse using a mems micromirror slm. *2008 Conference on Lasers and Electro-Optics and Quantum Electronics and Laser Science Conference, Vols 1-9*, pages 2832–2833, 2008.

[62] F. Courvoisier, V. Boutou, V. Wood, A. Bartelt, M. Roth, H. Rabitz, and J. P. Wolf. Femtosecond laser pulses distinguish bacteria from background urban aerosols. *Applied Physics Letters*, 87(6):063901, 2005.

[63] B. Q. Li, H. Rabitz, and J. P. Wolf. Optimal dynamic discrimination of similar quantum systems with time series data. *Journal of Chemical Physics*, 122(15):154103, 2005.

[64] M. O. Scully, G. W. Kattawar, R. P. Lucht, T. Opatrny, H. Pilloff, A. Rebane, A. V. Sokolov, and M. S. Zubairy. Fast cars: Engineering a laser spectroscopic technique for rapid identification of bacterial spores. *Proceedings of the National Academy of Sciences of the United States of America*, 99(17):10994–11001, 2002.

[65] D. Pestov, R. K. Murawski, G. O. Ariunbold, X. Wang, M. C. Zhi, A. V. Sokolov, V. A. Sautenkov, Y. V. Rostovtsev, A. Dogariu, Y. Huang, and M. O. Scully. Optimizing the laser-pulse configuration for coherent raman spectroscopy. *Science*, 316(5822):265–268, 2007.

[66] J. D. Jackson. *Classical Electrodynamics*. John Wiley and Sons, Inc., New York, 1965.

[67] J.-C. Diels and W. Rudolph. *Ultrashort Laser Pulse Phenomena*. Academic Press, second edition edition, 2006.

[68] S. M. Weber. *New concepts for optimal control experiments using femtosecond pulse shaping*. PhD thesis, Freie University, 2007.

[69] M. Plewicki. *Phase, amplitude and polarization pulse shaping in order to influence molecular processes*. PhD thesis, Freie University, 2006.

[70] T. Brixner. *Adaptive Femtosecond quantum Control*. PhD thesis, Julius-Maximilians University, 2001.

[71] S. Mukamel. *Nonlinear Optical Spectroscopy*. Oxford University Press, 1999.

[72] B. Boulanger and J. Zyss. Nonlinear optical properties. In Springer, editor, *International Tables for Crystallography Volume D: Physical properties of crystals*, volume D. 2006.

[73] M. Joffre. Comment on "coherent control of retinal isomerization in bacteriorhodopsin". *Science*, 317(5837):–, 2007.

[74] A. Yariv. *Quantum Electronics*. John Wiley and Sons, New York, 1989.

[75] D. A. Kleinman. Nonlinear dielectric polarization in optical media. *Physical Review*, 126(6):1977–1979, 1962.

[76] R.W. Boyd. *Nonlinear Optics*. Academic Press, second edition edition, 2003.

[77] J. A. Armstrong, N. Bloembergen, J. Ducuing, and P. S. Pershan. Interactions between light waves in a nonlinear dielectric. *Physical Review*, 127(6):1918–1939, 1962.

[78] M. Joffre. *Optique Non-Lineaire en regime continu et femtoseconde, http://cel.archives-ouvertes.fr/cel-00092964/fr*. Ecole Polytechnique, Paris, 2006.

[79] B. Richards and E. Wolf. Electromagnetic diffraction in optical systems .2. structure of the image field in an aplanatic system. *Proceedings of the Royal Society of London Series a-Mathematical and Physical Sciences*, 253(1274):358–379, 1959.

[80] E. Wolf. Electromagnetic diffraction in optical systems .1. an integral representation of the image field. *Proceedings of the Royal Society of London Series a-Mathematical and Physical Sciences*, 253(1274):349–357, 1959.

[81] L. Novotny and B. Hecht. *Principles of Nano-Optics*. Cambridge University Press, 2008.

[82] E. Y. S. Yew and C. J. R. Sheppard. Effects of axial field components on second harmonic generation microscopy. *Optics Express*, 14(3):1167–1174, 2006.

[83] J. Enderlein. Theoretical study of detection of a dipole emitter through an objective with high numerical aperture. *Optics Letters*, 25(9):634–636, 2000.

[84] G. Cox and C. J. R. Sheppard. Practical limits of resolution in confocal and nonlinear microscopy. *Microscopy Research and Technique*, 63(1):18–22, 2004.

[85] J. X. Cheng, A. Volkmer, and X. S. Xie. Theoretical and experimental characterization of coherent anti-stokes raman scattering microscopy. *Journal of the Optical Society of America B-Optical Physics*, 19(6):1363–1375, 2002.

[86] L. Novotny. Allowed and forbidden light in near-field optics .2. interacting dipolar particles. *Journal of the Optical Society of America a-Optics Image Science and Vision*, 14(1):105–113, 1997.

[87] V. Le Floc'h, S. Brasselet, J. F. Roch, and J. Zyss. Monitoring of orientation in molecular ensembles by polarization sensitive nonlinear microscopy. *Journal of Physical Chemistry B*, 107(45):12403–12410, 2003.

[88] D. J. Bradley and G. H. C. New. Ultrashort pulse measurements. *Proceedings of the Ieee*, 62(3):313–345, 1974.

[89] V. Wong and I. A. Walmsley. Linear filter analysis of methods for ultrashort-pulse-shape measurements. *Journal of the Optical Society of America B-Optical Physics*, 12(8):1491–1499, 1995.

[90] I. A. Walmsley and V. Wong. Characterization of the electric field of ultrashort optical pulses. *Journal of the Optical Society of America B-Optical Physics*, 13(11):2453–2463, 1996.

[91] J. K. Ranka, A. L. Gaeta, A. Baltuska, M. S. Pshenichnikov, and D. A. Wiersma. Autocorrelation measurement of 6-fs pulses based on the two-photon-induced photocurrent in a gaasp photodiode. *Optics Letters*, 22(17):1344–1346, 1997.

[92] T. Feurer, A. Glass, and R. Sauerbrey. Two-photon photoconductivity in sic photodiodes and its application to autocorrelation measurements of femtosecond optical pulses. *Applied Physics B-Lasers and Optics*, 65(2):295–297, 1997.

[93] C. Xu, J. Guild, W. W. Webb, and W. Denk. Determination of absolute 2-photon excitation cross-sections by in-situ 2nd-order autocorrelation. *Optics Letters*, 20(23):2372–2374, 1995.

[94] J. C. M. Diels, J. J. Fontaine, I. C. Mcmichael, and F. Simoni. Control and measurement of ultrashort pulse shapes (in amplitude and phase) with femtosecond accuracy. *Applied Optics*, 24(9):1270–1282, 1985.

[95] E. P. Ippen and C.V. Shank. Ultrashort light pulses, techniques for measurement. In S.L. Shapiro, editor, *Ultrashort Light Pulses*, volume 18. Springer-Verlag, Berlin, 1977.

[96] J. Jasapara and W. Rudolph. Characterization of sub-10-fs pulse focusing with high-numerical-aperture microscope objectives. *Optics Letters*, 24(11):777–779, 1999.

[97] R. Wolleschensky, T. Feurer, R. Sauerbrey, and I. Simon. Characterization and optimization of a laser-scanning microscope in the femtosecond regime. *Applied Physics B-Lasers and Optics*, 67(1):87–94, 1998.

[98] R. Trebino. *Frequency-Resolved Optical Gating*. Kluwer Academic Publishers, Boston, 2000.

[99] A. Baltuska, Z. Wei, M. S. Pshenichnikov, D. A. Wiersma, and R. Szipocs. All-solid-state cavity-dumped sub-5-fs laser. *Applied Physics B-Lasers and Optics*, 65(2):175–188, 1997.

[100] J. Peatross and A. Rundquist. Temporal decorrelation of short laser pulses. *Journal of the Optical Society of America B-Optical Physics*, 15(1):216–222, 1998.

[101] L. Lepetit, G. Cheriaux, and M. Joffre. Linear techniques of phase measurement by femtosecond spectral interferometry for applications in spectroscopy. *Journal of the Optical Society of America B-Optical Physics*, 12(12):2467–2474, 1995.

[102] C.L. Froehly, A. Lacourt, and J.-Ch Vienot. Time impulse response and time frequency response of optical pupils.:experimental confirmations and applications. *Nouvelle Revue d'Optique*, 4:183, 1973.

[103] C. Iaconis and I. A. Walmsley. Spectral phase interferometry for direct electric-field reconstruction of ultrashort optical pulses. *Optics Letters*, 23(10):792–794, 1998.

[104] P. Bowlan, P. Gabolde, A. Shreenath, K. McGresham, R. Trebino, and S. Akturk. Crossed-beam spectral interferometry: a simple, high-spectral-resolution method for completely characterizing complex ultrashort pulses in real time. *Optics Express*, 14(24):11892–11900, 2006.

[105] D. J. Kane and R. Trebino. Single-shot measurement of the intensity and phase of an arbitrary ultrashort pulse by using frequency-resolved optical gating. *Optics Letters*, 18(10):823–825, 1993.

[106] D. J. Kane and R. Trebino. Characterization of arbitrary femtosecond pulses using frequency-resolved optical gating. *Ieee Journal of Quantum Electronics*, 29(2):571–579, 1993.

[107] R. Trebino and D. J. Kane. Using phase retrieval to measure the intensity and phase of ultrashort pulses - frequency-resolved optical gating. *Journal of the Optical Society of America a-Optics Image Science and Vision*, 10(5):1101–1111, 1993.

[108] R. Trebino, K. W. DeLong, D. N. Fittinghoff, J. N. Sweetser, M. A. Krumbugel, B. A. Richman, and D. J. Kane. Measuring ultrashort laser pulses in the time-frequency domain using frequency-resolved optical gating. *Review of Scientific Instruments*, 68(9):3277–3295, 1997.

[109] J. Paye, M. Ramaswamy, J. G. Fujimoto, and E. P. Ippen. Measurement of the amplitude and phase of ultrashort light-pulses from spectrally resolved autocorrelation. *Optics Letters*, 18(22):1946–1948, 1993.

[110] K. W. Delong, R. Trebino, J. Hunter, and W. E. White. Frequency-resolved optical gating with the use of 2nd-harmonic generation. *Journal of the Optical Society of America B-Optical Physics*, 11(11):2206–2215, 1994.

[111] T. Tsang, M. A. Krumbugel, K. W. DeLong, D. N. Fittinghoff, and R. Trebino. Frequency-resolved optical-gating measurements of ultrashort pulses using surface third-harmonic generation. *Optics Letters*, 21(17):1381–1383, 1996.

[112] S. Linden, H. Giessen, and J. Kuhl. Xfrog - a new method for amplitude and phase characterization of weak ultrashort pulses. *Physica Status Solidi B-Basic Research*, 206(1):119–124, 1998.

[113] S. Linden, J. Kuhl, and H. Giessen. Amplitude and phase characterization of weak blue ultrashort pulses by downconversion. *Optics Letters*, 24(8):569–571, 1999.

[114] K. W. Delong, R. Trebino, and D. J. Kane. Comparison of ultrashort-pulse frequency-resolved-optical-gating traces for 3 common beam geometries. *Journal of the Optical Society of America B-Optical Physics*, 11(9):1595–1608, 1994.

[115] D. N. Fittinghoff, J. A. Squier, C. P. J. Barty, J. N. Sweetser, R. Trebino, and M. Muller. Collinear type ii second-harmonic-generation frequency-resolved optical gating for use with high-numerical-aperture objectives. *Optics Letters*, 23(13):1046–1048, 1998.

[116] I. Amat-Roldan, I. G. Cormack, P. Loza-Alvarez, E. J. Gualda, and D. Artigas. Ultrashort pulse characterisation with shg collinear-frog. *Optics Express*, 12(6):1169–1178, 2004.

[117] G. Stibenz and G. Steinmeyer. Interferometric frequency-resolved optical gating. *Optics Express*, 13(7):2617–2626, 2005.

[118] FemtoSoft Technologies. Frog 3.2.2, http://femtosoft.biz.

[119] V. V. Lozovoy, I. Pastirk, and M. Dantus. Multiphoton intrapulse interference. iv. ultrashort laser pulse spectral phase characterization and compensation. *Optics Letters*, 29(7):775–777, 2004.

[120] V. V. Lozovoy, B. Xu, Y. Coello, and M. Dantus. Direct measurement of spectral phase for ultrashort laser pulses. *Optics Express*, 16(2):592–597, 2008.

[121] W. J. Walecki, D. N. Fittinghoff, A. L. Smirl, and R. Trebino. Characterization of the polarization state of weak ultrashort coherent signals by dual-channel spectral interferometry. *Optics Letters*, 22(2):81–83, 1997.

[122] P. F. Moulton. Spectroscopic and laser characteristics of ti-al2o3. *Journal of the Optical Society of America B-Optical Physics*, 3(1):125–133, 1986.

[123] D. E. Spence, P. N. Kean, and W. Sibbett. 60-fsec pulse generation from a self-mode-locked ti-sapphire laser. *Optics Letters*, 16(1):42–44, 1991.

[124] M. T. Asaki, C. P. Huang, D. Garvey, J. P. Zhou, H. C. Kapteyn, and M. M. Murnane. Generation of 11-fs pulses from a self-mode-locked ti-sapphire laser. *Optics Letters*, 18(12):977–979, 1993.

[125] R. Szipocs and A. KohaziKis. Theory and design of chirped dielectric laser mirrors. *Applied Physics B-Lasers and Optics*, 65(2):115–135, 1997.

[126] D. Strickland and G. Mourou. Compression of amplified chirped optical pulses. *Optics Communications*, 55(6):447–449, 1985.

[127] O. E. Martinez. Grating and prism compressors in the case of finite beam size. *Journal of the Optical Society of America B-Optical Physics*, 3(7):929–934, 1986.

[128] S. A. Trushin, S. Panja, K. Kosma, W. E. Schmid, and W. Fuss. Supercontinuum extending from > 1000 to 250 nm, generated by focusing ten-fs laser pulses at 805 nm into ar. *Applied Physics B-Lasers and Optics*, 80(4-5):399–403, 2005.

[129] C. P. Hauri, W. Kornelis, F. W. Helbing, A. Heinrich, A. Couairon, A. Mysyrowicz, J. Biegert, and U. Keller. Generation of intense, carrier-envelope phase-locked few-cycle laser pulses through filamentation. *Applied Physics B-Lasers and Optics*, 79(6):673–677, 2004.

[130] R. Ackermann, G. Mejean, J. Kasparian, J. Yu, E. Salmon, and J. P. Wolf. Laser filaments generated and transmitted in highly turbulent air. *Optics Letters*, 31(1):86–88, 2006.

[131] S. Bendersky, N. S. Kopeika, and N. Blaunstein. Atmospheric optical turbulence over land in middle east coastal environments: prediction modeling and measurements. *Applied Optics*, 43(20):4070–4079, 2004.

[132] P. Bejot. *Theoretical and experimental investigation of ultrashort laser filamentation in gases*. PhD thesis, University of Geneva, 2008.

[133] Y. Nakayama, P. J. Pauzauskie, A. Radenovic, R. M. Onorato, R. J. Saykally, J. Liphardt, and P. D. Yang. Tunable nanowire nonlinear optical probe. *Nature*, 447(7148):1098–U8, 2007.

[134] L. Le Xuan, C. Zhou, A. Slablab, D. Chauvat, C. Tard, S. Perruchas, T. Gacoin, P. Villeval, and J. F. Roch. Photostable second-harmonic generation from a single ktiopo4 nanocrystal for nonlinear microscopy. *Small*, 4(9):1332–1336, 2008.

[135] A. V. Kachynski, A. N. Kuzmin, M. Nyk, I. Roy, and P. N. Prasad. Zinc oxide nanocrystals for nonresonant nonlinear optical microscopy in biology and medicine. *Journal of Physical Chemistry C*, 112(29):10721–10724, 2008.

[136] C. L. Hsieh, R. Grange, Y. Pu, and D. Psaltis. Three-dimensional harmonic holographic microcopy using nanoparticles as probes for cell imaging. *Optics Express*, 17(4):2880–2891, 2009.

[137] J. P. Jolivet, C. Froidefond, A. Pottier, C. Chaneac, S. Cassaignon, E. Tronc, and P. Euzen. Size tailoring of oxide nanoparticles by precipitation in aqueous medium. a semi-quantitative modelling. *Journal of Materials Chemistry*, 14(21):3281–3288, 2004.

[138] C. Galez, Y. Mugnier, J. Bouillot, Y. Lambert, and R. Le Dantec. Synthesis and characterisation of fe(io3)(3) nanosized powder. *Journal of Alloys and Compounds*, 416(1-2):261–264, 2006.

[139] K. Komorowska, S. Brasselet, G. Dutier, I. Ledoux, J. Zyss, L. Poulsen, M. Jazdzyk, H. Egelhaaf, J. Gierschner, and M. Hanack. Nanometric scale investigation of the nonlinear efficiency of perhydrotriphenylene inclusion compounds. *Chemical Physics*, 318(1-2):12–20, 2005.

[140] L. Bonacina, Y. Mugnier, F. Courvoisier, R. Le Dantec, J. Extermann, Y. Lambert, V. Boutou, C. Galez, and J. P. Wolf. Polar fe(io3)(3) nanocrystals as local probes for nonlinear microscopy. *Applied Physics B-Lasers and Optics*, 87(3):399–403, 2007.

[141] D. Phanon, B. Bentria, E. Jeanneau, D. Benbertal, A. Mosset, and I. Gautier-Luneau. Crystal structure of m(io3)(2) metal iodates, twinned by pseudo-merohedry, with m-ii: Mg-ii, mn-ii, co-ii, ni-ii and zn-ii. *Zeitschrift Fur Kristallographie*, 221(9):635–642, 2006.

[142] K. Kato. High-power difference-frequency-generation at 4.4-5.7 mu-m in liio3. *Ieee Journal of Quantum Electronics*, 21(2):119–120, 1985.

[143] V.G. Dmitriev, G.G. Gurzadyan, and D.N. Nikogosyan. *Handbook of Nonlinear Optical Crystals*. Optical Sciences. Springer, third edition edition, 1999.

[144] G. A. Blab, P. H. M. Lommerse, L. Cognet, G. S. Harms, and T. Schmidt. Two-photon excitation action cross-sections of the autofluorescent proteins. *Chemical Physics Letters*, 350(1-2):71–77, 2001.

[145] K. Nassau, J. W. Shiever, and B. E. Prescott. Transition-metal iodates .1. preparation and characterization of 3d iodates. *Journal of Solid State Chemistry*, 7(2):186–204, 1973.

[146] S. C. Abrahams, R. C. Sherwood, Bernstei.Jl, and K. Nassau. Transition-metal iodates .2. crystallographic, magnetic, and nonlinear optic survey of 3d iodates. *Journal of Solid State Chemistry*, 7(2):205–212, 1973.

[147] R. L. Sutherland. *Handbook of nonlinear optics*. Marcel Dekker, London, second edition edition, 2003.

[148] L. Moreaux, O. Sandre, and J. Mertz. Membrane imaging by second-harmonic generation microscopy. *Journal of the Optical Society of America B-Optical Physics*, 17(10):1685–1694, 2000.

[149] D. Debarre, W. Supatto, and E. Beaurepaire. Structure sensitivity in third-harmonic generation microscopy. *Optics Letters*, 30(16):2134–2136, 2005.

[150] M. Siltanen, S. Cattaneo, E. Vuorimaa, H. Lemmetyinen, T. J. Katz, K. E. S. Phillips, and M. Kauranen. A regression technique to analyze the second-order nonlinear optical response of thin films. *Journal of Chemical Physics*, 121(1):1–4, 2004.

[151] E. Delahaye, N. Tancrez, T. Yi, I. Ledoux, J. Zyss, S. Brasselet, and R. Clement. Second harmonic generation from individual hybrid mnps3-based nanoparticles investigated by nonlinear microscopy. *Chemical Physics Letters*, 429(4-6):533–537, 2006.

[152] M. Aufray, S. Menuel, Y. Fort, J. Eschbach, D. Rouxel, and B. Vincent. New synthesis of nanosized niobium oxides and lithium niobate particles and their characterization by xps analysis. *Journal of Nanoscience and Nanotechnology*, 9(8):4780–4785, 2009.

[153] R. Grange, J. W. Choi, C. L. Hsieh, Y. Pu, A. Magrez, R. Smajda, L. Forro, and D. Psaltis. Lithium niobate nanowires synthesis, optical properties, and manipulation. *Applied Physics Letters*, 95(14):143105, 2009.

[154] E. M. Rodriguez, A. Speghini, F. Piccinelli, L. Nodari, M. Bettinelli, D. Jaque, and J. G. Sole. Multicolour second harmonic generation by strontium barium niobate nanoparticles. *Journal of Physics D-Applied Physics*, 42(10):102003, 2009.

[155] B. Boulanger, J. P. Feve, G. Marnier, B. Menaert, X. Cabirol, P. Villeval, and C. Bonnin. Relative sign and absolute magnitude of d(2) nonlinear coefficients of ktp from 2nd-harmonic-generation measurements. *Journal of the Optical Society of America B-Optical Physics*, 11(5):750–757, 1994.

[156] J. Liu, Z. Shen, W. Yao, Y. Zhao, and A.K. Mukherjee. Visible and infrared transparency in lead-free bulk batio3 and srtio3 nanoceramics. *Nanotechnology*, 21, 2010.

[157] G. Wang, G. K. L. Wong, and J. B. Ketterson. Redetermination of second-order susceptibility of zinc oxide single crystals. *Applied Optics*, 40(30):5436–5438, 2001.

[158] K. Konig, P. T. C. So, W. W. Mantulin, and E. Gratton. Cellular response to near-infrared femtosecond laser pulses in two-photon microscopes. *Optics Letters*, 22(2):135–136, 1997.

[159] Y.R. Shen. *The principles of nonlinear optics*. John-Wiley and Sons, Hoboken, 2003.

[160] L. H. Wang, S. L. Jacques, and L. Q. Zheng. Mcml - monte-carlo modeling of light transport in multilayered tissues. *Computer Methods and Programs in Biomedicine*, 47(2):131–146, 1995.

[161] Craig F. Bohren and Donald R. Huffmann. *Absorption and Scattering by Small Particles*. Wiley Science paperbacks. Wiley & Sons, New York, 1983.

[162] X. Y. Ma, J. Q. Lu, R. S. Brock, K. M. Jacobs, P. Yang, and X. H. Hu. Determination of complex refractive index of polystyrene microspheres from 370 to 1610 nm. *Physics in Medicine and Biology*, 48(24):4165–4172, 2003.

[163] P. Parsa, S. L. Jacques, and N. S. Nishioka. Optical-properties of rat-liver between 350 and 2200 nm. *Applied Optics*, 28(12):2325–2330, 1989.

[164] B. B. Das, F. Liu, and R. R. Alfano. Time-resolved fluorescence and photon migration studies in biomedical and model random media. *Reports on Progress in Physics*, 60(2):227–292, 1997.

[165] A. Volkmer, L. D. Book, and X. S. Xie. Time-resolved coherent anti-stokes raman scattering microscopy: Imaging based on raman free induction decay. *Applied Physics Letters*, 80(9):1505–1507, 2002.

[166] I. Amat-Roldan, I. G. Cormack, P. Loza-Alvarez, and D. Artigas. Starch-based second-harmonic-generated collinear frequency-resolved optical gating pulse characterization at the focal plane of a high-numerical-aperture lens. *Optics Letters*, 29(19):2282–2284, 2004.

[167] C. Spindler, W. Pfeiffer, and T. Brixner. Field control in the tight focus of polarization-shaped laser pulses. *Applied Physics B-Lasers and Optics*, 89(4):553–558, 2007.

[168] T. Brixner, G. Krampert, P. Niklaus, and G. Gerber. Generation and characterization of polarization-shaped femtosecond laser pulses. *Applied Physics B-Lasers and Optics*, 74:S133–S144, 2002.

[169] B. von Vacano, W. Wohlleben, and M. Motzkus. Actively shaped supercontinuum from a photonic crystal fiber for nonlinear coherent microspectroscopy. *Optics Letters*, 31(3):413–415, 2006.

[170] J. Extermann, L. Bonacina, F. Courvoisier, D. Kiselev, Y. Mugnier, R. Le Dantec, C. Galez, and J. P. Wolf. Nano-frog: Frequency resolved optical gating by a nanometric object. *Optics Express*, 16(14):10405–10411, 2008.

[171] G. L. Duveneck, M. Pawlak, D. Neuschafer, E. Bar, W. Budach, and U. Pieles. Novel bioaffinity sensors for trace analysis based on luminescence excitation by planar waveguides. *Sensors and Actuators B-Chemical*, 38(1-3):88–95, 1997.

[172] P. N. Zeller, G. Voirin, and R. E. Kunz. Single-pad scheme for integrated optical fluorescence sensing. *Biosensors & Bioelectronics*, 15(11-12):591–595, 2000.

[173] K. Schmitt, K. Oehse, G. Sulz, and C. Hoffmann. Evanescent field sensors based on tantalum pentoxide waveguides - a review. *Sensors*, 8(2):711–738, 2008.

[174] C. Kappel, A. Selle, T. Fricke-Begemann, M. A. Bader, and G. Marowsky. Giant enhancement of two-photon fluorescence induced by resonant double grating waveguide structures. *Applied Physics B-Lasers and Optics*, 79(5):531–534, 2004.

[175] G. L. Duveneck, M. A. Bopp, M. Ehrat, M. Haiml, U. Keller, M. A. Bader, G. Marowsky, and S. Soria. Evanescent-field-induced two-photon fluorescence: excitation of macroscopic areas of planar waveguides. *Applied Physics B-Lasers and Optics*, 73(8):869–871, 2001.

[176] J. Extermann, L. Bonacina, E. Cuna, C. Kasparian, Y. Mugnier, T. Feurer, and J. P. Wolf. Nanodoublers as deep imaging markers for multi-photon microscopy. *Optics Express*, 17(17):15342–15349, 2009.

[177] L. Le Xuan, S. Brasselet, F. Treussart, J. F. Roch, F. Marquier, D. Chauvat, S. Perruchas, C. Tard, and T. Gacoin. Balanced homodyne detection of second-harmonic generation from isolated subwavelength emitters. *Applied Physics Letters*, 89(12):121118, 2006.

[178] P. Wnuk, L. Le Xuan, A. Slablab, C. Tard, S. Perruchas, T. Gacoin, J. F. Roch, D. Chauvat, and C. Radzewicz. Coherent nonlinear emission from a single ktp nanoparticle with broadband femtosecond pulses. *Optics Express*, 17(6):4652–4658, 2009.

[179] J. Extermann, P. Bejot, L. Bonacina, Y. Mugnier, R. Le Dantec, T. Mazingue, C. Galez, and J. P. Wolf. An inexpensive nonlinear medium for intense ultrabroadband pulse characterization. *Applied Physics B-Lasers and Optics*, 97(3):537–540, 2009.

[180] J. Jasny and J. Sepiol. Single molecules observed by immersion mirror objective. a novel method of finding the orientation of a radiating dipole. *Chemical Physics Letters*, 273(5-6):439–443, 1997.

[181] M. Bohmer and J. Enderlein. Orientation imaging of single molecules by wide-field epifluorescence microscopy. *Journal of the Optical Society of America B-Optical Physics*, 20(3):554–559, 2003.

[182] N. Sandeau, L. Le Xuan, D. Chauvat, C. Zhou, J. F. Roch, and S. Brasselet. Defocused imaging of second harmonic generation from a single nanocrystal. *Optics Express*, 15(24):16051–16060, 2007.

[183] J. I. Dadap. Optical second-harmonic scattering from cylindrical particles. *Physical Review B*, 78(20):205322, 2008.

[184] J. M. Dela Cruz, I. Pastirk, M. Comstock, and M. Dantus. Multiphoton intrapulse interference 8. coherent control through scattering tissue. *Optics Express*, 12(17):4144–4149, 2004.

[185] J. P. Ogilvie, E. Beaurepaire, A. Alexandrou, and M. Joffre. Fourier-transform coherent anti-stokes raman scattering microscopy. *Optics Letters*, 31(4):480–482, 2006.

[186] J. F. Chen, H. Kawano, Y. Nabekawa, H. Mizuno, A. Miyawaki, T. Tanabe, F. Kannari, and K. Midorikawa. Selective excitation between two-photon and three-photon fluorescence with engineered cost functions. *Optics Express*, 12(15):3408–3414, 2004.

[187] I. Otake, S. S. Kano, and A. Wada. Pulse shaping effect on two-photon excitation efficiency of alpha-perylene crystals and perylene in chloroform solution. *Journal of Chemical Physics*, 124(1):014501, 2006.

[188] J. P. Gordon, R. L. Fork, and O. E. Martinez. Negative dispersion from prisms. *Journal of the Optical Society of America B-Optical Physics*, 1(3):437–437, 1984.

[189] R. L. Fork, O. E. Martinez, and J. P. Gordon. Negative dispersion using pairs of prisms. *Optics Letters*, 9(5):150–152, 1984.

[190] A. Monmayrant and B. Chatel. New phase and amplitude high resolution pulse shaper. *Review of Scientific Instruments*, 75(8):2668–2671, 2004.

[191] A. Monmayrant. *Faconnage et caracterisation d'impulsions ultracourtes. Controle Coherent de systemes simples.* PhD thesis, University Paul Sabatier, 2005.

[192] T. Brixner and G. Gerber. Femtosecond polarization pulse shaping. *Optics Letters*, 26(8):557–559, 2001.

[193] T. Brixner, W. Pfeiffer, and F. J. G. de Abajo. Femtosecond shaping of transverse and longitudinal light polarization. *Optics Letters*, 29(18):2187–2189, 2004.

[194] L. Polachek, D. Oron, and Y. Silberberg. Full control of the spectral polarization of ultrashort pulses. *Optics Letters*, 31(5):631–633, 2006.

[195] M. Plewicki, S. M. Weber, F. Weise, and A. Lindinger. Independent control over the amplitude, phase, and polarization of femtosecond pulses. *Applied Physics B-Lasers and Optics*, 86(2):259–263, 2007.

[196] R. Selle, P. Nuernberger, F. Langhojer, F. Dimler, S. Fechner, G. Gerber, and T. Brixner. Generation of polarization-shaped ultraviolet femtosecond pulses. *Optics Letters*, 33(8):803–805, 2008.

[197] M. Ninck, A. Galler, T. Feurer, and T. Brixner. Programmable common-path vector field synthesizer for femtosecond pulses. *Optics Letters*, 32(23):3379–3381, 2007.

[198] F. Weise and A. Lindinger. Full control over the electric field using four liquid crystal arrays. *Optics Letters*, 34(8):1258–1260, 2009.

[199] O. Masihzadeh, P. Schlup, and R. A. Bartels. Complete polarization state control of ultrafast laser pulses with a single linear spatial light modulator. *Optics Express*, 15(26):18025–18032, 2007.

[200] M. B. Danailov and I. P. Christov. Time-space shaping of light-pulses by fourier optical-processing. *Journal of Modern Optics*, 36(6):725–731, 1989.

[201] M. M. Wefers and K. A. Nelson. Space-time profiles of shaped ultrafast optical waveforms. *Ieee Journal of Quantum Electronics*, 32(1):161–172, 1996.

[202] T. Feurer, J. C. Vaughan, R. M. Koehl, and K. A. Nelson. Multidimensional control of femtosecond pulses by use of a programmable liquid-crystal matrix. *Optics Letters*, 27(8):652–654, 2002.

[203] J. C. Vaughan, T. Hornung, T. Feurer, and K. A. Nelson. Diffraction-based femtosecond pulse shaping with a two-dimensional spatial light modulator. *Optics Letters*, 30(3):323–325, 2005.

[204] E. Frumker and Y. Silberberg. Femtosecond pulse shaping using a two-dimensional liquid-crystal spatial light modulator. *Optics Letters*, 32(11):1384–1386, 2007.

[205] Y. Esumi, M. D. Kabir, and F. Kannari. Spatiotemporal vector pulse shaping of femtosecond laser pulses with a multi-pass two-dimensional spatial light modulator. *Optics Express*, 17(21):19153–19159, 2009.

[206] C. W. Hillegas, J. X. Tull, D. Goswami, D. Strickland, and W. S. Warren. Femtosecond laser-pulse shaping by use of microsecond radiofrequency pulses. *Optics Letters*, 19(10):737–739, 1994.

[207] P. Tournois. Acousto-optic programmable dispersive filter for adaptive compensation of group delay time dispersion in laser systems. *Optics Communications*, 140(4-6):245–249, 1997.

[208] F. Verluise, V. Laude, Z. Cheng, C. Spielmann, and P. Tournois. Amplitude and phase control of ultrashort pulses by use of an acousto-optic programmable dispersive filter: pulse compression and shaping. *Optics Letters*, 25(8):575–577, 2000.

[209] A. Monmayrant, A. Arbouet, B. Girard, B. Chatel, A. Barman, B. J. Whitaker, and D. Kaplan. Aopdf-shaped optical parametric amplifier output in the visible. *Applied Physics B-Lasers and Optics*, 81(2-3):177–180, 2005.

[210] P. Tournois. Design of acousto-optic programmable filters in mercury halides for mid-infrared laser pulse shaping. *Optics Communications*, 281(15-16):4054–4056, 2008.

[211] M. R. Armstrong, P. Plachta, E. A. Ponomarev, and R. J. D. Miller. Versatile 7-fs optical parametric pulse generation and compression by use of adaptive optics. *Optics Letters*, 26(15):1152–1154, 2001.

[212] A. Baltuska and T. Kobayashi. Adaptive shaping of two-cycle visible pulses using a flexible mirror. *Applied Physics B-Lasers and Optics*, 75(4-5):427–443, 2002.

[213] P. Baum, S. Lochbrunner, L. Gallmann, G. Steinmeyer, U. Keller, and E. Riedle. Real-time characterization and optimal phase control of tunable visible pulses with a flexible compressor. *Applied Physics B-Lasers and Optics*, 74:S219–S224, 2002.

[214] P.G. de Gennes and J. Prost. *The Physics of Liquid Crystals*. Oxford University Press, Oxford, 2003.

[215] M. M. Wefers and K. A. Nelson. Generation of high-fidelity programmable ultrafast optical wave-forms. *Optics Letters*, 20(9):1047–1049, 1995.

[216] F. Courvoisier, L. Bonacina, V. Boutou, L. Guyon, C. Bonnet, B. Thuillier, J. Extermann, M. Roth, H. Rabitz, and J. P. Wolf. Identification of biological microparticles using ultrafast depletion spectroscopy. *Faraday Discussions*, 137:37–49, 2008.

[217] A. Gehner. Active-matrix addressed micromirror array for wavefront correction in adaptive optics. *Proceedings of SPIE*, 4561:265 – 275, 2001.

[218] M. Knapczyk, A. Krishnan, L. G. de Peralta, A. A. Bernussi, and H. Temkin. High-resolution pulse shaper based on arrays of digital micromirrors. *Ieee Photonics Technology Letters*, 17(10):2200–2202, 2005.

[219] S. Postma. *Spectral Phase Shaping*. PhD thesis, University of Twente, 2008.

[220] M. Dantus and V. V. Lozovoy. Experimental coherent laser control of physicochemical processes. *Chemical Reviews*, 104(4):1813–1859, 2004.

[221] J. W. Wilson, P. Schlup, M. Lunacek, D. Whitley, and R. A. Bartels. Calibration of liquid crystal ultrafast pulse shaper with common-path spectral interferometry and application to coherent control with a covariance matrix adaptation evolutionary strategy. *Review of Scientific Instruments*, 79(3):033103, 2008.

[222] K. Hazu, T. Sekikawa, and M. Yamashita. Spatial right modulator with an over-two-octave bandwidth from ultraviolet to near infrared. *Optics Letters*, 32(22):3318–3320, 2007.

[223] T. Tanigawa, Y. Sakakibara, S. B. Fang, T. Sekikawa, and M. Yamashita. Spatial light modulator of 648 pixels with liquid crystal transparent from ultraviolet to near-infrared and its chirp compensation application. *Optics Letters*, 34(11):1696–1698, 2009.

[224] D. Yelin, D. Meshulach, and Y. Silberberg. Adaptive femtosecond pulse compression. *Optics Letters*, 22(23):1793–1795, 1997.

[225] G. Stobrawa, M. Hacker, T. Feurer, D. Zeidler, M. Motzkus, and F. Reichel. A new high-resolution femtosecond pulse shaper. *Applied Physics B-Lasers and Optics*, 72(5):627–630, 2001.

[226] J. W. Wilson, P. Schlup, and R. A. Bartels. Ultrafast phase and amplitude pulse shaping with a single, one-dimensional, high-resolution phase mask. *Optics Express*, 15(14):8979–8987, 2007.

[227] S. Postma, P. van der Walle, H. L. Offerhaus, and N. F. van Hulst. Compact high-resolution spectral phase shaper. *Review of Scientific Instruments*, 76(12):123105, 2005.

[228] M. M. Wefers and K. A. Nelson. Analysis of programmable ultrashort waveform generation using liquid-crystal spatial light modulators. *Journal of the Optical Society of America B-Optical Physics*, 12(7):1343–1362, 1995.

[229] J. C. Vaughan, T. Feurer, K. W. Stone, and K. A. Nelson. Analysis of replica pulses in femtosecond pulse shaping with pixelated devices. *Optics Express*, 14(3):1314–1328, 2006.

[230] S. Weber, M. Barthelemy, and B. Chatel. Direct shaping of tunable uv ultrashort pulses. *Applied Physics B-Lasers and Optics*, 98(2-3):323–326, 2010.

[231] B. J. Sussman, R. Lausten, and A. Stolow. Focusing of light following a 4-f pulse shaper: Considerations for quantum control. *Physical Review A*, 77(4):043416, 2008.

[232] F. Frei, A. Galler, and T. Feurer. Space-time coupling in femtosecond pulse shaping and its effects on coherent control. *Journal of Chemical Physics*, 130(3):034302, 2009.

[233] M. A. Coughlan, M. Plewicki, and R. J. Levis. Parametric spatio-temporal control of focusing laser pulses. *Optics Express*, 17(18):15808–15820, 2009.

[234] T. Overstoltz. *Tunable Optical Microsystems featuring Vertical Electrostatic Comb Drives*. PhD thesis, University of Neuchatel, 2007.

[235] L. Landau and E. Lifchitz. *Theorie de l'Elasticite*. Editions Mir, Moscou, 1967.

[236] S.P. Timoshenko and J.N. Goodier. *Theory of Elasticity*. McGraw-Hill Book Co, New York, 1970.

[237] D. Kiselev. *Developpement d'un faconneur d'impulsions a large bande base sur des matrices de micromiroirs*. Master, University of Geneva, 2007.

[238] D. Meshulach and Y. Silberberg. Coherent quantum control of multiphoton transitions by shaped ultrashort optical pulses. *Physical Review A*, 60(2):1287–1292, 1999.

[239] N. Dudovich, B. Dayan, S. M. G. Faeder, and Y. Silberberg. Transform-limited pulses are not optimal for resonant multiphoton transitions. *Physical Review Letters*, 86(1):47–50, 2001.

[240] N. Dudovich, D. Oron, and Y. Silberberg. Quantum control of the angular momentum distribution in multiphoton absorption processes. *Physical Review Letters*, 92(10):103003, 2004.

[241] N. Dudovich, T. Polack, A. Pe'er, and Y. Silberberg. Simple route to strong-field coherent control. *Physical Review Letters*, 94(8):083002, 2005.

[242] S. Postma, A. C. W. van Rhijn, J. P. Korterik, P. Gross, J. L. Herek, and H. L. Offerhaus. Application of spectral phase shaping to high resolution cars spectroscopy. *Optics Express*, 16(11):7985–7996, 2008.

[243] A. C. W. van Rhijn, S. Postma, J. P. Korterik, J. L. Herek, and H. L. Offerhaus. Chemically selective imaging by spectral phase shaping for broadband cars around 3000 cm(-1). *Journal of the Optical Society of America B-Optical Physics*, 26(3):559–563, 2009.

[244] T. Brixner and G. Gerber. Quantum control of gas-phase and liquid-phase femtochemistry. *Chemphyschem*, 4(5):418–438, 2003.

[245] P. Nuernberger, G. Vogt, T. Brixner, and G. Gerber. Femtosecond quantum control of molecular dynamics in the condensed phase. *Physical Chemistry Chemical Physics*, 9(20):2470–2497, 2007.

[246] G. Turinici, C. Le Bris, and H. Rabitz. Efficient algorithms for the laboratory discovery of optimal quantum controls. *Physical Review E*, 70(1):016704, 2004.

[247] Y. Ohtsuki, G. Turinici, and H. Rabitz. Generalized monotonically convergent algorithms for solving quantum optimal control problems. *Journal of Chemical Physics*, 120(12):5509–5517, 2004.

[248] J. Roslund and H. Rabitz. Gradient algorithm applied to laboratory quantum control. *Physical Review A*, 79(5):053417, 2009.

[249] A. Jafarpour, J. Savolainen, R. de Jong, J. Middag, D. P. Sprunken, P. van der Walle, D. Yang, and J. L. Herek. Robust orthogonal parameterization of evolution strategy for adaptive laser pulse shaping. *Optics Express*, 17(14):11986–12000, 2009.

[250] D.E. Goldberg. *Genetic Algorithms in Search, Optimization, and Machine Learning*. Addison-Wesley Publishing Company, Boston, 1989.

[251] R. Bartels, S. Backus, E. Zeek, L. Misoguti, G. Vdovin, I. P. Christov, M. M. Murnane, and H. C. Kapteyn. Shaped-pulse optimization of coherent emission of high-harmonic soft x-rays. *Nature*, 406(6792):164–166, 2000.

[252] B. J. Pearson, J. L. White, T. C. Weinacht, and P. H. Bucksbaum. Coherent control using adaptive learning algorithms. *Physical Review A*, 6306(6):063412, 2001.

[253] D. Zeidler, S. Frey, K. L. Kompa, and M. Motzkus. Evolutionary algorithms and their application to optimal control studies. *Physical Review A*, 64(2):023420, 2001.

[254] T. Brixner, N. H. Damrauer, B. Kiefer, and G. Gerber. Liquid-phase adaptive femtosecond quantum control: Removing intrinsic intensity dependencies. *Journal of Chemical Physics*, 118(8):3692–3701, 2003.

[255] A. F. Bartelt, M. Roth, M. Mehendale, and H. Rabitz. Assuring robustness to noise in optimal quantum control experiments. *Physical Review A*, 71(6):063806, 2005.

[256] A. Lindinger, S. M. Weber, C. Lupulescu, F. Vetter, M. Plewicki, A. Merli, L. Woste, A. F. Bartelt, and H. Rabitz. Revealing spectral field features and mechanistic insights by control pulse cleaning. *Physical Review A*, 71(1):013419, 2005.

[257] T. Hornung, M. Motzkus, and R. de Vivie-Riedle. Teaching optimal control theory to distill robust pulses even under experimental constraints. *Physical Review A*, 65(2):021403, 2002.

[258] J. Roslund, M. Roth, and H. Rabitz. Laboratory observation of quantum control level sets. *Physical Review A*, 74(4):043414, 2006.

[259] K. Deb, A. Pratap, S. Agarwal, and T. Meyarivan. A fast and elitist multiobjective genetic algorithm: Nsga-ii. *Ieee Transactions on Evolutionary Computation*, 6(2):182–197, 2002.

[260] P. F. Heelis. The photophysical and photochemical properties of flavins (isoalloxazines). *Chemical Society Reviews*, 11(1):15–39, 1982.

[261] F. Courvoisier, V. Boutou, L. Guyon, M. Roth, H. Rabitz, and J. P. Wolf. Discriminating bacteria from other atmospheric particles using femtosecond molecular dynamics. *Journal of Photochemistry and Photobiology a-Chemistry*, 180(3):300–306, 2006.

[262] T. Baumert, T. Brixner, V. Seyfried, M. Strehle, and G. Gerber. Femtosecond pulse shaping by an evolutionary algorithm with feedback. *Applied Physics B-Lasers and Optics*, 65(6):779–782, 1997.

[263] J. P. Ogilvie, K. J. Kubarych, A. Alexandrou, and M. Joffre. Fourier transform measurement of two-photon excitation spectra: applications to microscopy and optimal control. *Optics Letters*, 30(8):911–913, 2005.

[264] K. A. Walowicz, I. Pastirk, V. V. Lozovoy, and M. Dantus. Multiphoton intrapulse interference. 1. control of multiphoton processes in condensed phases. *Journal of Physical Chemistry A*, 106(41):9369–9373, 2002.

[265] M. Roth, J. Roslund, and H. Rabitz. Assessing and managing laser system stability for quantum control experiments. *Review of Scientific Instruments*, 77(8):083107, 2006.

[266] E. C. Carroll, A. C. Florean, P. H. Bucksbaurn, K. G. Spears, and R. J. Sension. Phase control of the competition between electronic transitions in a solvated laser dye. *Chemical Physics*, 350(1-3):75–86, 2008.

[267] L. Bonacina, J. Extermann, A. Rondi, V. Boutou, and J. P. Wolf. Multiobjective genetic approach for optimal control of photoinduced processes. *Physical Review A*, 76(2):023408, 2007.

[268] X. Gu, S. Akturk, and R. Trebino. Spatial chirp in ultrafast optics. *Optics Communications*, 242(4-6):599–604, 2004.

[269] S. M. Weber, F. Sauer, M. Plewicki, A. Merli, L. Woste, and A. Lindinger. Multi-objective optimization on alkali dimers. *Journal of Modern Optics*, 54(16-17):2659–2666, 2007.

[270] R. Chakrabarti, R. B. Wu, and H. Rabitz. Quantum pareto optimal control. *Physical Review A*, 78(3):033414, 2008.

[271] C. Gollub and R. de Vivie-Riedle. Multi-objective genetic algorithm optimization of 2d-and 3d-pareto fronts for vibrational quantum processes. *New Journal of Physics*, 11:013019, 2009.

[272] N. Hansen and A. Ostermeier. Completely derandomized self-adaptation in evolution strategies. *Evolutionary Computation*, 9(2):159–195, 2001.

[273] J. Roslund, O. M. Shir, T. Back, and H. Rabitz. Accelerated optimization and automated discovery with covariance matrix adaptation for experimental quantum control. *Physical Review A*, 80(4):043415, 2009.

[274] C. Igel, N. Hansen, and S. Roth. Covariance matrix adaptation for multi-objective optimization. *Evolutionary Computation*, 15(1):1–28, 2007.

[275] J. Roslund and H. Rabitz. Experimental quantum control landscapes: Inherent monotonicity and artificial structure. *Physical Review A*, 80(1):013408, 2009.

[276] P. van der Walle, J. Savolainen, L. Kuipers, and J. L. Herek. Learning from evolutionary optimization by retracing search paths. *Chemical Physics Letters*, 483(1-3):164–167, 2009.

[277] P. van der Walle, H. Offerhaus, J. Herek, and A. Jafarpour. Tailoring a coherent control solution landscape by linear transforms of spectral phase basis. *Optics Express*, 18(2):973–987, 2010.

[278] M. Kotur, T. Weinacht, B. J. Pearson, and S. Matsika. Closed-loop learning control of isomerization using shaped ultrafast laser pulses in the deep ultraviolet. *Journal of Chemical Physics*, 130(13):134311, 2009.

[279] C. H. Tseng, S. Matsika, and T. C. Weinacht. Two-dimensional ultrafast fourier transform spectroscopy in the deep ultraviolet. *Optics Express*, 17(21):18788–18793, 2009.

[280] J. Mohring, T. Buckup, C. S. Lehmann, and M. Motzkus. Generation of phase-controlled ultraviolet pulses and characterization by a simple autocorrelator setup. *Journal of the Optical Society of America B-Optical Physics*, 26(8):1538–1544, 2009.

[281] J. Kasparian, M. Rodriguez, G. Mejean, J. Yu, E. Salmon, H. Wille, R. Bourayou, S. Frey, Y. B. Andre, A. Mysyrowicz, R. Sauerbrey, J. P. Wolf, and L. Woste. White-light filaments for atmospheric analysis. *Science*, 301(5629):61–64, 2003.

[282] K. Stelmaszczyk, P. Rohwetter, G. Mejean, J. Yu, E. Salmon, J. Kasparian, R. Ackermann, J. P. Wolf, and L. Woste. Long-distance remote laser-induced breakdown spectroscopy using filamentation in air. *Applied Physics Letters*, 85(18):3977–3979, 2004.

[283] O. Katz, A. Natan, Y. Silberberg, and S. Rosenwaks. Standoff detection of trace amounts of solids by nonlinear raman spectroscopy using shaped femtosecond pulses. *Applied Physics Letters*, 92(17):171116, 2008.

[284] H. W. Li, D. A. Harris, B. Xu, P. J. Wrzesinski, V. V. Lozovoy, and M. Dantus. Coherent mode-selective raman excitation towards standoff detection. *Optics Express*, 16(8):5499–5504, 2008.

[285] G. Mejean, J. Kasparian, E. Salmon, J. Yu, J. P. Wolf, R. Bourayou, R. Sauerbrey, M. Rodriguez, L. Woste, H. Lehmann, B. Stecklum, U. Laux, J. Eisloffel, A. Scholz, and A. P. Hatzes. Towards a supercontinuum-based infrared lidar. *Applied Physics B-Lasers and Optics*, 77(2-3):357–359, 2003.

[286] R. Ackermann, E. Salmon, N. Lascoux, J. Kasparian, P. Rohwetter, K. Stelmaszczyk, S. H. Li, A. Lindinger, L. Woste, P. Bejot, L. Bonacina, and J. P. Wolf. Optimal control of filamentation in air. *Applied Physics Letters*, 89(17):171117, 2006.

[287] H. Wille, M. Rodriguez, J. Kasparian, D. Mondelain, J. Yu, A. Mysyrowicz, R. Sauerbrey, J. P. Wolf, and L. Woste. Teramobile: A mobile femtosecond-terawatt laser and detection system. *European Physical Journal-Applied Physics*, 20(3):183–190, 2002.

[288] I. Pastirk, X. Zhu, R. M. Martin, and M. Dantus. Remote characterization and dispersion compensation of amplified shaped femtosecond pulses using miips. *Optics Express*, 14(19):8885–8889, 2006.

[289] J.W. Goodman. *Statistical Optics*. Wiley, New York, 2000.

[290] G.K. Batchelor. *The Theory of homogeneous turbulence*. Cambridge University Press, Cambridge, 1982.

[291] A. N. Kolmogorov. The local-structure of turbulence in incompressible viscous-fluid for very large reynolds-numbers. *Proceedings of the Royal Society of London Series a-Mathematical Physical and Engineering Sciences*, 434(1890):9–13, 1991.

[292] A. N. Kolmogorov. Dissipation of energy in the locally isotropic turbulence. *Proceedings of the Royal Society of London Series a-Mathematical Physical and Engineering Sciences*, 434(1890):15–17, 1991.

[293] C. M. Harding, R. A. Johnston, and R. G. Lane. Fast simulation of a kolmogorov phase screen. *Applied Optics*, 38(11):2161–2170, 1999.

[294] W. J. Liu and C. H. Zhou. Femtosecond laser speckles. *Applied Optics*, 44(30):6506–6510, 2005.

[295] R. Foy, A. Migus, F. Biraben, G. Grynberg, P. R. Mccullough, and M. Tallon. The polychromatic artificial sodium star - a new concept for correcting the atmospheric tilt. *Astronomy and Astrophysics Supplement Series*, 111(3):569–578, 1995.

[296] I. M. Vellekoop and A. P. Mosk. Universal optimal transmission of light through disordered materials. *Physical Review Letters*, 101(12):120601, 2008.

[297] I. M. Vellekoop and A. P. Mosk. Focusing coherent light through opaque strongly scattering media. *Optics Letters*, 32(16):2309–2311, 2007.

[298] M. Fink, D. Cassereau, A. Derode, C. Prada, P. Roux, M. Tanter, J. L. Thomas, and F. Wu. Time-reversed acoustics. *Reports on Progress in Physics*, 63(12):1933–1995, 2000.

[299] J. L. Robert and M. Fink. Green's function estimation in speckle using the decomposition of the time reversal operator: Application to aberration correction in medical imaging. *Journal of the Acoustical Society of America*, 123(2):866–877, 2008.

[300] M. Roth, L. Guyon, J. Roslund, V. Boutou, F. Courvoisier, J. P. Wolf, and H. Rabitz. Quantum control of tightly competitive product channels. *Physical Review Letters*, 102(25):253001, 2009.

[301] J. C. Owens. Optical refractive index of air - dependence on pressure temperature and composition. *Applied Optics*, 6(1):51–59, 1967.

[302] I. M. Vellekoop, A. Lagendijk, and A. P. Mosk. Exploiting disorder for perfect focusing. *Nature Photonics*, page doi:10.1038/nphoton.2010.3, 2010.

[303] S. M. Popoff, G. Lerosey, R. Carminati, M. Fink, A. C. Boccara, and S. Gigan. Measuring the transmission matrix in optics: An approach to the study and control of light propagation in disordered media. *Physical Review Letters*, 104(10):100601, 2010.